Estimation of crop key traits from multi-source remote sensing technologies

Wenjuan Li Wang

THÈSE DE DOCTORAT D'AVIGNON UNIVERSITÉ

École Doctorale N° 536

Agrosciences et Sciences

Spécialité / Discipline de doctorat : Télédétection de la Végétation

INRAE UMR 1114 EMMAH - UMT CAPTE (CAPteurs et TElédétection)

Présentée par

Wenjuan Li

Estimation of crop key traits from multi-source remote sensing technologies

---

Soutenance publique: 13 December 2021

Jury composé de:

Dr. Stéphane Jacquemoud	Institut de Physique du Globe de Paris, Université de Paris	Rapporteur
Dr. Katja Berger	Ludwig-Maximilians-Universität München	Rapporteur
Dr. Frederic Baret	EMMAH-CAPTE, INRAE Avignon	Directeur de thèse
Dr. Marie Weiss	EMMAH-CAPTE, INRAE Avignon	Co-encadrant de thèse
Dr. Sylvain Jay	EMMAH-CAPTE, INRAE Avignon	Co-encadrant de thèse
Dr. Aleixandre Verger	Desertification Research Centre, CIDE-CSIC Ecology and Global Change	Examinateur

Encadrement de la thèse : Dr Frederic Baret, Dr Marie Weiss, Dr Sylvain Jay

1 Acknowledgements

Time flies. When I look back to the past seven years spent in UMT CAPTE, many beautiful images appear in my mind.

I would first like to thank my supervisor, Dr Frederic Baret. If he had not accepted me into the IMAGINES program, I might not have come to France to start this new journey. During my time spent with him, I am very grateful for his supports on research and life, and I am deeply impressed by his wisdom, scientific rigor and hard work. I am also very grateful to Dr Maire Weiss for her help in my work and life. Each time I communicate with her, I am impressed by her positive and optimistic working attitude, as well as her love for research and her strong ability in research and applications. I have learned a lot from her. Thanks to Dr Sylvain Jay for his contribution to my thesis and papers. He takes each manuscript very seriously and is very responsible. Thanks to Benoit, Raul, Samuel, Jingyi, Simon, Kaaviya, and other colleagues in CAPTE, I am glad to have the opportunity to work with you.

I have worked for HIPHEN for four years. It was a great honour to have the opportunity to work with Dr Alexis Comar. I thank Alexis for offering me this opportunity to learn about the practical applications of remote sensing in industry and to learn amount of new knowledge related to phenotyping and smart agriculture. I benefit a lot from these experiences. I also want to express my thanks to my colleagues in HIPHEN. There are many nice memories when we worked together and closely to solve problems and worked on new projects.

I would like to thank my husband, my son and my family, as well as my friends in France, China and other countries. Without your supports and encouragements, I would not have been able to accomplish my dream.

Finally, thanks to all experts for your time.

2 List of abbreviations and acronyms

ACI	Apparent clumping index
ANN	Artificial neural networks
APAR	Absorbed PAR by green vegetation
BRDF	Bidirectional Reflectance Distribution Function
BRF	Bi-Directional Reflectance
CEOS	Committee on Earth Observing Satellite
CI	Clumping index
CNES	French Agency Centre National d'Etudes Spatiales
DBF	Deciduous broadleaf forests
DHF	Decametric Hectometric Fusion
DHP	Digital Hemispheric Photography
DNF	Deciduous needleleaf forests
DOY	Day of year
EBF	Evergreen broadleaf forests
ECV	Essential Climate Variables
EMP	Empirical
ENF	Evergreen needleleaf forests
ETM+	Enhanced Thematic Mapper Plus
fAPAR	Fraction of PAR absorbed by the green leaves
fCover	fraction of the green vegetation in the nadir direction
fIPAR	Fraction of PAR intercepted by the green leaves
GAI	Green area index
GCOS	Global Climate Observing System
GfAPAR	Green fAPAR
GfIPAR	Green fIPAR
GPR	Gaussian process regression
IGBP	International Geosphere Biosphere Program
IoT	Internet of things
LAI	Leaf area index
LPV	Land Product Validation
LUT	Look-up table
MAEs	Mean absolute errors
MODIS	Moderate Resolution Imaging Spectroradiometer
MSI	Multi Spectral Instrument
NDVI	Normalized difference vegetation index
NIR	Near infrared
OLI	Operational Land Imager
PAI	plant area indices
PAI_{eff}	the effective plant area indices
PAR	Photosynthetically Active Radiation
RGB	Red, green and blue
RMSE	Root-mean-square deviation
RO	Reproductive organs
RRMSE	Relative RMSE
SIM	Simulation
skyl	Fraction of diffuse PAR in total PAR

SLC	A coupled soil-leaf-canopy radiative transfer model
STARFM	Spatial and temporal adaptive reflectance fusion model
SVM	Support vector machine
TM	Thematic Mapper
UAV	Unmanned aerial vehicle
UGV	Unmanned Ground Vehicles
WGCV	Working Group Cal/Val

Table of Contents

3 Professional career summary

I received my bachelor's degree in the major of Cartography and Geographic Information system in 2008 from Department of Cartography and Geographic Information System, Northeast Normal University, China.

I obtained the master's degree in major "Rangeland remote sensing" under supervision of Prof. Quangong Chen in 2011 from Lanzhou University, China. The title of my master thesis was "The research on Chinese ecotone between agriculture and animal husbandry and population distribution". During the period of master, I worked as research assistant to:

- develop a new method to estimate livestock capacity for local farmers through satellite data and ground measurements.
- conduct data analysis between the population distribution and the ecotone capacity on Chinese Ecotone between agriculture and animal husbandry.

In the second year of my master, I won an opportunity to be exchanged in Chinese Academy of Sciences. From August 2010 to March 2011, I studied in the Institute of Geographic Sciences and Natural Resources Research (IGSNRR), Chinese Academy of Sciences, under the supervision of Prof. Jiulin Sun. My role was to develop a web interface for displaying natural resources and human related data of North-East Asia region. During this year, I read many scientific papers and realized simple vegetation indices had limitations on the applications. The book "quantitative remote sensing of land surfaces" by Prof. Shunlin Liang gave me insights. Inspired by this, I planned to conduct a doctoral degree in this institute on the subject of quantitative remote sensing.

Since September 2011, I was enrolled as a Ph.D candidate in the University of Chinese Academy of Science, China. I worked in the domain of vegetation quantitative remote sensing under the supervision by Prof. Hongliang Fang in the State Key Laboratory of Resources and Environmental Information System (LREIS) based in IGSNRR, Chinese Academy of Science. During the Ph.D period, I was the member of four projects of Prof. Hongliang Fang. Within these projects,

- I conducted the ground measurements of leaf area index (LAI), clumping index and fAPAR in Honghe Farm over rice crops, northeast China during the whole growing season of 2012 and 2013. The performances of different instruments and variable definitions were compared and analyzed.
- I developed an algorithm to estimate total, direct and diffuse fAPAR from remote sensing data.
- I validated the satellite-derived fAPAR products using ground measurements.
- I studied long term MODIS land cover and LAI data to analyze the impact of land cover misclassification on MODIS LAI products.

These studies finally resulted into several scientific paper, published in peer reviewed journals. Based on the ground measurements and algorithms, my thesis titled as "Estimation of direct and diffuse FAPAR from satellite data and field measurements" was finished and I successfully defended it on May 2015.

In the last year of my Ph.D, I wanted to go abroad to see how other teams work. Fortunately, I was hosted in Dr. Frédéric Baret's lab, who is the one of most famous vegetation remote sensing experts in the world. My professional journey in France started in 2014. I worked as a development engineer from May 2014 to February 2015 and post-doc from March 2015 to August 2017 in UMT CAPTE unit of INRAE, under the supervision of Dr. Frédéric Baret. During this period, I mainly participated to two projects: IMAGINES (European Community FP7) and PRECIDRONE (National French FUI).

- In the European project 'IMAGINES', I developed with Dr. Marie Weiss and colleagues from INRAE an algorithm for fusing satellite data PROBA-V and LANDSAT-8 to generate decametric products every 10 days to realize the crop monitoring at the field level with a 30 m resolution,. I also tested the feasibility of neural network inversion algorithms on multiple decametric resolution satellite datasets (e.g., LANDSAT-8 and SPOT-4). The generated biophysical products were finally used as inputs to improve the crop classification accuracy using satellite data.
- I participated to the 'PRECIDRONE' project during 2016 and 2017 and developed algorithms to estimate crop key biophysical variables using drone observations. This contributed to the crop monitoring at higher resolution (~1m) and at the microplot level. The code has been provided to the private company "Delair-Tech" for production purposes under the agreement of the project.

Since September 2017, I have been working as an R&D Scientist on a permanent contract (CDI in France) in the HIPHEN private company. I am in charge of developing innovative algorithms to monitor crop growth status at different scales using data from satellite, drone and field IOT (Internet of things). More specifically, I worked on several aspects with my HIPHEN and INRAE colleagues:

- I developed the processing pipeline of satellite data, from downloading to generation of biophysical products. This pipeline can be applied on satellite sensors including Sentinel-2, Landsat-8, Planet Scope and Planet Skysat. I also developed an algorithm to describe the heterogeneity of a field using the satellite images. This algorithm has been successfully applied on onions, maize and wheat fields for a better sampling strategy.
- I participated in the biophysical variable estimation from ground-based FieldSensor system fixed in the field. I was in charge of developing a pipeline to process data from micro spectrometer installed on the FieldSensor. The pipeline could generate daily continuous biophysical variables with the consideration of information from multiple sun and viewing angles. Then, I have developed an algorithm to fuse the daily data from FieldSensor with discrete satellite images over the field, to characterize the intra variability of fields in near real time. Both algorithms have been successfully applied by several clients and projects.
- I was also involved in the development of UAV data processing pipeline applied on multiple RGB and multispectral cameras. The pipeline includes alignments of all images in Agisoft Photoscan software, extraction of each microplot, selection of one best image for each microplot and retrieval of various traits from the RGB images using deep learning methods and radiative transfer model inversion from multispectral images.
- During this period, I participated several projects, such as PHENOME, P2S2 and IOTA. Some of the studies led to publications in peer reviewed papers.

Although my experience was resulting from several opportunities that were offered to me, they were very rich and gradually contributed to enrich my knowledge from the use of simple remote sensing indices to the estimation of biophysical variables based on radiative transfer model and crop traits from machine learning. Several vegetation types were investigated, from grassland, paddy rice, wheat, maize, sunflower, and many others. These studies were conducted at a wide range of scales from regional scale, global and regional to field and microplot levels. One of the main aspects of my work is the synergy across scales that I exploited to combine the high level of accuracy derived from observations at high spatial resolution with the high coverage achieved with larger spatial resolution observations. This was done either for calibrating and/or validating algorithms at a given spatial resolution using higher spatial resolution observations, or by fusing observations from low and high spatial resolution data to improve the temporal resolution.

4 Major achievements

4.1 Challenges in the agricultural context at different scales

Global agricultural production has tripled during the 1960 to 2015 period, thanks to the green revolution technologies, a large expansion of irrigation and fertilizers, of mechanization, increase exploitation of land and natural resources, and the industrialization and globalization of agriculture process (FAO, 2017). This increased agricultural production capacity followed the growth of world population during the same period, from 3 billion in 1960 to around 7 billion in 2015 (FAO, 2017). The global population continues to grow although at a slower pace. As estimates by Food and Agriculture Organization of the United Nations (FAO), the global population would grow up to 9.7 billion (32% increase) by 2050 and 11.2 billion (53% increase) by 2100, as compared to the 2015 population (FAO, 2018). This will require a huge boost of agricultural production to satisfy the population needs.

Although agricultural production and food security improved in recent years, hunger and malnutrition still exist and show a trend of expansion in the world. Between 720 and 811 million people in the world were undernourished in 2020, around 118 million more people were facing hunger in 2020 compared to 2019 (FAO, 2021a). More people might face hunger in 2021 under the shadow of the COVID-19 pandemic.

There are several factors that challenge agriculture in the coming years.

- Increases in the number and complexity of conflicts in the globe is the major threat to food security and nutrition. This also increases the risks of other factors, such as economic slowdowns and downturns (FAO, 2021b).
- To feed the growing population, sufficient food and other agricultural products should be provided. For example, to meet the demand of global population by 2050, 50% - 70% increase on food production must be achieved (Kamilaris et al., 2017; Muller et al., 2017).
- Global agricultural land area decreases in the world. In 2018, the global agricultural land area was 4.8 billion hectares (ha). It corresponds to a decrease of 2% or 0.08 billion ha as compared to 2000 (FAO, 2020). Cropland area per capita also decreased in all regions between 2000 and 2018, with the world average decline by 15% (0.21 ha per capita) in 2018 (FAO, 2020). Meanwhile, the decreasing storage of water and increasing competition for natural resources add uncertainties to the agricultural production.
- Although global economy grows, the share of agriculture in total production declines at various speed, which poses challenges across regions. Besides, the income growth in low- and middle-income countries would hasten a dietary transition towards higher consumption of meat, fruits and vegetables, relative to cereals (FAO, 2017).
- Recent research shows that the climate change impacts crop yields. The impacts of global climate changes on yields vary with crops, ranging from -13.4% (oil palm) to -3.5% (soybean), and vary between continents: mostly negative in Europe, Southern Africa and Australia but generally positive in Latin America (Ray et al., 2019). The global wheat production is supposed to fall by 6% for each increase of 1.0 °C (Asseng et al., 2015). Concurrently, the increased demand on agriculture is likely to increase the competition for natural resources and with negative impact on the greenhouse gas balance (FAO, 2017; Searchinger et al., 2019).
- Dietary patterns have been changed over recent decades. Obesity among adults of 18 years and above increased rapidly in every region of the world between 2000 and 2016 (FAO, 2020). This calls for healthy diets, which is not unaffordable in many regions of the world due to driving

factors in food production, food supply chains, food environment, consumer demand and the economy of food (FAO, 2021a).

All above challenges for food security or agricultural systems show the importance of reaching sustainable development, to meet rising human needs while contributing to resilience and sustainability of the Earth system (Rockström et al., 2017). To tackle the increasing challenges of agricultural production, the complex agricultural ecosystems need to be better understood. The emerging digital technologies allowing to monitor continuously the crop and its environment could be used to inform farmers for decision making in the management practices with the objective to optimize the use of natural resources (Basso and Antle, 2020; Kamilaris et al., 2017).

4.2 How remote/proxy sensing can bring some answers to these challenges and what are the associated issues

4.2.1 Why remote sensing data is useful?

To satisfy the increasing demand on agriculture production under the challenging context mentioned above, several studies and initiatives have been launched since several decades. The first question raised for a sustainable development of agriculture is to know evaluate crop state and coverage at different scales, e.g., global, regional, fields, microplots or even single plants. This will allow to organize the market of agricultural products at the larger scales, to provide information to the farmers for optimal field management, and to phenotype crops to develop innovative cultural practices and improved cultivars.

Conventional field survey is usually time-consuming and costly because agricultural activities are carried out over large regions (Chen et al., 2008). Moreover, crops growth follows strong seasonal patterns and is greatly dependent on human activities or climate conditions. This requires timely monitoring of crops to make efficient actions for higher production (Atzberger, 2013). Remote sensing appears as an efficient tool because the signal reflected by the crop canopy carries key information about crop state (structure, biochemistry). The signal captured by sensors on remote sensing platforms is transformed into pertinent information using advanced signal or image processing methods.

4.2.2 Source of remote sensing platforms

Since the early 1960s, remote sensing technologies have been widely used in agriculture. Currently, several operational remote sensing platforms have been launched and used for crop monitoring. According to the spatial and temporal resolutions of the data recoded, these platforms can be categorized into three categories: satellite, UAV and ground system (Fig. 1).

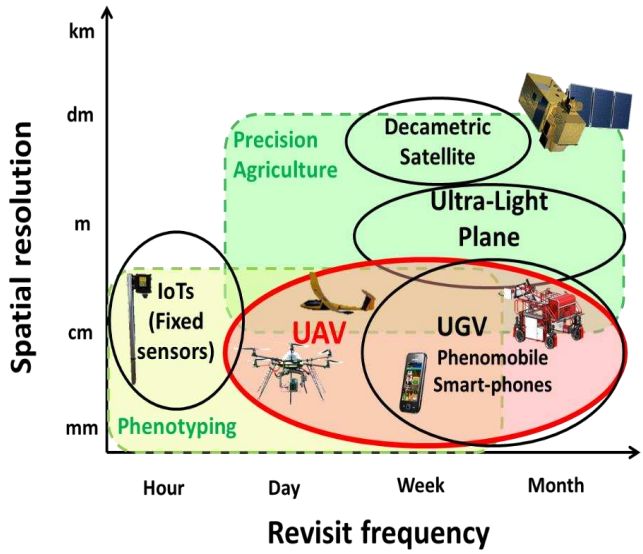

Fig. 1. Categories of remote sensing platforms based on spatial resolution and revisit frequency. The figure was generated by Prof. Fred Baret within the UMT CAPTE unit.

- Satellite

Over the past two decades, several optical satellite sensors at the kilometric resolution have been launched, such as NOAA/ AVHRR, MODIS, SEAWIFS, VEGETATION, MERIS, POLDER and MISR. They provide global daily reflectance observation thanks to their large swath. They contributed greatly to the studies at global to regional scales. However, the mixed nature of kilometric pixels raises both a scaling issue and difficulties when the cropland size is significantly smaller than the pixel size (Baret et al., 2013; Shabanov et al., 2003). Recent developments on sensor technologies improved the resolution into few hundred meters, such as MERIS (300 m), PROBA-V (300 m), SNPP-VIIRS (370 m) and Sentinel-3 (300 m). Biophysical products generated by these hectometric sensors are expected to get closer to the spatial resolution required for several applications at the regional scale (Baret et al., 2016; Croft et al., 2020; De Grave et al., 2020; Tum et al., 2016; Yan et al., 2018). However, they are still far from the requirements of decametric or metric resolutions at field scales.

Over the long term, Landsat is one of most successful satellite series that provides global monitoring at decametric resolution since the first launch in 1972 (Williams et al., 2006). The sensors that were onboard early Landsat missions are Multispectral Scanner (MSS), and later upgraded to Thematic Mapper (TM) on Landsat-4 and Landsat-5, and thenEnhanced Thematic Mapper Plus (ETM+) on Landsat-7. Launched in 2013, Landsat-8 is the most recent Landsat satellite with Operational Land Imager (OLI) sensor (Irons et al., 2012). The 30 m spatial resolution of Landsat-4, Landsat-5, Landsat-7 and Landsat-8 is ideal for detecting large fields which are few pixels size (Wulder et al., 2019). Although the 30 m resolution of Landsat series has been greatly improved compared to hectometric or kilometric resolutions, the low revisit frequency of Landsat observations (every 16 days) is not enough for crop growth monitoring. Under continuous cloudy days periods, the key growing stages might be missed without any data.

The Sentinel-2 mission launched in 2016 allows fulfilling both the spatial and temporal requirements for crop growth monitoring at the farm level (Drusch et al., 2012). It was designed to make a global coverage of the Earth's land surface every 10 days with one satellite and 5 days revisit with two satellites.

The Multi Spectral Instrument (MSI) onboard Sentinel-2 provides high-quality multispectral images with spatial resolutions ranging from 10 to 60 m. Several crop classifications, crop status monitoring and yield estimation studies have been conducted based on Sentinel-2 dataset (Amin et al., 2021; Hunt et al., 2019; Immitzer et al., 2016).

In the last decade, significant advances have been made to increase the spatial resolution of sensors down to meter or even submeter level, while still keeping close to daily revisit. This is mainly achieved through microsatellite, such as PlanetScope, VENUS, RapidEye, Worldview, Pleiades and Skysat. At this level of resolutions, crops status at field level can be monitored successfully (Cheng et al., 2020; Kross et al., 2015). But these sensors have several limitations (Dash and Ogutu, 2016; Houborg and McCabe, 2016). For example, they have few spectral bands (usually, only red, green, blue and NIR), leading to uncertainties in the crop status estimation. Another limitation is that almost all sensors are commercial, making images costly as compared to the free public datasets. The third one is the limited accuracy of cloud detection, atmospheric correction and georeferencing, generating some uncertainties in the interpretation of these data. In addition, the small scene coverage of these sensors, making them more difficult for global products generations.

- UAV

Low-altitude remote sensing system by UAV provides a practical complement to satellite platforms. These UAVs are always lightweight with a reasonable cost per flight. Equipped with new developed small RGB, multispectral or hyperspectral imaging sensors, the UAV systems can monitor the crop condition with a high spatial resolution (centimeter) and are more flexible in terms of revisit frequency (Salamí et al., 2014).

Among the imaging sensors, RGB camera with red, green and blue wavelengths can achieve very high spatial resolution (less than 1 cm) to satisfy many applications in precision agriculture, such as crop height estimation (Bendig et al., 2014; Holman et al., 2016; Madec et al., 2017), plant counting at emergence (Jin et al., 2017; Valente et al., 2020) and head counting during senescence stages (Velumani et al., 2020). Despite the high spatial resolution, the RGB sensors have obvious limitations on the spectral wavelengths, which are critical to compute several vegetation indices and estimate some biophysical variables.

Multispectral or hyperspectral cameras onboard UAV can solve this issue. Multispectral cameras incorporate bands in the visible (400 - 700 nm) and near infrared spectral ranges (700 - 1000 nm), and are well suited for vegetation monitoring (Baret and Guyot, 1991; Tucker, 1979). Hyperspectral cameras, on the other side, have a higher spectral resolution, with continuous or discrete spectral bands in the visible and infrared spectral regions. These hyperspectral bands are more sensitive to small changes in leaf pigments, such as carotenoids, chlorophyll a and b, and xanthophylls as well as leaf and canopy structure (Aasen et al., 2018). Compared with the RGB cameras, multispectral and hyperspectral camera have lower spatial resolutions.

Although the UAV platforms can be utilized under clear or cloudy conditions, it is also highly constrained by the meteorological conditions (e.g., low wind speed and lack of precipitation), by flight regulations of each region and by the spatial coverage that can be reduced by autonomy or the battery of sensors or drone (Weiss et al., 2020). Further, challenging radiometric calibration must be carried out on each band for the multispectral and hyperspectral cameras. The changing illumination conditions during the flight add uncertainties in the sensor calibration (Aasen and Bolten, 2018; Adão et al., 2017; Wang et al., 2019).

- Ground system

At the ground level, measurements can be taken using several hand-held instruments. However, they are generally labor-intensive and not applicable for continuous applications. With the development of automated systems and autonomous controls, Unmanned Ground Vehicles (UGV) have specific advantages on the monitoring. They can carry active sensors to take measurements fully independent from the illumination conditions and can provide submillimeter resolution measurements of the targets (Jay et al., 2020). Several UGV have been developed in the past few years (De Solan et al., 2015; Grimstad and From, 2017; Mueller-Sim et al., 2017). However, it is sensitive to soil conditions and microplots need to be well designed for the UGV system. The high price of several systems also limits its application widely.

Recent development of Internet of Things (IoT) has emerged as a new era of applications to monitor automatically crops in near-real time (Peng and Pal, 2020). In parallel, the advances on affordable micro-camera and micro-spectrometer provides opportunities to take very close-range photos of crops and measure the radiation reflected by the crop canopy in multiple spectral bands. A few automatic monitoring systems with RGB cameras or multispectral sensors have been produced to provide near-real-time crop monitoring (Baret et al., 2010; Bauer et al., 2016; Kim et al., 2019; Qu et al., 2014; Sakamoto et al., 2012; Velumani et al., 2020).

These ground IoT systems are well suited to provide continuous measurements under all meteorological conditions and has obvious advantages on very high spatial resolutions. The drawback of these systems is their limited sampling footprint and radiometric calibrations. The locations of the system need to be well designed so that they can represent the whole field. Multiple systems might be necessary for field presenting high spatial heterogeneity.

4.2.3 Interpretation of remote sensing data to traits

Using the above-mentioned platforms, a huge amount of data with different spatial and temporal resolution, as well as spectral properties are collected. The big remote sensing data is generally complex due to the diversity and high dimensionality characteristics (Chi et al., 2016; Ma et al., 2015). They cannot be used directly by the decision makers, especially those who are not in the domain of remote sensing and not familiar with data preprocessing. Interpretation of the raw remote sensing data into valuable agricultural traits or variables is therefore important and necessary to decision makers (e.g., farmers, companies) to improve the field management and productivity (Kamilaris et al., 2017).

As defined by Nock et al. (2016) and Madec (2020), traits are morphological, biochemical, physiological, structural, phenological or behavioral characteristics that influence organism performance or fitness, which are intrinsic characteristic of the organ, plant or canopy (e.g., height, length, surface, intercepted radiation,. etc). A variable is the estimate of a trait based on a dedicated method and quantified with a given unit. Raw remote sensing data cannot be interpreted into variables directly. Based on various models and empirical or mechanistic approaches, raw remote sensing measurements can be converted into agronomic variables (Weiss et al., 2020).

All my work was focusing on the estimation of traits from remote sensing data at different spatial scales, such as ground-based system, UAV and satellite. My main contributions on the development of algorithms to estimate traits is presented in the next section, with emphasis on the combination of observations at several scales and on the temporal dimension.

4.3 Major contributions

4.3.1 Traits

A number of traits have been proposed and estimated for application in precision agriculture and phenotyping. They might be broadly grouped into two categories: traits that characterize the canopy structure and traits associated to individual plant/organ. A full table about accessible traits by remote sensing technologies can be refer to (Velumani, 2021) and (Madec, 2020). This work is focus on a selection of these traits.

In the context of precision agriculture, leaf area index (LAI), the fraction of photosynthetically absorbed radiation (fAPAR) and fCOVER are among the most important biophysical traits that drive the radiative transfer within the canopy. Leaf area index (LAI) is defined as half the total developed area of green elements per unit horizontal ground area (Chen and Black, 1992). Recently, green area index (GAI) which corresponds to only green part of canopy is used as it is a more pertinent variable to describe the radiation transfer in the canopy (Baret et al., 2010; Duveiller et al., 2011). fAPAR is defined as the fraction of the photosynthetically active radiation (PAR) absorbed by the green leaves. It is a weighted sum of the direct fAPAR (black-sky fAPAR if only direct illumination conditions) and diffuse fAPAR (white-sky fAPAR if totally diffuse illumination conditions), depending on the source of the incoming radiation (M Weiss and Baret, 2010). fAPAR is often approximated by the fraction of intercepted PAR (fIPAR) because the vegetation present a strong absorption in this spectral domain and the reflectivities from background are usually small for well-developed canopies (Gower et al., 1999). Both LAI and fAPAR have been recognized as Essential Climate Variables (ECV) by Global Climate Observing System (GCOS) (GCOS, 2016), for their key roles in energy, mass and momentum exchanges between the land surface and the atmosphere. fCOVER, the fraction of the green vegetation in the nadir direction, is another important traits that is used to separate vegetation and soil in energy balance processes, including temperature and evapotranspiration (Gutman and Ignatov, 1998; Xiao et al., 2016).

Canopy clumping index (CI) that describes the spatial distribution of leaves in a canopy is another critical traits in determining the canopy radiation transfer, photosynthesis and hydrological processes (Chen et al., 2016; Fang, 2021; Nouvellon, 2000; Wei and Fang, 2016). It is defined as a ratio of the effective LAI to the true LAI (Nilson, 1971), i.e., value of 1 represents leaves that are randomly distributed and less than 1.0 means leaves are that aggregated. Effective LAI is thus equal to the LAI value assuming a random foliage distribution (Chen et al., 2005).

All these traits can be estimated from measurements using instruments at different platforms, such as ground system, UAV and satellites. Each platform provides observations under a specific directional configuration, resulting in directional effects characterized by the Bidirectional Reflectance Distribution Function (BRDF)(Nicodemus et al., 1977; Schaepman-Strub et al., 2006). Accounting explicitly for these effects in the retrieval algorithms is important.

As discussed in section 2.2, each platform has its advantages and disadvantages in the estimation of above-mentioned traits. In the context of crop monitoring for precision agriculture and field phenotyping applications, continuous and accurate estimations of these traits are required (Comar et al., 2012; McBRATNEY et al., 2005; Weiss et al., 2020). My work focuses on the development and evaluation of methods to retrieve traits from close-range and satellite observations. The work is composed of several studies that can be conveniently grouped per scale. We will start by the higher spatial resolution observations that can then be exploited in combination with the lower spatial resolution observations:

- Ground, which provides valuable calibration and validation datasets

- UAV, close-range phenotyping
- Satellite
    - Decametric satellite
    - Hectometric satellite
    - Fusion of decametric and hectometric satellites

4.3.2 Ground: instruments and methods to estimate LAI and FAPAR

Continuous and accurate ground measurements of LAI and fAPAR (or fIPAR) is important to monitor canopy functioning and validate remote sensing estimates called "products". Several methods and optical instruments to be used in the fields have been developed, such as AccuPAR (Decagon Devices, 2010), LAI-2200 and Digital Hemispheric Photography (DHP). Understanding the consistency and differences of these methods or instruments is important to applications in the field.

This section focuses on the estimation of LAI, fAPAR and CI from ground measurements over paddy rice fields. One study has been conducted for each variable:

- Intercomparison of several instruments to measure LAI over paddy rice fields (Fang et al., 2014).
- Analysis of methods to estimate fAPAR and fIPAR from ground measurements (Li et al., 2021a).
- Estimation of directional and whole apparent CI from indirect optical measurements (Fang et al., 2018).

4.3.2.1 The instruments and methods

- AccuPAR

Decagon's AccuPAR model LP-80 PAR/LAI ceptometer measures PAR using 80 individual sensors (field of view: 180◦) on its probe. The downward ($I_t^{\downarrow}$) and reflected ($I_t^{\uparrow}$) PAR at the top of canopy were measured by placing the probe approximately 1.5 m above the canopy, facing upward and downward, respectively. The canopy transmitted PAR ($I_b^{\downarrow}$) was measured by placing the probe below the canopy looking upward. The soil reflected PAR ($I_b^{\uparrow}$) was measured twice in two different rows by placing the probe approximately 5 cm above the ground looking downward. From the measurements, effective plant area index (PAI_{eff}) that represents the area from all components of canopy (green, senescent leaves, stems and seeds) is calculated as (Eq. 1)(Norman and Welles, 1983):

$$PAI_{eff} = \frac{[\left(1-\frac{1}{2k}\right)f_b - 1]lnT}{A(1-0.47f_b)} \quad (1)$$

where *T* is the transmission coefficient obtained through the ratio of the below canopy and the above canopy PARs, f_b is the fraction of incident beam PAR, and *A* is a function of the leaf absorptivity in the PAR band. The parameter *k* is the extinction coefficient for the canopy and is a function of the solar zenith angle (SZA) and leaf angular distribution (LAD) of the inclinations.

True LAI can be derived from measured PAI_{eff} and the clumping index (CI).

$$LAI = \frac{PAI_{eff}}{CI}(1-\alpha)(1-\gamma) \quad (2)$$

where CI is calculated as the ratio of PAI_{eff} and destructive PAI, α is the stem-to-total plant area ratio, and γ is the yellow to total leaf area ratio. Both α and γ are calculated based on destructive measurements.

fAPAR and fIPAR are calculated from all PAR measurements (Eqs. 2 & 3),

$$\text{fAPAR} = 1 - R_c - T(1 - R_s) \quad (3)$$

$$\text{fAPAR}_T = 1 - T \quad (4)$$

where $R_c = \frac{I_t^{\uparrow}}{I_t^{\downarrow}}$ is the canopy reflectance, $T = \frac{I_b^{\downarrow}}{I_t^{\downarrow}}$ is the canopy transmittance, and $R_s = \frac{I_b^{\uparrow}}{I_b^{\downarrow}}$ is the soil background reflectance in the PAR spectral domain.

- LAI-2200

LAI-2200 measures the blue radiation in 5 concentric rings centered at 7°, 23°, 38°, 53° and 68°. LAI-2200 measurements were conducted always under diffuse conditions. Each measurement was repeated twice, with one above and four below canopy readings along diagonal transects between the rows. For the below canopy readings, the instrument was held about 5 cm above the background. Throughout the season, a 270° view cap was used to shield the operator.

The incident light recorded by the five rings is used to calculate gap fraction P(θ). PAIeff is calculated as

$$PAI_{eff} = 2\int_0^{\frac{\pi}{2}} -\overline{lnP(\theta)}cos\theta sin\theta d\theta = 2\sum_{i=1}^{5}\overline{K_i}\,W_i \quad (5)$$

Where K_i and W_i are the contact number and the weighting factor, respectively (refer to manual of LAI-2200).

LAI of LAI-2200 also can be calculated from Eq. (2).

If leaves are considered opaque, fIPAR can be calculated from P. *P* is closely approximated by canopy transmittance (τ) and $\text{fIPAR} \approx \text{fAPAR}_{\tau}$.

$$fIPAR = 1 - P \quad (6)$$

- DHP

The DHP images were taken using a Nikon D5100 camera equipped with a 4.5 mm F2.8 EX DC fisheye convertor. The DHP camera was calibrated before measurements following the CAN-EYE manual (Weiss and Baret, 2010) to obtain the optical center and the projection function of the camera and fish-eye system. Images were taken at both downward and upward directions. All DHP images were processed using the CAN-EYE version 6.3.3 software (https://www6.paca.inrae.fr/can-eye). Green pixels were manually separated from senescent and background pixels for the downward images during the classification step. PAI_{eff} is retrieved in CAN EYE using lookup-table techniques and assuming an ellipsoidal distribution of the leaf inclination (Weiss and Baret, 2010),

$$PAI_{eff} = 2\int_0^{\pi/2} -lnP(\theta)cos\theta sin\theta d\theta \quad (7)$$

fIPAR from DHP is also calculated from Eq. (6).

4.3.2.2 Intercomparison of several instruments to measure LAI over paddy rice fields (Fang et al., 2014)

LAI measurement has become increasingly important for the validation of remote sensing LAI products. A seasonal field campaign was carried out to take continuous LAI measurements over paddy rice fields in NE China in 2012. Three indirect optical methods, LAI-2200, DHP, and AccuPAR, were compared with a

destructive sampling method conducted concurrently. Corrections for the clumping effect were applied to the PAI_{eff} estimated from the indirect optical measurements. Compared to PAI_{eff} which includes all components in the canopy, LAI in this paper represents contributions only from green and senescent leaves.

Seasonal dynamics of PAI_{eff} of rice obtained by the three optical instruments are shown in Fig. 2. PAI_{eff} increases with crop development up to a maximum in late July and then decreases slightly by less than 1.0 until the end of the season. The largest discrepancies (up to 2.7) between the optical instruments are noticed in late July (Day of year, DOY 210), whereas small deviations (~0.82) appear in mid-August.

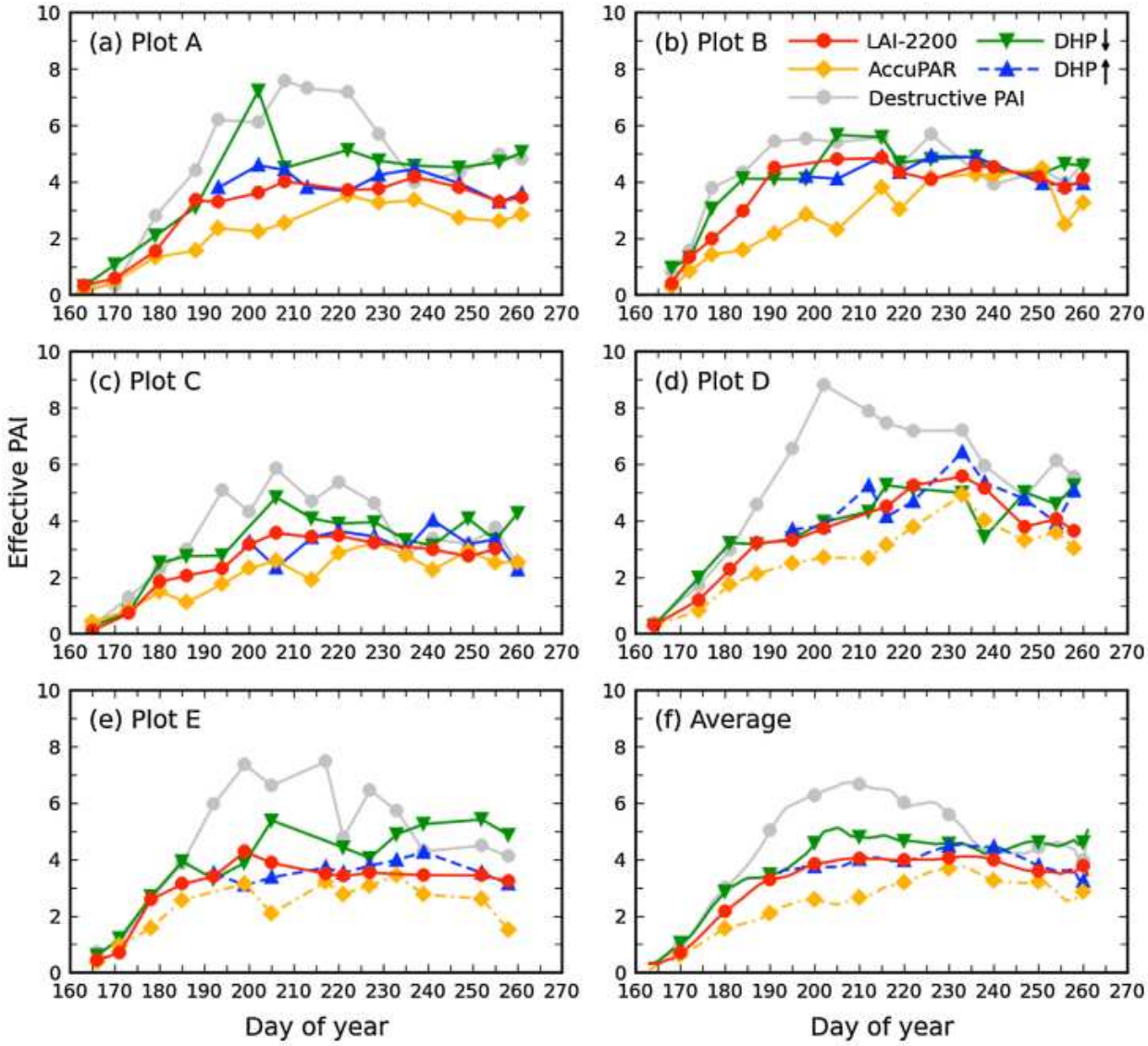

Fig. 2. Seasonal variation of the effective PAI (PAIeff) estimated from LAI-2200, DHP, and AccuPAR for five plots of paddy rice fields. Both upward and downward DHP measurements are shown. Destructive PAI is shown as light gray as a reference. The x-axis represents Day of year (DOY) in 2012. (Fig. 3 in Fang et al. (2014))

Both LAI-2200 and DHP produce consistent PAI_{eff} estimates over the season (R^2 = 0.76, RMSE = 0.97, Fig. 3). Good correspondence can also be observed between the upward DHP and LAI-2200 (R^2 = 0.50, RMSE

= 0.56). The downward DHP estimates show a positive bias (0.58, 14.5%) over the upward estimates. The best relationship is found between LAI-2200 and AccuPAR (R^2 = 0.80, RMSE = 0.95). However, AccuPAR is systematically lower than the LAI-2200 and DHP values (Bias>0.70, or 16%), especially for PAI_{eff} > 1.0.

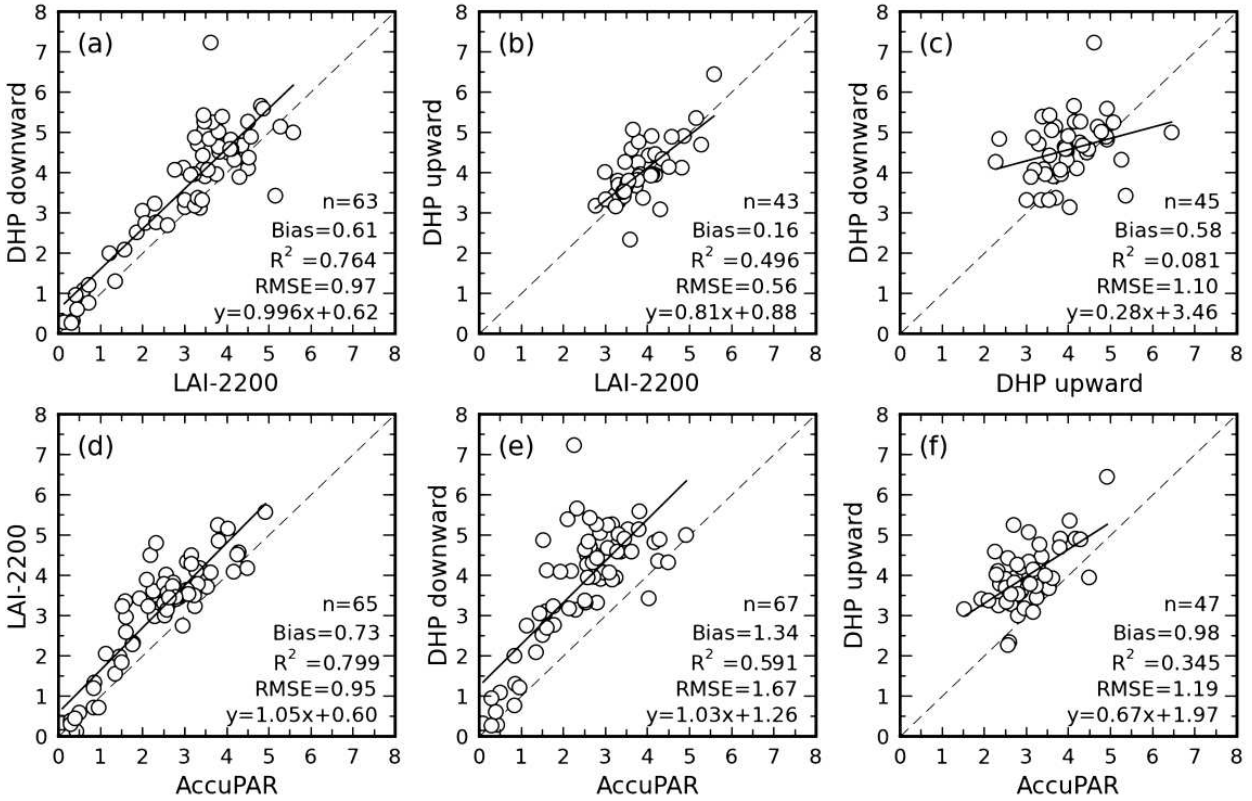

Fig. 3. Comparison of the effective PAIs (PAI_{eff}) estimated from the LAI-2200, DHP, and AccuPAR methods. (Fig. 4 in (Fang et al., 2014))

Fig. 4 compares the PAI and LAI values derived from optical methods against the destructive measurements. For DHP, the PAIs were derived by dividing the PAI_{eff} by the corresponding CIs. The PAI values for the LAI-2200 and AccuPAR were derived by dividing PAI_{eff} by the average CI of both DHP views. When the upward DHP CI was not available, the downward DHP CI was used. The destructive, LAI-2200, and DHP PAIs are consistent for most of the season, except after DOY 231 (August 18). During the peak season from DOY 201 to 230, the mean PAI values obtained from LAI-2200 and DHP are nearly identical to the average destructive PAI (Table 1). After the peak season, when the leaves become rolled, the deviations between direct and indirect methods become progressively larger. After DOY 231, the destructive PAI decreases by about 1.80 (−28.6%). However, this amplitude of decrease is not observed by the optical methods. The average LAI-2200 and DHP PAIs decrease by only 0.37 (−5.9%). In general, before DOY 230 (August 17), LAI-2200 provides a very good estimates of destructive PAI (relative errors < 10%), especially when ring 5 is discarded (Table 1). DHP gives even more accurate PAI estimates, with relative errors less than 5%. AccuPAR exhibits the highest underestimation of the destructive PAI by up to 30%. Like PAI, the LAI-2200 and DHP LAI values agree very well with the destructive values before DOY 230, with relative differences less than 10% (Fig. 4b and Table 1). After DOY 231, the relative differences are more than 20%. Comparisons between AccuPAR and the destructive LAIs show more than 30% underestimation before DOY 230 and a very good correspondence after DOY 231 (Table 5).

However, the good agreement after DOY 231 may need further verification to ascertain whether it occurs through correct derivation or by artifact.

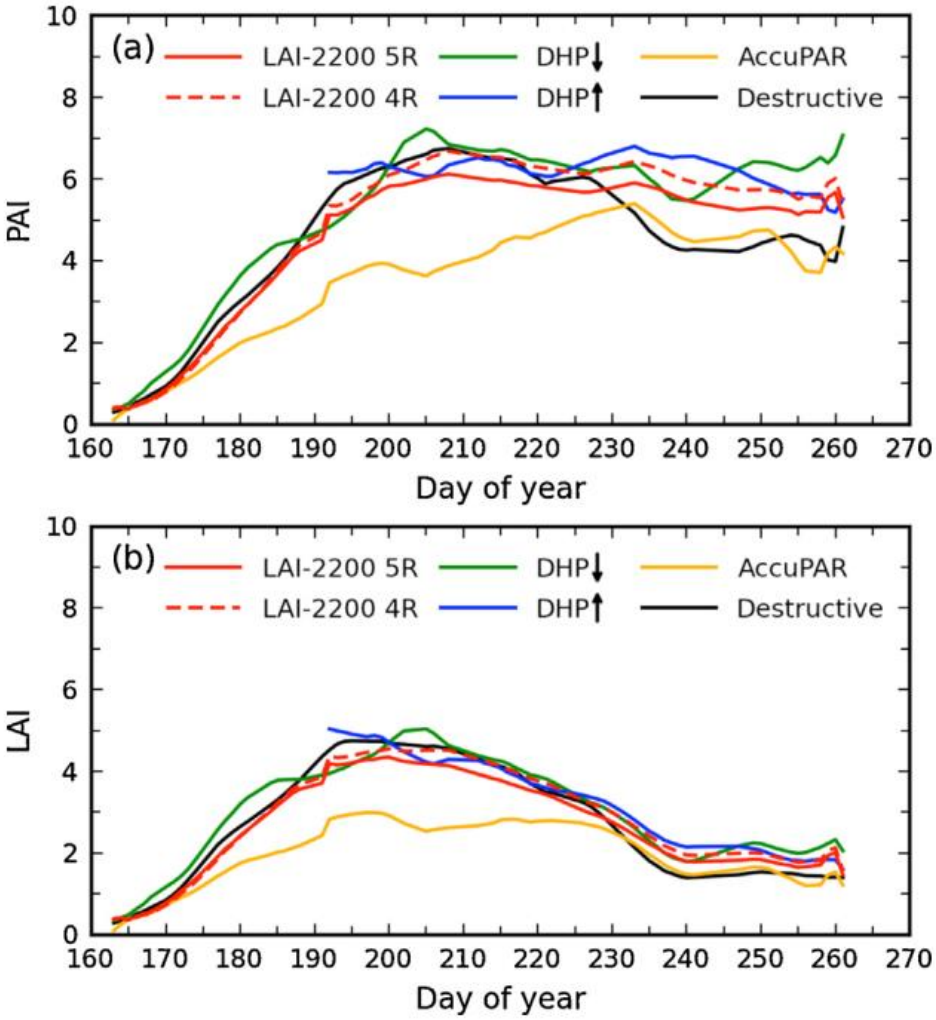

Fig. 4. Seasonal variation of PAI (a) and LAI (b) obtained from optical and destructive methods. PAI is calculated from PAI_{eff} divided by the average CI from the downward and upward DHPs. Optical LAI is estimated from Eq. (10) in Fang et al. (2014). (Fig. 11 in Fang et al. (2014))

Table 1. Comparison of the optical PAIs and LAIs over different periods of the season. The values in the brackets show the relative differences comparing to the destructive PAI and LAI. (Table 7 in Fang et al. (2014))

DOYs	160–200	201–230	231–261
PAI			
Destructive	3.29	6.31	4.50
LAI-2200 5R	3.00 (−8.8%)	5.89 (−6.7%)*	5.44 (20.9%)*
LAI-2200 4R	3.06 (−7.0%)	6.38 (1.1%)	5.89 (30.9%)*
DHP downward	3.38 (2.7%)	6.63 (5.1%)*	6.14 (36.4%)*
DHP upward		6.30 (0.0%)	6.15 (36.7%)*
AccuPAR	2.08 (−36.8%)*	4.40 (−30.3%)*	4.58 (1.8%)
LAI-2200 5R + DHP	3.51 (6.7%)	6.28 (−0.5%)	5.91 (31.3%)*
LAI-2200 4R + DHP	3.54 (7.6%)	6.44 (2.1%)	6.06 (34.7%)*
LAI			
Destructive	2.73	3.94	1.58
LAI-2200 5R	2.49 (−8.8%)	3.67 (−6.9%)	1.91 (20.9%)*
LAI-2200 4R	2.53 (−7.3%)	3.97 (−0.8%)	2.07 (31.0%)*
DHP downward	2.82 (3.3%)	4.14 (5.1%)	2.14 (35.4%)*
DHP upward		3.91 (−0.8%)	2.16 (36.7%)*
AccuPAR	1.73 (−36.6%)*	2.7 (−31.5%)*	1.61 (1.9%)
LAI-2200 5R + DHP	2.89 (5.9%)	3.91 (−0.8%)	2.07 (31.0%)*
LAI-2200 4R + DHP	2.91 (6.7%)	4.01 (1.8%)	2.12 (34.2%)*

* $p < 0.01$.

In general, rice PAI could be accurately estimated with LAI-2200 and DHP before senescence if the clumping effect could be properly taken into account. The seasonal continuous LAI measurements obtained from this study are valuable for the validation of remote sensing LAI products.

4.3.2.3 Analysis of methods to estimate fAPAR and fIPAR from ground measurements (Li et al., 2021a)

fAPAR and fIPAR respectively correspond to fraction of PAR absorbed or intercepted by the green canopy components. Both are sensitive to illumination conditions and non-green components during the senescence stage. While several methods have been developed to estimate fAPAR or fIPAR in the field from different methods including AccuPAR, LAI-2200 and DHP, the differences among these methods still need more investigations.

Two field campaigns were conducted in 2012 and 2013 in northeastern China over paddy rice fields. fAPAR and fIPAR measured using AccuPAR, DHP and LAI-2200 were compared. GAI and LAI measured simultaneously were used to calculate green fAPAR (GfAPAR) and green fIPAR (GfIPAR) in the senescence stage. Two methods have been proposed to calculate GfAPAR and GfIPAR from upward-looking systems (AccuPAR, LAI-2200 and upward-looking DHP). Assuming green leaves are located at the top of the canopy above the senescent elements, $GfAPAR^{top}$ is calculated (Chen, 1996); while assuming all green and senescent leaves are mixed in the canopy, $GfAPAR^{mix}$ is calculated (Viña and Gitelson, 2005).

Table 2. Quantities estimated from AccuPAR, DHP, and LAI-2200. R_c, R_s, R_{sen} and T represent the canopy reflectance, the background soil and senescent layer reflectance, and the canopy transmittance, respectively. P is the canopy gap fraction and GF is the green fraction.

Instruments	Notation	Equation
AccuPAR	$fAPAR(AccuPAR)$	$1 - R_c - T(1 - R_s)$
	$fAPAR_T(AccuPAR)$	$1 - T$
	$GfAPAR^{top}(AccuPAR)$	$1 - R_c - (1 - R_{sen})e^{\frac{GAI}{PAI} \cdot ln(\frac{1-R_c-fAPAR}{1-R_s})}$
	$GfAPAR^{mix}(AccuPAR)$	$fAPAR \cdot GAI/PAI$
Downward DHP	$GfIPAR(DHP_{down})$	GF
Upward DHP	$fIPAR(DHP_{up})$	$1 - P$
	$GfIPAR^{top}(DHP_{up})$	$1 - e^{\frac{GAI}{PAI} \cdot ln(1-fIPAR)}$
	$GfIPAR^{mix}(DHP_{up})$	$fIPAR \cdot GAI/PAI$
LAI-2200	$fIPAR(LAI - 2200)$	$1 - P$
	$GfIPAR^{top}(LAI - 2200)$	$1 - e^{\frac{GAI}{PAI} \cdot ln(1-fIPAR)}$
	$GfIPAR^{mix}(LAI - 2200)$	$fIPAR \cdot GAI/PAI$

Results show that considering only canopy light transmittance ($fAPAR_T$) measured with AccuPAR is a good proxy of fAPAR which is computed from AccuPAR under both black-sky and white-sky conditions (Fig. 5, R^2 = 0.94~1, RMSE = 0.03~0.08).

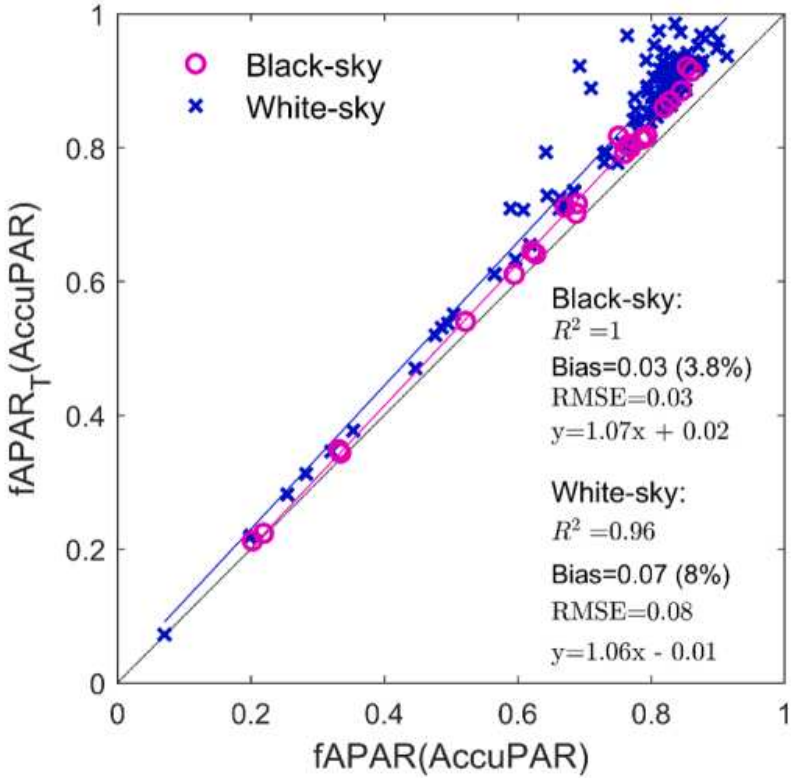

Fig. 5. Comparison of four-stream fAPAR(AccuPAR) (Eq. (3)) and the two-stream $fAPAR_T$ (AccuPAR)(Eq. (4)) values derived from AccuPAR measurements in 2012 and 2013 under both black (magenta) and white-sky (blue) conditions. (Fig. 4. in Li et al. (2021))

When the canopy is senescent, downward looking DHP method is recommended as a reference since it is the only method that directly measure the light intercepted by green elements. Methods based on upward looking (DHP upward, AccuPAR and LAI-2200) cannot distinguish between the green and senescent vegetation elements because the signal comes from the entire canopy with limited capacity to distinguish green and senescent vegetation. A correction based on ratio of GAI to the PAI needs to be used for these upward looking measurements, while assuming that green and senescent elements are well mixed in the canopy volume (Fig. 6 and 7).

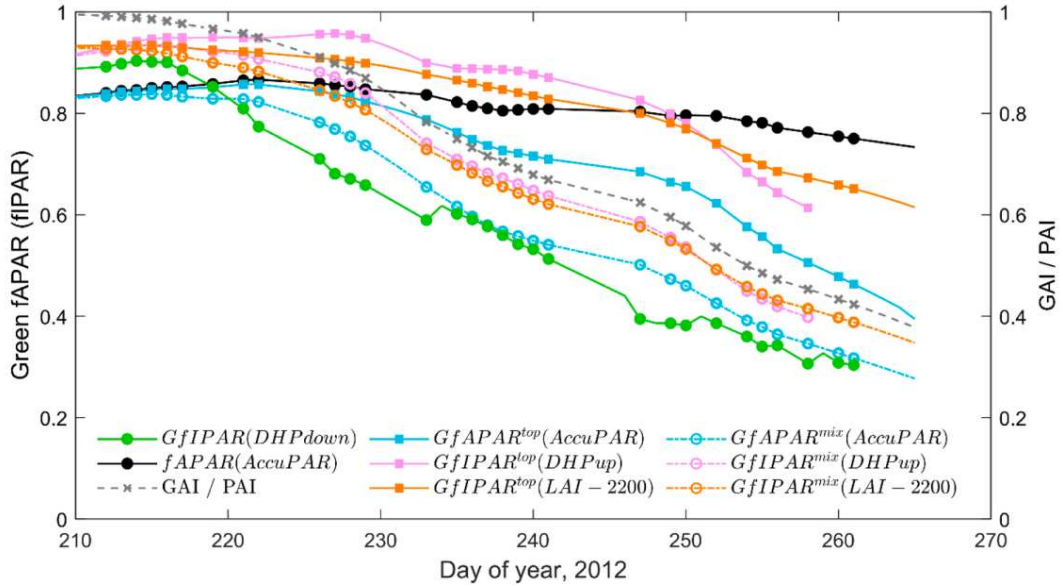

Fig. 6. Seasonal variation of fAPAR and fIPAR quantities considered in Table 1 during the senescent stage (after DOY 210). GAI/PAI is the ratio of GAI to PAI (right y-axis). All measurements were performed under white-sky illuminations in 2012. (Fig. 7 in Li et al. (2021))

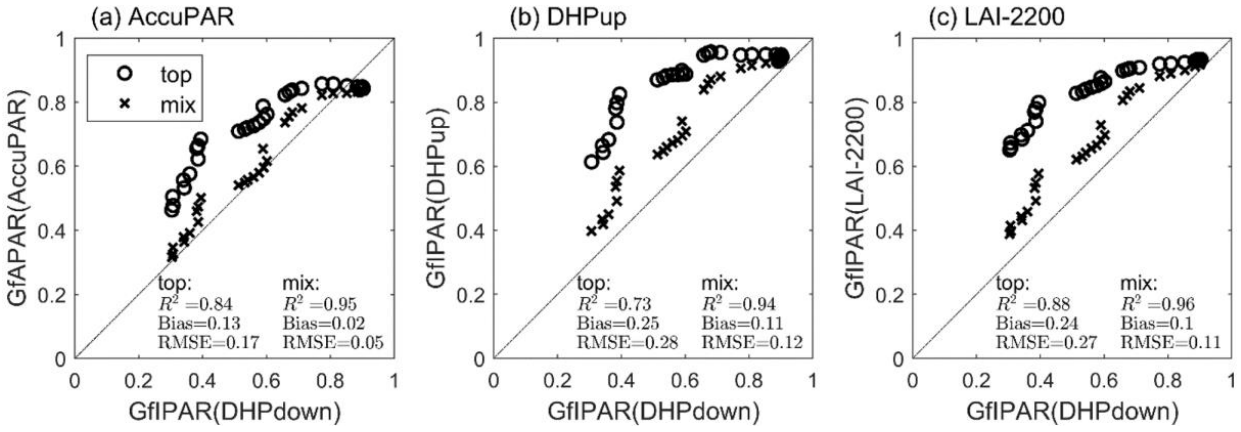

Fig. 7. After DOY 210 (senescence), from left to right: comparison of GfAPAR derived from AccuPAR, GfIPAR by upward DHP and LAI-2200 with the GfIPAR from downward DHP used as a reference. “top” and “mix” refers to the assumptions used to derive the green fAPAR, e.g. the senescence is occurring from the top of the canopy (Chen, 1996) or is randomly distributed within the canopy (Viña and Gitelson, 2005). (Fig. 8 in Li et al. (2021))

Downward looking DHP appears to be the preferred method for relatively short and dense canopies such as rice since it does not disturb the canopy, it is sensitive to the green elements only and allows to simulate fIPAR for any illumination conditions.

4.3.2.4 Estimation of directional and whole apparent CI from indirect optical measurements (Fang et al., 2018)

As shown above, several commercial optical instruments, e.g., DHP and LAI-2200 have been used to take indirect CI estimates when making field LAI measurements (Chen and Cihlar, 1995; Fang et al., 2014; Leblanc et al., 2005; Ryu et al., 2012). These methods vary for different field conditions and vegetation types.

Ryu et al. (2010) proposed an apparent clumping index (ACI) from LAI-2200 gap fraction measurements of rings, in order to compensate for the clumping factor inherent in LAI-2200 rings and to properly calculate true LAI. However, the ACI reported in LAI-2200 has rarely been investigated. Beside LAI-2200, other instruments also provide gap fraction measurements in cells or rings, such as DHP and AccuPAR. The objective of this study is to expand the ACI concept to other geometric units and instruments. The angular distribution of ACI with zenith and azimuth angles, and characteristics of ACI from different instruments were compared. Ground data obtained from seasonal continuous measurements over paddy rice fields in 2012 were used for the ACI calculation and analysis (Fang et al., 2014). Several ACI have been proposed for cell, directional and whole canopy levels (Table 3).

Table 3. List of directional ACI and ACI of whole canopy.

Category	Definition	Equation	Description	Instruments
Directional ACI (Ω_A)	$\Omega_A(\theta,\phi)$	$\Omega_A(\theta,\phi)=\frac{ln\overline{P(\theta,\phi)}}{\overline{lnP(\theta,\phi)}}$	It describes the non-random distribution of foliage at a particular angular location (θ, φ) and size (Δθ, Δφ).	DHP
	$\Omega_A(\theta)$	$\Omega_A(\theta)=\frac{ln\overline{P(\theta)}}{\overline{lnP(\theta)}}$	It describes the foliage clumping at a particular zenith ring.	DHP LAI-2200
	$\Omega_A(\phi)$	$\Omega_A(\phi)=\frac{ln\overline{P(\phi)}}{\overline{lnP(\phi)}}$	It describes the foliage clumping at a particular azimuth sector.	DHP
	$\Omega_A(v)$	$\Omega_A(v)=\frac{ln\overline{P(v)}}{\overline{lnP(v)}}$	It quantifies the canopy non-randomness in the horizontal direction. P(v) is computed as the canopy openness over all azimuth angles from a specified zenith angle (v) to nadir.	DHP LAI-2200 AccuPAR

Whole ACI (Ω)	Ω_{INT}	$\Omega_{INT} = 2\int_0^{\pi/2} \Omega(\theta)G(\theta)sin\theta d\theta$	Angular integration method. $G(\theta)$ is the foliage projection function	DHP LAI-2200 AccuPAR
	Ω_{AVG}	$\Omega_{AVG} = \frac{1}{N}\sum_{i=1}^{N} \Omega(\theta_i)$	Simple angular averaging method. N is the number of angular sectors.	DHP LAI-2200 AccuPAR
	Ω_{NLC}	$\Omega_{NLC} \approx 1 - 0.5\frac{\int_0^{\pi/2} \mathrm{S(P}(\theta))/\overline{\mathrm{P}(\theta)}^2 cos\theta sin\theta d\theta}{\int_0^{\pi/2} -\overline{ln\mathrm{P}(\theta)} cos\theta sin\theta d\theta}$	Non-linear correction method. S represents variance.	DHP LAI-2200 AccuPAR
	Ω_{VMR}	$\Omega_{VMR} = 2\int_0^{\frac{\pi}{2}} (1 - \frac{S(lnP(\theta))}{-\overline{lnP(\theta)}}) G(\theta)sin\theta d\theta$	Simple variance to mean ratio of the $lnP(\theta)$	DHP LAI-2200 AccuPAR

Results show that all ACI (directional ACI with zenith and azimuth angle $\Omega_A(\theta, \phi)$, ACI over a concentric ring $\Omega_A(\theta)$, and an azimuth section $\Omega_A(\phi)$, whole ACI over a landscape $\Omega_A(\upsilon)$) can be derived from DHP at different angular resolution, whereas both $\Omega_A(\theta)$ and $\Omega_A(\upsilon)$ can be estimated from LAI-2200, and $\Omega_A(\upsilon)$ from AccuPAR. For paddy rice fields, directional ACI values generally increase with the increasing segment size, in the order of $\Omega_A(\theta, \phi) < \Omega_A(\theta) < \Omega_A(\phi) < \Omega_A(\upsilon)$, displaying an increase of foliage randomness with the segment size (Fig. 8).

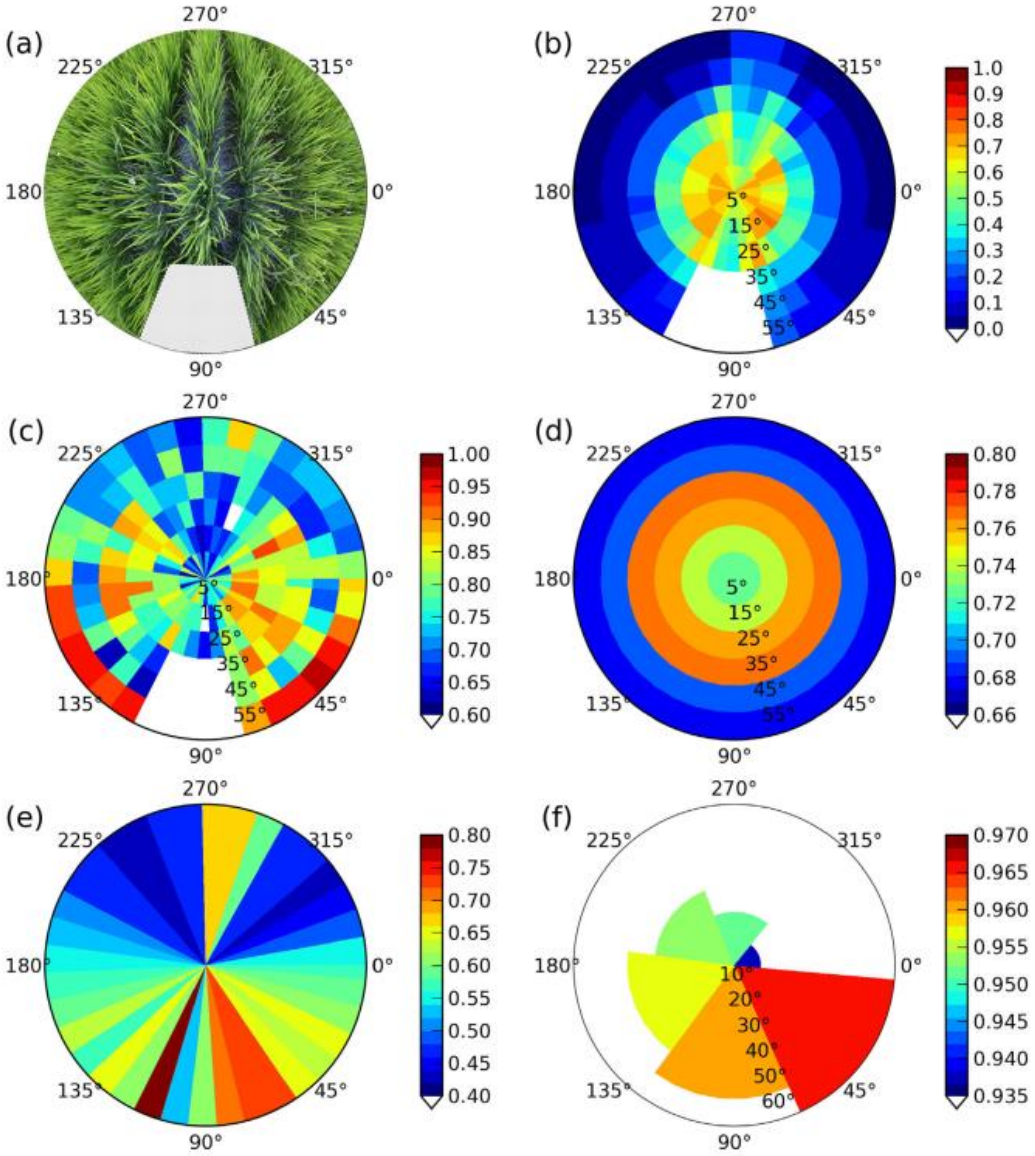

Fig. 8. A sample downward DHP image (a) and the gap fraction (b) over plot C on July 12, 2012 (DOY 194). Panels (c), (d), and (e) represent the $\Omega_A(\theta,\phi)$ values for each 10°×10° cell, $\Omega_A(\theta)$ for different rings, and $\Omega_A(\phi)$ for different azimuth sectors, respectively. Panel (f) indicates the $\Omega_A(\upsilon)$ values calculated over different solid angles (υ = 10–60°, respectively). Panels (c)−(f) are calculated over an ESU of 20 images. (Fig. 3 in Fang et al. (2018)).

The whole ACI can be calculated from the directional ACIs and the directional gap fractions (Section 2.3). Among the four methods to calculate the whole ACI, the INT and AVG methods agree very well and are robust over the season (Fig. 9). The NLC method can approximate the INT and AVG methods very well, but is easily affected by outlying gap fraction values. The VMR method is indicative of the seasonal ACI variation but gives systematically lower values. The whole ACIs calculated from LAI-2200 are on par with the values reported in LAI-2200 (Fig. 9).

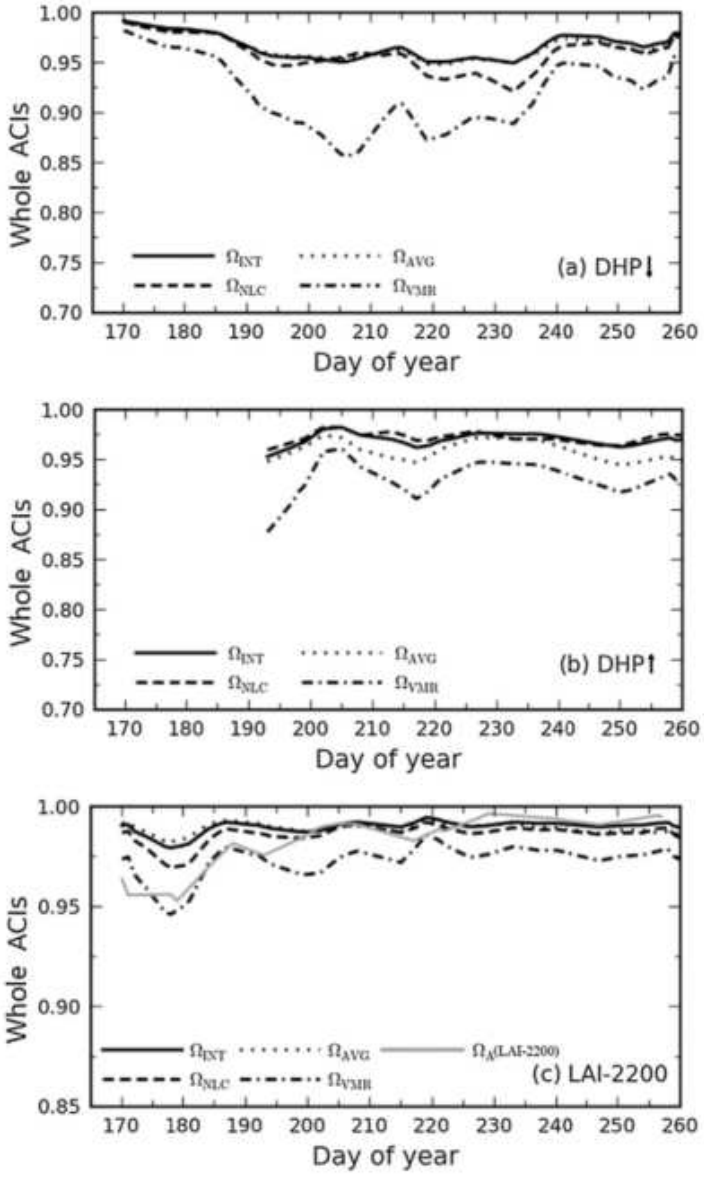

Fig. 9. Seasonal variation of the whole ACIs calculated from the directional $\Omega_A(\theta)$ for downward (a), upward DHPs (b) and LAI-2200 (c), respectively. Ω_{INT}, Ω_{AVG}, Ω_{NLC}, and Ω_{VRM} are from the integration, averaging, non-linear correction, and the variance-to-mean ratio methods. The Ω_{VRM} lines have been offset up by 0.2 (a) and 1.0 (b), respectively. The gray line in (c) shows the whole ACI reported in the LAI-2200 data file. (Fig. 9 in Fang et al. (2018))

The ACI metrics expand the current CI metrics and can be obtained with different optical instruments. The expanded metrics can be applied in the canopy radiative transfer modeling and in the estimation of canopy biophysical parameters for other vegetation ecosystems.

From the three above studies, we have thoroughly investigated uncertainties related to ground measurements of LAI, fAPAR and CI. The most appropriate measurement instruments and strategies were also proposed and evaluated. These datasets can enlarge the ground database over paddy rice and are valuable to validate satellite products.

4.3.3 UAV: BRDF description and influence of reproductive organs

Compared to the labor extensive ground measurements, UAV offers the advantage to avoid disturbing the crop and to sample the field or microplots exhaustively. The interpretation of data measured by UAV multispectral camera in terms of biophysical variables is generally based on assumptions on canopy structure. Knowledge on canopy structure and associated optical properties of canopy might significantly improve the estimates. Several crops bear reproductive organs (RO) at the top of the canopy after the flowering stage, such as ears for wheat, tassels for maize, and heads for sunflowers. RO present specific architecture and optical properties as compared to leaves and stems, which may impact canopy reflectance. However, only a few studies document the impact of RO on canopy reflectance. Cossani and Reynolds (2012) reported that wheat ears intercept up to 40% of the incident radiation around the flowering stage. Li et al. (2015) show that removing the ear layer at the flowering stage reduces normalized difference vegetation index (NDVI) values by up to 7% in relative values. This explains why Weiss et al. (2001) included explicitly an ear layer to describe the wheat canopy structure and simulate crop reflectance along the growth cycle. Gitelson (2003) and Viña et al. (2004) showed that the presence of the tassels at the top of maize canopies induced a significant decrease of the VARI index. Wanjura and Hatfield (1988) investigated variations in canopy reflectance of sorghum, cotton, and sunflower crops during the growth cycle using the scattering and absorption coefficients. However, they were not able to draw clear conclusions on the impact of sorghum panicles and sunflower heads on canopy reflectance for the Landsat TM bands. More detailed investigations are thus required to better quantify the role of RO on canopy reflectance. Besides, the impact of RO on canopy reflectance should be investigated for the possible view and illumination directions under which crops are usually observed from various remote sensing platforms. Few studies report detailed measurements of the BRDF for crops under field conditions. This paper aims to understand and quantify the influence of RO on the bi-directional variation of canopy reflectance and NDVI.

Multispectral camera observations from a UAV were completed over wheat, maize, and sunflower just after flowering when the RO are fully developed, and the leaf layer is with only marginal senescence. The flights were designed to sample the BRDF with view zenith angles spanning from nadir to 60° and many compass directions. Three flights corresponding to three sun positions were completed under clear sky conditions. The camera was always pointing to two adjacent plots of few tenths of square meters: the RO were manually removed on one plot, while the other plot was kept undisturbed.

The reflectance of three crops in two bands (red and NIR) present similar directional patterns across the three sun positions, e.g., the measurements for $\theta_s = 45°$. And they show a general symmetry of both sides of the principal plane, i.e. the plane containing the sun direction (Fig. 10).

Regarding to NDVI, which is frequently used to quantify vegetation amount, the addition of ears in wheat canopies increases the NDVI value (Fig. 11). For maize crops, the highly scattering tassels in the red and NIR decrease the NDVI values by -0.03. For the sunflower, the impact is slightly negative (− 0.02) for $\theta_s = 30°$, but positive (0.01) for $\theta_s = 60°$ and intermediate (0) for $\theta_s = 45°$. Our experimental results also show that the NDVI changes induced by the RO layer can be translated into a change in GAI estimates that can reach up to 25% (Table 4). It can be either positive as in the case of wheat crops and for the sunflower for the smaller solar zenith angle, or negative as in the case of the maize crop.

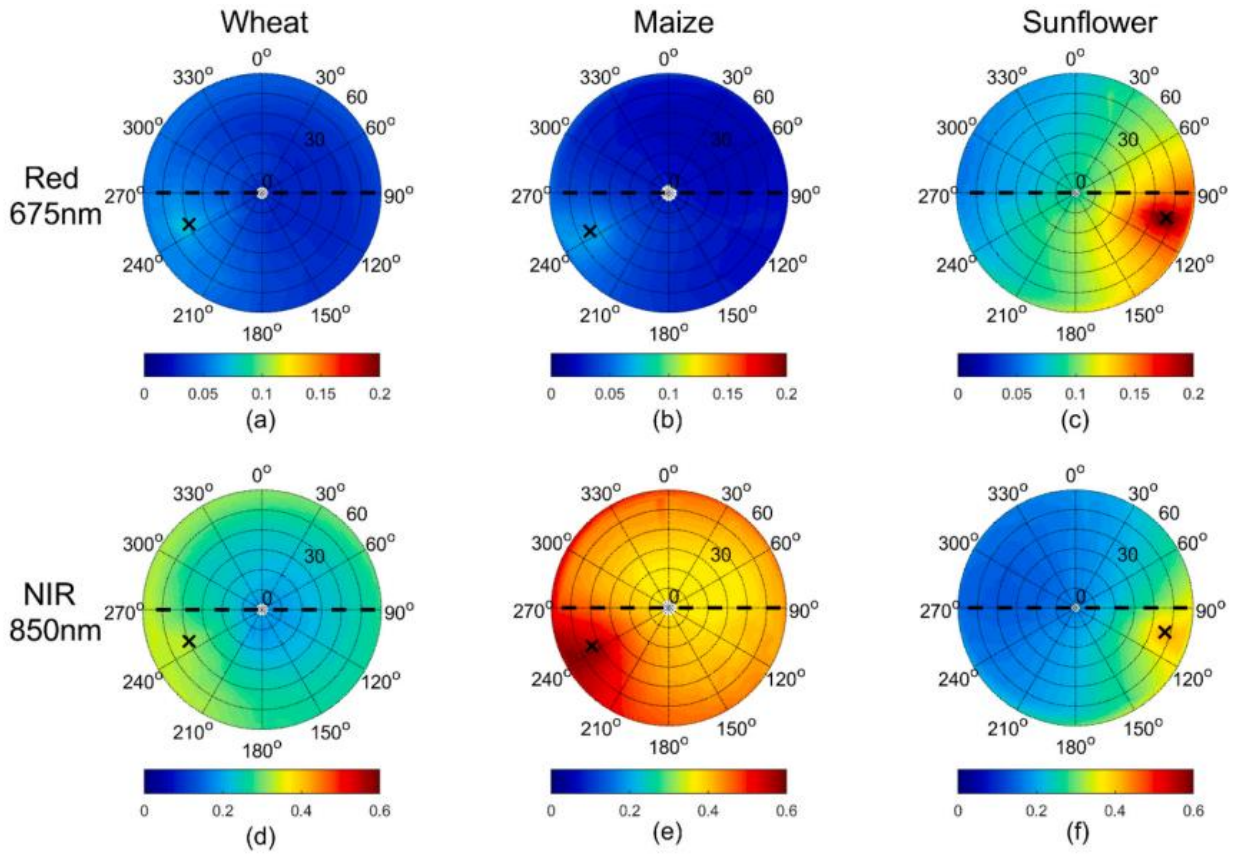

Fig. 10. Polar representation of the measured BRF distribution of the three experiments without the RO (RO-) for 675 nm and 850 nm bands. The sun is displayed as a black cross marker and was at $\theta_s = 45°$. The row orientation (east-west) is represented by the dashed black line. Values represent interpolations from raw measured BRF. (Fig. 5 in Li et al. (2021b))

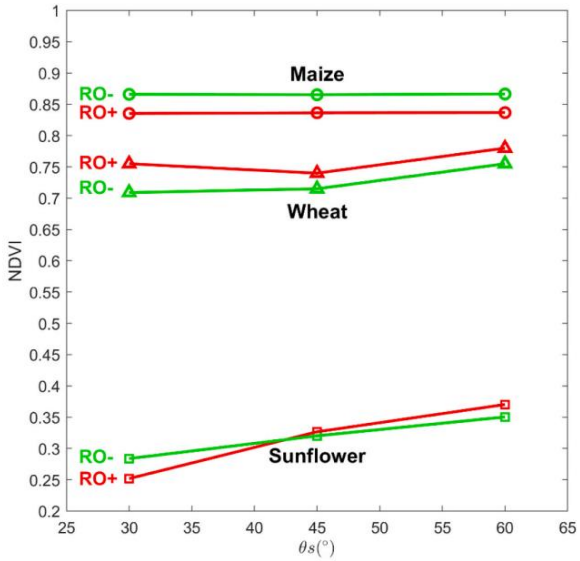

Fig. 11. Variation of NDVI values as observed near nadir (average of BRF for − 10 ◦ < θv < 10◦) for maize, sunflower, and wheat with θs = [30◦,45◦,60◦]. The canopy NDVI values measured with (RO+) and without (RO-) RO are displayed. (Fig. 11 in Li et al. (2021b))

Table 4. Impact of the RO on GAI estimates. The measured NDVI values for the canopy with (RO+) and without (RO-) RO are displayed along with the corresponding GAI. All GAI values are derived from NDVI using the empirical relationship proposed by Verger et al. (2011). The difference is then computed in absolute (ΔGAI) or relative value (ΔGAI %). (Table 4 in Li et al. (2021b))

Species	θ_s	RO-		RO+		ΔGAI	ΔGAI %
		NDVI	GAI	NDVI	GAI		
Maize	30°	0.86	4.6	0.83	3.9	−0.7	−15
	45°	0.86	4.6	0.83	3.9	−0.7	−15
	60°	0.87	4.8	0.83	3.9	−1.0	−19
Wheat	30°	0.70	2.2	0.76	2.7	0.5	23
	45°	0.71	2.3	0.74	2.6	0.3	13
	60°	0.76	2.7	0.78	3.1	0.3	15
Sunflower	30°	0.28	0.4	0.26	0.3	−0.1	−25
	45°	0.32	0.5	0.32	0.5	0.0	0
	60°	0.36	0.6	0.37	0.6	0.0	0

This study proposed a method to sample the BRDF from UAV multi-angular measurements. It offers the advantage to avoid disturbing the crop surface while using a single footprint where the multiangular observations are concentrated. The processing pipeline has been applied in many other research studies or industrial applications conducted in HIPHEN. This study finally demonstrated that the RO layer impacts the estimates of canopy traits such as GAI as derived from the multispectral observations.

4.3.4 Satellite interpretation methods exploit ground measurements to calibrate and validate the estimates of biophysical products

Over the last decade, several global LAI, fAPAR and fCOVER products have been generated from sensors at a spatial resolution close to 1 km and a temporal sampling of 8 to 16 days (Baret et al., 2013, 2007; Knyazikhin et al., 1998; Liang et al., 2013; Yan et al., 2018). However, this kilometric resolution is generally much larger than the typical length scales of most landscapes, limiting therefore the applications to the regional and local scales (Garrigues et al., 2008a). The development of GAI, fAPAR and fCOVER biophysical products from decametric spatial resolution sensors will be better suited for addressing these applications closely related to agriculture.

4.3.4.1 Decametric satellite: estimation of GAI, fAPAR and fCover

This section focuses on the estimation of GAI, fAPAR and fCOVER from satellite sensors at 10 m to 30 m spatial resolution. I mainly addressed three problems:

- Estimating fAPAR from direct, diffuse and total sunlight separately and analyzing the differences between fAPAR definitions and influences on APAR (Li and Fang, 2015).
- Evaluating the performance of a generic inversion algorithm to derive variables using simulated calibration databases without any knowledge of the landcover (Li et al., 2015).
- Evaluating the performance of GAI and fAPAR estimation either using empirical or simulated calibration databases and generic or crop-type specific algorithms (Camacho et al., 2021).

4.3.4.1.1 Estimation of direct, diffuse and total fAPAR (Li and Fang, 2015)

fAPAR represents the summed canopy absorption efficiency for both direct and diffuse PAR. Current satellite fAPAR products typically correspond to black-sky fAPAR under direct illumination only, thus ignoring the diffuse component of fAPAR. The only direct illumination assumption might lead to uncertainties on APAR and yield estimation because the proportion of diffuse PAR over the surface cannot be ignored, even under clear-sky conditions (Gu et al., 2002).

In Li and Fang, 2015, we developed an approach to estimate direct, diffuse and total fAPAR from Landsat-5 Thematic Mapper (TM) satellite measurements at 30 m spatial resolution. fAPAR was retrieved by comparing Landsat surface reflectance and simulated surface reflectance from a coupled soil-leaf-canopy radiative transfer model (SLC) (Verhoef and Bach, 2007) using a lookup table algorithm. Besides, field measured direct, diffuse and total fAPAR were derived from crops, deciduous broadleaf forests and evergreen needleleaf forests at six FLUXNET sites ((http://public.ornl.gov/FLUXNET/)). These ground data were used to validate satellite retrieved fAPAR. Landsat-estimated direct, diffuse and total APAR were finally calculated by multiplying Landsat fAPAR with corresponding ground measured direct, diffuse or total PAR at the satellite pass time.

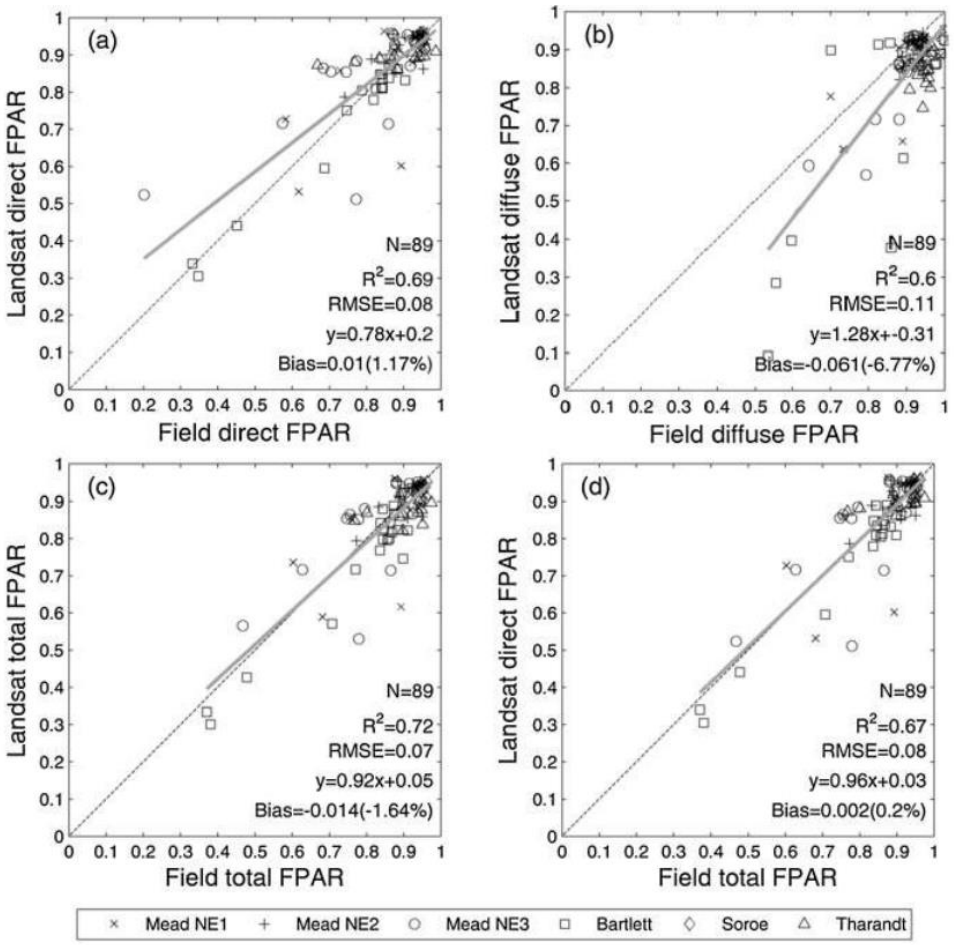

Fig. 12. Validation of Landsat-5 estimated fAPARs with field measured values. All field measurements are instantaneous values at 10:00 A.M. (Figure 9 from Li and Fang (2015))

In general, all Landsat-estimated fAPARs correspond well with the field measurements (Figure 12). The Landsat-estimated direct fAPAR is slightly higher than the field measurements by 1.17%, whereas the Landsat diffuse fAPAR is lower than the field measurements by -6.77%. Compared with the field-measured total fAPAR, the Landsat total fAPAR is larger by 1.64%, whereas the Landsat direct fAPAR is slightly lower by 0.2%. (Fig. 12).

The differences between fAPARs will influence the estimation of APARs. The direct and diffuse APARs were calculated using the field-measured direct and diffuse PAR, multiplied by the corresponding Landsat-estimated direct and diffuse fAPARs (Figure 13a). Generally, the relative difference between the direct and diffuse APAR decreases with increasing diffuse ratio (R^2 = 0.76), and the diffuse APAR tends to be lower than the direct APAR when diffuse ratio smaller than 50%. Conversely, the diffuse APAR is higher than the direct APAR when the diffuse ratio is larger than 50%. On average, the diffuse APAR is lower than the direct APAR by -421.36 µmol s^{-1} m^{-2} (-37.03%). The Landsat-estimated direct and total APARs were also calculated by multiplying the corresponding Landsat direct and total fAPARs, respectively, by the field-measured downwelling PAR. In general, the total APAR is higher than the direct APAR (277.72 µmol s^{-1} m^{-2}, 62.97%), and the difference increases with the diffuse ratio (R^2 = 0.76) (Figure 13b).

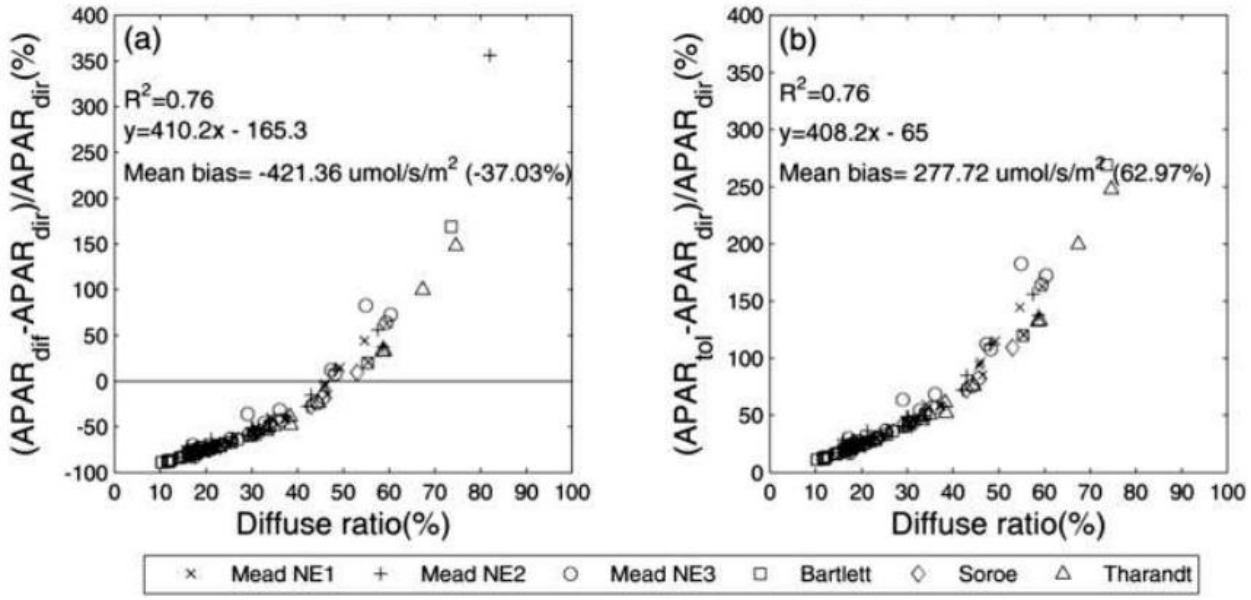

Fig. 13. (a) The relative differences between diffuse APAR ($APAR_{dif}$) and direct APAR ($APAR_{dir}$) as a function of diffuse ratio. (b) The relative differences between total APAR ($APAR_{tol}$) and direct APAR ($APAR_{dir}$) as a function of diffuse ratio. (Figure 10 from Li and Fang (2015))

The differences between the direct and diffuse fAPARs are mainly related to canopy structure and the solar zenith angle. The total fAPAR should be generated from current satellite sensors, and the differences in fAPAR definitions should be considered in the estimation of APAR in vegetation models. More frequent field measurements are necessary to improve the accuracy of ground fAPAR measurements and to validate satellite products. The present approach can be extended to estimate regional and global direct and diffuse fAPAR products utilizing existing and future satellite data.

4.3.4.1.2 A generic algorithm to retrieve GAI, fAPAR and fCOVER from Landsat-8 and SPOT4 time series ***(Li et al., 2015)***

Due to the impact of clouds or the design of sensors, the monitoring capacity and actual use of decametric sensors is always limited by the revisit frequency or the cost of images. The launch of Sentinel-2 in 2015 provided data at decametric resolution with a high revisit frequency to allow quantifying the canopy functioning at the local to regional scales. Before launching Sentinel-2, a SPOT4 (Take5) experiment was started in 2013 by the French Agency Centre National d'Etudes Spatiales (CNES), aiming at providing time series of images with similar revisit frequency and resolution as Sentinel-2 data (http://www.cesbio.ups-tlse.fr/multitemp/) to prepare for the use of Sentinel-2. Since the SPOT4 (Take5) only lasted few months which was not enough to cover a full vegetation cycle, Landsat-8 images at 30m spatial resolution were used to complete the measurements. The objective of this study was to evaluate the performance of a generic algorithm to generate consistent time series of LAI, fAPAR and fCOVER products from the combination of SPOT4_HRVIR and Landsat-8 surface reflectance data acquired during a growth season, without any prior knowledge of the landcover.

A time series of high spatial resolution SPOT4_HRVIR (16 scenes, 20m spatial resolution) and Landsat 8 (18 scenes, 30m spatial resolution) images acquired in 2013 over the France southwestern site were used to generate the LAI, fAPAR and fCOVER products. The SPOT4_HRVIR data was resampled to 30m to be consistent with the Landsat-8 data. For each sensor and each biophysical variable, a neural network was first trained over PROSPECT+SAIL radiative transfer model (Jacquemoud et al., 2009) simulations of top of canopy reflectance data for green, red, near-infrared and short wave infrared bands (Fig. 14).

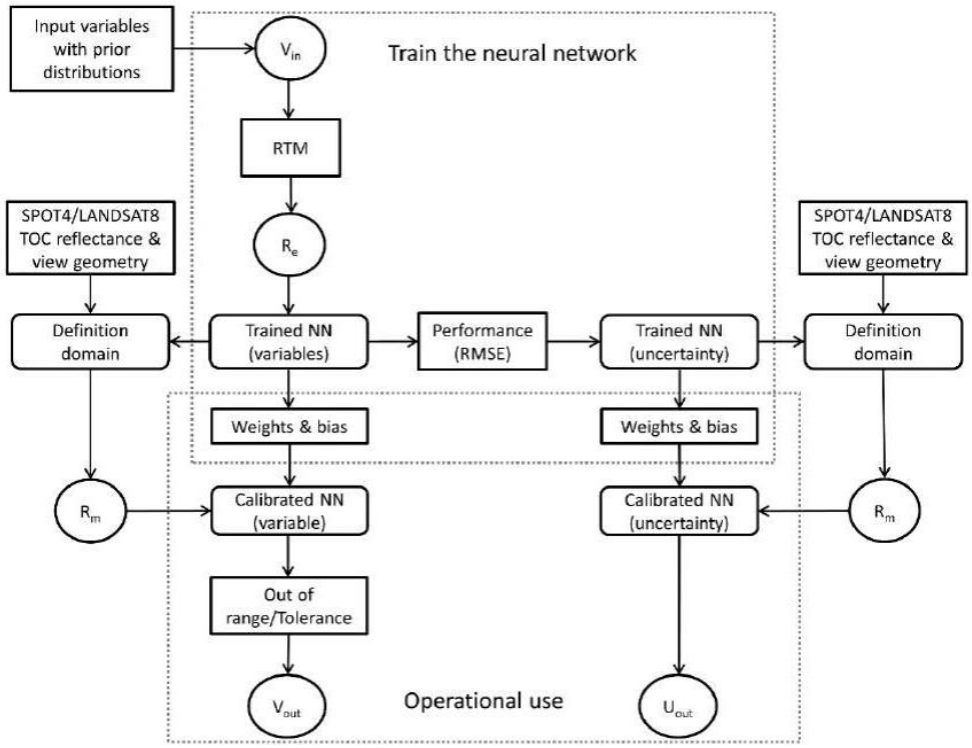

Fig. 14. The outline of the algorithm. (Figure 3 in Li et al. (2015))

Results show that variable retrieved from both sensors have a good spatial and temporal consistency, e.g., LAI in Fig. 15. For very close acquisition dates, SPOT4_HRVIR and Landsat 8 products are very similar and most of the differences are within a limited range. The results demonstrate the robustness of the proposed algorithm and its suitability to be applied to several satellites. The temporal profiles show that two sensors complement themselves to describe the seasonal variation of vegetation: the combination of sensors may overcome the typical low revisit frequency of decametric sensors, allowing to build virtual constellations.

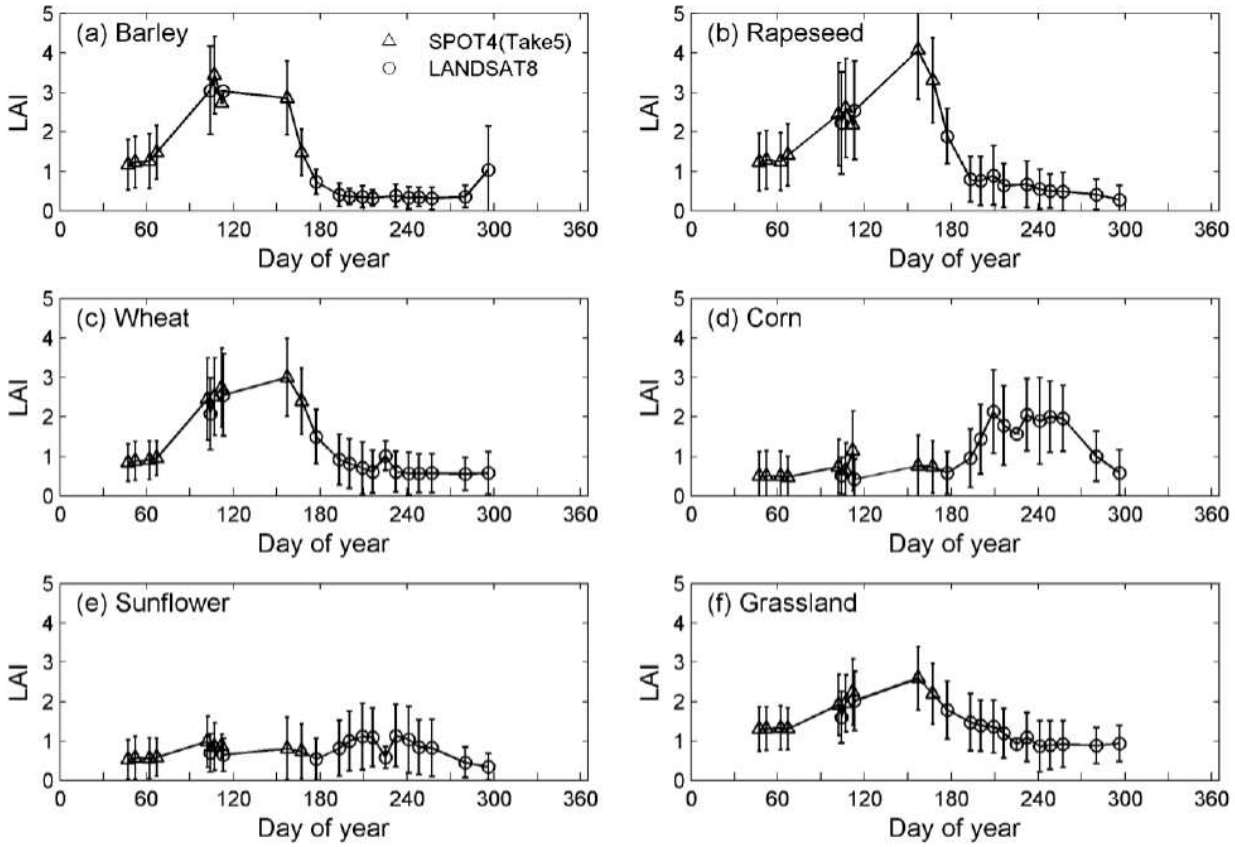

Fig. 15. Seasonal variation of LAI products estimated from SPOT4_HRVIR (Take5) and Landsat-8 sensors. (Figure 8 in Li et al. (2015))

Compared with ground measurements taken over wheat, maize and sunflower using digital hemispherical photographs, the satellite estimates were strongly correlated with the field measurements ($R^2 > 0.79$), corresponding to a RMSE = 0.49 for LAI, RMSE = 0.10 (RMSE = 0.12) for black-sky (white sky) fAPAR and RMSE = 0.15 for FCOVER (Fig. 16). It is concluded that the proposed generic algorithm provides a good basis to monitor the seasonal variation of the vegetation biophysical variables for important crops at decametric resolution.

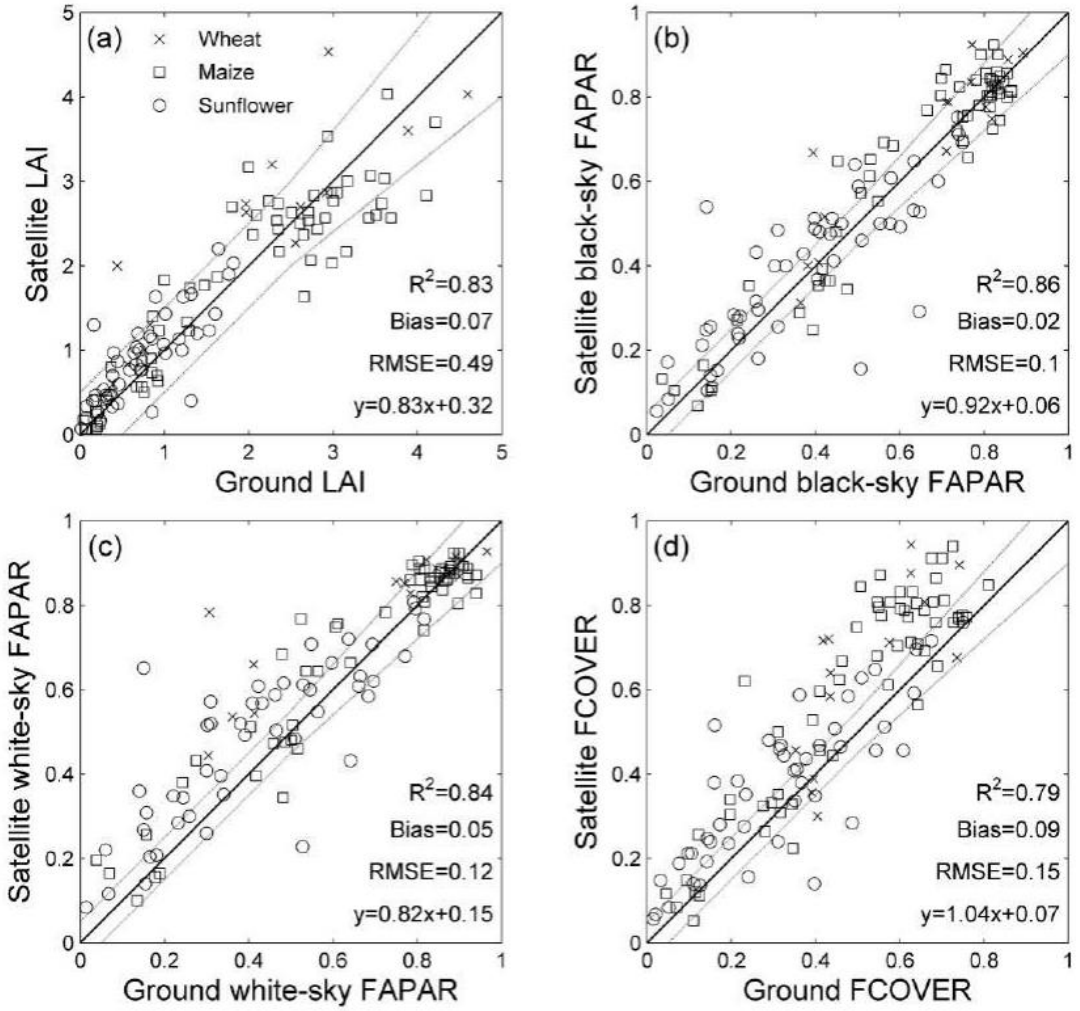

Fig. 16. Direct validation of (a) LAI, (b) black-sky FAPAR, (c) white-sky FAPAR and (d) FCOVER products derived from the SPOT4_HRVIR (Take5) and Landsat 8 sensors with the ground measurements. (Figure 11 in Li et al. (2015))

This study showed the interest of this generic algorithm to derive LAI, fAPAR and fCOVER consistent products from SPOT4_HRVIR and Landsat 8 over the study area. These principles were originally from the pipeline designed for Sentinel-2 and now have been applied to Sentinel-2 with a high revisit frequency and a decametric spatial resolution. This study was based on a generic algorithm that applied potentially to all landcover types. Major improvements were expected from the development of more specific algorithms, i.e., when the training is achieved over a limited set of cases defined for each landcover type. This 'specific algorithm' was studied in the next paper.

4.3.4.1.3 Performance of GAI and fAPAR estimation using empirical or simulated calibration databases and generic or crop-type specific algorithms (Camacho et al., 2021)

Several methodologies have been developed to estimate GAI and fAPAR from satellite data at decametric resolution (Amin et al., 2021; Delloye et al., 2018; Drusch et al., 2012; Ganguly et al., 2012; W. Li et al., 2015). According to the source of training datasets, e.g., ground measurements and model simulations, the retrieval algorithms can be categorized into empirical and physical approaches.

Empirical approaches rely on the ground measurements for calibration, and they were typically limited by the availability of ground dataset, representativeness of environmental and illumination conditions. Conversely, methods based on radiative transfer model simulations for calibration are generalizable but limited by the model assumptions and parameters setting of priors. Besides, depending on whether the approaches can be applied to all the crop types or only to a specific crop type, the retrieval approach also can be categorized as “generic” or “specific”, respectively. Although the generic method has been demonstrated to provide good estimation of GAI and fAPAR (W. Li et al., 2015), crops have particular structural and optical properties features may require ‘specific’ algorithms when considering contrasted crop types.

The objective of this study is to compare different retrieval approaches for GAI and fAPAR over crops using a comprehensive dataset covering worldwide sites and dates along the growing season. A unique ground database including 873 GAI and 730 fAPAR data points over 25 different crop types for a wide range of conditions and growth stages was used this study. They can match Landsat-8 observations because the ground measurements were taken when the satellite was working. Several machine learning techniques were investigated to retrieve GAI and fAPAR from the Landsat-8 top of canopy reflectance values, either using empirical (EMP) or simulated calibration (SIM) databases and generic or crop-type specific algorithms.

For the generic approach, results show that GAI and fAPAR estimation performances based on dataset simulated with the PROSAIL model were significantly degraded as compared to the machine learning techniques trained over the experiment datasets (Fig. 17). This is mainly because the PROSAIL model is a 1-D radiative transfer model that does not account for the 3-D architecture of crops. This emphasizes the importance of the prior-knowledge on the crop type and growth stages to estimate the biophysical variable. The results also demonstrate that gaussian process regression method provides best performance for GAI estimation trained either on simulation data or empirical datasets.

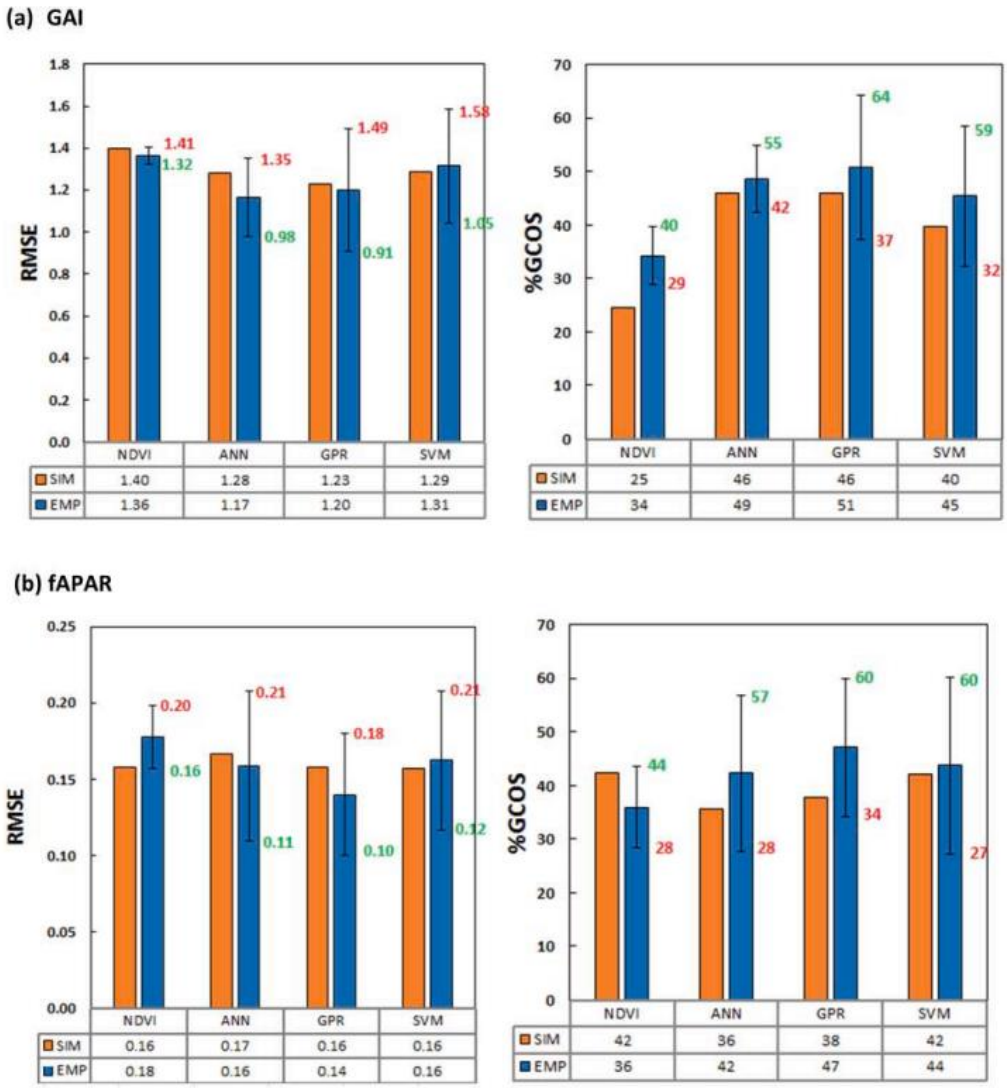

Fig. 17. Performances of NDVI, ANN, GPR and SVM machine learning techniques for GAI (a) and fAPAR (b) using generic SIM (orange) and EMP (blue) approaches. The blue bar shows the generic EMP midpoint between the best-case and worst-case performances. Generic SIM and EMP mean performances are shown in the table. (Fig. 3 in Camacho et al. (2021))

Compared with estimates from the generic approach, the specific approach provides generally better results when the training dataset on a specific crop is applied to the same crop as demonstrated by the lowest RMSE values observed on the diagonal of Table 5 for each variable (RMSE from 0.45 – 1.19 for GAI and 0.07 – 0.15 for fAPAR). However, the performance degraded significantly when the training on a specific crop is applied to other crops (Table 5, RMSE from 1.5 to 1.9 for GAI and 0.16 – 0.29 for fAPAR).

			Validation						
			Rice	Corn	Wheat & Barley	Sunflower	Soybean	Others	All
Training	GAI	Rice	**0,79**	1,82	2,46	2,44	2,00	2,14	1,81
		Corn	1,56	**0,77**	1,82	0,95	0,78	0,98	1,34
		Wheat & Barley	1,53	1,59	1,19	1,06	1,73	1,45	1,50
		Sunflower	2,08	1,15	2,38	**0,45**	0,85	1,34	1,74
		Soybean	2,53	1,35	2,06	1,17	0,80	1,53	1,88
		Others	1,82	0,87	2,18	0,89	0,77	0,89	1,52
		Generic *best-case*	0,82	0,83	**1,16**	0,61	**0,71**	**0,83**	**0,91**
		Generic *worst-case*	1,78	1,06	1,96	0,96	0,74	1,02	1,49
	fAPAR	Rice	**0,09**	0,30	0,41	0,39	0,33	0,41	0,29
		Corn	0,22	**0,10**	0,15	0,13	0,07	0,19	0,16
		Wheat & Barley	0,28	0,13	**0,09**	0,16	0,08	0,22	0,19
		Sunflower	0,21	0,14	0,18	**0,09**	0,09	0,21	0,18
		Soybean	0,28	0,18	0,19	0,19	**0,07**	0,22	0,21
		Others	0,21	0,17	0,24	0,18	0,13	0,15	0,19
		Generic *best-case*	0,09	0,11	0,11	0,12	0,10	**0,13**	**0,11**
		Generic *worst-case*	0,19	0,16	0,17	0,17	0,11	0,20	0,18

Table 5. Estimation performances expressed in RMSE of GAI (top) and fAPAR (bottom) when trained on a crop type and validated over all the other crop types. The GPR technique applied to the EMP training is used here. The diagonal of the matrix for each variable (cells with thick border line) corresponds to the validation on the same crop type as that used for the training. The generic approach for best-case and worst-case training is also displayed for comparison. Validation on 'All' crop type corresponds to the performances computed over all the crop types. Numbers in bold correspond to the smallest value for the validation on a given variable and crop type. Colors are scaled according to the RMSE value. (Table 5 from Camacho et al. (2021))

This study investigated several ways to estimate GAI and fAPAR variables from Landsat-8 satellite data. A large database over 25 different crops types for a wide range of conditions and growth stages was used in this study. Several retrieval processes were investigated, including band selection of Landsat-8, machine learning techniques (ANN, GPR, SVM) versus simple NDVI approach, training (EMP, SIM) and approach (generic, specific) for both GAI and fAPAR variables. Among the machine learning techniques considered, GPR appears to be the one performing the best over most cases investigated mainly for fAPAR. However, GPR is more computer demanding as compared to the other machine learning techniques. Compared to generic methods, crop-specific approach performed slightly better, indicating the knowledge of crop type is an important information when interpreting the satellite signal.

4.3.4.2 Validation of hectometric and kilometric satellite products

Currently, a number of kilometric and hectometric resolution LAI products have become available, e.g., MODIS (Knyazikhin et al., 1998), CYCLOPES (Baret et al., 2007), JRC-TIP (Pinty et al., 2011), GEOV1 and GEOV2 (Baret et al., 2013), EPS (García-Haro et al., 2018), GLASS (Xiao et al., 2015, 2014), GLOBMAP (Liu et al., 2012), PROBA-V (Baret et al., 2016) and VIIRS (Yan et al., 2018). A high quality of remote sensing biophysical products is mandatory for using them in models and applications (Morisette et al., 2006).

To properly understand and quantify the uncertainties associated with these products, a number of validation studies have been performed at the global or regional scale for a variety of land cover types (Camacho et al., 2013; Garrigues et al., 2008b; Weiss et al., 2007). Most of these validation studies have been conducted under the framework of the Land Product Validation sub-group (LPV) of the Working Group Cal/Val (WGCV) of the Committee on Earth Observing Satellite (CEOS) (http://lpvs.gsfc.nasa.gov/). These validation studies can be categorized in two types:

(1) evaluation of the spatial and temporal consistency of these products by intercomparison with reference products without ground measurements.
(2) direct comparison with ground measurements processed according to CEOS/WGCV LPV recommendations (Morisette et al., 2006);

In the past few years, I have participated in the validation of various LAI satellite products and made contributions in three aspects:

- The analysis of the impacts of vegetation mixture and misclassification on MODIS LAI products (Fang et al., 2013b).
- The study of spatial and temporal consistency of five major global LAI products and their associated uncertainties through intercomparison (Fang et al., 2013a).
- The evaluation of the quality of several global LAI moderate resolution products over croplands through direct comparisons with ground LAI measurements (Fang et al., 2019).

4.3.4.2.1 Impacts of vegetation mixture and misclassification on MODIS LAI products ***(Fang et al., 2013b)***

The MODIS LAI product (MCD15 C5) is one of the most popular products in the community. Understanding its uncertainties is critical to assimilate LAI into the ecosystem and land surface models (GCOS, 2016; Morisette et al., 2006). The algorithm of MODIS LAI products uses land cover types as prior information to constrain the vegetation structural and optical parameters in the canopy radiative transfer models (Knyazikhin et al., 1998). Thus, the errors in classifying land cover type may propagate into LAI uncertainties during the retrieval process. The objective of this study is to investigate the effect of biome misclassification on MODIS LAI estimation using a statistical approach.

The 8-day synergistic LAI products at 1km spatial resolution (MCD15 C5) and land cover products at 500m resolution (MCD12Q1 C5) during 2003 – 2009 were used in this study. The secondary land cover types retrieved in the International Geosphere Biosphere Program (IGBP) classification scheme (Friedl et al., 2002) was converted to the MODIS LAI/FAPAR biome types in the analysis. The paired primary and secondary land cover types provide possibilities to study potential LAI uncertainty caused by biome misclassification due to subpixel mixture and biome misclassification.

Pixels with high confidence in the primary land cover type and of identical primary and secondary type were regarded as representing ‘pure’ biome types with minimal biome mixing or misclassification.

Otherwise, the pixels were regarded as 'mixed' or 'misclassified'. A confusion matrix was constructed to explore the LAI discrepancies induced by potential subpixel mixture and biome misclassification.

Results show that 28.74% of MODIS LAI products are over pure pixels and the other 71.26% are retrieved as mixed biome types. When misclassification between distinct biome types occurs, it does not generally translate into strong disagreement in LAI retrievals. Misclassification between herbaceous types has minimal impact on LAI retrievals (<0.37 or 27.0%), partly due to their relatively lower LAI values (Table 6).

Table 6. (a) Confusion matrix for LAI mean values for pure (bold) and mixed pixels and (b) the relative LAI errors induced by biome misclassification. Statistics based on data from 2003−2009. EBF, DBF, ENF and DNF represent evergreen broadleaf forests, deciduous broadleaf forests, evergreen needleleaf forests and deciduous needleleaf forests, respectively. (Table 2 in Fang et al. (2013b)

(**a**) Mean LAI values

↓Primary Biome Type	**Secondary Biome Type**							
	Grasses/ Cereal Crops	**Shrubs**	**Broadleaf Crops**	**Savanna**	**EBF**	**DBF**	**ENF**	**DNF**
Grasses/cereal crops	**0.56**	0.27	0.70	0.39	(1.29)	(0.94)	(0.93)	(0.91)
Shrubs	0.41	**0.29**	(0.78)	0.46	(1.03)	(0.83)	(1.04)	(0.81)
Broadleaf crops	1.29	1.00	**1.37**	1.10	(1.34)	(1.21)	(1.23)	(1.18)
Savanna	1.41	1.63	1.68	**0.84**	(1.91)	2.18	(1.25)	(1.99)
EBF	4.02	3.50	4.48	3.97	**(4.17)**	3.76	(3.09)	(3.08)
DBF	(1.91)	2.07	(1.97)	2.07	2.14	**2.17**	(2.18)	2.04
ENF	(0.72)	1.37	(0.72)	1.12	1.86	1.76	**1.99**	1.75
DNF	(1.33)	1.52	(1.12)	1.51	1.60	1.64	(1.54)	**1.67**
(**b**) Relative errors								
Grasses/cereal crops	**0.0**	−51.8	25.0	−30.4	(130.4)	(67.9)	(66.1)	(62.5)
Shrubs	41.4	**0.0**	(169.0)	58.6	(255.2)	(186.2)	(258.6)	(179.3)
Broadleaf crops	−5.8	−27.0	**0.0**	−19.7	(−2.2)	(−11.7)	(−10.2)	(−13.9)
Savanna	67.9	94.1	100.0	**0.00**	(127.4)	159.5	(48.8)	(136.9)
EBF	−3.6	−16.1	7.4	−4.8	**(0.0)**	−9.8	(−25.9)	(−26.1)
DBF	(−12.0)	−4.6	(−9.2)	−4.6	−1.4	**0.0**	(0.5)	−6.0
ENF	(−63.8)	−31.2	(−63.8)	−43.7	−6.5	−11.6	**0.0**	−12.1
DNF	(−20.4)	−9.0	(−32.9)	−9.6	−4.2	−1.8	(−7.8)	**0.0**

Analysis in LAI climatologies show that biome misclassification generally leads to an LAI overestimation for savanna, but an underestimation for forests. The largest errors caused by misclassification are found for savanna (0.51), followed by evergreen needleleaf forests (0.44) and broadleaf forests (~0.31) (Table 7).

Month	Jan	Feb	Mar	Apr	May	Jun	Jul	Aug	Sep	Oct	Nov	Dec	Average	MAEs
Grasses/ cereal crops	−0.02	−0.01	−0.01	−0.02	−0.07	−0.13	−0.16	−0.11	−0.07	−0.05	−0.03	−0.04	−0.06	0.06
Shrubs	0.11	0.12	0.13	0.17	0.19	0.14	0.10	0.13	0.14	0.15	0.11	0.10	0.13	0.13
Broadleaf crops	−0.08	−0.06	−0.07	−0.14	−0.21	−0.17	−0.15	−0.21	−0.29	−0.28	−0.17	−0.11	−0.16	0.16
Savanna	0.57	0.58	0.55	0.54	0.48	0.42	0.41	0.39	0.37	0.46	0.66	0.64	0.51	0.51
EBF	−0.39	−0.43	−0.33	−0.25	−0.44	−0.50	−0.17	0.22	0.24	−0.14	−0.20	−0.43	−0.24	0.31
DBF	0.33	0.29	0.24	0.03	−0.45	−0.54	−0.46	−0.42	−0.43	−0.07	0.19	0.34	−0.08	0.32
ENF	−0.38	−0.28	−0.26	−0.33	−0.54	−0.56	−0.29	−0.63	−0.56	−0.30	−0.42	−0.67	−0.44	0.44
DNF	0.17	−0.03	−0.04	−0.07	−0.21	−0.47	−0.29	−0.41	−0.24	−0.04	0.03	0.25	−0.11	0.19

Table 7. Monthly average of the misclassification induced LAI errors for the eight primary biome types (2003−2009). The mean absolute errors (MAEs) are calculated from the average of the absolute monthly errors. (Table 3 in Fang et al. (2013b))

Biome misclassification is a major factor contributing to LAI uncertainties for savanna, while for forests, the main source of uncertainties may be due to algorithm deficits, especially in summer. To reduce the LAI uncertainties, further efforts should therefore be focused on improving the biome classification for the structurally complex savanna systems and refinement of the retrieval algorithms for forest biomes.

4.3.4.2.2 Intercomparison of five major global LAI products and their associated uncertainties ***(Fang et al., 2013a)***

To better assess the quality of global LAI products, five major LAI products (MODIS, GEOV1, GLASS, GLOBMAP and JRC-TIP) were compared between 2003 and 2010 at a 0.01° spatial resolution and with a monthly time step. The daily Land-SAF product was used as a regional reference to evaluate the performance of other global products in Africa. Special attention has been paid to the product quality indicators to investigate the uncertainties of the products. Cross-sensor LAI conversion equations were derived for different biome types defined by the MODIS landcover products.

Results show that MODIS, GEOV1, GLASS, and GLOBMAP are generally consistent in spatial patterns and magnitudes (Fig. 18). All the products show a smooth seasonal evolution and agree very well for grasses/cereal crops and shrubs, although differences are observed on forests and savanna. In particular, JRC-TIP LAI, which is defined as effective LAI, is continuously lower than the other true LAI products over broadleaf and needleleaf forests. The underestimation is more pronounced during the maturity stage, reaching nearly 4 for evergreen broadleaf forest (EBF).

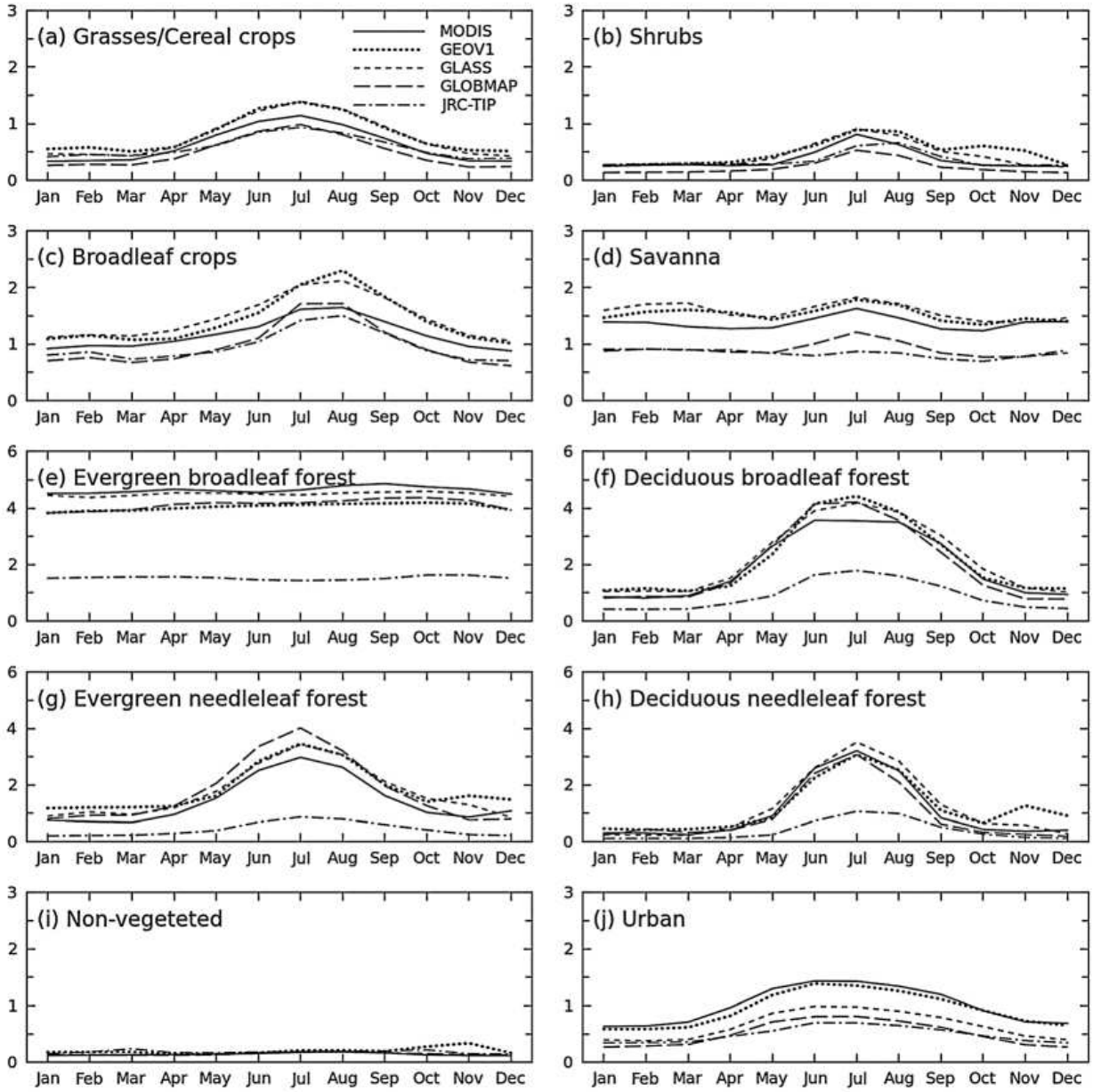

Fig. 18. Climatologies of global monthly MODIS, GEOV1, GLASS, GLOBMAP, and JRC-TIP LAI products for different biome types from 2003 to 2010 (0.05°). (Figure 2 in Fang et al. (2013a))

Regarding to pixel-level magnitude, MODIS, GEOV1, GLASS and GLOBMAP LAI products have strong linear correlations with each other, with R^2 ranging between 0.743 and 0.896 (Fig. 19). This indicates the products can be replaced if one is missing on some dates or regions. The results further demonstrate the underestimation of JRC-TIP LAI products, that JRC-TIP values are about one third of the other LAI values and have a low correspondence with these products ($R^2 \leq 0.66$).

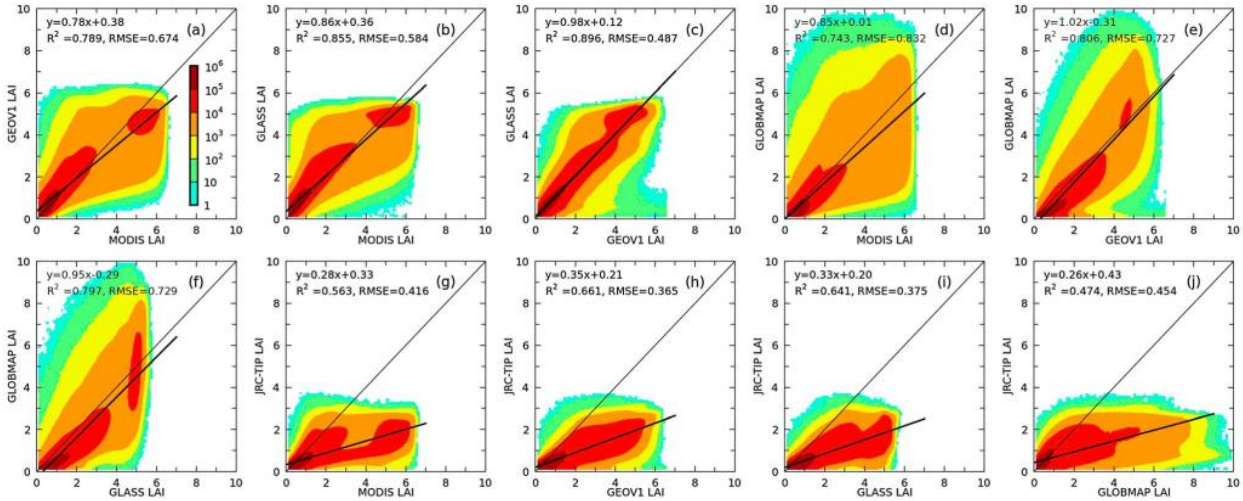

Fig. 19. Density scatter plots between MODIS, GEOV1, GLASS, GLOBMAP, and JRC-TIP global LAI products from 2003 to 2010 (0.05°).

The overall uncertainties and relative uncertainties are in the following order: MODIS (0.17, 11.5%) < GEOV1 (0.24, 26.6%) < Land-SAF (0.36, 37.8%) < JRC-TIP (0.43, 114.3%) (Table 8). The highest relative uncertainties usually appear in ecological transition zones (Fig. 20). More than 75% of MODIS, GEOV1, JRC-TIP, and Land-SAF pixels are within the absolute uncertainty requirements (±0.5) set by (GCOS, 2011), whereas more than 78.5% of MODIS and 44.6% of GEOV1 pixels are within the threshold for relative uncertainty (20%) (Fig. 20 and Table 8).

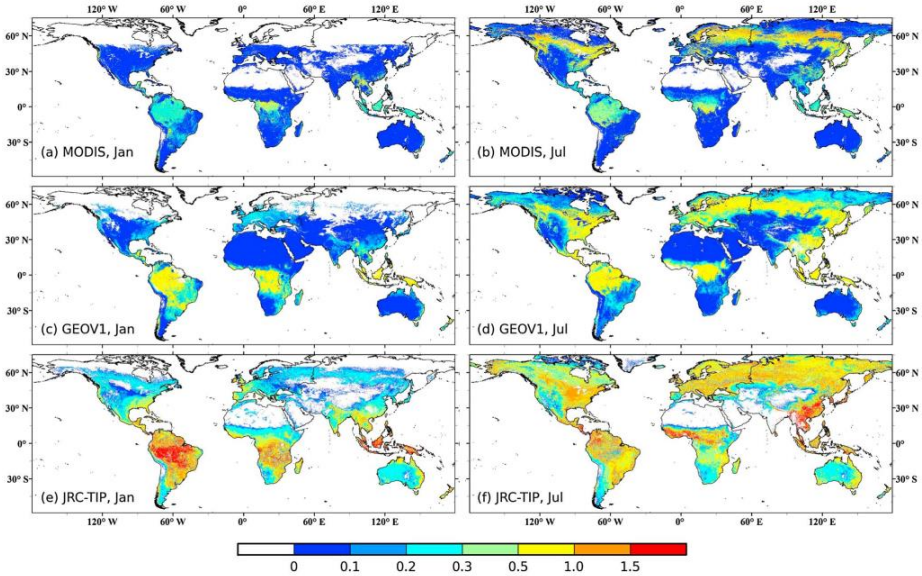

Fig. 20. LAI uncertainty maps for MODIS, GEOV1, and JRC-TIP from 2003 to 2010 (0.05) in January (left panels) and July (right panels), respectively. (Figure 4 in Fang et al. (2013a))

Table 8. Yearly Mean LAI, Uncertainties, and Relative Uncertainties for Different Biome Types, 2003–2010a (Table 3 in Fang et al. (2013a))

	Biome Types	Grass/Crop-C	Shrub	Crop-B	Savanna	EBF	DBF	ENF	DNF	Non-V	Urban	Average
Mean LAI	MODIS	0.64	0.41	1.17	1.38	4.64	2.04	1.58	1.34	0.14	1.01	1.43
	GEOV1	0.84	0.57	1.42	1.53	4.05	2.27	2.03	1.55	0.20	0.94	1.55
	GLASS	0.79	0.51	1.46	1.58	4.50	2.28	1.91	1.54	0.15	0.65	1.55
	GLOBMAP	0.51	0.27	0.98	0.92	4.13	2.07	1.95	1.30	0.15	0.51	1.23
	JRC-TIP	0.61	0.41	0.96	0.83	1.53	0.92	0.46	0.53	0.19	0.50	0.78
	Land-SAF	0.78	0.54	1.46	1.67	3.46	2.31	2.03		0.31	1.26	1.63
Uncertainty	MODIS	0.07	0.05	0.09	0.16	0.38	0.36	0.43	0.33	0.02	0.12	0.17
	GEOV1	0.17	0.13	0.26	0.31	0.66	0.41	0.36	0.33	0.00	0.22	0.24
	JRC-TIP	0.40	0.24	0.69	0.62	1.14	0.62	0.42	0.39	0.01	0.44	0.43
	Land-SAF	0.25	0.21	0.36	0.47	0.88	0.54	0.43		0.2	0.3	0.36
Relative uncertainty (%)	MODIS	9.1	11.8	6.5	11.0	8.8	15.8	23.9	19.0	4.8	3.8	11.5
	GEOV1	33.8	35.1	24.6	23.5	15.9	23.3	18.4	25.9	6.2	29.3	26.6
	JRC-TIP	126.7	133.9	101.0	103.9	78.9	103.3	137.2	141.3	104.0	130.7	114.3
	Land-SAF	56.8	57.2	37.4	30.3	25.2	25.4	30.1		102.3	32.1	37.8

[a]Land-SAF derived from 2007 to 2010 over Africa. The last column is calculated from the global average of all vegetated pixels. Crop-C and Crop-B refer to the cereal crops and broadleaf crops, respectively. EBF, DBF, ENF, and DNF stand for the evergreen broadleaf forest, deciduous broadleaf forest, evergreen needleleaf forest, and deciduous needleleaf forest, respectively. Non-V indicates the non-vegetated type. In all statistics, positive (>0) values were considered for LAI, and non-negative (≥0) values for uncertainty and relative uncertainty.

This study reveals the discrepancies mainly due to differences between definitions of LAI (true versus effective), retrieval algorithms, and input data. Future product development and validation studies should focus on areas (e.g., sparsely vegetated and savanna areas) and periods (e.g., winter time) with higher uncertainties.

4.3.4.2.3 Evaluation of global moderate resolution LAI products over croplands through direct comparisons with ground measurements and decametric satellite observations ***(Fang et al., 2019)***

Besides the previous global studies, there is also a need to conduct validation studies for specific ecosystems at a regional scale. However, the lack of continuous accurate ground measurements has hampered the effective validation of existing LAI products over agricultural fields. This study conducted rigorous validation of seven global LAI products (EPS, GEOV2, GLASS, GLOBMAP, MODIS, PROBA-V and VIIRS) over typical agricultural croplands in northeastern China. Seasonal continuous LAI measurements were obtained from field campaigns in paddy rice fields of Honghe in 2012 and 2013, and in maize, soybean, and sorghum fields in Hailun in 2016. High resolution reference LAI maps were first derived from HJ-1, Landsat 7, and Sentinel-2A images with the look-up table (LUT) inversion method from PROSAIL radiative transfer model and were evaluated with the field measured LAI (R^2 = 0.85 and RMSE = 0.66, Fig. 21).

Subsequently, the moderate resolution LAI products were validated with the upscaled high resolution reference LAI. Results show that there are huge variations among the different products when compared with upscaled reference LAI maps, with RMSE varying between 0.8 and 2.0, and the RRMSE between 25 and 60% (Fig. 22). The performance of the LAI products varies at different phenological stages: the global LAI tends to overestimate the high-resolution reference LAI during the green-up stage, largely fluctuates during the maturity stage, and underestimates during the senescence stage. The weak performance is mainly attributed to the lack of regional tuning of the global LAI algorithms over agricultural areas.

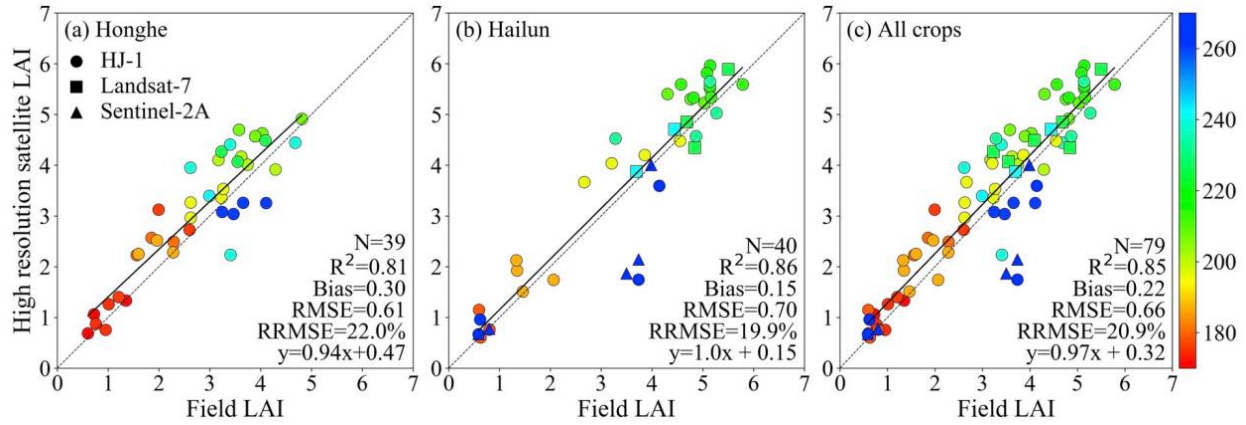

Fig. 21. Comparison of the high resolution reference LAI (3 × 3 pixels) with the field measured data for paddy rice in Honghe (a), maize, soybean, and sorghum in Hailun (b), and all crops (c). The colors represent different the day of year. (Fig. 5 in Fang et al. (2019))

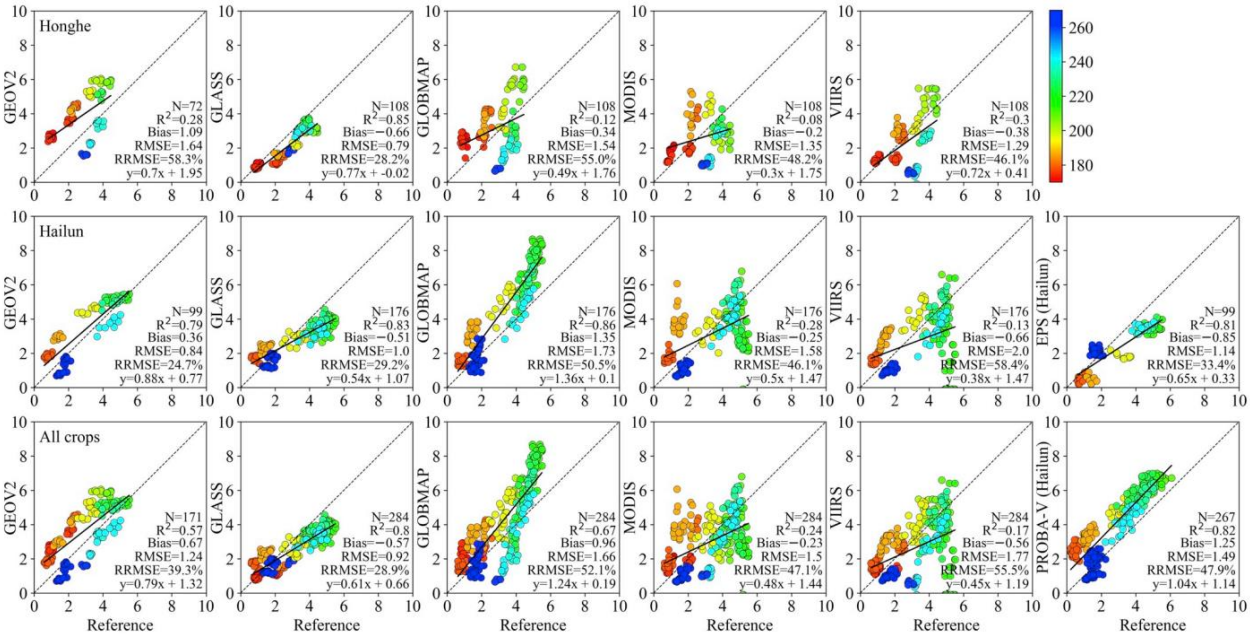

Fig. 22. Comparison of the moderate resolution LAI products with the upscaled reference LAI (3 × 3 pixels) at the Honghe (first row), Hailun (middle), and both sites (bottom). The right most column compares for EPS and PROBA-V over Hailun. The color bar indicates different observation dates. (Fig. 11 in Fang et al.(2019))

Further efforts are necessary to improve the LAI product quality in local and regional scales, especially for the water-logged paddy rice fields. This study highlights the importance of crop-specific and temporal validation at a regional scale. More validation studies are needed in other parts of the world with sufficient field LAI measurements. The uncertainty information exposed in this study is beneficiary for product improvement and the application community.

4.3.4.3 Fusion of decametric and hectometric satellite data

In the context of sustainable agriculture, reliable crop monitoring has become more and more important for agricultural practices. A good crop growth monitoring from remote sensing relies on two important points: dense time series and optimal spatial resolution (Azzari et al., 2017; Gao et al., 2017; Lobell et al., 2015; Yang et al., 2020; Zhu et al., 2018). However, due to the tradeoff between scanning swath and pixel size and the impacts of environmental factors (e.g., cloud), it is difficult to obtain measurements with both high temporal resolution and optimal spatial resolution from a single platform (Gao et al., 2006; Ghamisi et al., 2019). Spatio-temporal fusion of measurements acquired from various platforms is therefore a relevant solution to this problem.

Spatio-temporal fusion algorithms can be categorized in two classes: spatial unmixing-based fusion (Zhukov et al., 1999; Zurita-Milla et al., 2008) and image pair-based fusion, such as the widely used algorithm STARFM (spatial and temporal adaptive reflectance fusion model)(Gao et al., 2006) and its extensions (Ghamisi et al., 2019; Hilker et al., 2009; Wang et al., 2014, 2017; Weng et al., 2014; Wu et al., 2017; Zhu et al., 2010). Although these methods have been widely developed and used in different applications, there are still several issues that need to be solved. First, most algorithms were developed based on reflectance data from different sensors. The differences on spectral bands might lead to uncertainties to the fused products. Data fusion methods were proposed for some variables including land surface temperature (Weng et al., 2014) and evapotranspiration (Anderson et al., 2011; Semmens et al., 2016). However, only little attention was paid to biophysical variables such as FAPAR or LAI. Second, the fusion error from cross-scale spatial mismatch which is caused by geo-registration errors and point spread function calibration errors were not considered in these methods (Jiang et al., 2020; Zhu et al., 2018).

In this study (Li et al., 2017), an algorithm, named DHF (for Decametric Hectometric Fusion) was developed to provide near real time estimates of fAPAR at a decametric resolution and dekadal time step (Fig. 23). fAPAR was selected because of its important role in canopy models and small dependency to scaling issues. The algorithm assumes that the fAPAR time course is described by a second-degree polynomial function over a limited 60-days temporal window for each decametric pixel. To reduce the dimensionality of the problem, landcover classes are considered instead of each individual pixel. For each class, the coefficients of the polynomial function are adjusted using the temporal course of the available decametric fAPAR products, under the constraint of providing a good match with the time course of the hectometric dekadal fAPAR products. The point spread function associated to the hectometric fAPAR products and the possible biases between the decametric and hectometric fAPAR products are explicitly accounted for.

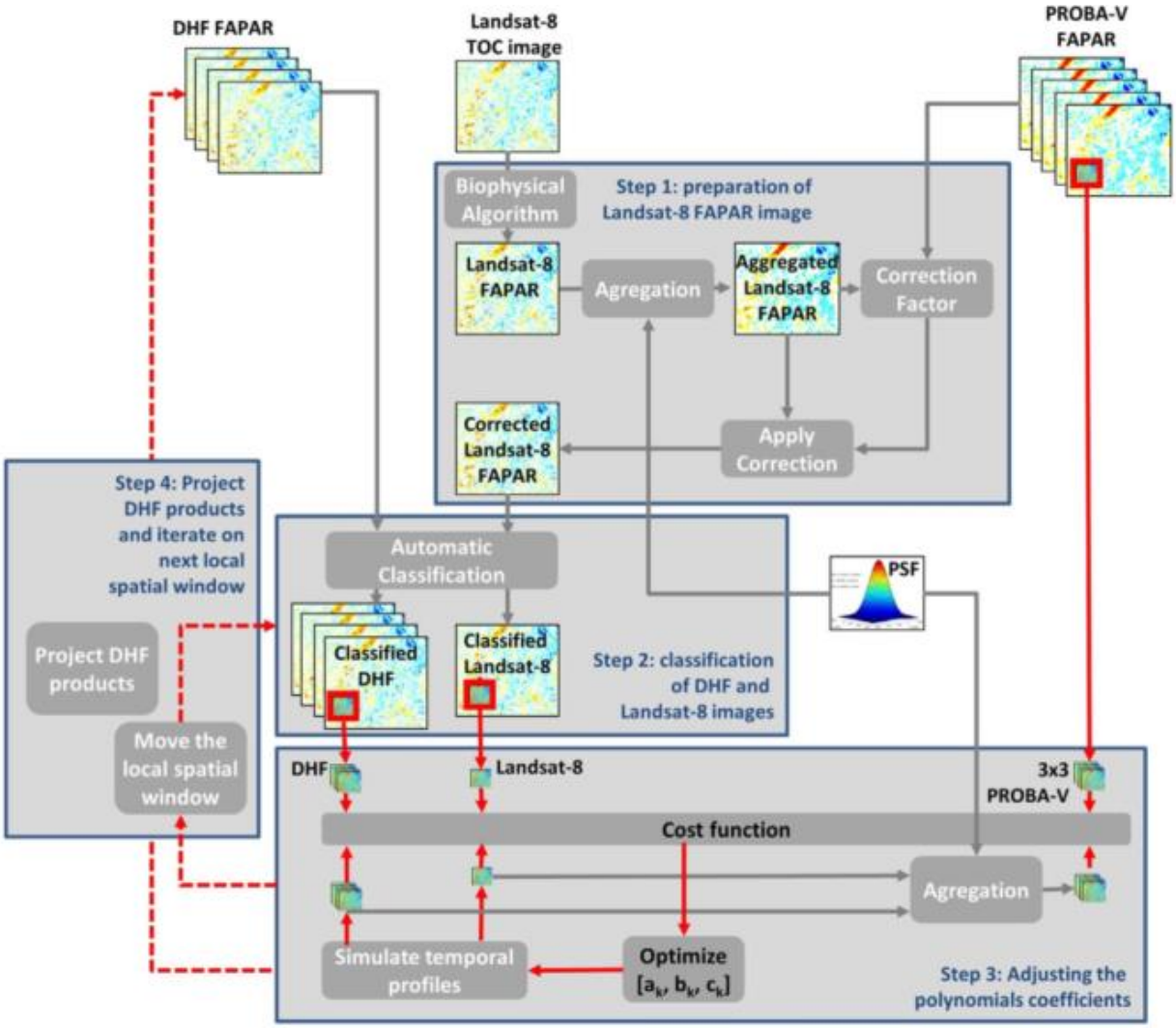

Fig. 23. Flowchart of the four steps of fusion main algorithm. (Fig. 4 in Li et al. (2017))

The algorithm was evaluated over a time series of decametric Landsat-8 fAPAR images (30 m) and hectometric (330 m) dekadal GEOV3 fAPAR derived from PROBA-V images acquired in 2014 over a site in the SouthWest of France. Results show that the DHF values are in very good agreement with the Landsat-8 fAPAR (RMSE = 0.05–0.14) that were not used when computing the DHF, using a leave-one-out method (Table 9).

Table 9. RMSE, R^2 and Bias between DHF products and the original ('Original') or corrected ('Corrected') Landsat-8 products on each Landsat-8 measurement date. The DHF FAPAR products were generated using either all the Landsat-8 images available ('Used') or when the Landsat-8 image used for performance evaluation was removed ('Remove') from the time series for DHF computation using the leave-one-out method. (Table 2 in Li et al. (2017))

	Day of year												
	107	132	139	164	171	180	196	203	212	228	244	260	276
RMSE													
Remove/Original	0.115	0.095	0.138	0.100	0.133	0.156	0.171	0.139	0.135	0.159	0.161	0.175	0.164
Remove/Corrected	0.078	0.053	0.113	0.088	0.120	0.099	0.140	0.072	0.101	0.090	0.126	0.125	0.119
Used/Original	0.090	0.090	0.090	0.080	0.080	0.100	0.120	0.140	0.110	0.130	0.160	0.130	0.160
Used/Corrected	0.050	0.050	0.070	0.070	0.070	0.060	0.090	0.070	0.070	0.060	0.120	0.090	0.100
R^2													
Remove/Original	0.915	0.894	0.810	0.717	0.473	0.555	0.656	0.825	0.826	0.657	0.577	0.590	0.641
Remove/Corrected	0.915	0.957	0.810	0.727	0.471	0.705	0.684	0.909	0.828	0.853	0.578	0.590	0.641
Used/Original	0.960	0.918	0.933	0.818	0.800	0.826	0.878	0.815	0.907	0.815	0.660	0.759	0.748
Used/Corrected	0.960	0.965	0.933	0.824	0.799	0.884	0.884	0.909	0.908	0.905	0.661	0.759	0.748
Bias													
Remove/Original	0.058	−0.019	0.054	−0.020	0.008	−0.013	0.004	−0.022	0.053	−0.065	0.054	0.095	0.079
Remove/Corrected	0.034	−0.012	0.039	−0.038	−0.025	−0.004	−0.031	−0.039	0.012	−0.046	−0.001	0.032	0.012
Used/Original	0.043	−0.014	0.038	−0.012	0.017	−0.006	0.013	−0.011	0.043	−0.054	0.074	0.056	0.093
Used/Corrected	0.019	−0.010	0.023	−0.031	−0.015	−0.016	−0.021	−0.031	0.004	−0.034	0.019	−0.007	0.026

Comparison with ground measurements collected over 14 sunflower fields along the growth season confirms the good performances of the DHF fAPAR products (RMSE = 0.11, Fig. 24).

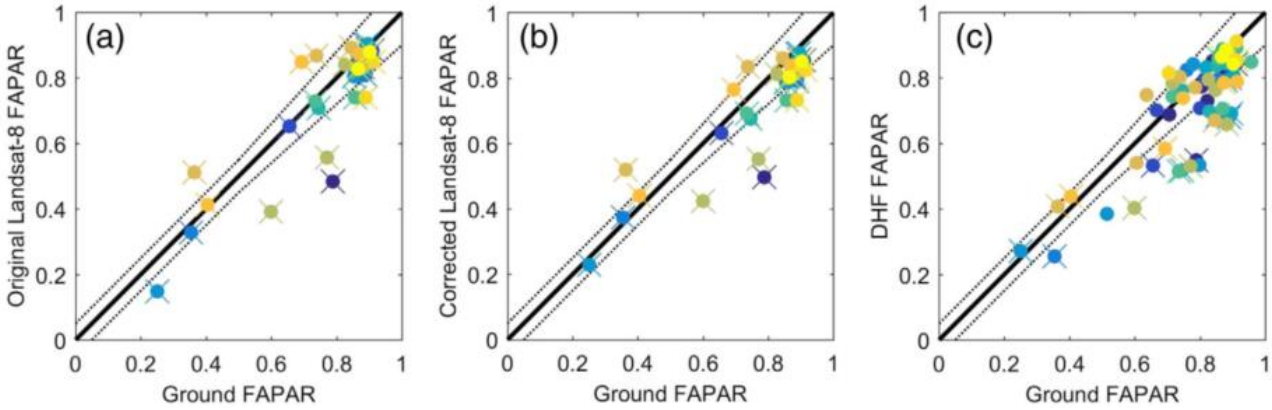

Fig. 24. Comparison of the ground FAPAR measurements with (a) the original Landsat-8 FAPAR, (b) the corrected Landsat-8 FAPAR and (c) the DHF FAPAR products. Results observed on 29 data points over the 14 sunflower fields. Each field corresponds to a particular color. (Fig. 11 in Li et al. (2017))

This study proposed an interesting algorithm to fuse the decametric and hectometric fAPAR products. It had the potential to be applied on Sentinel-2 and Sentinel-3 satellite datasets. However, more crops and growth stages should be considered in the validation of fused products.

4.4 Conclusion and perspectives

This thesis was structured around the estimation of crop key traits (LAI, fAPAR, fCOVER and CI) from non-contact and high-throughput technologies at a range of spatial scales. Accurate ground measurements are important to understand the principles used to retrieve information from the different instruments. It allows to optimize and calibrate the methods for while offering valuable datasets to validate them. We compared several optical instruments to obtain continuous

measurements of LAI, fAPAR and CI from ground measurements. LAI-2200 and DHP provided accurate LAI or GAI measurements when the senescence fraction is small. Conversely, when significant senescent fraction is present, downward-looking DHP was optimal to provide GAI and green fAPAR. Investigations of apparent clumping index computed from raw measurements of LAI-2200, AccuPAR and DHP expanded the understanding of current CI metrics.

Thanks to the previous ground measurements techniques, we calibrated and validated algorithms used to estimate GAI, fIPAR and fCOVER from decametric satellites. We demonstrated that specific algorithms were generally more accurate as compared to generic ones. Further, we also demonstrated that, even for the generic algorithms, empirical methods based on training machine learning techniques such as GPR were outperforming approaches based on radiative transfer model inversion. However, generic algorithms present the advantage of providing still reasonable estimates of these GAI, fIPAR and fCOVER variables without having to identify the landcover type. For precision agriculture, satellite data with spatial resolution within few meters will be very useful. More focuses will be put on newly launched satellites, such as PlanetScope, Skysat and GaoFen series. When estimating canopy structure variables from the spectral variation of the reflectance measured, we demonstrated the importance to account for the BRDF effects. Further, the reproductive organs impact significantly canopy BRDF with consequences when estimating GAI from multispectral observations. Further work should be dedicated to better quantify this effect with the development of methods that will explicitly account for the reproductive organs.

At coarser resolution satellite observations, the algorithms are generally based on radiative transfer model inversion since noy enough representative datasets are available to train empirical ones. We demonstrated for the MODIS algorithm, that only small differences in performances were separating generic and specific algorithms. The availability of decametric estimates of GAI, fIPAR and fCover were used to validate the coarser resolution satellite products. Further work should be needed to extend these activities to the calibration of empirical algorithms to retrieve these variables from hectometric and kilometric resolution sensors. However, because of the availability of frequent and extensive global coverage of the globe with metric to decametric observations, it would be more efficient to degrade the resolution of these higher spatial resolution data to get equivalent coarser resolution products dedicated to global applications.

All these studies were dedicated at solving scientific questions and lead to scientific research publications. I also conducted several application-oriented projects according to the knowledge obtained from these scientific works. In the context of sustainable agriculture, both the accuracy and throughput of traits estimation are important.

- At the ground level, measurements with IoT will become more and more popular. Algorithms to estimate traits from the sensors (RGB camera, multispectral camera or spectrometer) installed on IoT systems will need more investigations (Muangprathub et al., 2019; Velumani et al., 2020). Several key questions should be answered, such as the impact of illumination conditions during a the day and among different days, the representativeness of one-dimension radiative transfer model for crops measured in very close range, and time series filtering. However, the IoT system has obvious drawbacks due to its small footprint, which limits its application over heterogeneous fields due to soil background or with various genotype microplots. How many IoT systems should be installed and how to install them in an efficient and economical way pose a challenge to the real applications. As compared with IoT, UGV has obvious advantages on its coverage of whole fields and user-defined multiple instruments embedded on it. But the high cost might restrict its applications.

- UAV systems has been widely used for both scientific research and industrial applications due to its low price (compared to UGV and hand-held instruments), suitability over larger fields and ease of use. For multispectral cameras installed on UAV, the future interests will be improvements of radiative calibration under arbitrary illumination conditions, more deep investigations on the impact of canopy structural and optical properties on measurements, and the improvements of traits estimation accuracy using 3D radiative transfer models.
- The analysis of the consistency of trait estimates from different platforms should be carefully evaluated, especially at the field and microplot scales. Data fusion techniques should be more fully explored to take advantages of several platforms and monitor crops at the optimal spatial and temporal scales.

4.5 References

Aasen, H., Bolten, A., 2018. Multi-temporal high-resolution imaging spectroscopy with hyperspectral 2D imagers – From theory to application. Remote Sensing of Environment 205, 374–389. https://doi.org/10.1016/j.rse.2017.10.043

Aasen, H., Honkavaara, E., Lucieer, A., Zarco-Tejada, P., 2018. Quantitative Remote Sensing at Ultra-High Resolution with UAV Spectroscopy: A Review of Sensor Technology, Measurement Procedures, and Data Correction Workflows. Remote Sensing 10, 1091. https://doi.org/10.3390/rs10071091

Adão, T., Hruška, J., Pádua, L., Bessa, J., Peres, E., Morais, R., Sousa, J., 2017. Hyperspectral Imaging: A Review on UAV-Based Sensors, Data Processing and Applications for Agriculture and Forestry. Remote Sensing 9, 1110. https://doi.org/10.3390/rs9111110

Amin, E., Verrelst, J., Rivera-Caicedo, J.P., Pipia, L., Ruiz-Verdú, A., Moreno, J., 2021. Prototyping Sentinel-2 green LAI and brown LAI products for cropland monitoring. Remote Sensing of Environment 255, 112168. https://doi.org/10.1016/j.rse.2020.112168

Anderson, M.C., Kustas, W.P., Norman, J.M., Hain, C.R., Mecikalski, J.R., Schultz, L., González-Dugo, M.P., Cammalleri, C., d'Urso, G., Pimstein, A., Gao, F., 2011. Mapping daily evapotranspiration at field to continental scales using geostationary and polar orbiting satellite imagery. Hydrol. Earth Syst. Sci. 15, 223–239. https://doi.org/10.5194/hess-15-223-2011

Asseng, S., Ewert, F., Martre, P., Rötter, R.P., Lobell, D.B., Cammarano, D., Kimball, B.A., Ottman, M.J., Wall, G.W., White, J.W., Reynolds, M.P., Alderman, P.D., Prasad, P.V.V., Aggarwal, P.K., Anothai, J., Basso, B., Biernath, C., Challinor, A.J., De Sanctis, G., Doltra, J., Fereres, E., Garcia-Vila, M., Gayler, S., Hoogenboom, G., Hunt, L.A., Izaurralde, R.C., Jabloun, M., Jones, C.D., Kersebaum, K.C., Koehler, A.-K., Müller, C., Naresh Kumar, S., Nendel, C., O'Leary, G., Olesen, J.E., Palosuo, T., Priesack, E., Eyshi Rezaei, E., Ruane, A.C., Semenov, M.A., Shcherbak, I., Stöckle, C., Stratonovitch, P., Streck, T., Supit, I., Tao, F., Thorburn, P.J., Waha, K., Wang, E., Wallach, D., Wolf, J., Zhao, Z., Zhu, Y., 2015. Rising temperatures reduce global wheat production. Nature Clim Change 5, 143–147. https://doi.org/10.1038/nclimate2470

Atzberger, C., 2013. Advances in Remote Sensing of Agriculture: Context Description, Existing Operational Monitoring Systems and Major Information Needs. Remote Sensing 5, 949–981. https://doi.org/10.3390/rs5020949

Azzari, G., Jain, M., Lobell, D.B., 2017. Towards fine resolution global maps of crop yields: Testing multiple methods and satellites in three countries. Remote Sensing of Environment 202, 129–141. https://doi.org/10.1016/j.rse.2017.04.014

Baret, F., de Solan, B., Lopez-Lozano, R., Ma, K., Weiss, M., 2010. GAI estimates of row crops from downward looking digital photos taken perpendicular to rows at 57.5° zenith angle: Theoretical

considerations based on 3D architecture models and application to wheat crops. Agricultural and Forest Meteorology 150, 1393–1401. https://doi.org/10.1016/j.agrformet.2010.04.011

Baret, F., Guyot, G., 1991. Potentials and limits of vegetation indices for LAI and APAR assessment. Remote Sensing of Environment 35, 161–173. https://doi.org/10.1016/0034-4257(91)90009-U

Baret, F., Hagolle, O., Geiger, B., Bicheron, P., Miras, B., Huc, M., Berthelot, B., Niño, F., Weiss, M., Samain, O., Roujean, J.L., Leroy, M., 2007. LAI, fAPAR and fCover CYCLOPES global products derived from VEGETATION. Remote Sensing of Environment 110, 275–286. https://doi.org/10.1016/j.rse.2007.02.018

Baret, F., Weiss, M., Lacaze, R., Camacho, F., Makhmara, H., Pacholcyzk, P., Smets, B., 2013. GEOV1: LAI and FAPAR essential climate variables and FCOVER global time series capitalizing over existing products. Part1: Principles of development and production. Remote Sensing of Environment 137, 299–309. https://doi.org/10.1016/j.rse.2012.12.027

Baret, F., Weiss, M., Verger, A., Smets, B., 2016. ATBD for LAI, FAPAR and FCOVER From PROBA-V Products at 300M Resolution (GEOV3) (IMAGINES_RP2.1_ATBD-LAI300M).

Basso, B., Antle, J., 2020. Digital agriculture to design sustainable agricultural systems. Nat Sustain 3, 254–256. https://doi.org/10.1038/s41893-020-0510-0

Bauer, J., Siegmann, B., Jarmer, T., Aschenbruck, N., 2016. On the potential of Wireless Sensor Networks for the in-situ assessment of crop leaf area index. Computers and Electronics in Agriculture 128, 149–159. https://doi.org/10.1016/j.compag.2016.08.019

Bendig, J., Bolten, A., Bennertz, S., Broscheit, J., Eichfuss, S., Bareth, G., 2014. Estimating Biomass of Barley Using Crop Surface Models (CSMs) Derived from UAV-Based RGB Imaging. Remote Sensing 6, 10395–10412. https://doi.org/10.3390/rs61110395

Camacho, F., Cernicharo, J., Lacaze, R., Baret, F., Weiss, M., 2013. GEOV1: LAI, FAPAR essential climate variables and FCOVER global time series capitalizing over existing products. Part 2: Validation and intercomparison with reference products. Remote Sensing of Environment 137, 310–329. https://doi.org/10.1016/j.rse.2013.02.030

Camacho, F., Fuster, B., Li, W., Weiss, M., Ganguly, S., Lacaze, R., Baret, F., 2021. Crop specific algorithms trained over ground measurements provide the best performance for GAI and fAPAR estimates from Landsat-8 observations. Remote Sensing of Environment 260, 112453. https://doi.org/10.1016/j.rse.2021.112453

Chen, B., Liu, J., Chen, J.M., Croft, H., Gonsamo, A., He, L., Luo, X., 2016. Assessment of foliage clumping effects on evapotranspiration estimates in forested ecosystems. Agricultural and Forest Meteorology 216, 82–92. https://doi.org/10.1016/j.agrformet.2015.09.017

Chen, J., 1996. Canopy Architecture and Remote Sensing of the Fraction of Photosynthetically Active Radiation Absorbed by Boreal Conifer Forests. IEEE Transactions on Geoscience and Remote Sensing 34, 1353–1368.

Chen, J.M., Black, T.A., 1992. Defining leaf area index for non-flat leaves. Plant Cell Environ 15, 421–429. https://doi.org/10.1111/j.1365-3040.1992.tb00992.x

Chen, J.M., Cihlar, J., 1995. Plant canopy gap-size analysis theory for improving optical measurements of leaf-area index. Appl. Opt. 34, 6211. https://doi.org/10.1364/AO.34.006211

Chen, J.M., Menges, C.H., Leblanc, S.G., 2005. Global mapping of foliage clumping index using multi-angular satellite data. Remote Sensing of Environment 97, 447–457. https://doi.org/10.1016/j.rse.2005.05.003

Chen, Z., Li, S., Ren, J., Gong, P., Zhang, M., Wang, L., Xiao, S., Jiang, D., 2008. Monitoring and Management of Agriculture with Remote Sensing, in: Liang, S. (Ed.), Advances in Land Remote Sensing. Springer Netherlands, Dordrecht, pp. 397–421. https://doi.org/10.1007/978-1-4020-6450-0_15

Cheng, Y., Vrieling, A., Fava, F., Meroni, M., Marshall, M., Gachoki, S., 2020. Phenology of short vegetation cycles in a Kenyan rangeland from PlanetScope and Sentinel-2. Remote Sensing of Environment 248, 112004. https://doi.org/10.1016/j.rse.2020.112004

Chi, M., Plaza, A., Benediktsson, J.A., Sun, Z., Shen, J., Zhu, Y., 2016. Big Data for Remote Sensing: Challenges and Opportunities. Proc. IEEE 104, 2207–2219. https://doi.org/10.1109/JPROC.2016.2598228

Comar, A., Burger, P., de Solan, B., Baret, F., Daumard, F., Hanocq, J.-F., 2012. A semi-automatic system for high throughput phenotyping wheat cultivars in-field conditions: description and first results. Functional Plant Biol. 39, 914. https://doi.org/10.1071/FP12065

Cossani, C.M., Reynolds, M.P., 2012. Physiological Traits for Improving Heat Tolerance in Wheat. Plant Physiol. 160, 1710–1718. https://doi.org/10.1104/pp.112.207753

Croft, H., Chen, J.M., Wang, R., Mo, G., Luo, S., Luo, X., He, L., Gonsamo, A., Arabian, J., Zhang, Y., Simic-Milas, A., Noland, T.L., He, Y., Homolová, L., Malenovský, Z., Yi, Q., Beringer, J., Amiri, R., Hutley, L., Arellano, P., Stahl, C., Bonal, D., 2020. The global distribution of leaf chlorophyll content. Remote Sensing of Environment 236, 111479. https://doi.org/10.1016/j.rse.2019.111479

Dash, J., Ogutu, B.O., 2016. Recent advances in space-borne optical remote sensing systems for monitoring global terrestrial ecosystems. Progress in Physical Geography: Earth and Environment 40, 322–351. http://dx.doi.org/10.1177/0309133316639403

De Grave, C., Verrelst, J., Morcillo-Pallarés, P., Pipia, L., Rivera-Caicedo, J.P., Amin, E., Belda, S., Moreno, J., 2020. Quantifying vegetation biophysical variables from the Sentinel-3/FLEX tandem mission: Evaluation of the synergy of OLCI and FLORIS data sources. Remote Sensing of Environment 251, 112101. https://doi.org/10.1016/j.rse.2020.112101

De Solan, B., Baret, F., Thomas, S., 2015. Development and use of a fully automated PHENOMOBILE for field phenotyping. Presented at the EPPN Plant Phenotyping Symposium.

Decagon Devices, 2010. AccuPAR PAR/LAI ceptometer model LP-80 Operator's Manual Version 10 [WWW Document]. URL http://www.cen.ulaval.ca/nordicanad/donnees/n_45561/v582105/file/supp/Decagon_Accupar_LP80_Web.pdf

Delloye, C., Weiss, M., Defourny, P., 2018. Retrieval of the canopy chlorophyll content from Sentinel-2 spectral bands to estimate nitrogen uptake in intensive winter wheat cropping systems. Remote Sensing of Environment 216, 245–261.

Drusch, M., Del Bello, U., Carlier, S., Colin, O., Fernandez, V., Gascon, F., Hoersch, B., Isola, C., Laberinti, P., Martimort, P., Meygret, A., Spoto, F., Sy, O., Marchese, F., Bargellini, P., 2012. Sentinel-2: ESA's Optical High-Resolution Mission for GMES Operational Services. Remote Sensing of Environment 120, 25–36. https://doi.org/10.1016/j.rse.2011.11.026

Duveiller, G., Weiss, M., Baret, F., Defourny, P., 2011. Retrieving wheat Green Area Index during the growing season from optical time series measurements based on neural network radiative transfer inversion. Remote Sensing of Environment 115, 887–896. https://doi.org/10.1016/j.rse.2010.11.016

Fang, H., 2021. Canopy clumping index (CI): A review of methods, characteristics, and applications. Agricultural and Forest Meteorology 303, 108374. https://doi.org/10.1016/j.agrformet.2021.108374

Fang, H., Jiang, C., Li, W., Wei, S., Baret, F., Chen, J.M., Garcia-Haro, J., Liang, S., Liu, R., Myneni, R.B., Pinty, B., Xiao, Z., Zhu, Z., 2013a. Characterization and intercomparison of global moderate resolution leaf area index (LAI) products: Analysis of climatologies and theoretical uncertainties: INTERCOMPARISON OF GLOBAL LAI PRODUCTS. J. Geophys. Res. Biogeosci. 118, 529–548. https://doi.org/10.1002/jgrg.20051

Fang, H., Li, W., Myneni, R., 2013b. The Impact of Potential Land Cover Misclassification on MODIS Leaf Area Index (LAI) Estimation: A Statistical Perspective. Remote Sensing 5, 830–844. https://doi.org/10.3390/rs5020830

Fang, H., Li, W., Wei, S., Jiang, C., 2014. Seasonal variation of leaf area index (LAI) over paddy rice fields in NE China: Intercomparison of destructive sampling, LAI-2200, digital hemispherical photography (DHP), and AccuPAR methods. Agricultural and Forest Meteorology 198–199, 126–141. https://doi.org/10.1016/j.agrformet.2014.08.005

Fang, H., Liu, W., Li, W., Wei, S., 2018. Estimation of the directional and whole apparent clumping index (ACI) from indirect optical measurements. ISPRS Journal of Photogrammetry and Remote Sensing 144, 1–13. https://doi.org/10.1016/j.isprsjprs.2018.06.022

Fang, H., Zhang, Y., Wei, S., Li, W., Ye, Y., Sun, T., Liu, W., 2019. Validation of global moderate resolution leaf area index (LAI) products over croplands in northeastern China. Remote Sensing of Environment 233, 111377. https://doi.org/10.1016/j.rse.2019.111377

FAO, 2021a. The State of Food Security and Nutrition in the World 2021. FAO, IFAD, UNICEF, WFP and WHO. https://doi.org/10.4060/cb5409en

FAO, 2021b. In Brief to The State of Food Security and Nutrition in the World 2021. FAO, IFAD, UNICEF, WFP and WHO. https://doi.org/10.4060/cb5409en

FAO, 2020. World Food and Agriculture - Statistical Yearbook 2020. FAO. https://doi.org/10.4060/cb1329en

FAO, 2018. The future of food and agriculture – Alternative pathways to 2050. Food and Agriculture Organization of the United Nations, Rome.

FAO, 2017. The future of food and agriculture: trends and challenges. Food and Agriculture Organization of the United Nations, Rome.

Friedl, M.A., McIver, D.K., Hodges, J.C.F., Zhang, X.Y., Muchoney, D., Strahler, A.H., Woodcock, C.E., Gopal, S., Schneider, A., Cooper, A., Baccini, A., Gao, F., Schaaf, C., 2002. Global land cover mapping from MODIS: algorithms and early results. Remote Sensing of Environment 83, 287–302. https://doi.org/10.1016/S0034-4257(02)00078-0

Ganguly, S., Nemani, R.R., Zhang, G., Hashimoto, H., Milesi, C., Michaelis, A., Wang, W., Votava, P., Samanta, A., Melton, F., Dungan, J.L., Vermote, E., Gao, F., Knyazikhin, Y., Myneni, R.B., 2012. Generating global Leaf Area Index from Landsat: Algorithm formulation and demonstration. Remote Sensing of Environment 122, 185–202. https://doi.org/10.1016/j.rse.2011.10.032

Gao, F., Anderson, M.C., Zhang, X., Yang, Z., Alfieri, J.G., Kustas, W.P., Mueller, R., Johnson, D.M., Prueger, J.H., 2017. Toward mapping crop progress at field scales through fusion of Landsat and MODIS imagery. Remote Sensing of Environment 188, 9–25. https://doi.org/10.1016/j.rse.2016.11.004

Gao, F., Masek, J., Schwaller, M., Hall, F., 2006. On the blending of the Landsat and MODIS surface reflectance: predicting daily Landsat surface reflectance. IEEE Trans. Geosci. Remote Sensing 44, 2207–2218. https://doi.org/10.1109/TGRS.2006.872081

García-Haro, F.J., Campos-Taberner, M., Muñoz-Marí, J., Laparra, V., Camacho, F., Sánchez-Zapero, J., Camps-Valls, G., 2018. Derivation of global vegetation biophysical parameters from EUMETSAT Polar System. ISPRS Journal of Photogrammetry and Remote Sensing 139, 57–74. https://doi.org/10.1016/j.isprsjprs.2018.03.005

Garrigues, S., Allard, D., Baret, F., Morisette, J., 2008a. Multivariate quantification of landscape spatial heterogeneity using variogram models. Remote Sensing of Environment 112, 216–230. https://doi.org/10.1016/j.rse.2007.04.017

Garrigues, S., Shabanov, N.V., Swanson, K., Morisette, J.T., Baret, F., Myneni, R.B., 2008b. Intercomparison and sensitivity analysis of Leaf Area Index retrievals from LAI-2000, AccuPAR,

and digital hemispherical photography over croplands. Agricultural and Forest Meteorology 148, 1193–1209. https://doi.org/10.1016/j.agrformet.2008.02.014

GCOS, 2016. The Global Observing System for Climate: Implementation Needs (GCOS- 200). World Meteorological Organization.

GCOS, 2011. Systematic Observation Requirements for Satellite-Based Products for Climate, 2011 Update, Supplemental Details to the Satellite-Based Component of the Implementation Plan for the Global Observing System for Climate in Support of the UNFCCC (2010 Update), Reference Number GCOS-154.

Ghamisi, P., Rasti, B., Yokoya, N., Wang, Q., Hofle, B., Bruzzone, L., Bovolo, F., Chi, M., Anders, K., Gloaguen, R., Atkinson, P.M., Benediktsson, J.A., 2019. Multisource and Multitemporal Data Fusion in Remote Sensing: A Comprehensive Review of the State of the Art. IEEE Geosci. Remote Sens. Mag. 7, 6–39. https://doi.org/10.1109/MGRS.2018.2890023

Gitelson, A.A., 2003. Novel technique for remote estimation of CO_2 flux in maize. Geophys. Res. Lett. 30, 1486. https://doi.org/10.1029/2002GL016543

Gower, S.T., Kucharik, C.J., Norman, J.M., 1999. Direct and Indirect Estimation of Leaf Area Index, fAPAR, and Net Primary Production of Terrestrial Ecosystems. Remote Sensing of Environment 70, 29–51. https://doi.org/10.1016/S0034-4257(99)00056-5

Grimstad, L., From, P., 2017. The Thorvald II Agricultural Robotic System. Robotics 6, 24. https://doi.org/10.3390/robotics6040024

Gu, L., Baldocchi, D., Verma, S.B., Black, T.A., Vesala, T., Falge, E.M., Dowty, P.R., 2002. Advantages of diffuse radiation for terrestrial ecosystem productivity: advantages of diffuse radiation. J. Geophys. Res. 107, ACL 2-1-ACL 2-23. https://doi.org/10.1029/2001JD001242

Gutman, G., Ignatov, A., 1998. The derivation of the green vegetation fraction from NOAA/AVHRR data for use in numerical weather prediction models. International Journal of Remote Sensing 19, 1533–1543. https://doi.org/10.1080/014311698215333

Hilker, T., Wulder, M.A., Coops, N.C., Linke, J., McDermid, G., Masek, J.G., Gao, F., White, J.C., 2009. A new data fusion model for high spatial- and temporal-resolution mapping of forest disturbance based on Landsat and MODIS. Remote Sensing of Environment 113, 1613–1627. https://doi.org/10.1016/j.rse.2009.03.007

Holman, F., Riche, A., Michalski, A., Castle, M., Wooster, M., Hawkesford, M., 2016. High Throughput Field Phenotyping of Wheat Plant Height and Growth Rate in Field Plot Trials Using UAV Based Remote Sensing. Remote Sensing 8, 1031. https://doi.org/10.3390/rs8121031

Houborg, R., McCabe, M., 2016. High-Resolution NDVI from Planet's Constellation of Earth Observing Nano-Satellites: A New Data Source for Precision Agriculture. Remote Sensing 8, 768. https://doi.org/10.3390/rs8090768

Hunt, M.L., Blackburn, G.A., Carrasco, L., Redhead, J.W., Rowland, C.S., 2019. High resolution wheat yield mapping using Sentinel-2. Remote Sensing of Environment 233, 111410. https://doi.org/10.1016/j.rse.2019.111410

Immitzer, M., Vuolo, F., Atzberger, C., 2016. First Experience with Sentinel-2 Data for Crop and Tree Species Classifications in Central Europe. Remote Sensing 8, 166. https://doi.org/10.3390/rs8030166

Irons, J.R., Dwyer, J.L., Barsi, J.A., 2012. The next Landsat satellite: The Landsat Data Continuity Mission. Remote Sensing of Environment 122, 11–21. https://doi.org/10.1016/j.rse.2011.08.026

Jacquemoud, S., Verhoef, W., Baret, F., Bacour, C., Zarco-Tejada, P.J., Asner, G.P., François, C., Ustin, S.L., 2009. PROSPECT + SAIL models: A review of use for vegetation characterization. Remote Sensing of Environment 113, S56–S66. https://doi.org/10.1016/j.rse.2008.01.026

Jay, S., Comar, A., Benicio, R., Beauvois, J., Dutartre, D., Daubige, G., Li, W., Labrosse, J., Thomas, S., Henry, N., Weiss, M., Baret, F., 2020. Scoring Cercospora Leaf Spot on Sugar Beet: Comparison of

UGV and UAV Phenotyping Systems. Plant Phenomics 2020, 1–18. https://doi.org/10.34133/2020/9452123

Jiang, J., Zhang, Q., Yao, X., Tian, Y., Zhu, Y., Cao, W., Cheng, T., 2020. HISTIF: A new spatiotemporal image fusion method for high-tesolution monitoring of crops at the subfield level. IEEE Journal of Selected Topics in Applied Earth Observations and Remote Sensing 13, 4607–4626. https://doi.org/10.1109/JSTARS.2020.3016135

Jin, X., Liu, S., Baret, F., Hemerlé, M., Comar, A., 2017. Estimates of plant density of wheat crops at emergence from very low altitude UAV imagery. Remote Sensing of Environment 198, 105–114. https://doi.org/10.1016/j.rse.2017.06.007

Kamilaris, A., Kartakoullis, A., Prenafeta-Boldú, F.X., 2017. A review on the practice of big data analysis in agriculture. Computers and Electronics in Agriculture 143, 23–37. https://doi.org/10.1016/j.compag.2017.09.037

Kim, J., Ryu, Y., Jiang, C., Hwang, Y., 2019. Continuous observation of vegetation canopy dynamics using an integrated low-cost, near-surface remote sensing system. Agricultural and Forest Meteorology 264, 164–177. https://doi.org/10.1016/j.agrformet.2018.09.014

Knyazikhin, Y., Martonchik, J.V., Myneni, R.B., Diner, D.J., Running, S.W., 1998. Synergistic algorithm for estimating vegetation canopy leaf area index and fraction of absorbed photosynthetically active radiation from MODIS and MISR data. J. Geophys. Res. 103, 32257–32275. https://doi.org/10.1029/98JD02462

Kross, A., McNairn, H., Lapen, D., Sunohara, M., Champagne, C., 2015. Assessment of RapidEye vegetation indices for estimation of leaf area index and biomass in corn and soybean crops. International Journal of Applied Earth Observation and Geoinformation 34, 235–248. https://doi.org/10.1016/j.jag.2014.08.002

Leblanc, S.G., Chen, J.M., Fernandes, R., Deering, D.W., Conley, A., 2005. Methodology comparison for canopy structure parameters extraction from digital hemispherical photography in boreal forests. Agricultural and Forest Meteorology 129, 187–207. https://doi.org/10.1016/j.agrformet.2004.09.006

Li, H., Zhao, C., Yang, G., Feng, H., 2015. Variations in crop variables within wheat canopies and responses of canopy spectral characteristics and derived vegetation indices to different vertical leaf layers and spikes. Remote Sensing of Environment 169, 358–374. https://doi.org/10.1016/j.rse.2015.08.021

Li, W., Baret, F., Weiss, M., Buis, S., Lacaze, R., Demarez, V., Dejoux, J., Battude, M., Camacho, F., 2017. Combining hectometric and decametric satellite observations to provide near real time decametric FAPAR product. Remote Sensing of Environment 200, 250–262. https://doi.org/10.1016/j.rse.2017.08.018

Li, W., Fang, H., 2015. Estimation of direct, diffuse, and total FPARs from Landsat surface reflectance data and ground-based estimates over six FLUXNET sites. J. Geophys. Res. Biogeosci. 120, 96–112. https://doi.org/10.1002/2014JG002754

Li, W., Fang, H., Wei, S., Weiss, M., Baret, F., 2021a. Critical analysis of methods to estimate the fraction of absorbed or intercepted photosynthetically active radiation from ground measurements: application to rice crops. Agricultural and Forest Meteorology 297. https://doi.org/10.1016/j.agrformet.2020.108273

Li, W., Jiang, J., Weiss, M., Madec, S., Tison, F., Philippe, B., Comar, A., Baret, F., 2021b. Impact of the reproductive organs on crop BRDF as observed from a UAV. Remote Sensing of Environment 259, 14. https://doi.org/10.1016/j.rse.2021.112433

Li, W., Weiss, M., Waldner, F., Defourny, P., Demarez, V., Morin, D., Hagolle, O., Baret, F., 2015. A generic algorithm to estimate LAI, FAPAR and FCOVER variables from SPOT4_HRVIR and Landsat

sensors: Evaluation of the consistency and comparison with ground measurements. Remote Sensing 7, 15494–15516. https://doi.org/10.3390/rs71115494

Liang, S., Zhao, X., Liu, S., Yuan, W., Cheng, X., Xiao, Z., Zhang, X., Liu, Q., Cheng, J., Tang, H., Qu, Yonghua, Bo, Y., Qu, Ying, Ren, H., Yu, K., Townshend, J., 2013. A long-term Global LAnd Surface Satellite (GLASS) data-set for environmental studies. International Journal of Digital Earth 6, 5–33. https://doi.org/10.1080/17538947.2013.805262

Liu, Y., Liu, R., Chen, J.M., 2012. Retrospective retrieval of long-term consistent global leaf area index (1981-2011) from combined AVHRR and MODIS data: LONG-TERM GLOBAL LEAF AREA INDEX. J. Geophys. Res. 117, n/a-n/a. https://doi.org/10.1029/2012JG002084

Lobell, D.B., Thau, D., Seifert, C., Engle, E., Little, B., 2015. A scalable satellite-based crop yield mapper. Remote Sensing of Environment 164, 324–333. https://doi.org/10.1016/j.rse.2015.04.021

Ma, Y., Wu, H., Wang, L., Huang, B., Ranjan, R., Zomaya, A., Jie, W., 2015. Remote sensing big data computing: Challenges and opportunities. Future Generation Computer Systems 51, 47–60. https://doi.org/10.1016/j.future.2014.10.029

Madec, S., 2020. Phenotyping wheat structural traits from millimetric resolution RGB imagery in field conditions (Doctor). Avignon Université, Avignon.

Madec, S., Baret, F., de Solan, B., Thomas, S., Dutartre, D., Jezequel, S., Hemmerlé, M., Colombeau, G., Comar, A., 2017. High-Throughput Phenotyping of Plant Height: Comparing Unmanned Aerial Vehicles and Ground LiDAR Estimates. Front. Plant Sci. 8, 2002. https://doi.org/10.3389/fpls.2017.02002

McBRATNEY, A., Whelan, B., Ancev, T., Mcbratney, A., Bouma, J., 2005. Future Directions of Precision Agriculturew 17.

Morisette, J.T., Baret, F., Privette, J.L., Myneni, R.B., Nickeson, J.E., Garrigues, S., Shabanov, N.V., Weiss, M., Fernandes, R.A., Leblanc, S.G., Kalacska, M., Sanchez-Azofeifa, G.A., Chubey, M., Rivard, B., Stenberg, P., Rautiainen, M., Voipio, P., Manninen, T., Pilant, A.N., Lewis, T.E., Iiames, J.S., Colombo, R., Meroni, M., Busetto, L., Cohen, W.B., Turner, D.P., Warner, E.D., Petersen, G.W., Seufert, G., Cook, R., 2006. Validation of global moderate-resolution LAI products: a framework proposed within the CEOS land product validation subgroup. IEEE Trans. Geosci. Remote Sensing 44, 1804–1817. https://doi.org/10.1109/TGRS.2006.872529

Muangprathub, J., Boonnam, N., Kajornkasirat, S., Lekbangpong, N., Wanichsombat, A., Nillaor, P., 2019. IoT and agriculture data analysis for smart farm. Computers and Electronics in Agriculture 156, 467–474. https://doi.org/10.1016/j.compag.2018.12.011

Mueller-Sim, T., Jenkins, M., Abel, J., Kantor, G., 2017. The Robotanist: A ground-based agricultural robot for high-throughput crop phenotyping, in: 2017 IEEE International Conference on Robotics and Automation (ICRA). Presented at the 2017 IEEE International Conference on Robotics and Automation (ICRA), IEEE, Singapore, Singapore, pp. 3634–3639. https://doi.org/10.1109/ICRA.2017.7989418

Muller, A., Schader, C., El-Hage Scialabba, N., Brüggemann, J., Isensee, A., Erb, K.-H., Smith, P., Klocke, P., Leiber, F., Stolze, M., Niggli, U., 2017. Strategies for feeding the world more sustainably with organic agriculture. Nat Commun 8, 1290. https://doi.org/10.1038/s41467-017-01410-w

Nicodemus, F.E., Richmond, J.C., Hsia, J.J., Ginsberg, I.W., Limperis, T., 1977. Geometrical considerations and nomenclature for reflectance (No. NBS MONO 160). National Bureau of Standards, Gaithersburg, MD. https://doi.org/10.6028/NBS.MONO.160

Nilson, T., 1971. A theoretical analysis of the frequency of gaps in plant stands. Agricultural Meteorology 8, 25–38. https://doi.org/10.1016/0002-1571(71)90092-6

Nock, C.A., Vogt, R.J., Beisner, B.E., 2016. Functional Traits, in: John Wiley & Sons Ltd (Ed.), ELS. John Wiley & Sons, Ltd, Chichester, UK, pp. 1–8. https://doi.org/10.1002/9780470015902.a0026282

Norman, J.M., Welles, J.M., 1983. Radiative Transfer in an Array of Canopies [1]. Agron.j. 75, 481–488. https://doi.org/10.2134/agronj1983.00021962007500030016x

Nouvellon, Y., 2000. PAR extinction in shortgrass ecosystems: effects of clumping, sky conditions and soil albedo. Agricultural and Forest Meteorology 105, 21–41. https://doi.org/10.1016/S0168-1923(00)00194-5

Peng, S.-L., Pal, S., 2020. Principles of Internet of Things (IoT) Ecosystem: Insight Paradigm. Springer.

Pinty, B., Andredakis, I., Clerici, M., Kaminski, T., Taberner, M., Verstraete, M.M., Gobron, N., Plummer, S., Widlowski, J.-L., 2011. Exploiting the MODIS albedos with the Two-stream Inversion Package (JRC-TIP): 1. Effective leaf area index, vegetation, and soil properties. J. Geophys. Res. 116, D09105. https://doi.org/10.1029/2010JD015372

Qu, Y., Han, W., Fu, L., Li, C., Song, J., Zhou, H., Bo, Y., Wang, J., 2014. LAINet – A wireless sensor network for coniferous forest leaf area index measurement: Design, algorithm and validation. Computers and Electronics in Agriculture 108, 200–208. https://doi.org/10.1016/j.compag.2014.08.003

Ray, D.K., West, P.C., Clark, M., Gerber, J.S., Prishchepov, A.V., Chatterjee, S., 2019. Climate change has likely already affected global food production. PLoS ONE 14, e0217148. https://doi.org/10.1371/journal.pone.0217148

Rockström, J., Williams, J., Daily, G., Noble, A., Matthews, N., Gordon, L., Wetterstrand, H., DeClerck, F., Shah, M., Steduto, P., de Fraiture, C., Hatibu, N., Unver, O., Bird, J., Sibanda, L., Smith, J., 2017. Sustainable intensification of agriculture for human prosperity and global sustainability. Ambio 46, 4–17. https://doi.org/10.1007/s13280-016-0793-6

Ryu, Y., Nilson, T., Kobayashi, H., Sonnentag, O., Law, B.E., Baldocchi, D.D., 2010. On the correct estimation of effective leaf area index: Does it reveal information on clumping effects? Agricultural and Forest Meteorology 150, 463–472. https://doi.org/10.1016/j.agrformet.2010.01.009

Ryu, Y., Verfaillie, J., Macfarlane, C., Kobayashi, H., Sonnentag, O., Vargas, R., Ma, S., Baldocchi, D.D., 2012. Continuous observation of tree leaf area index at ecosystem scale using upward-pointing digital cameras. Remote Sensing of Environment 126, 116–125. https://doi.org/10.1016/j.rse.2012.08.027

Sakamoto, T., Gitelson, A.A., Nguy-Robertson, A.L., Arkebauer, T.J., Wardlow, B.D., Suyker, A.E., Verma, S.B., Shibayama, M., 2012. An alternative method using digital cameras for continuous monitoring of crop status. Agricultural and Forest Meteorology 154–155, 113–126. https://doi.org/10.1016/j.agrformet.2011.10.014

Salamí, E., Barrado, C., Pastor, E., 2014. UAV Flight Experiments Applied to the Remote Sensing of Vegetated Areas. Remote Sensing 6, 11051–11081. https://doi.org/10.3390/rs61111051

Schaepman-Strub, G., Schaepman, M.E., Painter, T.H., Dangel, S., Martonchik, J.V., 2006. Reflectance quantities in optical remote sensing—definitions and case studies. Remote Sensing of Environment 103, 27–42. https://doi.org/10.1016/j.rse.2006.03.002

Searchinger, T., Waite, R., Hanson, C., Ranganathan, J., 2019. Creating a sustainable food future -A menu of solutions to feed nearly 10 billion people by 2050. World Resources Institute.

Semmens, K.A., Anderson, M.C., Kustas, W.P., Gao, F., Alfieri, J.G., McKee, L., Prueger, J.H., Hain, C.R., Cammalleri, C., Yang, Y., Xia, T., Sanchez, L., Mar Alsina, M., Vélez, M., 2016. Monitoring daily evapotranspiration over two California vineyards using Landsat 8 in a multi-sensor data fusion approach. Remote Sensing of Environment 185, 155–170. https://doi.org/10.1016/j.rse.2015.10.025

Shabanov, N.V., Wang, Y., Buermann, W., Dong, J., Hoffman, S., Smith, G.R., Tian, Y., Knyazikhin, Y., Myneni, R.B., 2003. Effect of foliage spatial heterogeneity in the MODIS LAI and FPAR algorithm over broadleaf forests. Remote Sensing of Environment 85, 410–423. https://doi.org/10.1016/S0034-4257(03)00017-8

Tucker, C.J., 1979. Red and photographic infrared linear combinations for monitoring vegetation. Remote Sensing of Environment 8, 127–150. https://doi.org/10.1016/0034-4257(79)90013-0

Tum, M., Günther, K., Böttcher, M., Baret, F., Bittner, M., Brockmann, C., Weiss, M., 2016. Global Gap-Free MERIS LAI Time Series (2002–2012). Remote Sensing 8, 69. https://doi.org/10.3390/rs8010069

Valente, J., Sari, B., Kooistra, L., Kramer, H., Mücher, S., 2020. Automated crop plant counting from very high-resolution aerial imagery. Precision Agric 21, 1366–1384. https://doi.org/10.1007/s11119-020-09725-3

Velumani, K., 2021. Deep learning algorithms for high-throughput cereal plant and organ identification (Doctor). Avignon Université, Avignon.

Velumani, K., Madec, S., de Solan, B., Lopez-Lozano, R., Gillet, J., Labrosse, J., Jezequel, S., Comar, A., Baret, F., 2020. An automatic method based on daily in situ images and deep learning to date wheat heading stage. Field Crops Research 252, 107793. https://doi.org/10.1016/j.fcr.2020.107793

Verger, A., Baret, F., Camacho, F., 2011. Optimal modalities for radiative transfer-neural network estimation of canopy biophysical characteristics: Evaluation over an agricultural area with CHRIS/PROBA observations. Remote Sensing of Environment 115, 415–426. https://doi.org/10.1016/j.rse.2010.09.012

Verhoef, W., Bach, H., 2007. Coupled soil–leaf-canopy and atmosphere radiative transfer modeling to simulate hyperspectral multi-angular surface reflectance and TOA radiance data. Remote Sensing of Environment 109, 166–182. https://doi.org/10.1016/j.rse.2006.12.013

Viña, A., Gitelson, A.A., 2005. New developments in the remote estimation of the fraction of absorbed photosynthetically active radiation in crops: REMOTE ESTIMATION OF FAPAR IN CROPS. Geophys. Res. Lett. 32. https://doi.org/10.1029/2005GL023647

Viña, A., Gitelson, A.A., Rundquist, D.C., Keydan, G., Leavitt, B., Schepers, J., 2004. Monitoring Maize (*Zea mays* L.) Phenology with Remote Sensing. Agron. J. 96, 1139–1147. https://doi.org/10.2134/agronj2004.1139

Wang, P., Gao, F., Masek, J., 2014. Operational Data Fusion Framework for Building Frequent Landsat-Like Imagery. IEEE Trans. Geosci. Remote Sensing 52, 7353–7365. https://doi.org/10.1109/TGRS.2014.2311445

Wang, Q., Zhang, Y., Onojeghuo, A.O., Zhu, X., Atkinson, P.M., 2017. Enhancing Spatio-Temporal Fusion of MODIS and Landsat Data by Incorporating 250 m MODIS Data. IEEE J. Sel. Top. Appl. Earth Observations Remote Sensing 10, 4116–4123. https://doi.org/10.1109/JSTARS.2017.2701643

Wang, S., Baum, A., Zarco-Tejada, P.J., Dam-Hansen, C., Thorseth, A., Bauer-Gottwein, P., Bandini, F., Garcia, M., 2019. Unmanned Aerial System multispectral mapping for low and variable solar irradiance conditions: Potential of tensor decomposition. ISPRS Journal of Photogrammetry and Remote Sensing 155, 58–71. https://doi.org/10.1016/j.isprsjprs.2019.06.017

Wanjura, D.F., Hatfield, J.L., 1988. Vegetative and optical characteristics of four-row crop canopies. International Journal of Remote Sensing 9, 249–258. https://doi.org/10.1080/01431168808954849

Wei, S., Fang, H., 2016. Estimation of canopy clumping index from MISR and MODIS sensors using the normalized difference hotspot and darkspot (NDHD) method: The influence of BRDF models and solar zenith angle. Remote Sensing of Environment 187, 476–491. https://doi.org/10.1016/j.rse.2016.10.039

Weiss, M, Baret, F., 2010. fAPAR (fraction of Absorbed Photosynthetically Active Radiation) estimates at various scale. Presented at the 34th International Symposium on Remote Sensing and Environment (ISRSE), Sydney, Australia, p. 4.

Weiss, Marie, Baret, F., 2010. CAN-EYE V6.1 user manual [WWW Document]. URL https://www6.paca.inrae.fr/can-eye

Weiss, M., Baret, F., Garrigues, S., Lacaze, R., 2007. LAI and fAPAR CYCLOPES global products derived from VEGETATION. Part 2: validation and comparison with MODIS collection 4 products. Remote Sensing of Environment 110, 317–331. https://doi.org/10.1016/j.rse.2007.03.001

Weiss, M., Jacob, F., Duveiller, G., 2020. Remote sensing for agricultural applications: A meta-review. Remote Sensing of Environment 236, 111402. https://doi.org/10.1016/j.rse.2019.111402

Weiss, M., Troufleau, D., Baret, F., Chauki, H., Prévot, L., Olioso, A., Bruguier, N., Brisson, N., 2001. Coupling canopy functioning and radiative transfer models for remote sensing data assimilation. Agricultural and Forest Meteorology 108, 113–128. https://doi.org/10.1016/S0168-1923(01)00234-9

Weng, Q., Fu, P., Gao, F., 2014. Generating daily land surface temperature at Landsat resolution by fusing Landsat and MODIS data. Remote Sensing of Environment 145, 55–67. https://doi.org/10.1016/j.rse.2014.02.003

Williams, D.L., Goward, S., Arvidson, T., 2006. Landsat: Yesterday, Today, and Tomorrow. Photogrammetric Engineering & Remote Sensing 72, 1171–1178.

Wu, B., Huang, B., Cao, K., Zhuo, G., 2017. Improving spatiotemporal reflectance fusion using image inpainting and steering kernel regression techniques. International Journal of Remote Sensing 38, 706–727. https://doi.org/10.1080/01431161.2016.1271471

Wulder, M.A., Loveland, T.R., Roy, D.P., Crawford, C.J., Masek, J.G., Woodcock, C.E., Allen, R.G., Anderson, M.C., Belward, A.S., Cohen, W.B., Dwyer, J., Erb, A., Gao, F., Griffiths, P., Helder, D., Hermosilla, T., Hipple, J.D., Hostert, P., Hughes, M.J., Huntington, J., Johnson, D.M., Kennedy, R., Kilic, A., Li, Z., Lymburner, L., McCorkel, J., Pahlevan, N., Scambos, T.A., Schaaf, C., Schott, J.R., Sheng, Y., Storey, J., Vermote, E., Vogelmann, J., White, J.C., Wynne, R.H., Zhu, Z., 2019. Current status of Landsat program, science, and applications. Remote Sensing of Environment 225, 127–147. https://doi.org/10.1016/j.rse.2019.02.015

Xiao, Z., Liang, S., Sun, R., Wang, J., Jiang, B., 2015. Estimating the fraction of absorbed photosynthetically active radiation from the MODIS data based GLASS leaf area index product. Remote Sensing of Environment 171, 105–117. https://doi.org/10.1016/j.rse.2015.10.016

Xiao, Z., Liang, S., Wang, J., Chen, P., Yin, X., Zhang, L., Song, J., 2014. Use of General Regression Neural Networks for Generating the GLASS Leaf Area Index Product From Time-Series MODIS Surface Reflectance. IEEE Trans. Geosci. Remote Sensing 52, 209–223. https://doi.org/10.1109/TGRS.2013.2237780

Xiao, Z., Wang, T., Liang, S., Sun, R., 2016. Estimating the Fractional Vegetation Cover from GLASS Leaf Area Index Product. Remote Sensing 8, 337. https://doi.org/10.3390/rs8040337

Yan, K., Park, T., Chen, C., Xu, B., Song, W., Yang, B., Zeng, Y., Liu, Z., Yan, G., Knyazikhin, Y., Myneni, R.B., 2018. Generating Global Products of LAI and FPAR From SNPP-VIIRS Data: Theoretical Background and Implementation. IEEE Trans. Geosci. Remote Sensing 56, 2119–2137. https://doi.org/10.1109/TGRS.2017.2775247

Yang, W., Feng, H., Zhang, X., Zhang, J., Doonan, J.H., Batchelor, W.D., Xiong, L., Yan, J., 2020. Crop Phenomics and High-Throughput Phenotyping: Past Decades, Current Challenges, and Future Perspectives. Molecular Plant 13, 187–214. https://doi.org/10.1016/j.molp.2020.01.008

Zhu, X., Cai, F., Tian, J., Williams, T.K.-A., 2018. Spatiotemporal Fusion of Multisource Remote Sensing Data: Literature Survey, Taxonomy, Principles, Applications, and Future Directions. Remote Sensing 10, 527. https://doi.org/10.3390/rs10040527

Zhu, X., Chen, J., Gao, F., Chen, X., Masek, J.G., 2010. An enhanced spatial and temporal adaptive reflectance fusion model for complex heterogeneous regions. Remote Sensing of Environment 114, 2610–2623. https://doi.org/10.1016/j.rse.2010.05.032

Zhukov, B., Oertel, D., Lanzl, F., Reinhackel, G., 1999. Unmixing-based multisensor multiresolution image fusion. IEEE Trans. Geosci. Remote Sensing 37, 1212–1226. https://doi.org/10.1109/36.763276

Zurita-Milla, R., Clevers, J., Schaepman, M.E., 2008. Unmixing-Based Landsat TM and MERIS FR Data Fusion. IEEE Geosci. Remote Sensing Lett. 5, 453–457. https://doi.org/10.1109/LGRS.2008.919685

5 Full major papers

5 published papers are listed and attached in the end of the thesis.

(1) **Wenjuan Li**; Jingyi Jiang; Marie Weiss; Simon Madec; Franck Tison; Burger Philippe; Alexis Comar; Frédéric Baret; Impact of the reproductive organs on crop BRDF as observed from a UAV, *Remote Sensing of Environment*, 2021, 259.

(2) **Wenjuan Li**; Frédéric Baret; Marie Weiss; Samuel Buis; Roselyne Lacaze; Valerie Demarez; Jean-francois Dejoux; Marjorie Battude; Fernando Camacho; Combining hectometric and decametric satellite observations to provide near real time decametric FAPAR product, *Remote Sensing of Environment*, 2017, 200: 250-262.

(3) **Wenjuan Li**; Hongliang Fang; Shanshan Wei; Marie Weiss; Fréderic Baret; Critical analysis of methods to estimate the fraction of absorbed or intercepted photosynthetically active radiation from ground measurements: Application to rice crops, *Agricultural and Forest Meteorology*, 2021, 297.

(4) **Wenjuan Li**; Marie Weiss; Francois Waldner; Pierre Defourny; Valerie Demarez; David Morin; Olivier Hagolle; Frédéric Baret; A Generic Algorithm to Estimate LAI, FAPAR and FCOVER Variables from SPOT4 HRVIR and Landsat Sensors: Evaluation of the Consistency and Comparison with Ground Measurements, *Remote Sensing*, 2015, 7(11): 15494-15516.

(5) **Wenjuan Li**; Hongliang Fang; Estimation of direct, diffuse, and total FAPARs from Landsat surface reflectance data and ground-based estimates over six FLUXNET sites, *Journal of Geophysical Research-Biogeosciences*, 2015, 120 (1): 96-112.

6 List of publications

(1) **Wenjuan Li**; Jingyi Jiang; Marie Weiss; Simon Madec; Franck Tison; Burger Philippe; Alexis Comar; Frédéric Baret; Impact of the reproductive organs on crop BRDF as observed from a UAV, *Remote Sensing of Environment*, 2021, 259.

(2) **Wenjuan Li**; Frédéric Baret; Marie Weiss; Samuel Buis; Roselyne Lacaze; Valerie Demarez; Jean-francois Dejoux; Marjorie Battude; Fernando Camacho; Combining hectometric and decametric satellite observations to provide near real time decametric FAPAR product, *Remote Sensing of Environment*, 2017, 200: 250-262.

(3) **Wenjuan Li**; Hongliang Fang; Shanshan Wei; Marie Weiss; Fréderic Baret; Critical analysis of methods to estimate the fraction of absorbed or intercepted photosynthetically active radiation from ground measurements: Application to rice crops, *Agricultural and Forest Meteorology*, 2021, 297.

(4) **Wenjuan Li**; Marie Weiss; Francois Waldner; Pierre Defourny; Valerie Demarez; David Morin; Olivier Hagolle; Frédéric Baret; A Generic Algorithm to Estimate LAI, FAPAR and FCOVER Variables from SPOT4 HRVIR and Landsat Sensors: Evaluation of the Consistency and Comparison with Ground Measurements, *Remote Sensing*, 2015, 7(11): 15494-15516.

(5) **Wenjuan Li**; Hongliang Fang; Estimation of direct, diffuse, and total FAPARs from Landsat surface reflectance data and ground-based estimates over six FLUXNET sites, *Journal of Geophysical Research-Biogeosciences*, 2015, 120 (1): 96-112.

(6) Fernando Camacho; Beatriz Fuster; **Wenjuan Li**; Marie Weiss; Sangram Ganguly; Roselyne Lacaze; Fred Baret; Crop specific algorithms trained over ground measurements provide the best performance for GAI and fAPAR estimates from Landsat-8 observations, *Remote Sensing of Environment*, 2021, 260.

(7) Wojciech Wojnowski; Shanshan Wei; **Wenjuan Li**; Tiangang Yin; XianXiang Li; Genevieve Lai Fern Ow; Mohamed Lokman Mohd Yusof; Andrew J. Whittle; Comparison of absorbed and intercepted fractions of PAR for individual trees based on radiative transfer model simulations, *Remote Sensing*, 2021, 13(6).

(8) S., Jay; A., Comar; R., Benicio; J., Beauvois; D., Dutartre; G., Daubige; **W., Li**; J., Labrosse; S., Thomas; N., Henry; M., Weiss; F., Baret; Scoring Cercospora Leaf Spot on Sugar Beet: Comparison of UGV and UAV Phenotyping Systems, *Plant Phenomics*, 2020, 2020: 1-18.

(9) Hongliang Fang; Yinghui Zhang; Shanshan Wei; **Wenjuan Li**; Yongchang Ye; Tao Sun; Weiwei Liu; Validation of global moderate resolution leaf area index (LAI) products over croplands in northeastern China, *Remote Sensing of Environment*, 2019, 233: 0-111377.

(10) Hongliang Fang; Weiwei Liu; **Wenjuan Li**; Shanshan Wei; Estimation of the directional and whole apparent clumping index (ACI) from indirect optical measurements, *ISPRS Journal of Photogrammetry and Remote Sensing*, 2018, 144: 1-13.

(11) François Waldner; Marie-Julie Lambert; **Wenjuan Li**; Marie Weiss; Valérie Demarez; David Morin; Claire Marais-Sicre; Olivier Hagolle; Frédéric Baret; Pierre Defourny; Land Cover and Crop Type Classification along the Season Based on Biophysical Variables Retrieved from Multi-Sensor High Resolution Time Series, *Remote Sensing*, 2015, 7(8): 10400-10424.

(12) Hongliang Fang; **Wenjuan Li**; Shanshan Wei; Chongya Jiang; Seasonal variation of leaf area index (LAI) over paddy rice fields in NE China: Intercomparison of destructive sampling, LAI-2200, digital hemispherical photography (DHP), and AccuPAR methods, *Agricultural and Forest Meteorology*, 2014, 198: 126-141.

(13) Hongliang Fang; Chongya Jiang; **Wenjuan Li**; Shanshan Wei; Frédéric Baret; Jing M. Chen; Javier Garcia-Haro; Shunlin Liang; Ronggao Liu; Ranga B. Myneni; Bernard Pinty; Zhiqiang Xiao; Zaichun Zhu; Characterization and intercomparison of global moderate resolution leaf area index (LAI) products:

Analysis of climatologies and theoretical uncertainties, *Journal of Geophysical Research-Biogeosciences*, 2013, 118(2): 529-548.

(14) Hongliang Fang; **Wenjuan Li**; Ranga B. Myneni; The Impact of Potential Land Cover Misclassification on MODIS Leaf Area Index (LAI) Estimation: A Statistical Perspective, *Remote Sensing*, 2013, 5(2): 830-844.

Agricultural and Forest Meteorology 297 (2021) 108273

Contents lists available at ScienceDirect

Agricultural and Forest Meteorology

journal homepage: www.elsevier.com/locate/agrformet

Critical analysis of methods to estimate the fraction of absorbed or intercepted photosynthetically active radiation from ground measurements: Application to rice crops

Wenjuan Li [a,b,c,*], Hongliang Fang [a,b], Shanshan Wei [a,b], Marie Weiss [c], Fréderic Baret [c]

[a] LREIS, Institute of Geographic Sciences and Natural Resources Research, Chinese Academy of Sciences, Beijing 100101, China
[b] College of Resources and Environment, University of Chinese Academy of Sciences, Beijing 100049, China
[c] INRAE, Avignon Université, UMR 1114 EMMAH, UMT CAPTE, F-84000, Avignon, France

ARTICLE INFO

Keywords:
fAPAR
fIPAR
Green fAPAR
Green fIPAR
Paddy rice
Diffuse fraction

ABSTRACT

Continuous and accurate ground measurements of the fraction of absorbed (fAPAR) or intercepted (fIPAR) photosynthetically active radiation by green canopy components is important to monitor canopy functioning. fAPAR and fIPAR are sensitive to illumination conditions and non-green components during the senescence stage. While several methods have been developed to estimate fAPAR or fIPAR in the field from different methods including AccuPAR, LAI-2200 and Digital Hemispheric Photograph Photography (DHP), the differences among these methods still need more investigations. The principles on which they are based are first reviewed with due attention to the assumptions used and approximations made. Two field campaigns conducted in 2012 and 2013 in northeastern China over paddy rice fields were then used to compare fAPAR and fIPAR measured using AccuPAR, DHP and LAI-2200. Results demonstrated that considering only canopy light transmittance (fIPAR), measured with AccuPAR, DHP or LAI-2200, is a good proxy of fAPAR which is computed from AccuPAR measurements of the four fluxes of the radiation balance. However, when canopy is senescing, downward looking DHP method is recommended since it is the only method that directly measures the light intercepted by green elements. Methods based on upward looking (DHP upward, AccuPAR, LAI-2200) cannot distinguish between the green and senescent vegetation elements. Corrections based on independent measurements of the ratio of the green area index (GAI) to the plant area index (PAI) (GAI/PAI) need to be used in this case, while assuming that green and senescent elements are well mixed in the canopy volume. Downward looking DHP appears to be the preferred method for relatively short and dense canopies such as rice since it does not disturb the canopy, it is sensitive to the green elements only and allows to simulate fIPAR for any illumination conditions.

1. Introduction

The fraction of photosynthetically active radiation (PAR, 400-700nm) absorbed by green vegetation elements (fAPAR) is closely linked to canopy functioning processes such as photosynthesis and transpiration. It also quantifies the incoming radiation available at the soil level that is mandatory for modeling soil temperature and evaporation. It is thus a key variable required in many ecosystems and crop functioning models to simulate photosynthesis and primary production (Goward and Huemmrich, 1992; McCallum et al., 2010; Monteith, 2015). fAPAR is listed as an essential climate variable (ECV) by the Global Climate Observing System (GCOS, 2016). It is often approximated by the fraction of intercepted PAR (fIPAR) because the vegetation pigments present a strong absorption in this spectral domain and the reflectivities from background are usually small for well-developed canopies (Gower et al., 1999).

Several methods have been developed to estimate fAPAR and fIPAR from ground measurements. Handheld optical devices, such as AccuPAR (Meter Group, Inc., USA), provide an efficient way to measure fAPAR under different illumination conditions (Steinberg et al., 2006). AccuPAR measures the downward and upward PAR fluxes at the top and bottom of the canopy by placing the probes above and below the canopy. Other methods such as Digital Hemispherical Photography (DHP) measure the gap fraction (upward looking) or green fraction (downward looking) to derive fIPAR in all directions. Pixel classification of the RGB images is mainly based on color contrast between leaves and the sky for the upward looking DHP to get the gap, and between green leaves and

* Corresponding author.
E-mail addresses: wenjuan.li122@gmail.com, wli@hiphen-plant.com (W. Li).

https://doi.org/10.1016/j.agrformet.2020.108273
Received 18 May 2020; Received in revised form 26 November 2020; Accepted 30 November 2020

Nomenclature

$I_t^{\downarrow}$	Incoming downward flux measured at the top of the canopy
$I_t^{\uparrow}$	Upward flux reflected by the canopy
$I_b^{\downarrow}$	Downward fluxes measured at the bottom of the canopy
$I_b^{\uparrow}$	Upward fluxes measured at the bottom of the canopy
R_c	Canopy reflectance
R_c^{bs}	Black-sky canopy reflectance under direct illumination conditions
R_c^{ws}	White-sky canopy reflectance under diffuse illumination conditions
T	Canopy transmittance
T^{bs}	Black-sky transmittance under direct illumination conditions
T^{ws}	White-sky transmittance under diffuse illumination conditions
R_s	Soil background reflectance
R_s^{bs}	Black-sky soil reflectance under direct illumination conditions
R_s^{ws}	White-sky soil reflectance under diffuse illumination conditions
R_∞	Canopy reflectance for very dense foliage
R_{sen}	Reflectance of senescent layer
P	Canopy gap fraction
θ	Zenith angle
$G(\theta)$	Leaf projection function
$\Omega(\theta)$	Canopy clumping index
DOY	Day of Year
ESU	Elementary Sampling Units
DHP	Digital Hemispherical Photography
PAR	Photosynthetically Active Radiation
f	Fraction of diffuse PAR in total PAR
fAPAR	Fraction of Absorbed PAR
$fAPAR_T$	fAPAR measured from the two-stream method using transmittance only
$fAPAR^{bs}$	Black-sky fAPAR under direct illumination conditions
$fAPAR^{ws}$	White-sky fAPAR under diffuse illumination conditions
$fAPAR_T^{bs}$	Black-sky fAPAR measured from the two-stream method
$fAPAR_T^{ws}$	White-sky fAPAR measured from the two-stream method
fIPAR	Fraction of Intercepted PAR
fIPAR(LAI-2200)	fIPAR measured from LAI-2200
$fIPAR^{ws}$(LAI-2200)	White-sky fIPAR measured from LAI-2200
fIPAR(DHP_{up})	fIPAR measured from the upward DHP
$fIPAR^{bs}$(DHP_{up})	Black-sky fIPAR from the upward DHP
$fIPAR^{ws}$(DHP_{up})	White-sky fIPAR from the upward DHP
GfIPAR(DHP_{down})	fIPAR of green canopy components measured from the downward DHP
$GfIPAR^{bs}$	Black-sky GfIPAR measured from the downward DHP
$GfIPAR^{ws}$	White-sky GfIPAR measured from the downward DHP
GfAPAR	fAPAR of canopy green components
$GfAPAR_{top}$	GfAPAR corrected from canopy fAPAR using Eq. (14)
$GfAPAR_{mix}$	GfAPAR corrected from canopy fAPAR using Eq. (15)
GF	Green Fraction
GAI	Green Area Index
GLAI	Green Leaf Area Index
PAI	Plant Area Index

non-green elements including the background to get the green pixels for the downward looking DHP (Baret et al., 1993; Demarez et al., 2008; Leblanc et al., 2005). However, image segmentation may be affected by the illumination conditions, especially when shadows or specular reflection are observed (Fang et al., 2014a, 2018; Ye et al., 2015). LAI-2200 (LI-COR Inc., Lincoln, Nebraska, USA) measures the transmittance in the blue wavelength domain in five zenithal directions from which fIPAR can be estimated. However LAI-2200 measurements are also sensitive to the illumination conditions (Asner et al., 1998; Kobayashi et al., 2013; Leblanc and Chen, 2001). A thorough intercomparison of these instruments is still lacking. fAPAR depends on solar zenith angle and illumination conditions, e.g., overcast or clear sky condition. The instantaneous fAPAR is highly sensitive to variations of the solar zenith angle and presents diurnal variations under clear sky conditions (Fensholt et al., 2004; Rahman et al., 2015; Zhao et al., 2018), while it shows a much smaller diurnal variations under cloudy conditions (Nouvellon, 2000; Thomas et al., 2006). The daily integrated fAPAR, which is a variable used by many canopy functioning models, has been demonstrated to be smaller under clear sky as compared to overcast conditions (Gower et al., 1999; Thomas et al., 2006). Therefore, it is required to compare the fAPAR quantities measured by different instruments under a range of illumination conditions and solar zenith angles. However, direct comparison between instruments is not always feasible due to the intrinsic properties of each device. As an example, the fAPAR measured by AccuPAR accounts for the diffuse fraction, while devices based on gap fraction measurements (DHP) may account both for the direct sunlight and the diffuse illumination. To facilitate the comparison between those different instruments, we used the decomposition proposed by Martonchik et al. (2000): fAPAR is considered as the sum of a black-sky and a white-sky components, weighted by the PAR diffuse fraction. The black-sky fAPAR, $fAPAR^{bs}$, corresponds to the direct component (collimated beam irradiance in the sun direction only) while the white-sky fAPAR, $fAPAR^{ws}$, corresponds to diffuse illumination conditions generally assumed perfectly isotropic (GCOS, 2016). Although the impact of diffuse fraction on fAPAR has been investigated (Gu et al., 2002; Jongschaap et al., 2006; Lizaso et al., 2005), few studies focused on the estimation of the black-sky and white-sky components of fAPAR or fIPAR in crops (Cohen et al., 1997; Hanan and Bégué, 1995) and none of them have intercompared the ability of the current instruments to well measure these quantities.

Since only the green photosynthetically active elements contribute directly to key processes such as photosynthesis and transpiration, green vegetation elements should be isolated to estimate fAPAR (Huemmrich et al., 2005; Pinter, 1993; Weiss et al., 2007; Xiao, 2004; Zhang et al., 2005). The presence of senescent leaves during late crop growth stages have a significant impact on fAPAR, and the relationship between fAPAR and vegetation indices (Di Bella et al., 2004; Rahman et al., 2019; Viña and Gitelson, 2005). The ground measured canopy fAPAR can be partitioned into fAPAR of green components and non-green components. Among optical instruments listed above, only downward looking DHPs allow to separate the green from the non-green elements to estimate the corresponded fraction of intercepted light. Upward looking DHPs should not be used for such a purpose since senescence often starts from the bottom layer of the crop, while the light penetrates from the top of the canopy (Baret et al., 2010). The other upward looking techniques, such as AccuPAR and LAI-2200, do not allow distinguishing between green and non-green elements. Some corrections have been proposed to consider only the green elements depending on the canopy type, either assuming that the green elements are located at the top of the canopy (Chen, 1996), or assuming that green and non-green elements are well mixed in the canopy volume (Viña and Gitelson, 2005).

The objective of this study is to compare the several methods proposed and evaluate the impact of the presence of non-green vegetation elements during the senescence phase, under different illumination

conditions. For this purpose, a dedicated experiment was conducted in 2012 and 2013 where AccuPAR, DHP and LAI-2200 devices were concurrently used over paddy rice fields in northeastern China.

2. Methods

2.1. Theoretical background

2.1.1. Derivation of canopy fAPAR and fIPAR

fAPAR is calculated from the radiation balance in the PAR domain:

$$\mathrm{fAPAR} = \frac{I_t^{\downarrow} - I_t^{\uparrow} - \left(I_b^{\downarrow} - I_b^{\uparrow}\right)}{I_t^{\downarrow}} \tag{1}$$

where $I_t^{\downarrow}$ and $I_t^{\uparrow}$ are the downward and upward fluxes measured at the top of the canopy. $(I_b^{\downarrow} - I_b^{\uparrow})$ is the radiation absorbed by the soil background calculated as the difference between the downward $(I_b^{\downarrow})$ and upward $(I_b^{\uparrow})$ fluxes measured at the bottom of the canopy. Note that the net horizontal PAR fluxes are considered negligible as we focus on rice crops which are short canopies that do not present major heterogeneity at the scale investigated corresponding to few square meters located in an homogeneous field (Widlowski, 2010). Eq. (1) can be expressed more simply as:

$$\mathrm{fAPAR} = 1 - R_c - T(1 - R_s) \tag{2}$$

where $R_c = \frac{I_t^{\uparrow}}{I_t^{\downarrow}}$ is the canopy reflectance, $T = \frac{I_b^{\downarrow}}{I_t^{\downarrow}}$ is the canopy transmittance, and $R_s = \frac{I_b^{\uparrow}}{I_b^{\downarrow}}$ is the soil background reflectance in the PAR spectral domain. For short canopies such as paddy rice, it is usually difficult to measure the upward flux at the bottom of the canopy because of the short distance between the sensors and the soil surface and the large spatial heterogeneity of this flux. However, the soil background reflectance can be estimated from other independent measurements in the laboratory or over bare soils at nearby locations.

In the PAR domain, the canopy reflectance can be approximated as a linear decomposition of soil and foliage reflectance:

$$R_c \approx TR_s + (1 - T)R_{\infty} \tag{3}$$

where R_{∞} is the reflectance for very dense foliage. Combining Eqs. (2) and (3), fAPAR can be approximated using two terms:

$$fAPAR \approx (1 - T)(1 - R_{\infty}) \tag{4}$$

For dense vegetation, R_{∞} is very small ($R_{\infty} \approx 0.04$) because of the strong absorption by chlorophyll pigments in the PAR domain (Weiss et al., 2018). Therefore, Eq. (4) can be further simplified as:

$$\mathrm{fAPAR} \approx \mathrm{fAPAR}_T = 1 - T \tag{5}$$

The accuracy of this simplification depends on the fluxes reflected by the canopy and the soil background, which vary with canopy structure, illumination conditions, and background properties (Widlowski, 2010). If leaves are considered opaque, the fraction of intercepted PAR (fIPAR) can be calculated from the gap fraction P (Eq. (6)). In these conditions, P is closely approximated by canopy transmittance (T) and $\mathrm{fIPAR} \approx \mathrm{fAPAR}_T$.

$$fIPAR = 1 - P \approx 1 - T \approx \mathrm{fAPAR}_T \tag{6}$$

2.1.2. Estimation of the canopy fAPAR and fIPAR under different illumination conditions

At a given time of the day, the total canopy fAPAR is the sum of the black-sky and white-sky fAPAR, weighted by the fraction of the incoming diffuse PAR radiation (f):

$$fAPAR = (1 - f) \cdot fAPAR^{bs} + f \cdot fAPAR^{ws} \tag{7}$$

The same black-sky and white-sky components are also defined for the fIPAR quantities. During a day, if clear-sky $fAPAR(\theta)$ and white-sky observations, $fAPAR^{ws}$, are measured, instantaneous black-sky fAPAR (fAPAR^{bs}) can be estimated based on Eq. (8):

$$fAPAR^{bs}(\theta) = \frac{fAPAR(\theta) - f(\theta) \cdot fAPAR^{ws}}{1 - f(\theta)} \tag{8}$$

Similarly, transmittance measured in the five directions by the LAI-2200 allows to compute the black-sky fIPAR, $\mathrm{fIPAR}^{bs}(\theta)$ for $\theta < 68°$ by linear interpolation between the five crowns.

The fraction of intercepted black-sky PAR ($\mathrm{fIPAR}^{bs}(\theta)$) was calculated from the green fraction (GF) for downward looking DHP or gap fraction (P) for upward looking DHP after classifying the green (downward) or sky (upward) pixels:

$$\begin{cases} fIPAR^{bs}(\theta) = GF(\theta) & \text{for downward DHP} \\ fIPAR^{bs}(\theta) = 1 - P(\theta) & \text{for upward DHP} \end{cases} \tag{9}$$

For each zenith direction, θ, with $\theta < 60°$, the green or gap fraction is averaged across all azimuthal directions from all images in an ESU to compute $GF(\theta)$ or $P(\theta)$ (Weiss and Baret, 2010). Data for $\theta > 60°$ were not considered because of the large uncertainties in the green fraction estimation due to the degraded resolution for these directions.

White-sky fIPAR (fIPAR^{ws}) for LAI-2200 and DHP devices can be derived by integrating $fIPAR^{bs}$ over the hemisphere (Weiss and Baret, 2010):

$$fIPAR^{ws} = 2\int_0^{\pi/2} \left(fIPAR^{bs}(\theta)\right)\cos\theta\sin\theta d\theta \tag{10}$$

For $\theta > 60°$ (DHP) or $\theta > 68°$ (LAI-2200), the term $(fIPAR^{bs}(\theta))\cos\theta\sin\theta$ was approximated by linear interpolation between $\theta = 60°$ or $\theta = 68°$ and $\theta = 90°$ with $(fIPAR^{bs}(90°))\cos 90°\sin 90° = 0$.

2.1.3. Derivation of the green fAPAR and fIPAR (GfAPAR and GfIPAR)

Assuming that all canopy elements are randomly distributed in the canopy volume, the canopy transmittance can be derived using the Poisson model (Nilson, 1971):

$$T = e^{-G(\theta) \cdot PAI \cdot \Omega(\theta)/\cos\theta} \tag{11}$$

where $G(\theta)$ is the projection function that depends on the leaf inclination distribution and direction (θ), and $\Omega(\theta)$ is the canopy clumping index. It is here assumed that $G(\theta)$ and $\Omega(\theta)$ values are the same for the green and non-green elements. The four-stream fAPAR (Eq. (2)) can then be approximated as:

$$fAPAR = 1 - R_c - (1 - R_s) \cdot e^{-G(\theta) \cdot PAI \cdot \Omega(\theta)/\cos\theta} \tag{12}$$

When there are no senescent elements, GfAPAR=fAPAR. Conversely, for canopies having senescent elements, GfAPAR can be estimated from fAPAR measurements using an independent estimate of GAI/PAI and assumptions about the distribution of the senescent elements in the canopy. When the green leaves are located at the top of the canopy above the senescent elements, Chen (1996) proposed to estimate GfAPAR using the following formulation:

$$GfAPAR^{top} = 1 - R_c - (1 - R_{sen}) \cdot e^{-G(\theta) \cdot GAI \cdot \Omega(\theta)/\cos\theta} \tag{13}$$

where R_{sen} is the reflectance of the senescent layer above the soil background. It plays the same role as R_s in Eq. (12) when there is no senescent element. Finally, GAI in Eq. (13) can be replaced by PAI in Eq. (12) using the GAI/PAI ratio:

$$GfAPAR^{top} = 1 - R_c - (1 - R_{sen}) \cdot e^{\frac{GAI}{PAI} \cdot \ln\left(\frac{1 - R_c - fAPAR}{1 - R_s}\right)} \tag{14}$$

Conversely, Viña and Gitelson (2005) assumed that the green and non-green elements are well mixed within the canopy volume, proposed

Table 1
Quantities estimated from AccuPAR, DHP, and LAI-2200. R_c, R_s, R_{sen} and T represent the canopy reflectance, the background soil and senescent layer reflectance, and the canopy transmittance, respectively. P is the canopy gap fraction and GF is the green fraction.

Instruments	Notation	Equation	Eq. #
AccuPAR	$fAPAR(AccuPAR)$	$1 - R_c - T(1 - R_s)$	(2)
	$fAPAR_T(AccuPAR)$	$1 - T$	(5)
	$GfAPAR^{top}(AccuPAR)$	$\frac{1 - R_c - (1 - R_{sen})}{e^{\frac{GAI}{PAI}\ln\left(\frac{1 - R_c - fAPAR}{1 - R_s}\right)}}$	(14)
	$GfAPAR^{mix}(AccuPAR)$	$fAPAR \cdot GAI/PAI$	(15)
Downward DHP	$GfIPAR(DHP_{down})$	GF	(9)
Upward DHP	$fIPAR(DHP_{up})$	$1 - P$	(9)
	$GfIPAR^{top}(DHP_{up})$	$1 - e^{\frac{GAI}{PAI}\cdot\ln(1 - fIPAR)}$	(16)
	$GfIPAR^{mix}(DHP_{up})$	$fIPAR \cdot GAI/PAI$	(17)
LAI-2200	$fIPAR(LAI - 2200)$	$1 - P$	(9)
	$GfIPAR^{top}(LAI - 2200)$	$1 - e^{\frac{GAI}{PAI}\cdot\ln(1 - fIPAR)}$	(16)
	$GfIPAR^{mix}(LAI - 2200)$	$fIPAR \cdot GAI/PAI$	(17)

the following formulation of the green fAPAR as a function of the total canopy fAPAR and the GAI/PAI ratio:

$$GfAPAR^{mix} = fAPAR \cdot GAI/PAI \quad (15)$$

Based on the same considerations, Eqs. (14) and (15) can be applied to fIPAR values derived from upward DHP and LAI-2200 devices to get the corresponding green fIPAR, GfIPAR:

$$GfIPAR^{top} = 1 - e^{\frac{GAI}{PAI}\ln(1 - fIPAR)} \quad (16)$$

$$GfIPAR^{mix} = fIPAR \cdot GAI/PAI \quad (17)$$

Table 1 lists the fAPAR and fIPAR quantities derived from the several instruments and the associated notations and equations used. All these quantities can be computed for both black-sky and white-sky conditions.

2.2. Study area

The study area is located at the Honghe Farm (47.65° N, 133.52° E) in the Heilongjiang Province, China. The area is subjected to a humid continental monsoon climate with long and cold winter and warm, short, and humid summer. The water and soil are frozen from late October to April and thaw in late April. A single rice cultivar (*Longjing 29*) is grown in flat fields sharing the same soil properties and where the same cropping practices are applied. Rice crops are grown once a year from May to September (Fig. A1). The fields are flooded during most of the growing season.

A total of 55 Elementary Sampling Units (ESUs) of about 20 × 20 m^2 each were selected in five fields closely located and chosen to be homogeneous and similar in terms of soils and management practices. This allows to consider each ESU as representative of all the other ESUs. All ESUs were located at least at 1.5 m from the field border to limit potential edge effects. More details about the site and sampling strategy can be found in Fang et al. (2014a, 2014b).

2.3. Ground measurements

Ground measurements were carried out frequently from June 11 to September 17 in 2012, and from June 22 to August 29 in 2013 (Fig. 1).

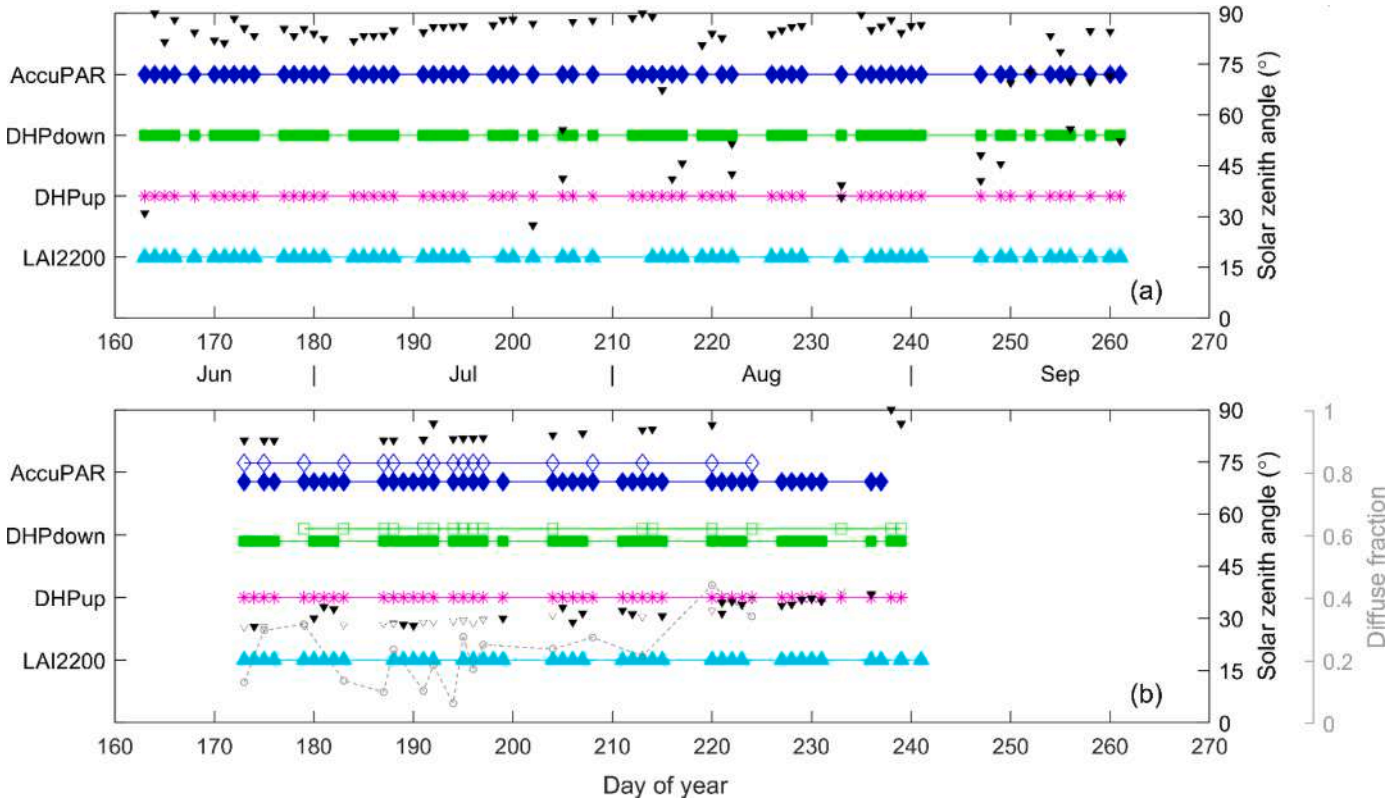

Fig. 1. Measurement dates for AccuPAR (blue diamond), DHP_{down} (green square), DHP_{up} (pink asterisk) and LAI-2200 (cyan triangle) in (a) 2012 and (b) 2013 under cloudy (filled marker) and clear (open marker, 2013) conditions. Black filled and open downward-pointing triangles represent solar zenith angles for cloudy and clear conditions (first right y-axis). Gray dashed line with open circles in (b) indicate the diffuse fraction measured for clear sky conditions in 2013 (second right y-axis).

We used the "moving ESU strategy" as described by Fang et al. (2014a), considering that the measurements achieved in one ESU at a given date are representative of all the other ESUs. This allows to prevent disturbances caused by the handheld measurements along the growing season and makes destructive measurements possible. In 2012, all the measurements were taken close to sunset or under overcast conditions to estimate the white-sky fAPAR. In 2013, white-sky fAPAR was also measured near sunset or under overcast conditions and completed the same day by black-sky fAPAR measurements when the sky was clear in the morning (9:30 to 10:30 am). The field measurement dates and the corresponding solar zenith angles and diffuse fraction are shown in Fig. 1 for the several instruments considered in this study.

Decagon's AccuPAR LP-80 PAR/LAI Ceptometer measures PAR using 80 individual sensors with a 180° field of view on a 1-m probe (Huemmrich et al., 2005; Senna, 2005; Steinberg et al., 2006; Thomas et al., 2006). The downward and reflected PAR fluxes at the top of canopy were measured by placing the probe approximately 1.5 m above the canopy, facing upward and downward, respectively. The canopy transmitted PAR was measured by placing the probe below the canopy looking upward. The below-canopy measurements were repeated four times in different directions to account for the row effect (Campos et al., 2017; Timlin et al., 2014; Zhong et al., 2015). The soil reflected PAR was measured twice in two different rows by placing the probe approximately 5 cm above the ground looking downward. Prior to each measurement, the AccuPAR was calibrated when the above canopy PAR was > 600 μmol/m^{2}s as recommended in the user manual (Decagon Devices, 2010). Under clear skies in 2013, the diffuse PAR was measured by blocking the direct solar illumination with a black board placed 0.5 m from the sensor. The diffuse fraction was then computed as the ratio of the diffuse to the total downward PAR. The measurement was repeated three times within one minute before, during, and after fAPAR measurements. Because the three replicates were generally consistent, their average value was considered as the diffuse fraction at the time of the fAPAR measurements.

The DHP images were taken using a Nikon D5100 camera equipped with a 4.5 mm F2.8 EX DC fisheye convertor. The DHP camera was calibrated before measurements following the CAN-EYE manual (Weiss and Baret, 2010) to obtain the optical center and the projection function of the camera and fish-eye system. The total height of the camera, including the lens, was about 16.5 cm. Two bubble levels were attached to the camera to keep it horizontal for both downward and upward measurements. In each ESU, 15 to 20 DHPs were acquired for both downward and upward directions (Fang et al., 2014a). The downward images were taken by holding the camera 0.8−1.5 m above the canopy. When the rice was higher than 70 cm, upward images were taken by placing the camera right above the background soil or water in the row. All DHP images were processed using the CAN-EYE version 6.3.3 software (https://www6.paca.inrae.fr/can-eye). Green pixels were manually separated from senescent and background pixels for the downward images during the classification step. This step was performed by the same operator throughout the season.

LAI-2200 measures the blue radiation in 5 concentric rings centered at 7°, 23°, 38°, 53° and 68°. LAI-2200 measurements were conducted always under diffuse conditions. Each measurement was repeated twice, with one above and four below canopy readings along diagonal transects between the rows. For the below canopy readings, the instrument was held about 5 cm above the background. Throughout the season, a 270° view cap was used to shield the operator. The four measurements over an ESU were averaged to obtain the mean transmittance (Fang et al., 2014a, 2014b). All AccuPAR, DHP, and LAI-2200 measurements were made within a maximum time difference of 10 minutes.

In addition to the optical measurements, canopy green area index (GAI) and plant area index (PAI) were measured in 2012 using a destructive method (Fang et al., 2014a, 2014b). Five plants were randomly harvested in the ESU and the area of green and non-green leaves, stems and ears were measured using a LI-3100C Area Meter (LI-COR, Lincoln, NE, USA). Leaf, stem, and ear area are the sum of the corresponding green and non-green measured areas. The corresponding area indices were then computed using the plant density to get the area of elements per unit ground area. GLAI corresponds to the green leaves only, while LAI includes green and non-green parts. GAI corresponds to the area of all green elements, while PAI includes the senescent parts as well.

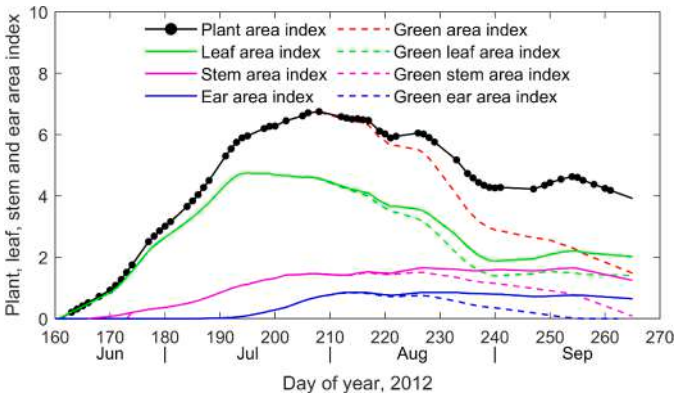

Fig. 2. Seasonal variation of plant, leaf, stem and ear area index measured by destructive method in 2012. The corresponding area of the green parts are indicated by the dashed lines. The black circles represent the actual measurements days.

3. Results

3.1. Dynamics of LAI, GLAI, GAI and PAI

During the rice green-up stage from sowing to the end of July (Day of year (DOY) 210), no senescence is observed: GAI and PAI are equal (Fig. 2). When the senescence starts to progress, some leaves disappear, and both PAI and GAI decrease gradually after DOY 210. Once the stems and ears are fully developed around DOY 220, their total area keep about constant. However, senescence is also progressing gradually up to almost full senescence at maturity, i.e. DOY 265 (Fig. 2). Conversely, senescence of leaves stops on DOY 240: LAI and GLAI and PAI keep about constant up to maturity, while GAI still decreases because of the senescing stems and ears. The high consistency observed between measurements across time demonstrates that the spatial variability among the several ESUs sampled was very small.

3.2. fAPAR from AccuPAR

Results show that for both 2012 and 2013, canopy reflectance (R_c) is slightly higher in the beginning when the soil background is not fully covered by the vegetation, and at the end of season after the ears and senescent components began to appear. When the canopy is fully covering the soil, R_c keeps about to a low and stable value with $R_c \approx 0.04$ (Fig. 3). Soil background reflectance (R_s) shows little variation during the growing season and is low because the soil was always wet or covered by water. Canopy transmittance (T) decreases continuously from the beginning of the season until DOY 210 and then increases slightly during the senescent stage (Fig. 3) since part of the leaves are dead while another part of them show a decrease in chlorophyll, leading to an increase in leaf reflectance and transmittance in the PAR domain. Accordingly, canopy fAPAR increases from the beginning of the season up to DOY 210 and decreases during the senescent stage (Fig. 3a). The influence of the illumination conditions on the different components can be analyzed in 2013 (Fig. 3b). Canopy and soil reflectance are little impacted and remain stable. Conversely, the canopy transmittance depends on the illumination conditions mostly before DOY 210 when the canopy is not fully covering the soil. The black-sky transmittance is

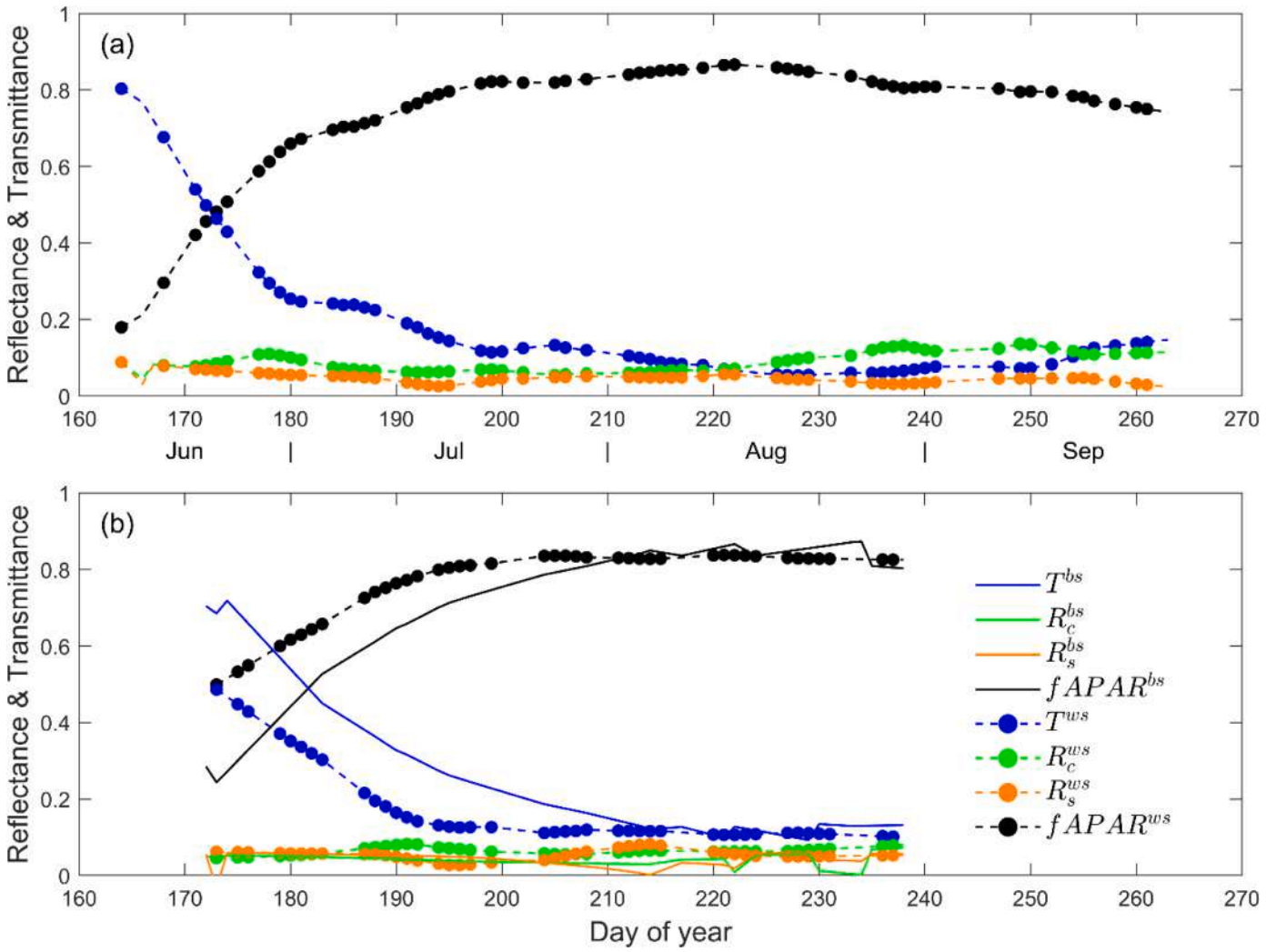

Fig. 3. Seasonal variation of canopy reflectance (R_c), soil reflectance (R_s), canopy transmittance (T), and fAPAR measured in 2012 (a) and 2013 (b) with AccuPAR. The solid and dashed lines represent the black-sky (with superscript '^{bs}') and white-sky (with superscript '^{ws}') conditions. The filled circles on lines represent the actual measurement days.

higher than its white-sky counterpart, and consequently the black-sky fAPAR is smaller than the white-sky fAPAR. After DOY 210, the difference between black-sky and white-sky values for both transmittance and fAPAR becomes very small due to the saturation of the canopy transmittance.

Our experimental results (Fig. 4) show that $fAPAR_T$(AccuPAR) estimated from the two-stream assumption (Eq. (5)) agrees very well with the reference four-stream fAPAR, fAPAR(AccuPAR) (Eq. (2)) under both black-sky and white-sky conditions ($R^2 = 0.94{\sim}1$, RMSE = 0.03~0.08). These two fAPAR quantities differ from less than 0.03 (4%) under black-sky conditions, the differences being larger when fAPAR(AccuPAR) is higher than 0.7 and under white-sky conditions.

3.3. *fAPAR and fIPAR of different instruments*

White-sky fAPAR and fIPAR values rapidly increase until DOY 210 in 2012 and 2013 (Fig. 5). As expected, $fAPAR_T$(AccuPAR), $fIPAR(DHP_{up})$ and fIPAR(LAI-2200) and fAPAR (AccuPAR) are very close together during the entire season. Conversely, $GfIPAR(DHP_{down})$ is slightly higher than fAPAR(AccuPAR) during the early development stages and is much lower than the other quantities during the later stages: White-sky $GfIPAR(DHP_{down})$ decreases sharply after DOY 210. In contrast, the other quantities remain stable from DOY 210 to DOY 250 and slightly decrease after DOY 250. In 2013 where both black-sky and white-sky values were measured (Fig. 5b), the black-sky values are substantially smaller than the white-sky counterparts. However black-sky $GfIPAR(DHP_{down})$ is higher than the white-sky values at the end of the season (Fig. 5b).

We will focus here on the first growth period (before DOY 210) where senescence is marginal (Fig. 2) and GAI=PAI. As a consequence, GfAPAR=fAPAR and GfIPAR=fIPAR. We will therefore use here only the terms fAPAR and fIPAR except for GfIPAR(DHPdown) for which only the green elements are accessible (Table 1). The comparison between fAPAR and fIPAR will be made using $fAPAR_T$(AccuPAR) as a reference since we demonstrated previously that fAPAR(AccuPAR)≈0.96 × $fAPAR_T$(AccuPAR) (Fig. 4).

$GfIPAR(DHP_{down})$ shows a high agreement with $fAPAR_T$(AccuPAR) under white-sky conditions (Fig. 6a) ($R^2 = 0.82$) with almost no bias. A strong correlation is also observed under black-sky conditions (Fig. 6a) with however a systematic overestimation (Bias=0.13). The correlation between $fAPAR_T$(AccuPAR) and the $fIPAR(DHP_{up})$ is weak both for the white-sky and black-sky values (Fig. 6b). fIPAR(LAI-2200) shows a high agreement with $fAPAR_T$(AccuPAR) (Fig. 6c), particularly under white-sky conditions.

3.4. *GfAPAR and GfIPAR during the senescence stage*

We focus on the period starting after DOY 210 when senescence

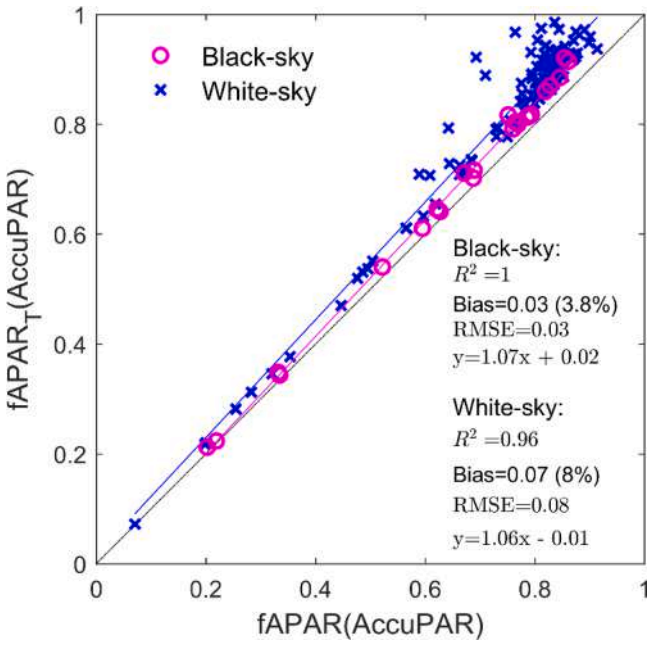

Fig. 4. Comparison of four-stream fAPAR(AccuPAR) (Eq. (2)) and the two-stream fAPAR$_T$ (AccuPAR)(Eq. (5)) values derived from AccuPAR measurements in 2012 and 2013 under both black (magenta) and white-sky (blue) conditions.

increases up to the maturity stage (Fig. 2). As a consequence, the GAI/PAI ratio decreases regularly with time (Fig. 7). The canopy fAPAR measured by AccuPAR shows small variations due to saturation when PAI is generally higher than 4.0. Conversely, the green fIPAR derived from downward looking DHP, which can be taken as the best proxy of GfIPAR, decreases swiftly from 0.9 to 0.3 (Fig. 7). Assuming that green and non-green elements are mixed within the canopy (Viña and Gitelson, 2005), GfAPAR measured by AccuPAR (Eq. (15)) and GfIPAR measured by LAI-2200 (Eq. (17)) show a temporal profile close to the reference GfIPAR from downward looking DHP. Conversely, all green quantities derived with Chen (1996), (Eq. (14)) (e.g. assuming that the green elements are distributed at the top of canopy) are systematically higher than the reference GfIPAR from downward looking DHP. GfIPAR^{mix} estimated from LAI-2200 and upward looking DHP are similar and higher than GfAPAR^{mix} derived from AccuPAR.

Fig. 8 shows that GfAPAR(AccuPAR), GfIPAR(DHP$_{up}$) and GfIPAR (LAI-2200) are well correlated with GfIPAR(DHP$_{down}$) considered as the reference. However, significant biases are observed. Under the assumption that the green and non-green elements are mixed in the canopy (Viña and Gitelson, 2005, Eq. (15)), GfAPAR^{mix}(AccuPAR) is closer to the reference GfIPAR(DHP$_{down}$) (Bias = 0.02, Fig. 8a), while the GfIPAR^{mix}(DHP$_{up}$) and GfIPAR^{mix}(LAI-2200) are larger by around 0.1 (Fig. 8b and 8c). Conversely, assuming that the green elements are distributed at the top of canopy as proposed by Chen (1996), GfAPAR^{top}(AccuPAR), GfIPAR^{top}(DHP$_{up}$) and GfIPAR^{top}(LAI-2200) are systematically higher by 0.13 ~ 0.25 than reference GfIPAR(DHP$_{down}$).

4. Discussion

4.1. Four-stream fAPAR versus two-stream fAPAR$_T$ estimation from AccuPAR

AccuPAR is appropriate to measure the fAPAR based on the four-stream approach (Eq. (2)). However, application of the four-stream assumption to compute fAPAR requires measuring simultaneously canopy reflectance and transmittance, together with the background reflectance. Measurement of the background reflectance is difficult since it requires setting the sensors close to the background which may disturb the canopy and influence the measurement. Furthermore, the spatial representativeness may also be an issue considering the high local spatial variability of the radiation field at the bottom of the canopy, due to the row spacing and canopy cover (Timlin et al., 2014). Conversely, the two-stream assumption (Eq. (5)) based on the sole measurement of canopy transmittance is appealing to estimate fAPAR.

The high consistency between fAPAR(AccuPAR) and fAPAR$_T$(AccuPAR) (Fig. 4) is mainly due to the small values of canopy and soil reflectance (Fig. 3). Furthermore, both terms are partly counterbalancing each other: in Eq. (2), canopy reflectance (R_c) varies between R_s for PAI=0 to R∞ for very large PAI values. Conversely, the term T_{Rs} varies between R_s for PAI=0 to 0 for large PAI values. These experimental results are consistent with that of other studies (Gallo and Daughtry, 1986; Gobron et al., 2006; Gower et al., 1999; Kukal and Irmak, 2020). However, as shown by Eq. (4), the measured transmittance includes the contribution from multiple scattering between the bottom of the canopy and the ground, leading to an overestimation of the actual transmittance and thus on fAPAR$_T$ (Eklundh et al., 2011). Closer inspection of the values shows that fAPAR$_T$(AccuPAR) is systematically higher than fAPAR(AccuPAR), particularly for the well-developed canopies fAPAR$_T$(AccuPAR)≈1 when fAPAR (AccuPAR)≈1-R_∞≈0.96 as expected from Eq. (4) since R_∞≈0.04 (Fig. 3). We also computed the actual transmittance which is smaller than the measured one by -0.78% to -0.14% under cloudy conditions and -0.41% to -0.01% under clear sky conditions. Similarly, fAPAR$_T$ computed when considering multiple scattering is slightly larger than the fAPAR$_T$ we estimated by 0.22% to 3.3% under cloudy conditions and 0.2% to 3.09% under clear conditions. This small uncertainty is mainly due to low background reflectance of paddy rice. Nevertheless, higher uncertainties may occur for canopies with brighter backgrounds (Asner et al., 1998; Gower et al., 1999; Widlowski, 2010).

4.2. Comparison of fAPAR and fIPAR measured from different instruments during the green-up stage

The overestimations observed between GfIPAR^{bs}(DHP$_{down}$) and fAPAR^{bs}(AccuPAR) under black-sky conditions are mostly due to the limited spatial sampling when considering only the sun direction. In case of the black-sky conditions, AccuPAR measurements provide a better spatial sampling with the 80 sensors set along the 1 m long device. Conversely, for white-sky conditions, GfIPAR^{ws}(DHP$_{down}$) results from the integration of the black-sky values over all the directions (Eq. (10)) which provides to a much larger area sampled. fIPAR(DHP$_{up}$) has a weak correlation with fAPAR$_T$(AccuPAR). This is mostly explained by the limited range of variation of fAPAR$_T$ points available. DHP measurements looking upward requires to set the camera at the bottom of the canopy. When the back of the camera is laying on the ground, the focal point of the lens is at about 16.5 cm above the ground. It is therefore not possible to use this technique for the early growth stages when the canopy is too short. This explains why no points are available for the low values of fAPAR or fIPAR (Fig. 6b). Further, only part of the vegetation elements are seen by the camera looking upward, resulting in possible underestimation of fIPAR(DHP$_{up}$). In addition, setting the camera on the ground disturbs canopy architecture and may also bias the spatial sampling since it is not possible to set the camera at the position of the row. Finally, the area sampled by the camera looking upward from the bottom of the canopy is lower than in the case of fIPAR(DHP$_{down}$): the distance between the camera and the top of the canopy (upward looking DHP) is shorter than the distance from the camera to the ground (downward looking DHP). This explains why significant scattering of data is observed between fIPAR(DHP$_{up}$) and fAPAR$_T$(AccuPAR). It is therefore recommended to use a very small camera and to improve the spatial sampling by taking more images. Nevertheless, fIPAR(DHP$_{up}$) should be used mostly for relatively high and sparse canopies such as maize crops to limit both the disturbances when taking the pictures and

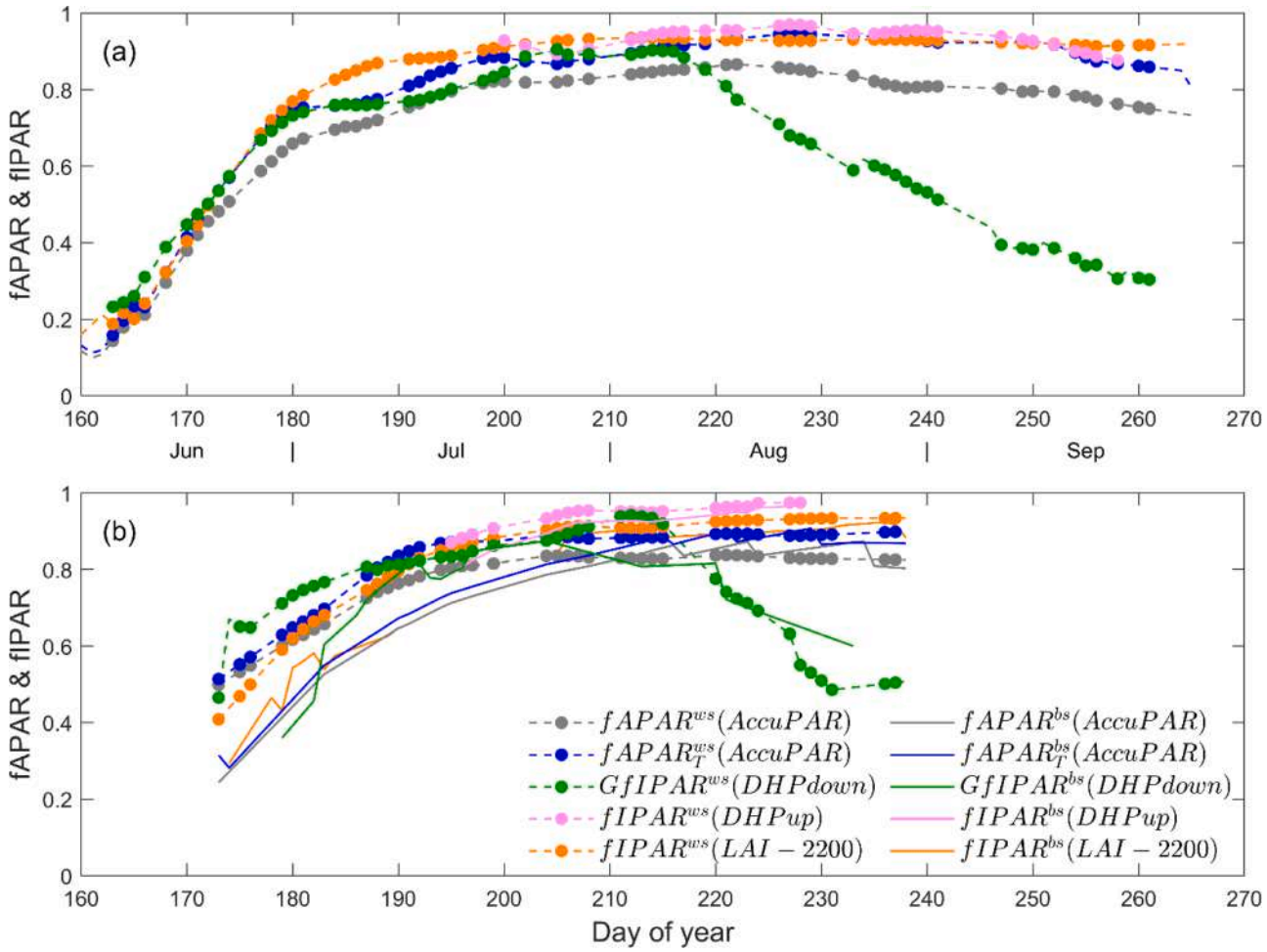

Fig. 5. Seasonal variation of fAPAR and fIPAR in 2012 (a) and 2013 (b). The solid and dashed lines represent the black-sky (with superscript 'bs') and white-sky (with superscript 'ws') conditions, respectively. In 2012, only white-sky conditions are presented.

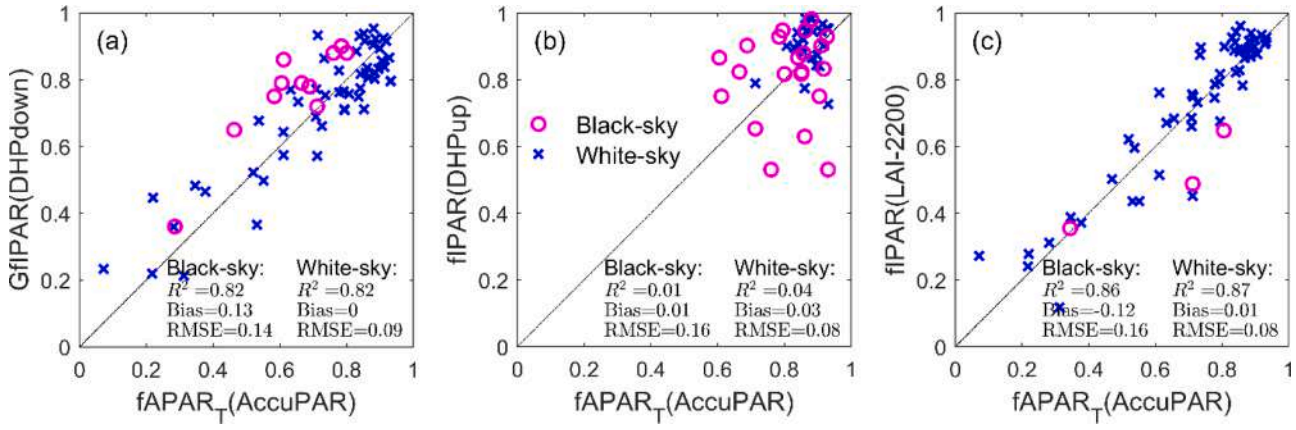

Fig. 6. Comparison between $fAPAR_T$(AccuPAR) used as a reference and GfIPAR(DHP_{down}), fIPAR(DHP_{up}) and fIPAR(LAI-2200). Data from the first period (before DOY 210) when no senescent elements are present. Black-sky (pink circles) and white-sky illumination conditions (blue crosses) are presented.

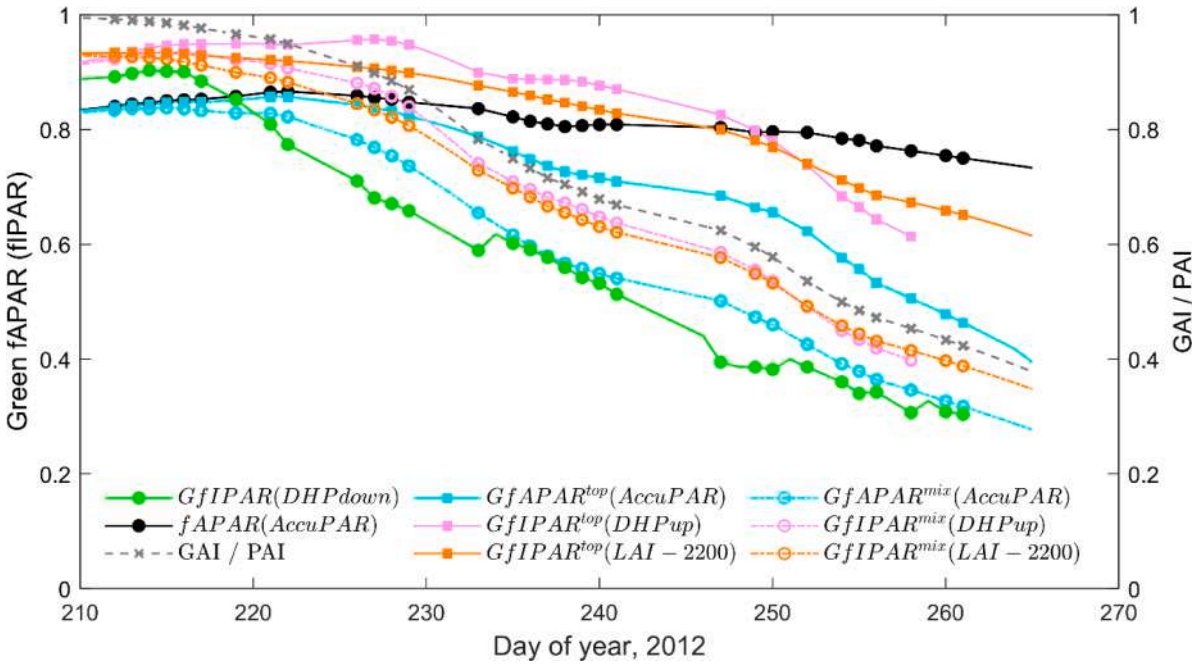

Fig. 7. Seasonal variation of fAPAR and fIPAR quantities considered in Table 1 during the senescent stage (after DOY 210). GAI/PAI is the ratio of GAI to PAI (right y-axis). All measurements were performed under white-sky illuminations in 2012.

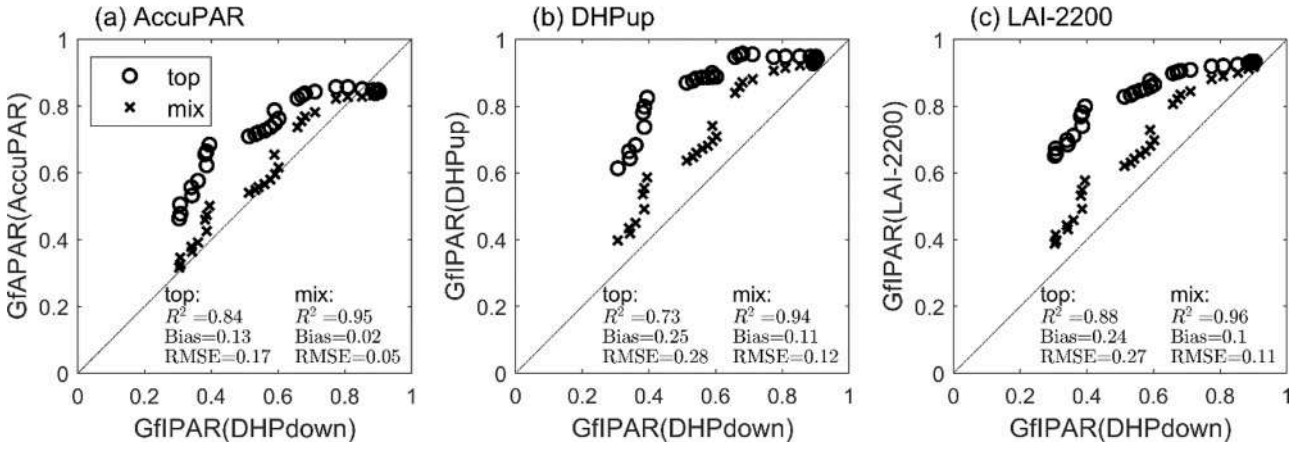

Fig. 8. After DOY 210 (senescence), from left to right: comparison of GfAPAR derived from AccuPAR, GfIPAR by upward DHP and LAI-2200 with the GfIPAR from downward DHP used as a reference. "top" and "mix" refers to the assumptions used to derive the green fAPAR, e.g. the senescence is occurring from the top of the canopy (Chen, 1996) or is randomly distributed within the canopy (Viña and Gitelson, 2005).

the parts not sampled at the bottom of the canopy because of the height of the lens above the ground.

The small discrepancies observed between both quantities demonstrate that the spatial sampling was sufficient for LAI-2200 (8 points per ESU), although more limited than that of the AccuPAR (4 readings of the 80 PAR sensors set along the 1m probe). Under black-sky conditions, only three matching pairs were available because the LAI-2200 was only performed under cloudy conditions and the large sun zenith angles prevent the black-sky $fIPAR^{bs}$(LAI-2200) calculations.

Among the three methods investigated (DHP_{down}, DHP_{up} and LAI2200), DHP_{down} shows obvious advantages: it provides a good agreement with $fAPAR_T$, while not disturbing canopy architecture since the camera is placed above the canopy. However, in the case of deriving black-sky fIPAR values, more samples should be taken to compensate the small footprint of the camera in the sun direction. Further, great care should be taken when segmenting the image which is more difficult and uncertain for dense canopies and sunny illumination conditions (Garrigues et al., 2008). Indeed, more advanced classification method is necessary to improve the DHP data processing (Duveiller and Defourny, 2010; Jonckheere et al., 2017).

4.3. Impacts of illumination conditions on fAPAR and fIPAR estimations

fAPAR and fIPAR present diurnal variations due to variations of the solar zenith angle and the proportion of diffuse PAR in the total downwelling radiation. These variations have a significant impact on the photosynthetic efficiency and on the canopy light regime (Aikman, 1989; Grant, 1999; Wang et al., 2006). We therefore compared the ability of instruments to retrieve the black-sky and white-sky fAPAR components. Our results show that instantaneous fAPAR and fIPAR under white-sky conditions are slightly higher than under black-sky conditions, which is consistent with previous results based on both model simulation and ground measurements (Li and Fang, 2015; Nouvellon, 2000; Thomas et al., 2006). The resulting daily integrated fAPAR

can be more or less affected depending on the variation of the diffuse PAR fraction throughout the day. Therefore, except for AccuPAR, accurate daily fAPAR estimation requires auxiliary measurements of the PAR diffuse fraction or specific development such as proposed by Hanan and Bégué (1995) for LAI-2200.

4.4. Estimations of green fAPAR and fIPAR during the senescence period

During the senescence period, both green and senescent elements contribute to fAPAR at the canopy level (Asner et al., 1998; Di Bella et al., 2004; Huemmrich et al., 2005; Rahman et al., 2019). Since only the green components are used for photosynthesis and transpiration, the green fAPAR should be the quantity to be considered. Downward DHP is the only method that provides a direct estimate of green fIPAR because it minimizes problems due to senescent elements generally located at the bottom of the canopy (Baret et al., 2010). Green fIPAR from downward DHP is therefore used as the reference method. Conversely, the green fAPAR cannot be directly measured by the other methods since the instruments are looking from the bottom of the canopy and green and non-green components cannot be easily distinguished. We evaluated two methods to derive green fAPAR or green fIPAR from canopy fAPAR and fIPAR measured quantities using the GAI/PAI ratio, based on different assumptions on the spatial distribution of green and non-green elements. In paddy rice crops, the senescence happens right after the ear appearance, and is observed at leaf tips and at the bottom of the canopy. The ears, distributed mainly at the top layer and mixed with green leaves, become yellow and brown, and the senescent leaves at the bottom layer grow upward and mix with other green stems and leaves. This behavior is thus closer to the random mixing hypothesis of Viña and Gitelson (2005) than to the Chen (1996) assumption that green elements are concentrated in the top layer. However, these two correction methods developed to get the green fAPAR or fIPAR from the canopy fAPAR or fIPAR requires the measurement of the GAI/PAI ratio during the senescence period.

5. Conclusion

The main objective of this study was to compare several methods and instruments for fAPAR or fIPAR estimates over paddy rice and investigate the impact of canopy senescence under different illumination conditions. Results showed that using only canopy transmittance ($fAPAR_T$(AccuPAR)) measured by AccuPAR provides a good proxy of the four-stream reference fAPAR(AccuPAR). This allows to simplify the AccuPAR measurements over paddy rice fields while keeping a high degree of accuracy.

Canopy transmittance can also be measured using DHP looking upward or downward and LAI-2200, resulting respectively into fIPAR (DHP_{up}), GfIPAR(DHP_{down}) and fIPAR(LAI2200). Our results demonstrated that fIPAR(DHP_{up}) was leading to uncertainties mostly because of the dimensions of the camera used, disturbing canopy architecture when placed at the bottom of the crop and missing also a significant fraction of the vegetation elements located below the lens of the camera. For these reasons, downward looking DHP (GfIPAR(DHP_{down})), AccuPAR ($fAPAR_T$(AccuPAR)) and LAI-2200 (fIPAR(LAI-2200)) are better suited for rice crops that are dense and relatively short. However, the spatial sampling should be adapted to the actual footprint of each instrument. Three AccuPAR, four LAI-2200 or 15 to 20 DHPs seems sufficient to get precise estimates of white-sky fAPAR or fIPAR over an area of $\approx 100 m^2$ of homogeneous rice crops. This minimum sampling appears also sufficient under black-sky conditions, except for DHPs for which the footprint is very small in the sun direction. To avoid taking more images in order to improve the area sampled, it is advised to integrate canopy transmittance over all the compass directions as done for LAI-2200. Nevertheless, the daily integrated green fAPAR and fIPAR are required in many vegetation functional models (Baret and Guyot, 1991; Gower et al., 1999; Weiss et al., 2007). The daily integrated fAPAR and fIPAR values can be derived from the DHP images, which will also result in a much larger area sampled. Note that DHPs appear the best suited method to estimate daily variation and daily integrated values of fIPAR since a single image taken during the day allows to derive canopy transmittance for all possible incoming light directions, assuming that canopy architecture keeps stable during the day. This assumption seems reasonable for rice crops, but not realistic for heliotropic species and species presenting leaf rolling reaction to water stresses (Baret et al., 2018).

Downward looking DHPs is the only method that measures directly GfIPAR, the fraction of incoming light intercepted by the green photosynthetically active parts of the vegetation. This offers a great advantage over the other instruments when a significant part of the organs are senescing as observed over rice crops after flowering. AccuPAR and LAI-2200 are measuring canopy transmittance from the bottom of the canopy and are not able to distinguish between the green and non-green parts. Corrections are proposed for these instruments, based on independent measurement of the GAI/PAI ratio. Measuring the GAI/PAI ratio is generally done by destructive methods, which is laborious, time consuming, and not well suited for crop monitoring. Further, the corrections need assumptions on the vertical distribution of the senescing parts. For rice crops, we demonstrated that the method proposed by Viña and Gitelson (2005), assuming that green and non-green elements are well mixed, provides the best agreement with GfIPAR(DHP_{down}) considered as the reference method.

Downward looking DHPs appears thus to be the best method to estimate GfIPAR under relatively short canopies. It is currently used intensively over a number of crops (Camacho et al., 2013; Li et al., 2015; Weiss et al., 2007). For taller canopies that prevents easy characterization from the top, $fAPAR_T$(AccuPAR), fIPAR(DHPup) and fIPAR (LAI-2200) should be preferred. Exploitation of DHPs requires images with good resolution and acquired under favorable illumination conditions. As a matter of facts, sunny conditions are not ideal since the distinction between green and non-green parts (background and senescent elements) is difficult in the shadows because of the small dynamics of the pixel values as well as in the specularly reflected areas where colors are lost. Using HDR (High Dynamic Range) features and applying a gamma factor should partly solve the problem. Nevertheless, image segmentation to identify the green pixels is still not fully automatic which is the main limitation of the DHP downward looking method as compared to AccuPAR and LAI-2200. Additional work is therefore required to develop algorithms capable of identifying automatically the green pixels in the images with a high degree of accuracy.

Declaration of Competing Interest

The authors declare that they have no known competing financial interests or personal relationships that could have appeared to influence the work reported in this paper.

Acknowledgements

This study was supported by the National Natural Science Foundation of China (41171333, H.F.). We would like to thank the local farmers for allowing us to take experiment on their fields and the students who helped in the field campaigns in 2012 and 2013. We also would like to thank Dr. Chongya Jiang and Dr. Tao Sun in the preparation of field measurements. Anonymous reviewers are thanked for valuable comments.

Appendix A. Rice field pictures during growing season

Fig. A1

Fig. A1. Rice field pictures of Plot B from end of July to September, 2012.

References

Aikman, D.P., 1989. Potential Increase in Photosynthetic Efficiency from the Redistribution of Solar Radiation in a Crop. J Exp Bot 40, 855–864. https://doi.org/10.1093/jxb/40.8.855.

Asner, G.P., Wessman, C.A., Archer, S., 1998. Scale Dependence of Absorption of Photosynthetically Active Radiation in Terrestrial Ecosystems. Ecological Applications 8, 1003–1021.

Baret, F., Andrieu, B., Steven, M., 1993. Gap frequency and canopy architecture of sugar beet and wheat crops. Agricultural and Forest Meteorology 65, 261–279. https://doi.org/10.1016/0168-1923(93)90008-6.

Baret, F., de Solan, B., Lopez-Lozano, R., Ma, K., Weiss, M., 2010. GAI estimates of row crops from downward looking digital photos taken perpendicular to rows at 57.5° zenith angle: Theoretical considerations based on 3D architecture models and application to wheat crops. Agricultural and Forest Meteorology 150, 1393–1401. https://doi.org/10.1016/j.agrformet.2010.04.011.

Baret, F., Guyot, G., 1991. Potentials and limits of vegetation indices for LAI and APAR assessment. Remote Sensing of Environment 35, 161–173. https://doi.org/10.1016/0034-4257(91)90009-U.

Baret, F., Madec, S., Irfan, K., Lopez, J., Comar, A., Hemmerlé, M., Dutartre, D., Praud, S., Tixier, M.H., 2018. Leaf-rolling in maize crops: from leaf scoring to canopy-level measurements for phenotyping. Journal of Experimental Botany 69, 2705–2716. https://doi.org/10.1093/jxb/ery071.

Camacho, F., Cernicharo, J., Lacaze, R., Baret, F., Weiss, M., 2013. GEOV1: LAI, FAPAR essential climate variables and FCOVER global time series capitalizing over existing products. Part 2: Validation and intercomparison with reference products. Remote Sensing of Environment 137, 310–329. https://doi.org/10.1016/j.rse.2013.02.030.

Campos, I., Neale, C.M.U., Calera, A., 2017. Is row orientation a determinant factor for radiation interception in row vineyards?: Row direction influences light capture in vineyard. Australian Journal of Grape and Wine Research 23, 77–86. https://doi.org/10.1111/ajgw.12246.

Chen, J., 1996. Canopy Architecture and Remote Sensing of the Fraction of Photosynthetically Active Radiation Absorbed by Boreal Conifer Forests. IEEE Transactions on Geoscience and Remote Sensing 34, 1353–1368.

Cohen, S., Rao, R.S., Cohen, Y., 1997. Canopy transmittance inversion using a line quantum probe for a row crop. Agricultural and Forest Meteorology 86, 225–234.

Decagon Devices, 2010. AccuPAR PAR/LAI ceptometer model LP-80 Operator's Manual Version 10 [WWW Document]. URL http://www.cen.ulaval.ca/nordicanad/donnees/n_45561/v582105/file/supp/Decagon_Accupar_LP80_Web.pdf.

Demarez, V., Duthoit, S., Baret, F., Weiss, M., Dedieu, G., 2008. Estimation of leaf area and clumping indexes of crops with hemispherical photographs. Agricultural and Forest Meteorology 148, 644–655. https://doi.org/10.1016/j.agrformet.2007.11.015.

Di Bella, C.M., Paruelo, J.M., Becerra, J.E., Bacour, C., Baret, F., 2004. Effect of senescent leaves on NDVI-based estimates of *f* APAR: Experimental and modelling evidences. International Journal of Remote Sensing 25, 5415–5427. https://doi.org/10.1080/01431160412331269724.

Duveiller, G., Defourny, P., 2010. Batch processing of hemispherical photography using object-based image analysis to derive canopy biophysical variables. Presented at the GEOBIA 2010-Geographic Object-Based Image Analysis. Ghent University, Ghent, Belgium, p. 5.

Eklundh, L., Jin, H., Schubert, P., Guzinski, R., Heliasz, M., 2011. An Optical Sensor Network for Vegetation Phenology Monitoring and Satellite Data Calibration. Sensors 11, 7678–7709. https://doi.org/10.3390/s110807678.

Fang, H., Li, W., Wei, S., Jiang, C., 2014a. Seasonal variation of leaf area index (LAI) over paddy rice fields in NE China: Intercomparison of destructive sampling, LAI-2200, digital hemispherical photography (DHP), and AccuPAR methods. Agricultural and Forest Meteorology 198–199, 126–141. https://doi.org/10.1016/j.agrformet.2014.08.005.

Fang, H., Li, W., Wei, S., Sun, T., Jiang, C., 2014b. Paddy Rice Experiment in the Sanjiang Plain (PRESP) Field Measurement Report. Institute of Geographic Sciences and Natural Resources Research. Chinese Academy of Sciences, Beijing, China.

Fang, H., Ye, Y., Liu, W., Wei, S., Ma, L., 2018. Continuous estimation of canopy leaf area index (LAI) and clumping index over broadleaf crop fields: An investigation of the PASTIS-57 instrument and smartphone applications. Agricultural and Forest Meteorology 253–254, 48–61. https://doi.org/10.1016/j.agrformet.2018.02.003.

Fensholt, R., Sandholt, I., Rasmussen, M.S., 2004. Evaluation of MODIS LAI, fAPAR and the relation between fAPAR and NDVI in a semi-arid environment using in situ measurements. Remote Sensing of Environment 91, 490–507. https://doi.org/10.1016/j.rse.2004.04.009.

Gallo, K.P., Daughtry, C.S.T., 1986. Techniques for Measuring Intercepted and Absorbed Photosynthetically Active Radiation in Corn Canopies [1]. Agron. J. 78, 752–756. https://doi.org/10.2134/agronj1986.00021962007800040039x.

Garrigues, S., Shabanov, N.V., Swanson, K., Morisette, J.T., Baret, F., Myneni, R.B., 2008. Intercomparison and sensitivity analysis of Leaf Area Index retrievals from LAI-2000, AccuPAR, and digital hemispherical photography over croplands. Agricultural and Forest Meteorology 148, 1193–1209. https://doi.org/10.1016/j.agrformet.2008.02.014.

GCOS, 2016. The Global Observing System for Climate: Implementation Needs (GCOS-200). World Meteorological Organization.

Gobron, N., Pinty, B., Aussedat, O., Chen, J.M., Cohen, W.B., Fensholt, R., Gond, V., Huemmrich, K.F., Lavergne, T., Mélin, F., Privette, J.L., Sandholt, I., Taberner, M., Turner, D.P., Verstraete, M.M., Widlowski, J.-L., 2006. Evaluation of fraction of absorbed photosynthetically active radiation products for different canopy radiation transfer regimes: Methodology and results using Joint Research Center products derived from SeaWiFS against ground-based estimations. J. Geophys. Res. 111, D13110. https://doi.org/10.1029/2005JD006511.

Goward, S.N., Huemmrich, K.E., 1992. Vegetation Canopy PAR Absorptance and the Normalized Difference Vegetation Index: An Assessment Using the SAIL Model. Remote Sensing of Environment 39, 119–140.

Gower, S.T., Kucharik, C.J., Norman, J.M., 1999. Direct and Indirect Estimation of Leaf Area Index, fAPAR, and Net Primary Production of Terrestrial Ecosystems. Remote Sensing of Environment 70, 29–51. https://doi.org/10.1016/S0034-4257(99)00056-5.

Grant, R.H., 1999. Ultraviolet-B and photosynthetically active radiation environment of inclined leaf surfaces in a maize canopy and implications for modeling. Agricultural and Forest Meteorology 95, 187–201. https://doi.org/10.1016/S0168-1923(99)00023-4.

Gu, L., Baldocchi, D., Verma, S.B., Black, T.A., Vesala, T., Falge, E.M., Dowty, P.R., 2002. Advantages of diffuse radiation for terrestrial ecosystem productivity: advantages of diffuse radiation. J. Geophys. Res. 107 https://doi.org/10.1029/2001JD001242. ACL 2-1-ACL 2-23.

Hanan, N.P., Bégué, A., 1995. A method to estimate instantaneous and daily intercepted photosynthetically active radiation using a hemispherical sensor. Agricultural and Forest Meteorology 74, 155–168. https://doi.org/10.1016/0168-1923(94)02196-Q.

Huemmrich, K.F., Privette, J.L., Mukelabai, M., Myneni, R.B., Knyazikhin, Y., 2005. Time-series validation of MODIS land biophysical products in a Kalahari woodland. Africa. International Journal of Remote Sensing 26, 4381–4398. https://doi.org/10.1080/01431160500113393.

Jonckheere, I.G.C., Macfarlane, C., Walter, J.-M.N., 2017. Image Analysis of Hemispherical Photographs, Algorithms and Calculations. Hemispherical Photography in Forest Science: Theory, Methods, Applications. Springer, Netherlands, Dordrecht, pp. 115–151.

Jongschaap, R.E.E., Dueck, T.A., Marissen, N., Hemming, S., Marcelis, L.F.M., 2006. Simulating seasonal patterns of increased greenhouse crop production by conversion of direct radiation into diffuse radiation. Acta Hortic. 315–322. https://doi.org/10.17660/ActaHortic.2006.718.36.

Kobayashi, H., Ryu, Y., Baldocchi, D.D., Welles, J.M., Norman, J.M., 2013. On the correct estimation of gap fraction: How to remove scattered radiation in gap fraction measurements? Agricultural and Forest Meteorology 174–175, 170–183. https://doi.org/10.1016/j.agrformet.2013.02.013.

Kukal, M.S., Irmak, S., 2020. Light interactions, use and efficiency in row crop canopies under optimal growth conditions. Agricultural and Forest Meteorology 284, 107887. https://doi.org/10.1016/j.agrformet.2019.107887.

Leblanc, S.G., Chen, J.M., 2001. A practical scheme for correcting multiple scattering effects on optical LAI measurements. Agricultural and Forest Meteorology 15.

Leblanc, S.G., Chen, J.M., Fernandes, R., Deering, D.W., Conley, A., 2005. Methodology comparison for canopy structure parameters extraction from digital hemispherical photography in boreal forests. Agricultural and Forest Meteorology 129, 187–207. https://doi.org/10.1016/j.agrformet.2004.09.006.

Li, W., Fang, H., 2015. Estimation of direct, diffuse, and total FPARs from Landsat surface reflectance data and ground-based estimates over six FLUXNET sites: Landsat direct, diffuse and total FPARs. J. Geophys. Res. Biogeosci. 120, 96–112. https://doi.org/10.1002/2014JG002754.

Li, W., Weiss, M., Waldner, F., Defourny, P., Demarez, V., Morin, D., Hagolle, O., Baret, F., 2015. A generic algorithm to estimate LAI, FAPAR and FCOVER variables from SPOT4_HRVIR and Landsat sensors: Evaluation of the consistency and comparison with ground measurements. Remote Sensing 7, 15494–15516.

Lizaso, J.I., Batchelor, W.D., Boote, K.J., Westgate, M.E., Rochette, P., Moreno-Sotomayor, A., 2005. Evaluating a Leaf-Level Canopy Assimilation Model Linked to CERES-Maize. Agron. J. 97, 734–740. https://doi.org/10.2134/agronj2004.0172.

Martonchik, J.V., Bruegge, C.J., Strahler, A.H., 2000. A review of reflectance nomenclature used in remote sensing. Remote Sensing Reviews 19, 9–20. https://doi.org/10.1080/02757250009532407.

McCallum, I., Wagner, W., Schmullius, C., Shvidenko, A., Obersteiner, M., Fritz, S., Nilsson, S., 2010. Comparison of four global FAPAR datasets over Northern Eurasia for the year 2000. Remote Sensing of Environment 114, 941–949. https://doi.org/10.1016/j.rse.2009.12.009.

Monteith, J.L., 2015. Light Interception and Radiative Exchange in Crop Stands. In: Eastin, J.D., Haskins, F.A., Sullivan, C.Y., van Bavel, C.H.M. (Eds.), Physiological Aspects of Crop Yield. American Society of Agronomy. Crop Science Society of America, Madison, WI, USA, pp. 89–111. https://doi.org/10.2135/1969.physiologicalaspects.c9.

Nilson, T., 1971. A theoretical analysis of the frequency of gaps in plant stands. Agricultural Meteorology 8, 25–38. https://doi.org/10.1016/0002-1571(71)90092-6.

Nouvellon, Y., 2000. PAR extinction in shortgrass ecosystems: effects of clumping, sky conditions and soil albedo. Agricultural and Forest Meteorology 105, 21–41. https://doi.org/10.1016/S0168-1923(00)00194-5.

Pinter, P.J., 1993. Solar angle independence in the relationship between absorbed PAR and remotely sensed data for alfalfa. Remote Sensing of Environment 46, 19–25. https://doi.org/10.1016/0034-4257(93)90029-W.

Rahman, M.M., Lamb, D.W., Samborski, S.M., 2019. Reducing the influence of solar illumination angle when using active optical sensor derived NDVIAOS to infer fAPAR for spring wheat (Triticum aestivum L.). Computers and Electronics in Agriculture 156, 1–9. https://doi.org/10.1016/j.compag.2018.11.007.

Rahman, M.M., Lamb, D.W., Stanley, J.N., 2015. The impact of solar illumination angle when using active optical sensing of NDVI to infer fAPAR in a pasture canopy. Agricultural and Forest Meteorology 202, 39–43. https://doi.org/10.1016/j.agrformet.2014.12.001.

Senna, M.C.A., 2005. Fraction of photosynthetically active radiation absorbed by Amazon tropical forest: A comparison of field measurements, modeling, and remote sensing. J. Geophys. Res. 110, G01008. https://doi.org/10.1029/2004JG000005.

Steinberg, D.C., Goetz, S.J., Hyer, E.J., 2006. Validation of MODIS F/sub PAR/ products in boreal forests of Alaska. IEEE Trans. Geosci. Remote Sensing 44, 1818–1828. https://doi.org/10.1109/TGRS.2005.862266.

Thomas, V., Finch, D.A., McCaughey, J.H., Noland, T., Rich, L., Treitz, P., 2006. Spatial modelling of the fraction of photosynthetically active radiation absorbed by a boreal mixedwood forest using a lidar–hyperspectral approach. Agricultural and Forest Meteorology 140, 287–307. https://doi.org/10.1016/j.agrformet.2006.04.008.

Timlin, D.J., Fleisher, D.H., Kemanian, A.R., Reddy, V.R., 2014. Plant Density and Leaf Area Index Effects on the Distribution of Light Transmittance to the Soil Surface in Maize. Agronomy Journal 106, 1828–1837. https://doi.org/10.2134/agronj14.0160.

Viña, A., Gitelson, A.A., 2005. New developments in the remote estimation of the fraction of absorbed photosynthetically active radiation in crops: REMOTE ESTIMATION OF FAPAR IN CROPS. Geophys. Res. Lett. 32 https://doi.org/10.1029/2005GL023647.

Wang, Xiping, Guo, Y., Li, B., Wang, Xiyong, Ma, Y., 2006. Evaluating a three dimensional model of diffuse photosynthetically active radiation in maize canopies. Int J Biometeorol 50, 349–357. https://doi.org/10.1007/s00484-006-0032-0.

Weiss, M., Baret, F., 2010. CAN-EYE V6.1 user manual [WWW Document]. URL https://www6.paca.inrae.fr/can-eye.

Weiss, M., Baret, F., Garrigues, S., Lacaze, R., 2007. LAI and fAPAR CYCLOPES global products derived from VEGETATION. Part 2: validation and comparison with MODIS collection 4 products. Remote Sensing of Environment 110, 317–331. https://doi.org/10.1016/j.rse.2007.03.001.

Weiss, M., Baret, F., Li, W., Fang, H., 2018. Differences in FAPAR definitions for the validation of satellite products against ground measurements. In: Presented at the Workshop on Land Product Validation and Evolution.

Widlowski, J.-L., 2010. On the bias of instantaneous FAPAR estimates in open-canopy forests. Agricultural and Forest Meteorology 150, 1501–1522. https://doi.org/10.1016/j.agrformet.2010.07.011.

Xiao, X., 2004. Modeling gross primary production of temperate deciduous broadleaf forest using satellite images and climate data. Remote Sensing of Environment 91, 256–270. https://doi.org/10.1016/j.rse.2004.03.010.

Ye, M., Cao, Z., Yu, Z., Bai, X., 2015. Crop feature extraction from images with probabilistic superpixel Markov random field. Computers and Electronics in Agriculture 114, 247–260. https://doi.org/10.1016/j.compag.2015.04.010.

Zhang, Q., Xiao, X., Braswell, B., Linder, E., Baret, F., Mooreiii, B., 2005. Estimating light absorption by chlorophyll, leaf and canopy in a deciduous broadleaf forest using MODIS data and a radiative transfer model. Remote Sensing of Environment 99, 357–371. https://doi.org/10.1016/j.rse.2005.09.009.

Zhao, L., Liu, Z., Xu, S., He, X., Ni, Z., Zhao, H., Ren, S., 2018. Retrieving the Diurnal FPAR of a Maize Canopy from the Jointing Stage to the Tasseling Stage with Vegetation Indices under Different Water Stresses and Light Conditions. Sensors 18, 3965. https://doi.org/10.3390/s18113965.

Zhong, W.W., Liu, J.Q., Zhou, X.B., Chen, Y.H., Bi, J.J., 2015. Row spacing and irrigation effect on radiation use efficiency of winter wheat. J. Anim. Plant Sci. 25, 448–455.

Remote Sensing of Environment 259 (2021) 112433

Contents lists available at ScienceDirect

Remote Sensing of Environment

journal homepage: www.elsevier.com/locate/rse

Impact of the reproductive organs on crop BRDF as observed from a UAV

Wenjuan Li [a,b,1,*], Jingyi Jiang [a,d,1], Marie Weiss [a], Simon Madec [a], Franck Tison [a], Burger Philippe [c], Alexis Comar [b], Frédéric Baret [a]

[a] INRAE, Avignon Université, UMR EMMAH, F-84000 Avignon, France
[b] HIPHEN, F-84000 Avignon, France
[c] INRAE, UMR AGIR, Toulouse, France
[d] Research Center of Forest Management Engineering of State Forestry and Grassland Administration, Beijing Forestry University, 100083 Beijing, China

ARTICLE INFO

Editor: Jing M. Chen

Keywords:
BRDF
Wheat
Maize
Sunflower
Reproductive organs
UAV
Row effect

ABSTRACT

Several crops bear reproductive organs (RO) at the top of the canopy after the flowering stage, such as ears for wheat, tassels for maize, and heads for sunflowers. RO present specific architecture and optical properties as compared to leaves and stems, which may impact canopy reflectance. This study aims to understand and quantify the influence of RO on the bi-directional variation of canopy reflectance and NDVI.

Multispectral camera observations from a UAV were completed over wheat, maize, and sunflower just after flowering when the RO are fully developed and the leaf layer with only marginal senescence. The flights were designed to sample the BRDF with view zenith angles spanning from nadir to 60°and many compass directions. Three flights corresponding to three sun positions were completed under clear sly conditions. The camera was always pointing to two adjacent plots of few tenths of square meters: the RO were manually removed on one plot, while the other plot was kept undisturbed.

Results showed that the three visible bands (450 nm, 570 nm, 675 nm), and in a lesser way the red edge band (730 nm) were strongly correlated. We, therefore, focused on the 675 nm and 850 nm bands. The Bi-Directional Reflectance (BRF) of the canopy without RO shows that the BRF values were almost symmetrical across the principal plane, even for maize and sunflower canopies with a strong row structure. Examination of the BRF difference between the canopy with and without RO indicate that the RO impact canopy BRDF for the three crops. The magnitude of the impacts depends on crop, wavelength and observational geometry. These observations are generally consistent with realistic 3D reflectance simulations. However, some discrepancies were noticed, mainly explained by the small magnitude of the RO effect on canopy BRF, and the approximations made when simulating the RO layer and its coupling with the bottom canopy layer. We finally demonstrated that the RO layer impact the estimates of canopy traits such as GAI as derived from the multispectral observations.

1. Introduction

Continuous monitoring of crop growth is required for many applications including the evaluation of available resources, precision agriculture (McBRATNEY et al., 2005), and plant phenotyping (Comar et al., 2012). Remote sensing from satellites, planes, or UAVs (Unmanned Aerial Vehicles) are well-suited to describe the crop dynamics from reflectance acquired in several spectral bands. The interpretation of the data in terms of structural and biochemical properties is usually achieved using two main approaches: (1) an empirical approach, based on a set of experiments where both reflectance and canopy characteristics are concurrently measured; (2) a physically based approach using radiative transfer model simulations. For both approaches, assumptions on canopy structure are required to improve the accuracy of canopy characteristics estimates. In the case of the empirical approach, knowledge of the species observed and on the developmental stage may improve the retrieval performances. Similarly, in the case of the physically-based approach, knowledge on the expected range of canopy structure and associated optical properties of the elements may significantly improve the estimates.

Apart from the canopy structure differences between species, major differences are experienced along the growth cycle because of the

* Correspondig author at: HIPHEN, F-84000 Avignon, France
E-mail addresses: wli@hiphen-plant.com, wenjuan.li122@gmail.com (W. Li).
[1] These authors contributed equally.

https://doi.org/10.1016/j.rse.2021.112433
Received 9 September 2020; Received in revised form 17 February 2021; Accepted 1 April 2021

appearance of the reproductive organs (RO). RO have structural and optical properties very different from those of the leaves: they are generally thicker than leaves with lower contents in chlorophyll and sometimes elements with specific colors such as petals. These differences are expected to impact the radiative transfer in the canopy significantly since the RO are often located at the top of the canopy to ease pollen and seed dissemination either by the insects, birds, or by the wind. However, only a few studies document the impact of RO on canopy reflectance. Cossani and Reynolds (2012) reported that wheat ears intercept up to 40% of the incident radiation around the flowering stage. Li et al. (2015) show that removing the ear layer at the flowering stage reduces normalized difference vegetation index (NDVI) values by up to 7% in relative values. This explains why Weiss et al. (2001) included explicitly an ear layer to describe the wheat canopy structure and simulate crop reflectance along the growth cycle. Gitelson (2003) and Viña et al. (2004) showed that the presence of the tassels at the top of maize canopies induced a significant decrease of the VARI index. Wanjura and Hatfield (1988) investigated variations in canopy reflectance of sorghum, cotton, and sunflower crops during the growth cycle using the scattering and absorption coefficients. However, they were not able to draw clear conclusions on the impact of sorghum panicles and sunflower heads on canopy reflectance for the Landsat TM bands. More detailed investigations are thus required to better quantify the role of RO on canopy reflectance.

Canopy reflectance depends on the observational configuration. Therefore, the impact of RO on canopy reflectance should be investigated for the possible view and illumination directions under which crops are usually observed from various remote sensing platforms. Few studies report detailed measurements of the Bidirectional Reflectance Distribution Function (BRDF) (Nicodemus et al., 1977; Schaepman-Strub et al., 2006) for crops under field conditions. Goniometers have been used in the lab and in the field to characterize the BRDF (Sandmeier and Itten, 1999). However, their use is tedious and time-consuming, while generally corresponding to a very small footprint, questioning its suitability for characterizing the BRDF of tall crops such as maize and sunflower. Alternative airborne instruments such as the Parabola (Deering and Leone, 1986) and Airborne POLDER (Jacob et al., 2002) have been used to measure the BRDF of a range of canopies. They require specific flight design to sample the BRDF over a given target. The recent development of UAVs allows now to easily document the surface BRDF. Different sampling schemes have been used depending on the camera field of view. For a camera equipped with a wide field of view, the UAV is either moving along different tracks to sample the same target from several positions and directions (Hakala et al., 2013) or tilting the camera from about half the total field of view and keeping the UAV at about the same position while rotating in the compass direction (Roosjen et al., 2016). This later technique assumes that the surface is sufficiently homogenous to build the BRDF from points located at different places in the scene. For the small field of view cameras, the UAV is moving around the target while the orientation in view zenith and azimuth is changed continuously to keep the camera pointing towards the target (Burkart et al., 2015; Burkart et al., 2014; Grenzdörffer and Niemeyer, 2012). UAVs appear thus very convenient to document the surface BRDF.

Crop 3D modeling offers an efficient way to generate realistic canopies and simulate the associated reflectance for a range of source and view directions (España et al., 1999). Several open-source 3D ray tracing render engines were developed concurrently for computer graphics applications, such as LuxCoreRender (LuxCoreRender, 2018), MITSUBA (Jacob, 2014), and Pov-ray (POV-team, 2013). They have been successfully used by the remote sensing community to simulate canopy reflectance for a range of vegetation types (Casa and Jones, 2005; Disney et al., 2006; Duthoit et al., 2008; España et al., 1999; Génard et al., 2000; Jiang et al., 2020; Lopez-Lozano et al., 2009). However, most studies focus on crops before the reproductive stage: very few authors have included RO in their simulations due to the complexity of their morphology, topology, and optical properties.

The objective of this study is to quantify the influence of the RO on canopy BRDF in the visible and near-infrared (NIR) spectral domains. We present a new experimental design to measure canopy BRDF using a multispectral camera onboard an UAV. This allowed evaluating the influence of reproductive organs on the spectral and directional behavior of canopy reflectance. Three main crops are studied, with very different RO at the top of the canopy layer: wheat, maize, and sunflower. Field experiments were conducted for the three species during the reproductive stage to compare the BRDF measured from a UAV between the canopy with and without the RO. These measurements are complemented by reflectance simulations over 3D virtual scenes to better understand and quantify the impact of RO.

2. Materials and methods

2.1. Experimental sites and crops sampled

The wheat, maize, and sunflower experiments were located in Avignon, France (43.9°N, 4.9°E). The study focused on fully developed crops soon after the flowering stage, when the final height was reached and all leaves were fully developed with only a little senescence appearing at the bottom of the canopy. The wheat (*ISILDUR*) ears were mostly green and bearing awns, the tassels of maize (*Zea mays*) were light yellow. The heads of the sunflower (*MAS 88 OL*) were bearing yellow petals, the flower heads mostly facing the soil. Its back was green, and well seen from the top of the canopy. Note that the rows were oriented East-West for the three experiments (Table 1).

The sites were selected in a 20 × 20 m homogeneous area of the field. Two micro plots of at least 5 × 5 m^2 area were considered, one with the RO manually removed (RO-), the other (RO+) being undisturbed (Fig. 1). A 0.6 × 0.6 m^2 reference panel was placed horizontally slightly higher than the surrounding canopy to avoid possible interactions with the crops and between the two micro plots (Fig. 1). Four circular gray panels of 60 cm diameter were additionally placed on the four corners of the 20 × 20 m^2 site (Fig. 1) to be used as ground control points (GCP) for accurate projection of the images taken from the UAV. The coordinates of the center of the two reference panels and the four GCPs were measured with an RTK GPS (Trimble Geo 7 ×, 2 cm precision).

2.2. UAV experiment for BRDF characterization

A hexacopter UAV designed by Atechsys (http://atechsys.fr/) was carrying the AIRPHEN multispectral camera (https://www.hiphen-plant.com/our-solutions/airphen/). The camera had 6 spectral bands with 10 nm full width at half maximum. Five bands were equipped with an 8 mm focal length (450 nm, 530 nm, 675 nm, 730 nm, and 850 nm), which provided a field of view (FOV) of 33° × 25°. The sixth band (570 nm) was equipped with a 4.2 mm focal length providing a 60° × 46°

Table 1
Summary of the flights over wheat, maize, and sunflower experiments. The row azimuth, measurement date, take-off time, average sun zenith (θ_s) and azimuth (φ_s) and illumination conditions during the flight are indicated. The azimuth angles are calculated regarding the North.

Species	Date	Row azimuth (°)	Time (GMT + 1)	θ_s (°)	φ_s (°)
Wheat	23/05/2017	90.1	15:09	30	226
			16:12	40	246
			09:00	61	91
Maize	08/08/2016	89.2	14:17	29	221
			16:26	44	244
			18:00	61	264
Sunflower	28/07/2017	90.5	12:20	30	137
			10:40	45	108
			09:20	60	89

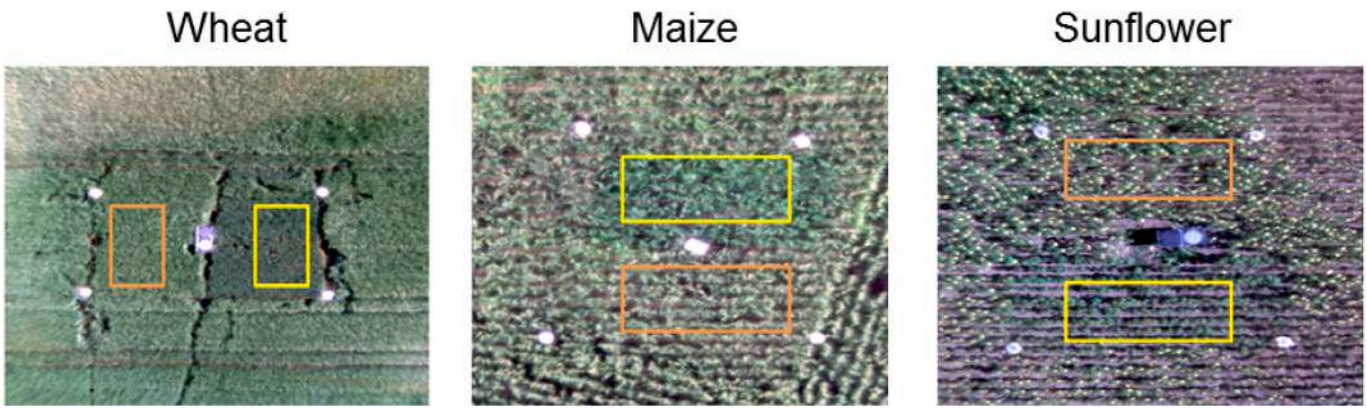

Fig. 1. The three experiments showing the RO+ (with RO, orange rectangle) and RO- (without RO, yellow rectangle) micro plots, the ground control points (GCPs), and the reference panel in the middle. (For interpretation of the references to colour in this figure legend, the reader is referred to the web version of this article.)

FOV. The 4.2 mm lens benefits from a higher overlap (80%) at the expense of a lower spatial resolution (4.06 cm at nadir). It was thus only used to improve the image alignment while the 8 mm lenses for the five other bands were used in the following of the study for their highest spatial resolution (2.11 cm at nadir). Besides the lower spatial resolution, the 4.2 mm lens at 570 nm would not add much spectral information as it is strongly correlated with the 8 mm lens at 530 nm. The camera was triggered every second, the integration time is automatically adjusted using a global shutter. The images were saved into a 12 bit TIFF format with metadata information including time of the acquisition, integration time, and GPS coordinates.

Over each site, the UAV flew three times during the day corresponding approximately to 30°, 45°, and 60° nominal sun zenith angles (θ_s) (Table 1). For each θ_s, the UAV sampled five view zenith angles (θ_v = [0°, 15°, 30°, 45°, 60°) for all view azimuth angles (φ_v) by flying along with five concentric circles, each one being at a specific altitude (Fig. 2). Two additional view zenith angles, $\theta_v = \theta_s$+5° and $\theta_v = \theta_s$-5° were complementing the five nominal θ_v angles to better sample directions close to the hotspot. The flight path was designed before the experiment and included an automatic adjustment of the compass orientation of the camera on the gimbal so that it was always pointing the reference gray panels, the view zenith angle being adjusted for each of the seven circles (Fig. 2). The distance to the ground along the view direction was around 45 m at maximum when cameras were close to the nadir direction (Fig. 2). This provided a ground spatial resolution of about 2.11 cm and 4.06 cm respectively for the 8 mm and 4.2 mm focal length. The UAV was flying at about 1 m/s speed and it took 7 to 10 min to sample all the view directions considered. During the UAV flights, the sky was clear without clouds (Table 1). The wind was gentle for maize and sunflower while significant for wheat with consequences on the faithful realization of the flight plan, with however no severe degradation of the sampling scheme.

2.3. Image extraction

The raw single frames taken concurrently by the six cameras were firstly co-registered to the reference image at 530 nm using the code developed by Rabatel and Labbé (2015). Vignetting effects were then corrected following the procedure proposed by Verger et al. (2014). Agisoft Photoscan software (Version 1.2.4.2399, Agisoft LLC., Russia) was then run using as input the images taken with the 530 nm and 570 nm cameras equipped respectively with 8 mm and 4.2 mm focal lengths. Agisoft Photoscan computed the corresponding position and orientation of the camera for each image. The GCPs were manually identified on the images and used to improve the georeferencing accuracy. The band at 570 nm was not used afterward because of the degraded resolution provided by the 4.2 mm focal length. Furthermore, it was mostly redundant with that at 530 nm with a higher spatial resolution. The pixels corresponding respectively to the two micro plots and the radiometric reference panel were then extracted for the five bands corresponding to the 8 mm focal lengths. The average digital number (DN) value was finally computed and associated with the corresponding integration time (t) and the view direction (θ_v, φ_v). None of the images used were showing saturated pixels.

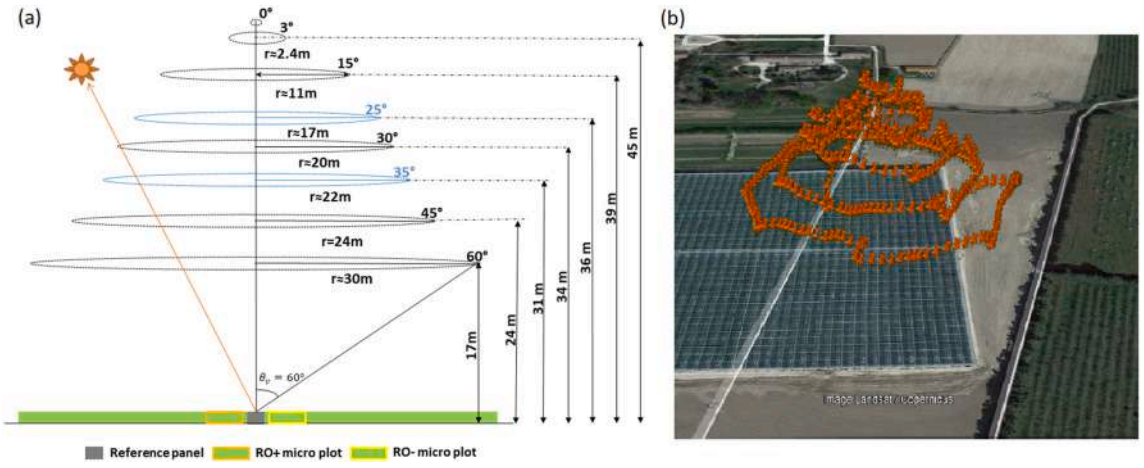

Fig. 2. (a) The flight plan for $\theta_s = 30°$; (b) the actual flight path over the maize experiment at 14:17 local time on 08/08/2016. RO+ and RO- represent micro plots with and without RO, respectively. The background image was from Google Earth™.

2.4. Radiometric calibration

The radiometric reference panel used in the field was made of a gray carpet that was previously characterized in the lab using a goniometer and a white spectralon as primary reflectance reference (Labsphere, Inc., North Sutton, NH, USA). Reflectance measurements were made with a spectral evolution SM-3500 spectrometer (www.spectralevolution.com). The Roujean BRDF model (Roujean et al., 1992) was then adjusted over the goniometer measurements. It was used to simulate the bi-directional reflectance (BRF) of the reference panel for any direction Ω. The 'gray' nature of the panel with all the bands having the same BRF value was well verified (Fig. 3). While the panel was relatively Lambertian for near nadir illumination, significant anisotropy is observed for $\theta_s > 30°$. For this reason, we preferred using only the nadir viewing observations for the radiometric calibration of the camera, assuming that the incoming radiation was stable during the flight.

The $BRF(\Omega, \lambda)$ of the canopy was computed from the DN values extracted from the images using the known BRF value of the reference panel (BRF_{ref}) and the DN values of the reference panel $DN_{ref}(\Omega, \lambda)$ extracted on the same image (Smith and Milton, 1999):

$$BRF(\Omega,\lambda) = \frac{DN(\Omega,\lambda)/t(\Omega,\lambda)}{DN_{ref}(\Omega o,\lambda)/t_{ref}(\Omega o,\lambda)} BRF_{ref}(\Omega o,\lambda) \quad (1)$$

where λ is the wavelength, Ω corresponds to the observation configuration with $\Omega = [\theta_v, \varphi_v, \theta_s, \varphi_s]$ where θ and φ represent respectively the zenith and azimuth angles, and subscripts v and s correspond respectively to the view and sun directions. t is the integration time. The measurements of the reference panel used for the calibration correspond to viewing geometry close to the nadir direction noted here Ωo.

The radiance from the reference panel measured in the field includes a contribution of the direct sunlight as well as a diffuse component coming from the light scattered by the sky. The bi-directional reflectance measured in the lab was therefore converted into a blue-sky reflectance factor to account for the diffuse component. The hemispherical-directional reflectance factor was computed based on Roujean's model with the coefficients previously adjusted. The diffuse fraction was finally used to compute the corresponding blue-sky BRF (Schaepman-Strub et al., 2006). The diffuse fraction was derived from the 6S model simulations (Vermote et al., 1997) using the atmospheric characteristics measured from the local AERONET sun photometer as inputs (Holben et al., 1998).

Once the BRF at each measurement angle Ω was calculated, they were linearly interpolated from 0° to 60° zenith angles and from 0° to 360° azimuth angles with a 1° step for polar representation. Results are shown in the following analysis for the perpendicular and principal planes.

2.5. Reproductive organs characterization

For each crop, a sample of a representative RO was collected in the field. A set of photos were then taken with a SONY alpha 6000 RGB camera from multiple views: the organ was put vertically over a manually rotating plate in front of a uniform blue background. About 40 to 120 photos were taken by rotating the plate. These multi-view RGB photos were aligned using Agisoft Photoscan software (Version 1.2.4.2399, Agisoft LLC., Russia) to build a dense 3D point cloud used later to model the organ morphology. The lengths of wheat ears and maize tassels and the diameter of sunflower heads were also measured (Table 2). The optical properties in five bands were measured using the AIRPHEN camera: organs were placed horizontally over a black background and viewed from nadir under clear sky field conditions, the sun being at around 45° zenith angle. Organ surface reflectance was then computed using a reference panel placed horizontally in the camera field of view. Average values of sunlit wheat ears, maize tassels, and sunflower petals and front-side and back-side of the heads were then computed (Table 2, Table B1).

2.6. Reflectance simulations

The canopy was considered as composed of two layers, the top one corresponding to the RO. The bottom layer corresponds to the canopy without the RO. It was characterized by the measured BRF(Ω, λ) value over the RO- modality, with BRF value equal to that measured in the considered view-illumination geometry. The reproductive organ layer

Table 2
Fields and RO characteristics used for the 3D scene generation. The reflectance of sunflower frontside flower and backside flower does not include yellow petals.

Characteristics	Unit	Wheat	Maize	Sunflower
RO- layer height (m)	m	0.8	1.6	1.03
RO- Green Area Index GAI[a]	–	2.7	4.9	0.40
Row spacing (m)	m	0.155	0.77	0.63
Density of RO (nb/m^2)	nb/m^2	450	8	4
Length of RO (m)	m	0.11	0.25	
Diameter of RO (m)[b]	m	0.015	0.005	0.25
RO area index (m^2/m^2)[c]	–	1.23	0.16	0.20
Reflectance of RO @675 nm	–	0.1	0.25	Flower front-side: 0.122 Flower back-side: 0.25 Flower yellow petal: 0.34
Reflectance of RO @850 nm	–	0.45	0.7	Flower front-side: 0.219 Flower back-side: 0.5 Flower yellow petal: 0.36

[a] GAI was estimated using a simple empirical model described in Verger et al. (2011) and based on the measured NDVI.
[b] Diameter of maize tassel corresponds to the mean value of all branches.
[c] RO area of wheat head is calculated as half the developed area of a cylinder. For maize, tassels were considered as made of five cylindric branches. The area of sunflower head was calculated as a disc.

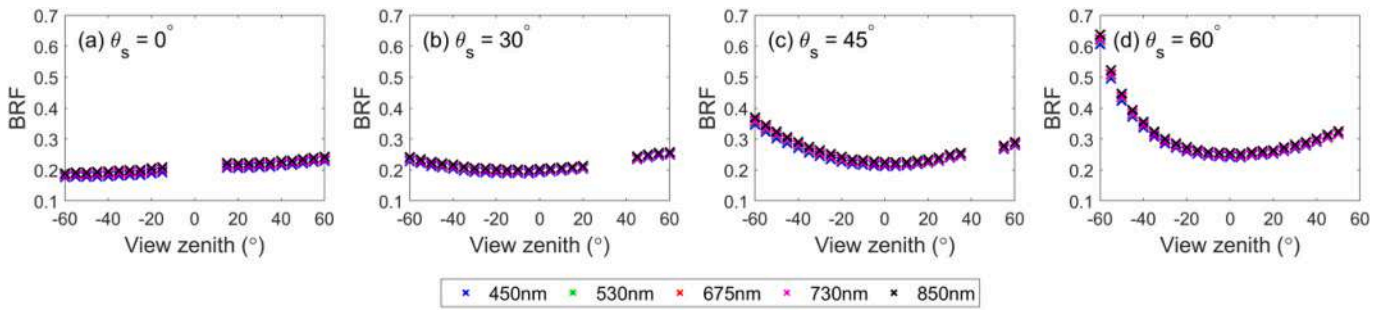

Fig. 3. BRF of the reference panel measured in the lab in the principal plane for four sun zenith angles as a function of the view zenith angle. Positive view zenith angles correspond to the backward direction, while negative values correspond to forward direction.

was built by replicating the typical reproductive organ (Table 2). For wheat, the ears were vertical and placed regularly according to the plant density For maize, the panicles were randomly oriented and placed according to the row spacing and plant density. For sunflowers, all the flowers were oriented towards the east and placed according to the row spacing and plant density. For the three crops, a small random shift of the nominal position was added to mimic the actual localization of the RO (Fig. 4). Scenes of 2.0 × 2.8 m^2 were built and replicated 179 times around the center one to avoid border effects. The reflectance of the RO material was assumed Lambertian and characterized by the corresponding measured reflectance (Table 2) with transmittance equal to zero.

Canopy reflectance with RO was simulated using the LuxCoreRender 3D render engine (LuxCoreRender, 2018). LuxCoreRender is open-source software (LuxCoreRender, 2018), which was validated with a set of state-of-the-art models by Jiang et al. (2020) using the RAMI Online Model Checker (ROMC) (Widlowski et al., 2008). We used the LuxCoreRender ray-tracing integrator with 128 rays per camera pixel to guarantee the accuracy of the simulated reflectance. A perspective camera was selected to simulate the AIRPHEN camera with a 33° x 25°field-of-view. For each θ_s = [30°, 45°, 60°], the observation configuration including $[\theta_v, \varphi_v]$ and the height of the camera was kept the same as in the field experiments. Since the three experiments were conducted under clear sky conditions, no diffuse sky light was considered in our simulations.

3. Results

3.1. Selecting a subset of bands for further analysis

The correlations between the red band (675 nm) and the other four bands were first analyzed to select a subset of bands that will be later investigated for the sake of clarity. Results (Table 3) show that the 450 nm and 530 nm bands were very strongly correlated to the 675 nm band for all sun zenith angles and the three experiments ($r^2 > 0.8$). This is explained by the marginal contribution of multiple scattering and the soil background as well as the fact that most of the elements have similar optical properties in the visible domain. Conversely, bands at 730 nm and mainly that at 850 nm show degraded correlations with the visible bands due mostly to the importance of the multiple scattering in the NIR domain. Therefore, we selected the 675 nm and 850 nm bands as a representative subset to illustrate in the following sections the impact of the RO on the directional reflectance.

3.2. Directional effects over the canopy without the reproductive organs (RO-)

Before quantifying the impact of the reproductive organs on canopy reflectance, the directional properties of the canopies without the RO (RO-) corresponding only to the leaf and stem layer over the soil background were first investigated. They will be used later to compute canopy BRDF using the simulated layer of RO.

3.2.1. Main directional features

The directional features for the three crops and two bands show similar patterns across the three sun positions. We, therefore, illustrate it using only the measurements for $\theta_s = 45°$ (Fig. 5). Measurements for the other two sun directions are presented in Fig. A1 and Fig. A2. The polar plots were obtained by linear interpolation of the raw measured BRF in both zenith and azimuth directions with a 1° angular resolution. A peak corresponding to the sun direction is observed in the hotspot, i.e. when the shadows cast by the leaves or soil roughness are not seen (Qin and Goel, 1995). The hotspot is relatively narrow for the maize and sunflower crops both in the red and NIR bands, while it appears broader for te wheat in these two bands. Note that the hotspot is located in the South-Eastern compass directions for the sunflower experiments since measurements were completed in the morning (Table 1). Conversely, the hotspot is in the South-Western compass direction for maize and wheat, corresponding to afternoon flights. For directions opposite to the hotspot corresponding to the forward scattering, the reflectance is generally lower.

For the visible and NIR bands, the three crops show a general symmetry on both sides of the principal plane, i.e. the plane containing the sun direction (Fig. 5). To better evaluate the symmetry across the principal plane, for each 5° zenith by 5° azimuth cells, the BRF difference, $\delta BRF(\Omega, \lambda)$, with the average of the two symmetrical directions across the principal plane was computed: a perfectly symmetric BRDF with regards to the principal plane should verify $\delta BRF(\Omega, \lambda) = 0$. Results (Fig. 6) confirm that a general symmetry exists across the principal plane since the BRF differences of symmetrical directions are generally within $-0.01 < \delta BRF(\Omega, \lambda) < 0.01$. This is well verified for dense canopies such as maize for both bands (Fig. 6). This is also the case for wheat that presents little row structure at the flowering stage. Nevertheless, in the NIR, a slight dissymmetry is observed for the three sun directions, with slightly higher reflectance in the directions north to the principal plane (Fig. 6). The sunflower shows very similar patterns in both bands (Fig. 6). A persistent dissymmetry is observed for the three sun positions, with slightly higher reflectance in the directions south to the principal plane. Since the rows were oriented East-West, this can be easily explained for $\theta_s = 30°$ and $\theta_s = 45°$: the illuminated plants and soil in the row are preferentially seen from the southern directions as compared to the northern ones. This agrees very well with the results from (Ranson et al., 1985) as well as reflectance simulations of row canopies (Goel and Grier, 1987; Suits, 1983; Zhao et al., 2010). However, when the sun is almost parallel to the row direction as observed for $\theta_s = 60°$, the southern side appears more reflective than the northern one. This was not expected and is more difficult to explain unless invoking some non-isotropic distribution of leaf azimuthal directions, or some uncorrected

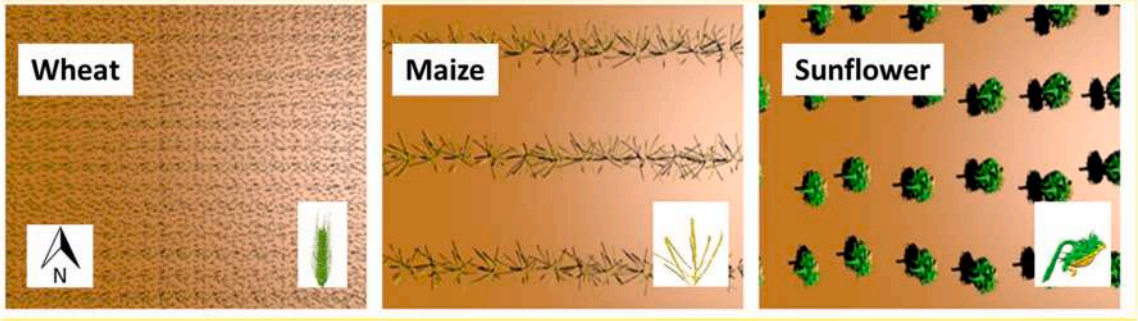

Fig. 4. Nadir view of the 3D scenes (2.0 × 2.8 m^2) for wheat, maize, and sunflower as rendered with Luxrender. The sun position is in the east at 45° zenith angle. The reproductive layer was put here on a brown background for better visualization. A side view of the typical reproductive organ replicated in the scene is also displayed for each crop. (For interpretation of the references to colour in this figure legend, the reader is referred to the web version of this article.)

Table 3
Correlation coefficients (r^2) between canopy reflectance @675 nm and the four other bands for wheat, maize, and sunflower experiments over all images. It includes RO- and RO+ observations for the three sun zenith angles (θ_s).

	θ_s	Wheat				Maize				Sunflower			
	(°)	450	530	730	850	450	530	730	850	450	530	730	850
RO+	30	0.95	0.95	0.9	0.75	0.99	0.98	0.89	0.65	0.96	0.95	0.72	0.63
	45	0.98	0.96	0.81	0.6	0.99	0.98	0.93	0.76	0.99	0.97	0.88	0.83
	60	1.00	1.00	0.98	0.96	0.99	0.98	0.93	0.8	0.99	0.97	0.91	0.86
RO-	30	0.81	0.91	0.8	0.44	0.99	0.97	0.91	0.66	0.94	0.93	0.8	0.73
	45	0.9	0.92	0.77	0.47	0.99	0.98	0.92	0.75	0.98	0.98	0.92	0.88
	60	0.97	0.98	0.93	0.84	0.99	0.96	0.89	0.68	0.98	0.98	0.94	0.89

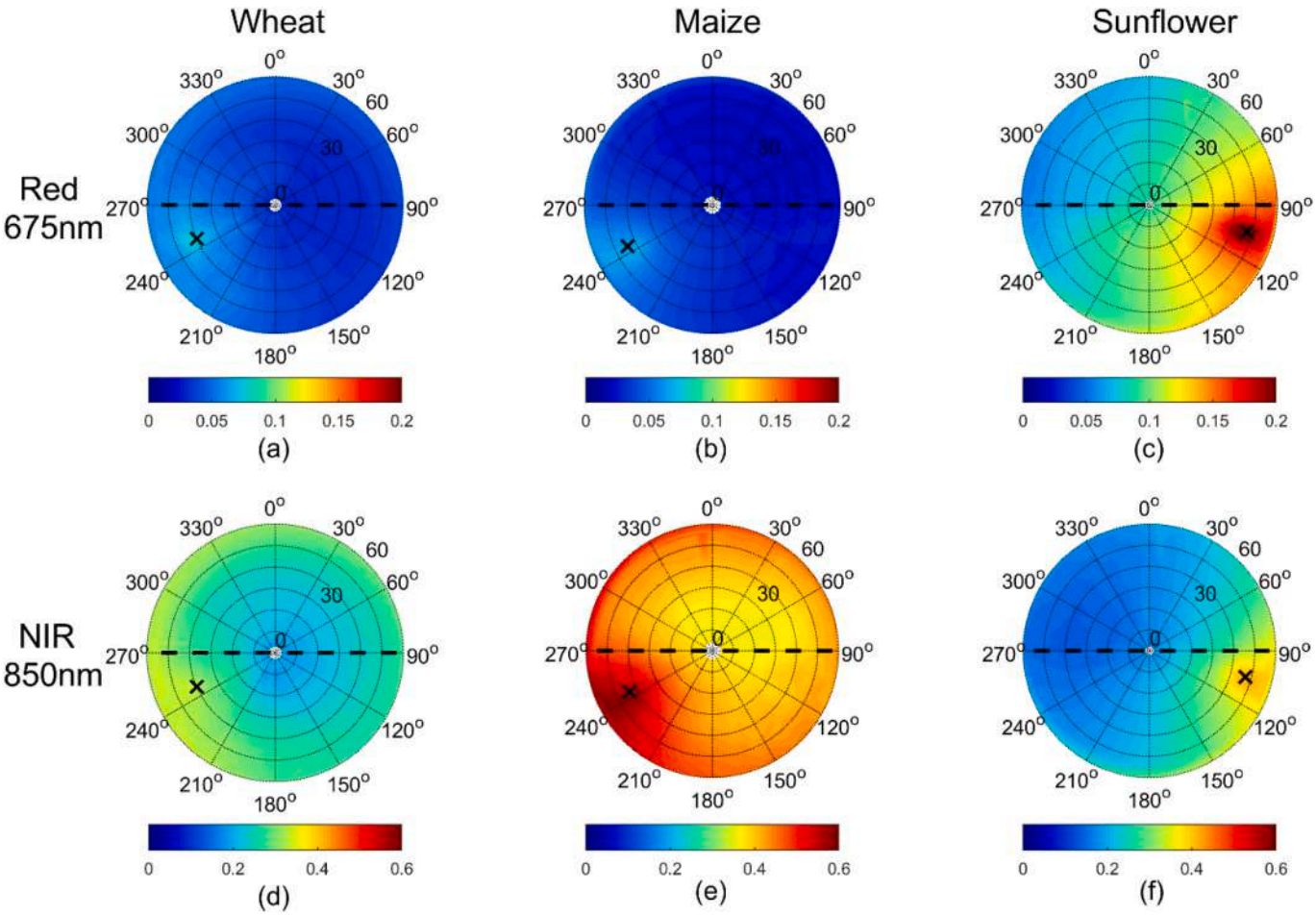

Fig. 5. Polar representation of the measured BRF distribution of the three experiments without the RO (RO-) for 675 nm and 850 nm bands. The sun is displayed as a black cross marker and was at θ_s=45°. The row orientation (east-west) is represented by the dashed black line. Values represent interpolations from raw measured BRF.

biases in the measurements. However, the magnitude of the difference is generally lower than 0.01 which is probably close to the measurement uncertainties.

Because of the general symmetry across the principal plane, we will focus in the following on the average BRF between the two symmetrical directions across the principal plane. This will offer the advantage to

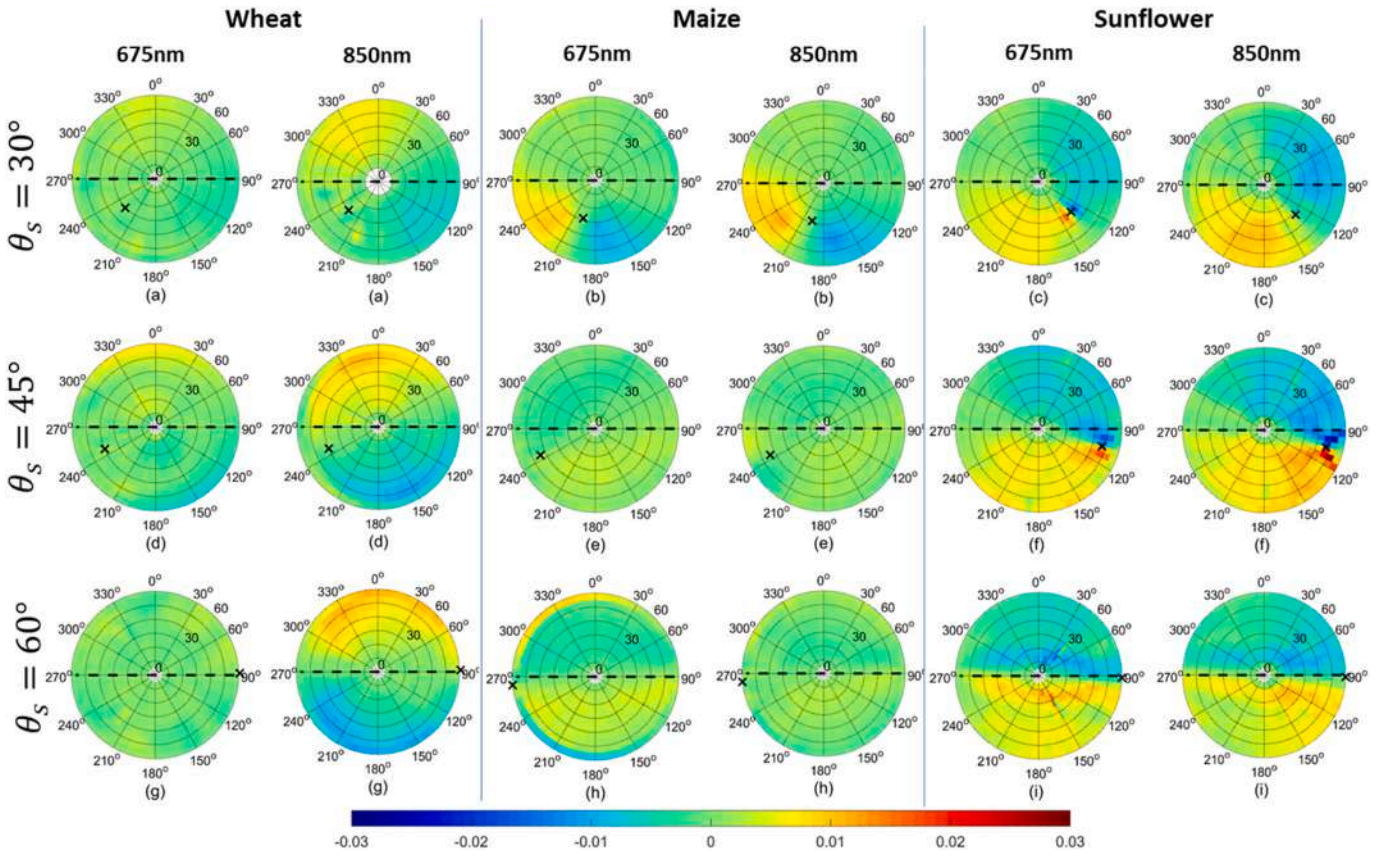

Fig. 6. Polar plot of $\delta BRF(\Omega, \lambda)$ for wheat, maize, and sunflower without RO @675 nm and 850 nm, and the three sun positions considered. $\delta BRF(\Omega, \lambda)$ represents for each view direction the BRF differences with the average BRF values of the two symmetrical directions across the principal plane: when $\delta BRF(\Omega, \lambda) = 0$, the BRF of both symmetrical directions across the principal planes are the same. The black cross marker represents the sun position during the flight. The black dashed line is the row direction.

smooth out possible local uncertainties.

3.2.2. *Directional effects in the principal plane*

The BRF in the principal plane was approximated as the BRF measured values within ±5° azimuth difference with that of the sun direction. All the crops, bands, and directions show similar patterns (Fig. 7) with however large differences in magnitude. The maximum BRF is observed always close to the hotspot direction as expected. The minimum BRF values are observed close to the nadir for the NIR band, and in the forward scattering directions for the visible bands. The difference between red and NIR bands depends on the species as a function of the green area index values: the wheat has the largest GAI and the largest difference between red and NIR. Conversely, sunflower has the lowest GAI and the lowest difference between the BRF in both domains.

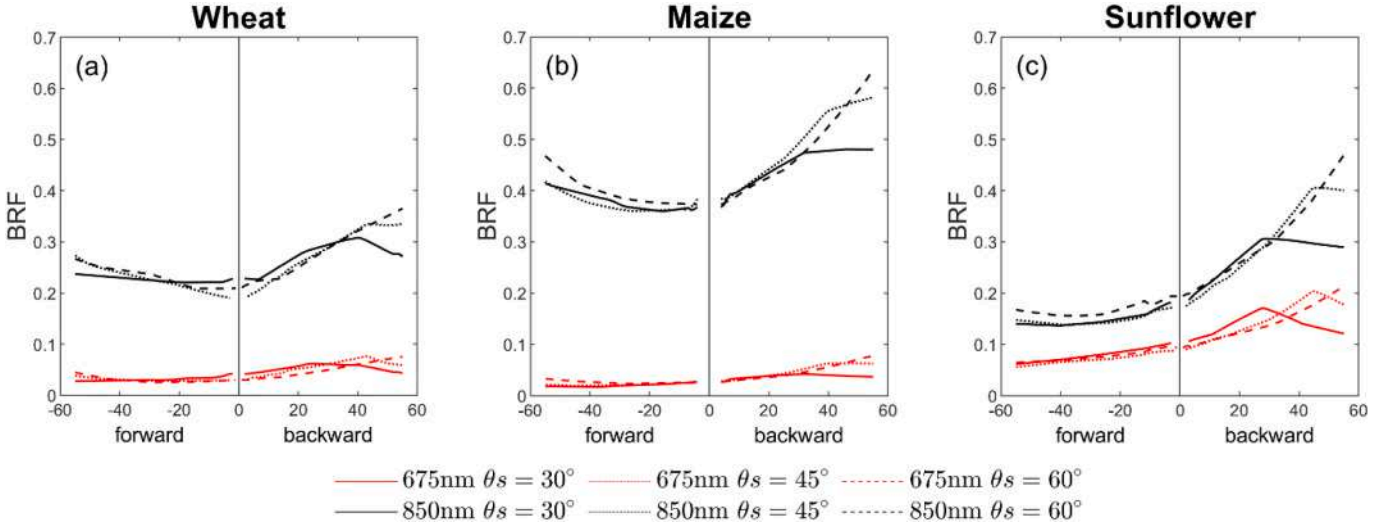

Fig. 7. BRF values in the red (675 nm) and NIR (850 nm) in the principal plane as a function of the view zenith angles. Observations over canopies without the RO for θ_s=[30°, 45°, 60°]. (For interpretation of the references to colour in this figure legend, the reader is referred to the web version of this article.)

Outside the hotspot directions, small differences of BRFs are observed between the three sun directions with however slightly higher values for θ_s= 60° for the more oblique view directions in the NIR, while the contrary is observed in the visible domain (Fig. 7).

3.3. Effects of reproductive organs on canopy reflectance

3.3.1. Main directional features

We focused first on $\Delta BRF(\Omega,\lambda)$, i.e. the canopy BRF difference between canopy with organs (RO+) and without organs (RO-). This was computed based on the average BRF between the two symmetrical directions across the principal plane as explained earlier. Results show that the impact of RO on canopy BRF is relatively small in absolute value, with $-0.02 < \Delta BRF(\Omega,\lambda) < 0.02$ in the red, and $-0.04 < \Delta BRF(\Omega,\lambda) < 0.04$ in the NIR (Fig. 8). However, when computed in relative values, $\Delta BRF(\Omega,\lambda)$ can reach substantial levels up to 85% in the red because of the small $BRF(\Omega,\lambda)$ observed (Fig. 5) and up to 34% in the NIR. The impact of RO depends mainly on the crop, on the spectral domain as well as on the directions considered.

For wheat, the ears generally decrease canopy reflectance both in the red and NIR bands (Fig. 8). This is consistent with studies by Li et al. (2015). Little directional effects due to the sun and view directions are observed, with however larger impacts close to the hotspot. We observe some higher differences (in absolute value) for $\theta_v > 55°$, which may

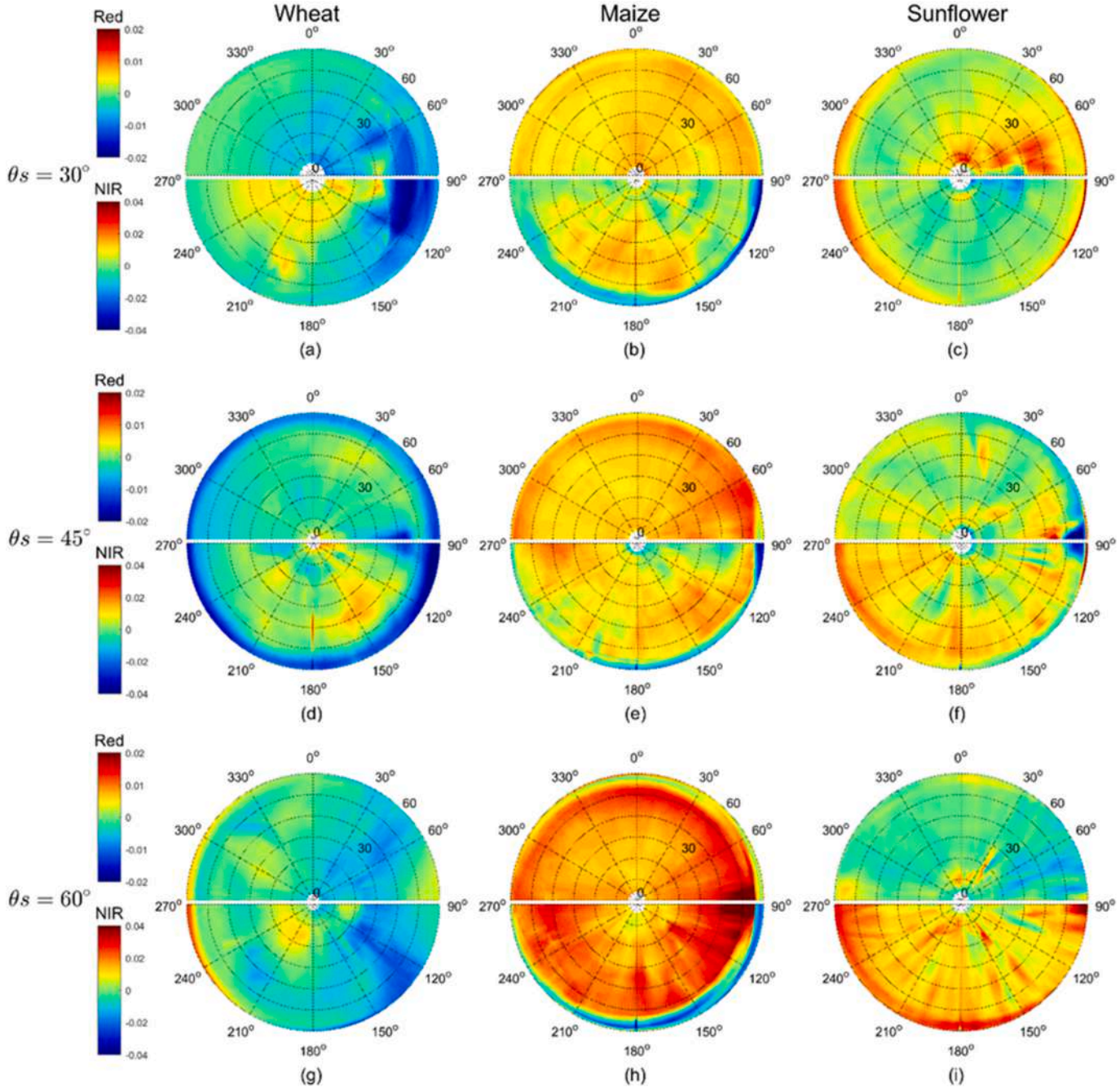

Fig. 8. Directional distribution of $\Delta BRF(\Omega,\lambda)$, the canopy BRF difference with (RO+) and without (RO-) the RO. Wheat (left), maize (middle), and sunflower (right) are displayed for θ_s = [30°,45°,60°]. Each half polar plot represents the average BRF values between the two symmetrical directions across the principal plane. The top hemisphere represents the red band and the bottom one the NIR band. The principal plane is in the 90° - 270° azimuthal direction, with the hotspot located on the right side (90° azimuth). (For interpretation of the references to colour in this figure legend, the reader is referred to the web version of this article.)

correspond to artifacts in the measurements. Similar artifacts are also noticed for maize and sunflower.

The tassels of maize generally increase canopy BRF for all sun and view directions both in the red and NIR domains. The impact increases substantially with the solar zenith angle, while the effect of view direction is marginal (Fig. 8).

For sunflower, the influence of heads is contrasted between the red and NIR domains: in the red, the impact is small with $\Delta BRF(\Omega,\lambda) \approx 0$ for the three sun directions; conversely, in the NIR, the heads increase canopy reflectance, particularly for the larger sun zenith angles (Fig. 8).

3.3.2. *Consistency between observations and simulations*

Since the experimental evidence of the impact of RO on canopy reflectance appears difficult due to the small differences observed and possible confounding measurement uncertainties, we wanted to consolidate the findings based on radiative transfer simulations. We concentrated on the principal plane where most directional features are expected and computed $\Delta BRF(\Omega,\lambda)$.

In the red domain (Fig. 9), simulations confirm that the impact of RO is small. It is slightly negative for wheat, slightly positive for maize, and neglectable for sunflower. For wheat, the addition of the ear layer representing an area index around 1.2 (Table 2) decreases canopy BRF since ears are green with low reflectance (Table 2) without transmitting light, i.e. a very absorbing layer. Furthermore, their vertical position acts as a light trap, increasing light absorption by the lower layers of the canopy. For maize, the tassels act as a scattering layer since they reflect more light than the lower layer of green vegetation due to their higher reflectance (Table 2). When the sun zenith increases, $\Delta BRF(\Omega,\lambda)$ increases because of the longer path length in the tassel layer. The same is also observed for more inclined views, particularly in the backward scattering direction. The small impact of sunflower heads on canopy reflectance can be explained by their small contribution in terms of area index (Table 2), on top of the green layer of leaves. The more subtle differences observed as a function of the observational geometry are difficult to explain.

In the NIR domain (Fig. 10), the small impact of the ears on $\Delta BRF(\Omega,\lambda)$ is explained by the light trap feature as described previously and the small scattering properties of the ears that do not transmit light. For maize, the discrepancies between measurements and simulations may be partly explained by the fact that the strong row structure of the vegetation layer was not accounted for in our simulations. Measurements show a positive impact of the tassels for $\theta_s = 60^\circ$ and oblique viewing. For the sunflower, the heads induce a slight increase of canopy reflectance, probably due to the high values of the reflectance of the back-side of heads (Table 2) that are pointing upward.

Furthermore, the discrepancies found between observed and simulated $\Delta BRF(\Omega,\lambda)$ values may be explained by the possible measurement uncertainties as well as the assumptions made for the canopy reflectance simulations regarding the spatial homogeneity (i.e. no row structure) of the bottom vegetation layer that is coupled with the RO layer.

3.4. *Impact on NDVI values and GAI estimation*

Previous results demonstrated that the effect of RO on canopy reflectance was variable in the visible and NIR bands. We thus investigated how NDVI (Rouse Jr. et al., 1973), a vegetation index widely used

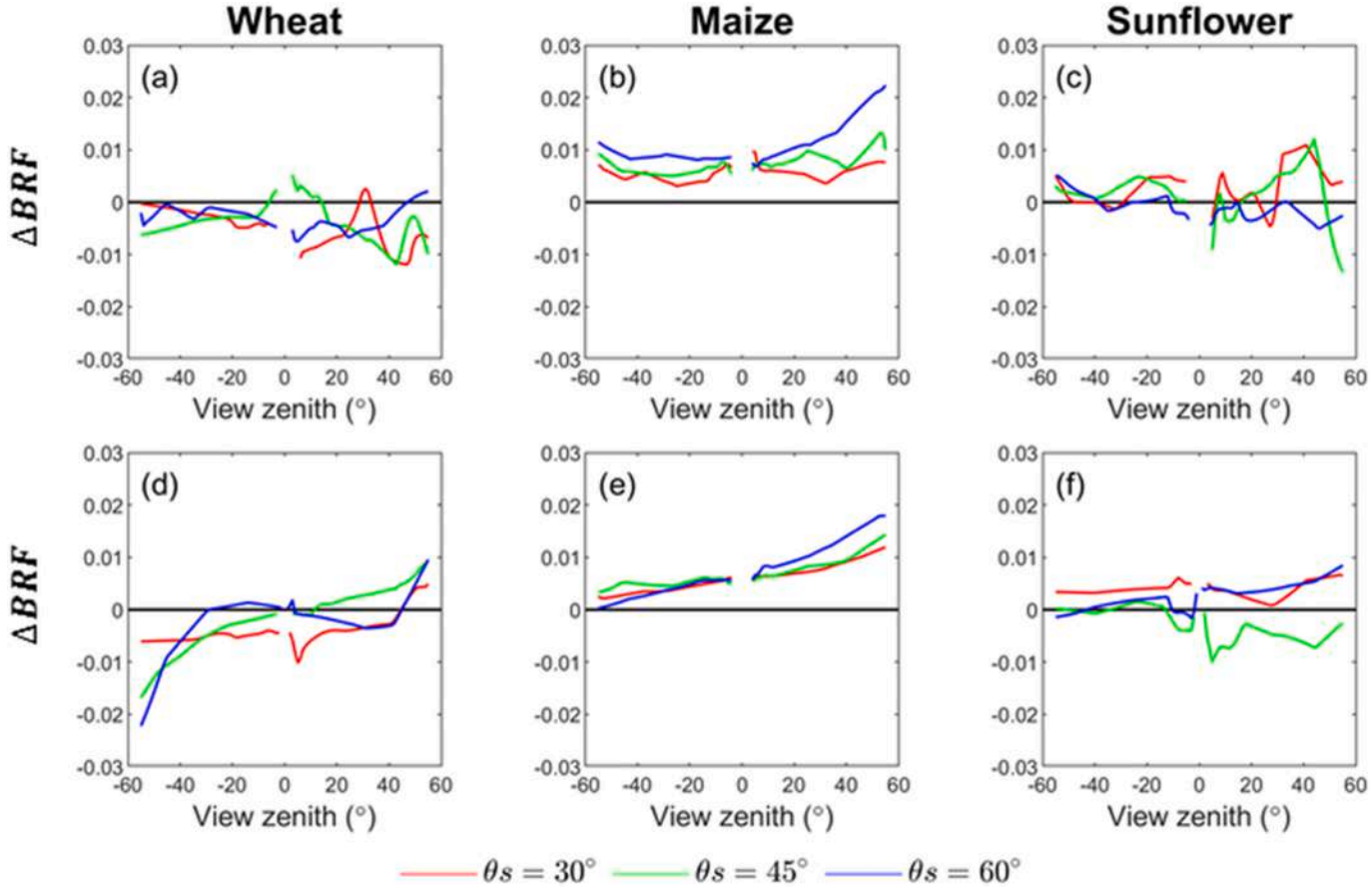

Fig. 9. Measured BRF differences between canopy with (RO+) and without (RO-) RO as a function of the view zenith angle in the principal plane at 675 nm from measurements (top) and 3D simulation (bottom). The back-scattering direction corresponds to positive view zenith angles. Crops are shown from left to right: wheat, maize, and sunflower. Several solar zenith angles are considered: $\theta_s = 30^\circ$ (red), $\theta_s = 45^\circ$ (green), and $\theta_s = 60^\circ$ (blue). (For interpretation of the references to colour in this figure legend, the reader is referred to the web version of this article.)

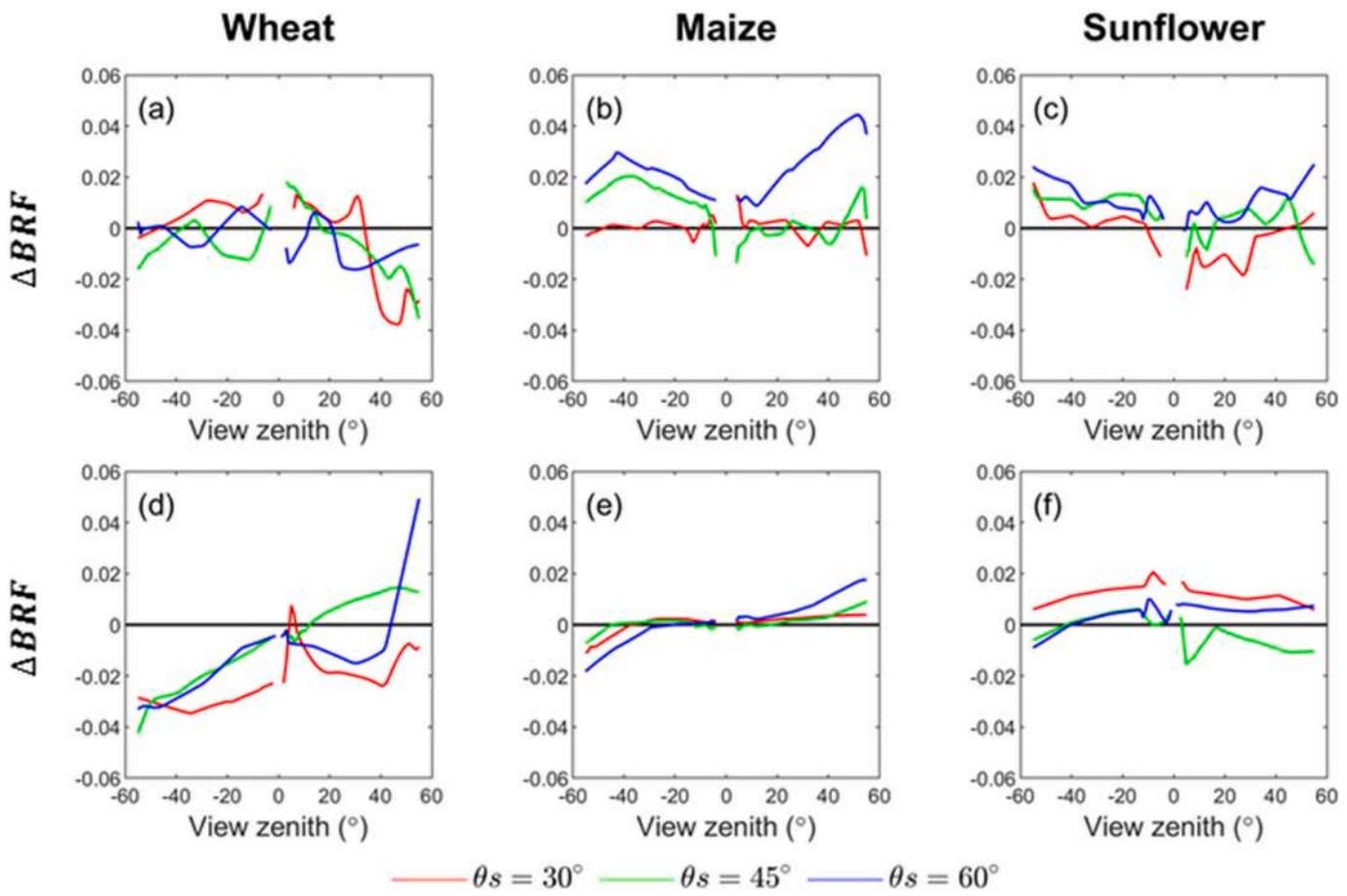

Fig. 10. Measured BRF differences between canopy with and without RO as a function of the view zenith angle in the principle plane at 850 nm from measurements (top) and 3D simulation (bottom). The back-scattering direction corresponds to positive view zenith angles. Crops are shown from left to right: wheat, maize, and sunflower (right) and different solar zenith angles are considered: θ_s of 30° (red), 45° (green) and 60° (blue). (For interpretation of the references to colour in this figure legend, the reader is referred to the web version of this article.)

to quantify vegetation amount and combining the red and NIR bands, was impacted by the RO. We focused here on near nadir observations ($-10^\circ < \theta_v < 10^\circ$), which is the typical geometry used to observe crops from high-spatial resolution satellites.

NDVI indicates the amount of green vegetation that can be also quantified by the green area index (GAI): a gradient is observed between wheat, maize, and sunflower as a function of the GAI value (Table 2), with maize having the larger GAI, and sunflower the lower one (Fig. 11). The addition of ears in wheat canopies increases the NDVI value. This is consistent with the results from Li et al. (2015) and is mainly explained by the green nature of the ears at the flowering stage that absorb strongly in the red and scatter light in the NIR. Note that the area index of the ear layer is close to 1.2 over a GAI of the wheat crop at the flowering stage around 2.7 (Table 2). The variation in NDVI due to the ear layer is around $\Delta NDVI \approx 0.04$.

For maize crops, the highly scattering tassels in the red and NIR decrease the NDVI values by $\Delta NDVI \approx -0.03$. These results are consistent with those reported by Gitelson (2003).

For the sunflower, the impact is slightly negative ($\Delta NDVI \approx -0.02$) for $\theta_s = 30^\circ$ which is explained mainly by the higher scattering properties of the sunflower heads (Table 2). Conversely, the impact is positive ($\Delta NDVI \approx 0.01$) for $\theta_s = 60^\circ$: under this geometry where the sun is parallel to the rows, the heads cast shadows on the row, inducing a larger decrease of the BRF in the red while NIR BRF remains about the same because of the multiple scattering in the canopy. As expected, for medium solar zenith angles ($\theta_s = 45^\circ$) the impact of the heads is intermediate between the two previous situations with $\Delta NDVI \approx 0$.

Our experimental results also show that the NDVI changes induced by the RO layer can be translated into a change in GAI estimates that can reach up to 25% (Table 4). It can be either positive as in the case of wheat crops and for the sunflower for the smaller solar zenith angle, or negative as in the case of the maize crop.

4. Discussion and conclusions

4.1. BRF measured by UAVs

We proposed a method to sample the BRDF from UAV multi-angular measurements that appears very efficient as compared to the use of goniometers in the field (Sandmeier and Itten, 1999): it offers the advantage to avoid disturbing the crop surface while using a single footprint where the multiangular observations are concentrated (Roosjen et al., 2016).

Although UAV provides a very promising way to sample the canopy reflectance as demonstrated in this study, uncertainties could be raised in several aspects. We designed carefully the flight plan by taking into account the micro plot size, camera FOV, variation of viewing angles and flight duration. We thus achieved a very good directional sampling of each micro plot. However, around the hotspot direction where very strong variation of canopy reflectance is expected, the sampling density was probably too loose to get a very accurate description of this BRDF feature. Further, the necessary spatial averaging over the microplot induces also a degradation of the directional resolution of the measurements which was around 7°.

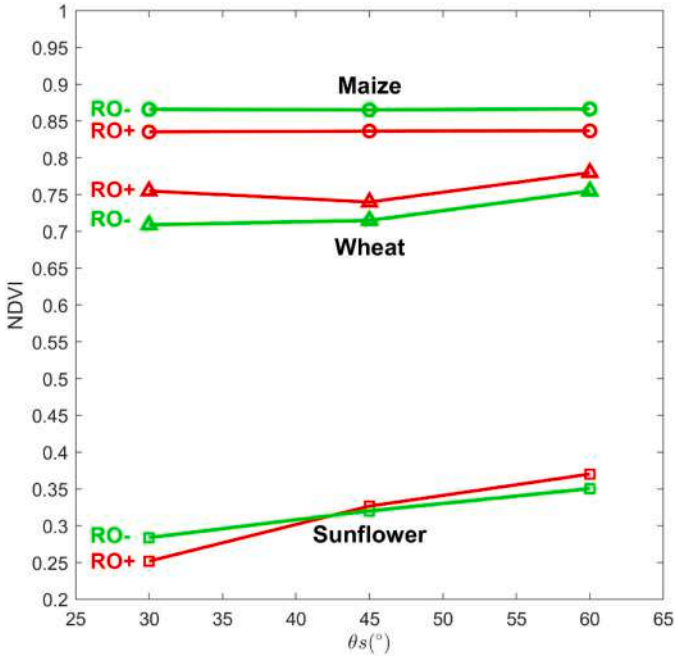

Fig. 11. Variation of NDVI values as observed near nadir (average of BRF for $-10\ ^{\circ} < \theta_v < 10^{\circ}$) for maize, sunflower, and wheat with $\theta_s = [30^{\circ}, 45^{\circ}, 60^{\circ}]$. The canopy NDVI values measured with (RO+) and without (RO-) RO are displayed.

Table 4
Impact of the RO on GAI estimates. The measured NDVI values for the canopy with (RO+) and without (RO-) RO are displayed along with the corresponding GAI. The difference is then computed in absolute (ΔGAI) or relative value (ΔGAI %). All GAI values are derived from NDVI using the empirical relationship proposed by Verger et al. (2011).

Species	θ_s	RO-		RO+		ΔGAI	ΔGAI %
		NDVI	GAI	NDVI	GAI		
Maize	30°	0.86	4.6	0.83	3.9	−0.7	−15
	45°	0.86	4.6	0.83	3.9	−0.7	−15
	60°	0.87	4.8	0.83	3.9	−1.0	−19
Wheat	30°	0.70	2.2	0.76	2.7	0.5	23
	45°	0.71	2.3	0.74	2.6	0.3	13
	60°	0.76	2.7	0.78	3.1	0.3	15
Sunflower	30°	0.28	0.4	0.26	0.3	−0.1	−25
	45°	0.32	0.5	0.32	0.5	0.0	0
	60°	0.36	0.6	0.37	0.6	0.0	0

Our radiometric calibration based on nadir measurements of the reference panel assumes that the irradiance did not change during the flight. This was preferred as compared to using more frequent observations of the panel under the several view directions sampled un order to reduce the uncertainties attached to the BRDF characterization of the panel as well as the illumination geometry. However, the clear sky conditions and the small time interval necessary to complete the flight (7–10 min) ensured that the illumination conditions were about constant during image acquisition. The method also assumes that the camera responds linearly with the radiance and that the black current is neglectable (Smith and Milton, 1999; Wang and Myint, 2015). Although this was verified for few AIRPHEN cameras, using multiple calibration panels in the field as proposed by Pozo et al. (2014) and Smith and Milton (1999) could allow to confirm this important assumption.

4.2. Impact of RO on canopy reflectance and NDVI

UAV measurements and 3D model simulations show that the RO have a small effect on the absolute reflectance values, with magnitudes of ±0.02 in the red and ± 0.04 in the NIR band (Fig. 8 and Fig. 9). However, expressed in relative values the differences can reach up to 85% in the red and 34% in the NIR. The impact of RO on canopy reflectance vary with crop, spectral bands and show directional effects. This may translate into substantial changes in vegetation index values: for view directions close to nadir, the wheat ears layer increases the NDVI by up to 0.06 (8.57%), while the maize tassels decrease canopy NDVI by up to 0.04 (4.60%) (Table 4). The sunflower heads impact differently NDVI depending on sun position due to the complex structure and optical properties of the heads, including difference between the two sides and the presence of yellow petals.

These results were derived from measurements acquired at a single date during the crop reproductive stage. However, the impact of RO on reflectance may vary greatly depending on the reproductive stages. For instance, the wheat senescence occurs from the bottom to the top of the canopy and the timing of the disappearance of the chlorophyll pigments in ears will affect the spectral response of the crops (Weiss et al., 2001). Furthermore, the presence of awns, the ear shape or its inclination also vary substantially with the genotype and time, with impact on the spectral and directional behavior on the canopy (Gutierrez et al., 2015). Conversely, for maize, the structure of the tassels is supposed to vary in a lesser extent as compared to wheat, while the yellowing will still have an impact on the spectral variation of the reflectance (Martin et al., 2007). The effect of RO on sunflower reflectance should also be variable depending on the phenological stage as they have the biggest reproductive organs, with contrasted reflectance between each side of the head associated to a complex behavior regarding their orientation due to the heliotropism. Therefore, this study represents a first step to highlight the influence of RO on canopy reflectance but more investigations are required, especially regarding the temporal variations of the spectral properties, the orientation of the organs, genotypic variations and changes in the crop environmental conditions.

4.3. Consequences on GAI estimates and applications

The presence of the RO may also impact estimates of GAI. In this study, we used NDVI as a proxy of GAI. Two cases can be considered: (1) if the organs are green and photosynthetically active as in the case of the wheat ears or the sunflower heads, they should be included in the GAI computation since they will contribute to light interception and photosynthesis. However, because the architecture of the reproductive layer at the top of the canopy is different from that of the bottom layer, artifacts may be introduced in the retrieval of GAI if the same architecture is assumed for the two layers. This explains why Weiss et al. (2001) introduced explicitly an ear layer in their dynamic model of wheat canopy architecture. (2) if the RO are not green as for the maize tassels, they will partly absorb and scatter the incoming light without contributing to the GAI. This explains the experimental results from Gitelson et al. (2014) over maize crops who showed that the relationship between the fraction of intercepted radiation and NDVI during the vegetative stage was different from that during the reproductive stage. In both cases, the dynamics of canopy refelectance and NDVI will be altered when the RO are appearing during the flowering stage, leading to possible artifacts on GAI estimation. These artifacts introduced by the presence of the RO layer will depend on the specific structural and optical properties features of each genotype. The perturbations in the dynamics due to the apparition of the RO layer offers the potentials to be exploited to date this important growth stage.

Declaration of Competing Interest

The authors declare that they have no known competing financial interests or personal relationships that could have appeared to influence the work reported in this paper.

Acknowledgments

This study was supported by "Programme d'investissement d'Avenir" PHENOME (ANR-11-INBS-0012). It was carried within the CAPTE-Mixed unit.

Appendix A

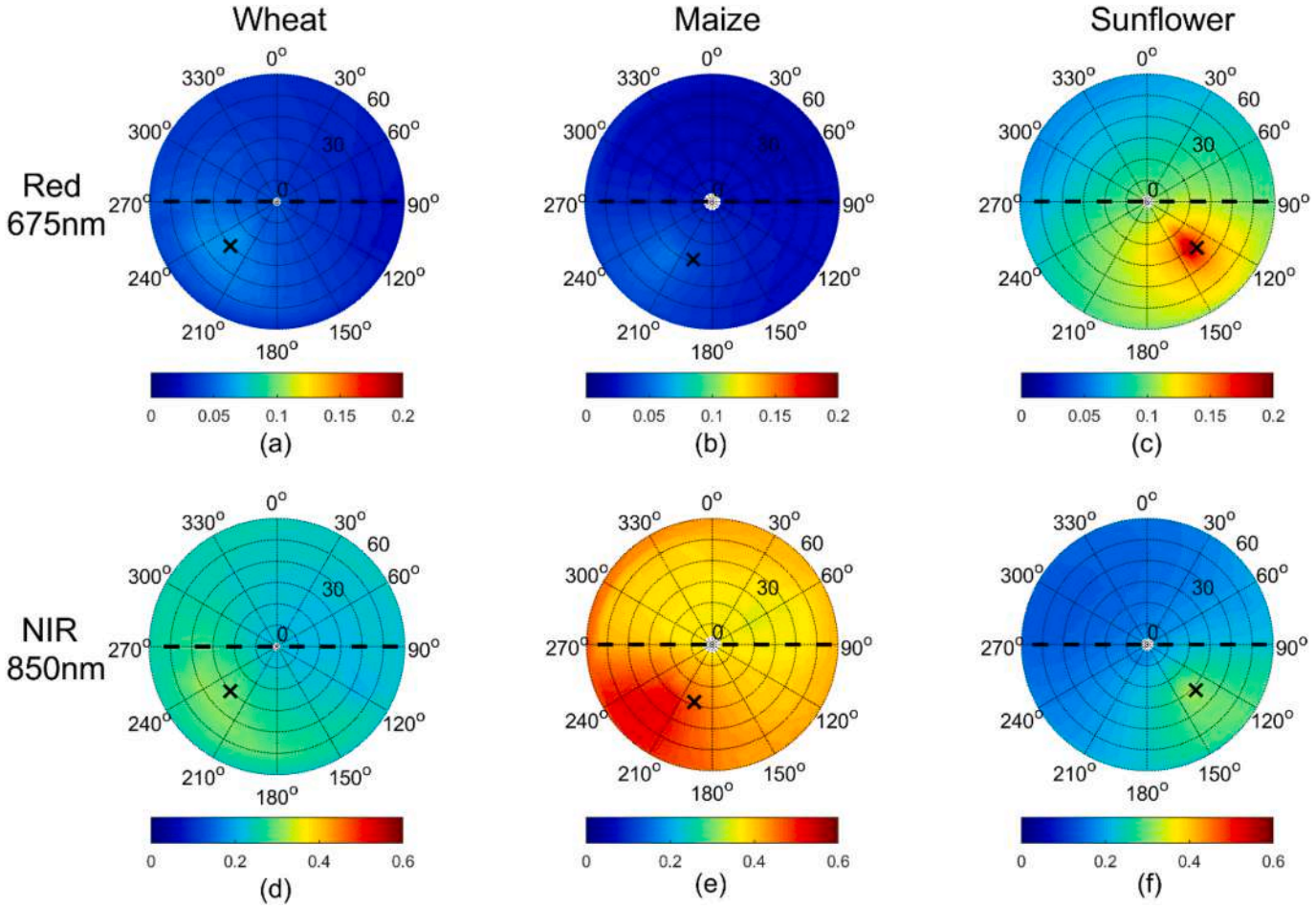

Fig. A1. Polar representation of the measured BRF distribution of the three experiments without the RO (RO-) for 675 nm and 850 nm bands. The sun is displayed as a black cross marker and was at θ_s= 30°. The row orientation (east-west) is represented by the dashed black line. Values represent interpolations from raw measured BRF.

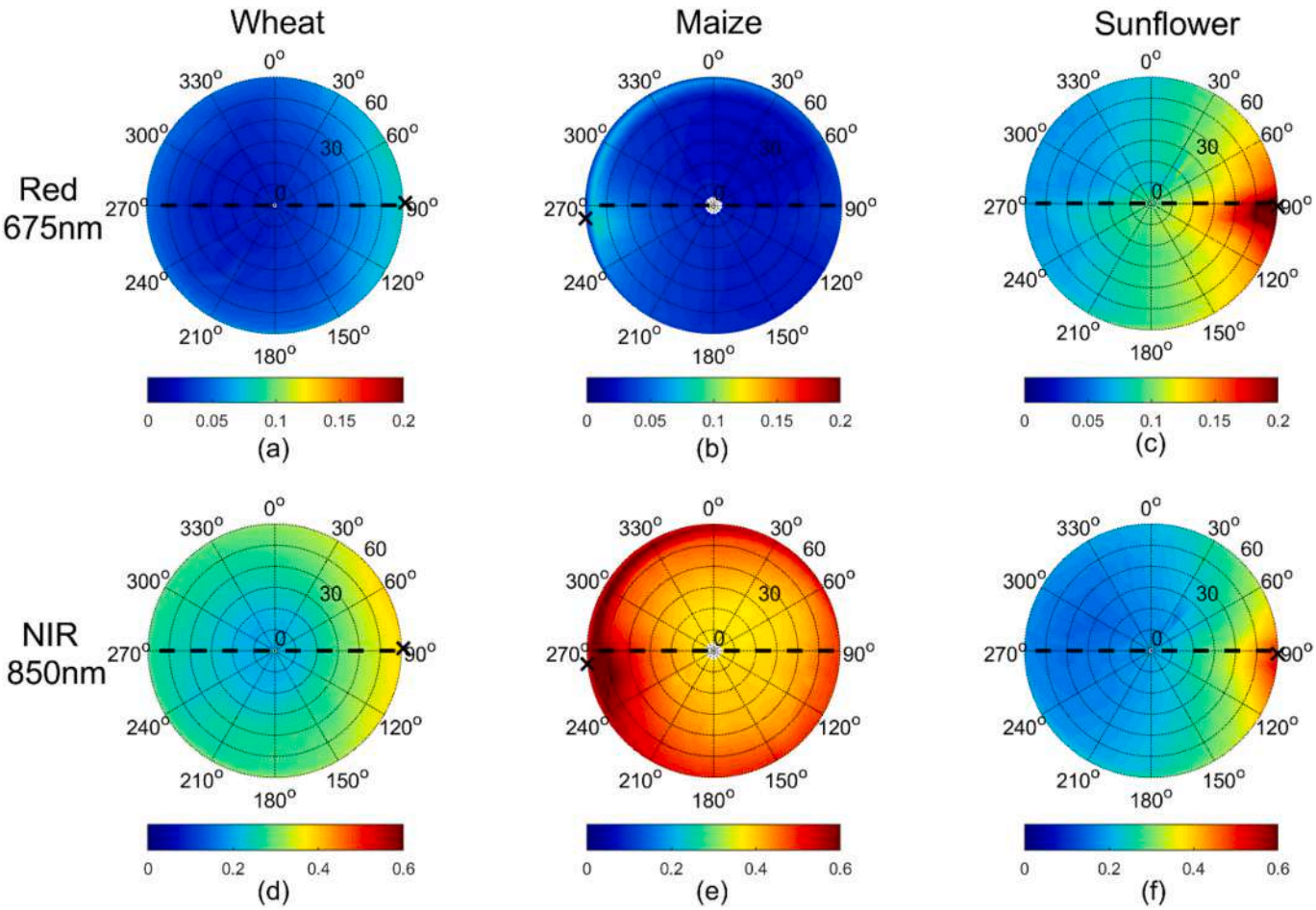

Fig. A2. Polar representation of the measured BRF distribution of the three experiments without the RO (RO-) for 675 nm and 850 nm bands. The sun is displayed as a black cross marker and was at θ_s= 60°. The row orientation (east-west) is represented by the dashed black line. Values represent interpolations from raw measured BRF.

Appendix B

Table B1
Measured reflectance of wheat ears, maize tassels, and sunflower petals, front-side and back-side from AIRPHEN camera on 450 nm, 530 nm, and 730 nm. The reflectance of sunflower frontside flower and backside flower does not include yellow petals.

	450 nm	530 nm	730 nm
Wheat	0.04	0.25	0.35
Maize	0.13	0.2	0.45
Sunflower front-side	0.021	0.10	0.21
Sunflower back-side	0.06	0.17	0.38
Sunflower yellow pedal	0.024	0.27	0.35

References

Burkart, A., Cogliati, S., Schickling, A., Rascher, U., 2014. A novel UAV-based ultra-light weight spectrometer for field spectroscopy. IEEE Sensors J. 14, 62–67. https://doi.org/10.1109/JSEN.2013.2279720.

Burkart, A., Aasen, H., Alonso, L., Menz, G., Bareth, G., Rascher, U., 2015. Angular dependency of Hyperspectral measurements over wheat characterized by a novel UAV based goniometer. Remote Sens. 7, 725–746. https://doi.org/10.3390/rs70100725.

Casa, R., Jones, H., 2005. LAI retrieval from multiangular image classification and inversion of a ray tracing model. Remote Sens. Environ. 98, 414–428. https://doi.org/10.1016/j.rse.2005.08.005.

Comar, A., Burger, P., de Solan, B., Baret, F., Daumard, F., Hanocq, J.-F., 2012. A semi-automatic system for high throughput phenotyping wheat cultivars in-field conditions: description and first results. Funct. Plant Biol. 39, 914. https://doi.org/10.1071/FP12065.

Cossani, C.M., Reynolds, M.P., 2012. Physiological traits for improving heat tolerance in wheat. Plant Physiol. 160, 1710–1718. https://doi.org/10.1104/pp.112.207753.

Deering, D., Leone, P., 1986. A sphere-scanning radiometer for rapid directional measurements of sky and ground radiance. Remote Sens. Environ. 19, 1–24. https://doi.org/10.1016/0034-4257(86)90038-6.

Disney, M., Lewis, P., Saich, P., 2006. 3D modelling of forest canopy structure for remote sensing simulations in the optical and microwave domains. Remote Sens. Environ. 100, 114–132. https://doi.org/10.1016/j.rse.2005.10.003.

Duthoit, S., Demarez, V., Gastellu-Etchegorry, J.-P., Martin, E., Roujean, J.-L., 2008. Assessing the effects of the clumping phenomenon on BRDF of a maize crop based on 3D numerical scenes using DART model. Agric. For. Meteorol. 148, 1341–1352. https://doi.org/10.1016/j.agrformet.2008.03.011.

España, M.L., Baret, F., Aries, F., Chelle, M., Andrieu, B., Prévot, L., 1999. Modeling maize canopy 3D architecture application to reflectance simulation. Ecol. Model. 122, 25–43.

Génard, M., Baret, F., Simon, D., 2000. A 3D peach canopy model used to evaluate the effect of tree architecture and density on photosynthesis at a range of scales. Ecol. Model. 128, 197–209.
Gitelson, A.A., 2003. Novel technique for remote estimation of CO $_2$ flux in maize. Geophys. Res. Lett. 30, 1486. https://doi.org/10.1029/2002GL016543.
Gitelson, A.A., Peng, Y., Arkebauer, T.J., Schepers, J., 2014. Relationships between gross primary production, green LAI, and canopy chlorophyll content in maize: implications for remote sensing of primary production. Remote Sens. Environ. 144, 65–72. https://doi.org/10.1016/j.rse.2014.01.004.
Goel, N.S., Grier, T., 1987. Estimation of canopy parameters of row planted vegetation canopies using reflectance data for only four view directions. Remote Sens. Environ. 21, 37–51. https://doi.org/10.1016/0034-4257(87)90005-8.
Grenzdörffer, G.J., Niemeyer, F., 2012. UAV based BRDF-measurements of agricultural surfaces with pfiffikus. Int. Arch. Photogramm. Remote. Sens. Spat. Inf. Sci. XXXVIII-1 (C22), 229–234. https://doi.org/10.5194/isprsarchives-XXXVIII-1-C22-229-2011.
Gutierrez, M., Reynolds, M.P., Klatt, A.R., 2015. Effect of leaf and spike morphological traits on the relationship between spectral reflectance indices and yield in wheat. Int. J. Remote Sens. 36, 701–718. https://doi.org/10.1080/01431161.2014.999878.
Hakala, T., Honkavaara, E., Saari, H., Mäkynen, J., Kaivosoja, J., Pesonen, L., Pölönen, I., 2013. Spectral imaging from UAVS under varying illumination conditions. Int. Arch. Photogramm. Remote. Sens. Spat. Inf. Sci. XL-1/W2, 189–194. https://doi.org/10.5194/isprsarchives-XL-1-W2-189-2013.
Holben, B.N., Eck, T.F., Slutsker, I., Tanré, D., Buis, J.P., Setzer, A., Vermote, E., Reagan, J.A., Kaufman, Y.J., Nakajima, T., Lavenu, F., Jankowiak, I., Smirnov, A., 1998. AERONET—A federated instrument network and data archive for aerosol characterization. Remote Sens. Environ. 66, 1–16. https://doi.org/10.1016/S0034-4257(98)00031-5.
Jacob, F., Olioso, A., Weiss, M., Baret, F., Hautecoeur, O., 2002. Mapping short-wave albedo of agricultural surfaces using airborne PolDER data. Remote Sens. Environ. 80, 36–46. https://doi.org/10.1016/S0034-4257(01)00265-6.
Jacob, W., 2014. Mitsuba Documentation Version 0.5.0 [WWW Document]. URL. https://www.mitsuba-renderer.org/.
Jiang, J., Weiss, M., Liu, S., Rochdi, N., Baret, F., 2020. Speeding up 3D radiative transfer simulations: a physically based metamodel of canopy reflectance dependency on wavelength, leaf biochemical composition and soil reflectance. Remote Sens. Environ. 237, 111614. https://doi.org/10.1016/j.rse.2019.111614.
Li, H., Zhao, C., Yang, G., Feng, H., 2015. Variations in crop variables within wheat canopies and responses of canopy spectral characteristics and derived vegetation indices to different vertical leaf layers and spikes. Remote Sens. Environ. 169, 358–374. https://doi.org/10.1016/j.rse.2015.08.021.
Lopez-Lozano, R., Baret, F., García de Cortázar-Atauri, I., Tisseyer, B., Lebon, E., 2009. Reflectance modeling of vineyards under water stress based on the coupling between 3D architecture and water balance model. In: Remote Sensing for Agriculture, Ecosystems, and Hydrology XI. Proceedings of SPIE. Berlin (Germany). https://doi.org/10.1117/12.830057.
LuxCoreRender, 2018. LuxCoreRender Wiki [WWW Document]. URL. https://wiki.luxcorerender.org/LuxCoreRender_Wiki.
Martin, K.L., Girma, K., Freeman, K.W., Teal, R.K., Stone, M.L., Raun, W.R., 2007. Expression of variability in corn as influenced by growth stage using optical sensor measurements. Agron. J. 99, 384–389. https://doi.org/10.2134/agronj2005.0268.
McBratney, A., Whelan, B., Ancev, T., Mcbratney, A., Bouma, J., 2005. Future Directions of Precision Agriculturew, p. 17.
Nicodemus, F.E., Richmond, J.C., Hsia, J.J., Ginsberg, I.W., Limperis, T., 1977. Geometrical Considerations and Nomenclature for Reflectance (no. NBS MONO 160). National Bureau of Standards, Gaithersburg, MD. https://doi.org/10.6028/NBS.MONO.160.
POV-team, 2013. Introduction to POV-Ray for POV-Ray version 3.7 [WWW Document]. URL. http://www.povray.org.
Pozo, S.D., Rodríguez-Gonzálvez, P., Hernández-López, D., Felipe-García, B., 2014. Vicarious Radiometric Calibration of a Multispectral Camera on Board an Unmanned Aerial System, p. 20.
Qin, W., Goel, N.S., 1995. An evaluation of hotspot models for vegetation canopies. Remote Sens. Rev. 13, 121–159. https://doi.org/10.1080/02757259509532299.
Rabatel, G., Labbé, S., 2015. A fully automatized processing chain for high-resolution multispectral image acquisition of crop parcels by UAV. In: Stafford, J.V. (Ed.), Precision Agriculture '15. Wageningen Academic Publishers, The Netherlands, pp. 135–142. https://doi.org/10.3920/978-90-8686-814-8_16.
Ranson, K.J., Daughtry, C.S.T., Biehl, L.L., Bauer, M.E., 1985. Sun-view angle effects on reflectance factors of corn canopies. Remote Sens. Environ. 18, 147–161. https://doi.org/10.1016/0034-4257(85)90045-8.
Roosjen, P., Suomalainen, J., Bartholomeus, H., Clevers, J., 2016. Hyperspectral reflectance anisotropy measurements using a Pushbroom spectrometer on an unmanned aerial vehicle—results for barley, winter wheat, and potato. Remote Sens. 8, 909. https://doi.org/10.3390/rs8110909.
Roujean, J.-L., Leroy, M., Deschamps, P.-Y., 1992. A Bidirectional Reflectance Model of the Earth's Surface for the Correction of Remote Sensing Data, 97, pp. 20455–20468.
Rouse Jr., J.W., Haas, R.H., Schell, J.A., Deering, D.W., 1973. MOMonitoring vegetation systems in the Great Plains with ERTS. Presented at the third earth Resour. Technol. Satell. Symp 309–317. Doi:citeulike-articleid:12009708.
Sandmeier, S.R., Itten, K.I., 1999. A field goniometer system (FIGOS) for acquisition of hyperspectral BRDF data. IEEE Trans. Geosci. Remote Sens. 37, 978–986. https://doi.org/10.1109/36.752216.
Schaepman-Strub, G., Schaepman, M.E., Painter, T.H., Dangel, S., Martonchik, J.V., 2006. Reflectance quantities in optical remote sensing—definitions and case studies. Remote Sens. Environ. 103, 27–42. https://doi.org/10.1016/j.rse.2006.03.002.
Smith, G.M., Milton, E.J., 1999. The use of the empirical line method to calibrate remotely sensed data to reflectance. Int. J. Remote Sens. 20, 2653–2662. https://doi.org/10.1080/014311699211994.
Suits, G.H., 1983. Extension of a uniform canopy reflectance model to include row effects. Remote Sens. Environ. 13, 113–129. https://doi.org/10.1016/0034-4257(83)90017-2.
Verger, A., Baret, F., Camacho, F., 2011. Optimal modalities for radiative transfer-neural network estimation of canopy biophysical characteristics: evaluation over an agricultural area with CHRIS/PROBA observations. Remote Sens. Environ. 115, 415–426. https://doi.org/10.1016/j.rse.2010.09.012.
Verger, A., Vigneau, N., Chéron, C., Gilliot, J.-M., Comar, A., Baret, F., 2014. Green area index from an unmanned aerial system over wheat and rapeseed crops. Remote Sens. Environ. 152, 654–664. https://doi.org/10.1016/j.rse.2014.06.006.
Vermote, E.F., Tanre, D., Deuzé, J.L., Herman, M., Morcrette, J.-J., 1997. Second simulation of the satellite signal in the solar Spectrum, 6S: an overview. IEEE Trans. Geosci. Remote Sens. 35, 675–686.
Viña, A., Gitelson, A.A., Rundquist, D.C., Keydan, G., Leavitt, B., Schepers, J., 2004. Monitoring maize (*Zea mays* L.) phenology with remote sensing. Agron. J. 96, 1139–1147. https://doi.org/10.2134/agronj2004.1139.
Wang, C., Myint, S.W., 2015. A simplified empirical line method of radiometric calibration for small unmanned aircraft systems-based remote sensing. IEEE J. Sel. Top. Appl. Earth Observations Remote Sensing 8, 1876–1885. https://doi.org/10.1109/JSTARS.2015.2422716.
Wanjura, D.F., Hatfield, J.L., 1988. Vegetative and optical characteristics of four-row crop canopies. Int. J. Remote Sens. 9, 249–258. https://doi.org/10.1080/01431168808954849.
Weiss, M., Troufleau, D., Baret, F., Chauki, H., Prévot, L., Olioso, A., Bruguier, N., Brisson, N., 2001. Coupling canopy functioning and radiative transfer models for remote sensing data assimilation. Agric. For. Meteorol. 108, 113–128. https://doi.org/10.1016/S0168-1923(01)00234-9.
Widlowski, J.-L., Robustelli, M., Disney, M., Gastellu-Etchegorry, J.-P., Lavergne, T., Lewis, P., North, P.R.J., Pinty, B., Thompson, R., Verstraete, M.M., 2008. The RAMI on-line model checker (ROMC): a web-based benchmarking facility for canopy reflectance models. Remote Sens. Environ. 112, 1144–1150. https://doi.org/10.1016/j.rse.2007.07.016.
Zhao, F., Gu, X., Verhoef, W., Wang, Q., Yu, T., Liu, Q., Huang, H., Qin, W., Chen, L., Zhao, H., 2010. A spectral directional reflectance model of row crops. Remote Sens. Environ. 114, 265–285. https://doi.org/10.1016/j.rse.2009.09.018.

Remote Sensing of Environment 200 (2017) 250–262

Contents lists available at ScienceDirect

Remote Sensing of Environment

journal homepage: www.elsevier.com/locate/rse

Combining hectometric and decametric satellite observations to provide near real time decametric FAPAR product

Wenjuan Li[a,*], Frédéric Baret[a], Marie Weiss[a], Samuel Buis[a], Roselyne Lacaze[b], Valerie Demarez[c], Jean-francois Dejoux[c], Marjorie Battude[c], Fernando Camacho[d]

[a] INRA-EMMAH, UMR 1114, 228 route de l'Aérodrome CS 40509, 84914 Avignon Cedex 9, France
[b] HYGEOS, Euratechnologies, 165 Avenue de Bretagne, 59000 Lille, France
[c] CESBIO, Université de Toulouse, CNES/CNRS/IRD/UPS, 18 avenue Edouard Belin, 31401 Toulouse Cedex 4, France
[d] EOLAB, Parc Cientific Universitat de Valencia, C/Catedrático Agustín Escardino, 9, 46980 Paterna, Valencia, Spain

ARTICLE INFO

Keywords:
FAPAR
Decametric
Hectometric
Near real time
Landsat-8
GEOV3
Data fusion

ABSTRACT

A wide range of ecological, agricultural, hydrological and meteorological applications at local to regional scales requires decametric biophysical data. However, before the launch of SENTINEL-2A, only few decametric products are produced and most of them remain limited by the small number of available observations, mostly due to a moderate revisit frequency combined with cloud occurrence. Conversely, kilometric and hectometric biophysical products are now widely available with almost complete and continuous coverage, but the associated spatial resolution limits the application over heterogeneous landscapes. The objective of this study is to combine unfrequent decametric spatial resolution products with frequent hectometric spatial resolution products to improve the temporal frequency and completeness of decametric observations. The study focuses on the fraction of photosynthetically active radiation absorbed by the green vegetation (FAPAR) because of its important role in canopy models and small dependency to scaling issues.

An algorithm is developed to provide near real time estimates of FAPAR called DHF (for Decametric Hectometric Fusion) at a decametric resolution and dekadal time step. It is assumed that the FAPAR time course is described by a second-degree polynomial function over a limited 60-days temporal window for each decametric pixel. To reduce the dimensionality of the problem, landcover classes are considered instead of each individual pixel. For each class, the coefficients of the polynomial function are adjusted using the temporal course of the available decametric FAPAR products, under the constraint of providing a good match with the time course of the hectometric dekadal FAPAR products. The point spread function associated to the hectometric FAPAR products and the possible biases between the decametric and hectometric FAPAR products are explicitly accounted for.

The algorithm was evaluated over a time series of decametric Landsat-8 FAPAR images (30 m) and hectometric (330 m) dekadal GEOV3 FAPAR derived from PROBA-V images acquired in 2014 over a site in the South-West of France.

Results show that the estimated DHF FAPAR products capture well the expected seasonal variation and spatial distribution while improving the temporal frequency and spatial and temporal completeness of the original Landsat-8 products. A leave one out exercise shows that the DHF values are in very good agreement with the Landsat-8 FAPAR (RMSE = 0.05–0.14) that were not used when computing the DHF. This demonstrates the robustness of the algorithm and interest under cloudy regions. Additional comparison with ground measurements collected over 14 sunflower fields along the growth season confirms the good performances of the DHF FAPAR products (RMSE = 0.11).

1. Introduction

A wide range of environmental and agricultural applications at local to regional scales requires accurate and frequent estimation of biophysical vegetation characteristics at the decametric spatial resolution. Satellite sensors such as Landsat-5 (30 m), Landsat-7 (30 m), Landsat-8 (30 m), SPOT4 (20 m), SPOT5 (20 m), FORMOSAT (8 m) and Sentinel-2A (10 m) provide observations at decametric resolutions.

* Corresponding author.
E-mail addresses: wenjuan.li@inra.fr, wenjuan.li122@gmail.com (W. Li).

http://dx.doi.org/10.1016/j.rse.2017.08.018
Received 31 October 2016; Received in revised form 31 July 2017; Accepted 14 August 2017

Several algorithms have already been proposed to generate biophysical products from these sensors, including Jiang et al. (2016), Li and Fang (2015), Li et al. (2015), Verger et al. (2011a), Verger et al. (2011c) and Ganguly et al. (2012). However, the use of these products is always limited by the reduced revisit frequency even degraded by cloud occurrence. Conversely, due to their large swath, kilometric resolution sensors such as VEGETATION, PROBA-V or MODIS provide daily observation of the globe. Few kilometric biophysical products have been generated operationally from these sensors at four to ten days interval, including MODIS (Knyazikhin et al., 1998), CYCLOPES (Baret et al., 2007), GEOV1 (Baret et al., 2013a), GEOV2 and GLASS (Liang et al., 2013; Xiao et al., 2015). They have been extensively validated and applied in several studies (Camacho et al., 2013; Garrigues et al., 2008; Weiss et al., 2007). However, the generally mixed nature of kilometric pixels raises both a scaling issue and difficulties when the landscape object of interest is significantly smaller than the pixel size (Baret et al., 2013a; Shabanov et al., 2003). Recent improvement of the spatial resolution down to hectometers such as PROBA-V (daily 330 m), Sentinel-3 (every 2 days, 300 m), and VIIRS (daily 370 m) is expected to get closer to the spatial resolution required for several applications. However, this is still far from the expected decametric resolution, more suited to the typical length scale of most landscapes (Garrigues et al., 2008).

The current technological constraints of sensors having only a limited number of pixels prevent from getting at the same time a large swath enabling frequent global coverage and keeping a sufficiently high spatial resolution. Constellation of high spatial resolution satellites may solve the question at the expense of an increased cost. Alternatively, the combination of decametric satellite observations with frequent hectometric or kilometric observations is a promising way to increase the temporal frequency of decametric products. Previous studies have demonstrated the ability of fusing observations at different spatial resolutions (Cardot et al., 2008; Faivre and Fischer, 1997; Gao et al., 2006; Hilker et al., 2009; Jiang et al., 2016; Zhu et al., 2015). These methods can be divided into several groups depending on (1) if the land cover map is used; (2) if time series information is used; and (3) if biophysical variables are estimated.

Faivre and Fischer (1997) used a linear unbiased prediction method to estimate reflectance at 20 m spatial resolution from an image with resolution of 400 m by assuming that the reflectance of a mixed pixel is a linear combination of several high resolution pure pixels. This method was later extended to LAI estimation (Faivre and Delecolle, 1997). Under the same assumption, Cardot et al. (2008) proposed a non-parametric statistical model to derive high spatial resolution reflectance or vegetation index from the temporal trajectory of frequent low spatial resolution data. This method was applied by Guyon et al. (2011) to monitor the phenology specific to the deciduous forest from kilometric satellite data. Both methods assume the a priori knowledge of the land cover at the decametric resolution. This constitutes a strong limitation of these methods, particularly over agricultural landscapes where the land cover may change significantly within a single year.

Gao et al. (2006), Hilker et al. (2009) and Zhu et al. (2010) proposed a method to fill gaps in Landsat surface reflectance images using MODIS data over a limited spatial window centered on the missing Landsat pixels. These algorithms do not require ancillary land cover map. However, they need a MODIS image close to the prediction time and are highly dependent on the number of input images (Gevaert and García-Haro, 2015). These requirements may limit the application of these methods in cloudy regions. Alternative methods performing only over multi-year time series of Landsat surface reflectance images have contributed to improve the spatial and temporal completeness of data (Zhu et al., 2015). However, the high dependency of these methods to the availability of Landsat clear images may be limiting in regions with high cloud occurence.

Data fusion methods were proposed for some variables including land surface temperature (Weng et al., 2014) and evapotanspiration (Anderson et al., 2011; Semmens et al., 2016). However, only little attention was paid to biophysical variables such as FAPAR or LAI (Jiang et al., 2016). The fusion of individual biophysical products derived from several sensors accounts implicitly for the differences between their observational characteristics since they are already explicitly used when computing the individual biophysical products. Current kilo/hectometric biophysical products show a good continuity and completeness in both the spatial and the temporal domains. The quasi dekadal temporal sampling also satisfies the requirements of several applications. Jiang et al. (2016) generated spatial consistent and complete Landsat LAI products by fusing Landsat and MODIS reflectance observation using an ensemble of multiscale filter and canopy radiative transfer model inversion. However, this study receives only limited validation and has not been applied for multi-date estimations.

The objective of this study is to develop an algorithm generating near real time decametric FAPAR products at a dekadal time step called DHF (Decametric-Hectometric Fused) from the combination of available decametric and kilometric FAPAR products. The algorithm is applied to Landsat-8 FAPAR products (Baret et al., 2016) and GEOV-3 FAPAR products (Baret et al., 2013b) biophysical products to generate the dekadal 30 m FAPAR time series of DHF products. The study area, satellite data and ground measurements used for the validation are first presented. Then the principles of the algorithm are described. Finally, the performances of the algorithm and corresponding products are evaluated and the limits discussed.

2. Materials

2.1. Study area and ground measurements

The 30 km × 30 km study area is located in the Southwest of France (Fig. 1) (43.52° N, 1.18° E). Several crops including wheat, sunflower, barley, rapeseed and maize are covering most of the area. The site is conveniently located where two Landsat-8 neighboring tracks overlap, offering potentially one image every 7 to 9 days at minimum.

FAPAR was measured six times in the sunflower fields of this region from June 12, 2014 to August 27, 2014, almost every 15 days, by using digital hemispherical photographs (DHP). In each field, a 20 m × 20 m Elementary sampling unit (ESU) was selected for the measurements (Fig. 1). Each ESU was sampled with 12–20 DHPs according to the VALERI spatial sampling protocol (http://w3.avignon.inra.fr/valeri). The DHPs were taken using a Nikon CoolPix 8400 camera equipped with a FC-E8 fisheye lens. The downward-looking camera was fixed at the top of a pole. The height of the pole keeps a constant distance (~1.2 m) between the lens and the top of the canopy (Demarez et al., 2008). All photos within an ESU were processed simultaneously using the CAN-EYE software (http://www4.paca.inra.fr/can-eye) to extract the FAPAR variable. The black-sky FAPAR (GCOS, 2011) observed at 10:00 solar time was used for the ground validation in this study was calculated from CAN-EYE.

2.2. LANDSAT-8 30 m FAPAR product

The derivation of FAPAR products from the Landsat-8 individual images at 30 m spatial resolution is achieved according to the algorithm described in Li et al. (2015). The Landsat-8 30 m FAPAR top of the atmosphere (TOA) reflectance images are first transformed into top of canopy (TOC) reflectance using the algorithm developed by Hagolle et al. (2008) and Hagolle et al. (2010). TOC reflectance in the green, red, near infrared and the two short wave infrared bands are then transformed into FAPAR values using a neural network, based on the BV-NNET (Biophysical Variables Neural Network) tool developed by Baret et al., 2007. FAPAR corresponds here to the black-sky value at 10:00 local solar time which provides a close approximation of the daily integrated black-sky value (Baret et al., 2007). The neural network was trained over a synthetic database made of PROSAIL radiative transfer

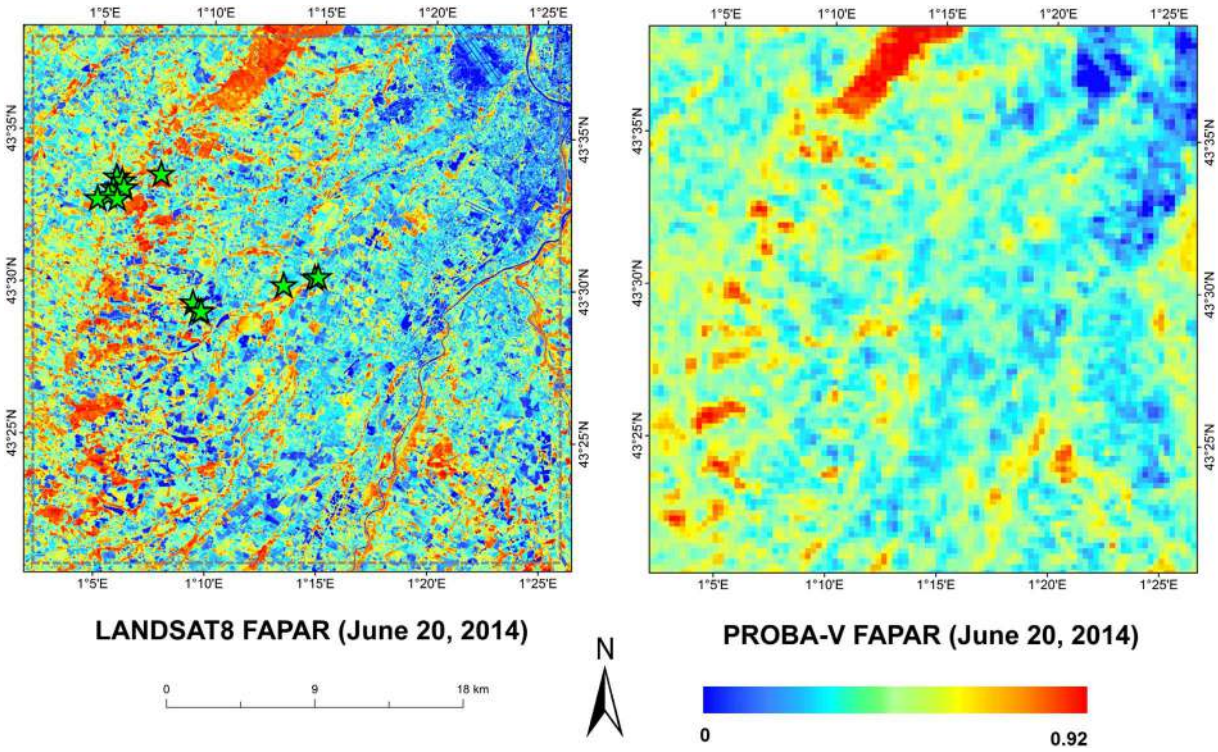

Fig. 1. (a) Landsat-8 FAPAR product and (b) PROBA-V FAPAR derived over the study area for June 20th 2014. Green stars represent the positions of ground measurements over sunflower fields in 2014. (For interpretation of the references to color in this figure legend, the reader is referred to the web version of this article.)

model simulations of TOC reflectance data (Jacquemoud et al., 2009). The distribution and co-distribution laws of the input variables of canopy structure, leaf and soil properties are designed to represent the expected actual distribution and co-distribution over the land surface. In addition to the FAPAR value, a quality flag is associated to each pixel to indicate the cloud contamination or cloud shadow, water or possible failure in the algorithm. The FAPAR 30 m product is provided in its original UTM projection on the WGS-84 datum and was validated over the same site of interest (R^2 = 0.86, RMSE = 0.1) (Li et al., 2015). The nominal Landsat revisit time is 16 days. However, the actual temporal sampling frequency of the FAPAR product derived from LANDSAT-8 varies from 7 to 16 days over the study area where 2 consecutive tracks overlap (Fig. S1).

2.3. GEOV3 FAPAR 330 m product

The FAPAR values at 330 m resolution are derived from the PROBA-V reflectance measurements according to the GEOV3 algorithm developed by Baret et al. (2013b). GEOV3 FAPAR is defined the same way as for Landsat-8. It is generated in near real time every ten days in two consecutive steps. In the first step, the daily FAPAR values are computed for each available PROBA-V observation using a neural network approach. The Neural network is trained over a specific data set corresponding to a weighted average of MODIS Collection5 and CYCLOPES V3.1 FAPAR products similarly to what was proposed by Baret et al. (2013a) for the GEOV1 products. The second step consists in compositing the daily FAPAR products to get the near real time final product at a dekadal time step by smoothing the temporal profile, filling possible gaps and making a short-term projection. Quality flags and quantitative uncertainties are also computed. The performances of GEOV3 products have been evaluated (R^2 = 0.84, RMSE = 0.1) (Camacho et al., 2016). GEOV3 products are provided in a plate carrée projection at 0.0089° spatial resolution (330 m at the equator) on WGS-84 datum. More details on the algorithm can be found in Baret et al. (2013b). The original GEOV3 products were projected in the UTM projection consistently with the Landsat-8 derived FAPAR products.

3. Methods

The general principles are first described with reference to decametric and hectometric FAPAR products. The implementation is then presented with application to LANDSAT-8 30 m and GEOV3/PROBA-V FAPAR products.

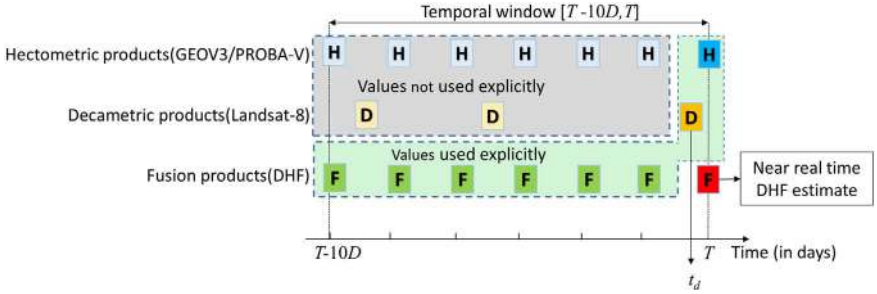

Fig. 2. The three available sources of FAPAR values used to compute the DHF FAPAR near real time estimates for the last dekad of the temporal window. t_d is the measurement date of Landsat-8, T is the last day of the temporal window and D is the length of temporal window expressed in dekads (here D = 6 dekads).

3.1. General principles

3.1.1. The fusion algorithm

The proposed algorithm is based on the combination of three FAPAR products (Fig. 2): (1) the hectometric GEOV3 FAPAR products available at the dekadal time step and derived from PROBA-V, $FAPAR^h$ (h stands for hectometric); (2) the decametric FAPAR products derived from Landsat-8, $FAPAR^d$ (d stands for decametric), available at a frequency ranging between 7 and 16 days with significant missing values due mainly to cloud occurrence; Fig. S1 in the supplementary information section describes the actual Landsat-8 available images and the corresponding percentage of valid pixels; (3) the previous DHF FAPAR products, $FAPAR^f$ (f stands for fusion), available at the decametric resolution and at the dekadal time step.

The computation of the DHF product for date T corresponding to the last day of the temporal window, composed of D dekads, rely on the previous time series of DHF products updated with the last hectometric product at time T (GEOV3/PROBA-V) and the possible decametric (Landsat-8) image available during the last dekad $[T-10, T]$. The other hectometric and possible decametric products existing within $[T-10D, T-10]$ temporal window are not explicitly taken into account in the algorithm since they have already been used to estimate the previous DHF products at T-10.

The algorithm assumes that the dynamics of $FAPAR$ of a given decametric pixel is described by a second degree polynomial in a restricted temporal window $[T-10D, T]$ where D is the length of the temporal window expressed in dekads:

$$FAPAR_i^d(t) = a_i + tb_i. + t^2 c_i \quad (1)$$

where $FAPAR_i^d(t)$ is the $FAPAR$ value at the decametric resolution d for pixel i and for time t and $[a_i, b_i, c_i]$ are the corresponding polynomial coefficients. This assumption is justified by the expected smooth temporal variation of $FAPAR$. Indeed, FAPAR is mainly driven by the green area index and therefore results from incremental processes of growth and senescence. Once the coefficients $[a_i, b_i, c_i]$ are estimated, the DHF value for time t = T is computed. This corresponds to a short-term projection of the polynomials since the last date with a decametric information is generally observed for t < T (see Fig. 2). When the resulting DHF product value at time T is out of the expected physical range for the vegetation canopies ($0 \le FAPAR \le 0.94$) including a small tolerance (± 0.05), it is considered as a missing value. When the FAPAR value is in the tolerance domain ($-0.05 \le FAPAR \le 0.00$ - or $0.94 \le FAPAR \le 0.99$) the DHF value is set to the closest bound of the physical range (0.00 or 0.94).

The coefficients $[a_i, b_i, c_i]$ are estimated by fitting Eq. (1) to the previous DHF products and the possible decametric Landsat-8 image available during the last dekad. In addition, the constraints imposed by the hectometric observations are exploited: the $FAPAR$ value of a pixel I at the hectometric resolution and time t, $FAPAR_I^h(t)$, is the weighted average of decametric resolution pixels $FAPAR^d(t)$ values because of the scaling properties of $FAPAR$ (Weiss and Baret, 2010):

$$FAPAR_I^h(t) = \sum_{i=1}^{k} PSF_i . FAPAR_i^d(t) \quad (2)$$

The weights are described by the point spread function (PSF_i) considering that a limited number (k) of decametric resolution pixels contribute significantly to each hectometric pixel. The PSF of the PROBA-V hectometric $FAPAR$ products must therefore be known. It is computed using quasi-simultaneous Landsat-8 and PROBA-V $FAPAR$ products as shown later. Then, a correction is applied to avoid possible bias between hectometric and decametric products that are derived from the different sensors and algorithms.

A cost function J that uses three sources of information is minimized to estimate the 3 polynomial coefficients over each decametric pixel. The cost function J is the weighted sum of the corresponding three components.

$$J = J_f + J_d + J_h \quad (3)$$

where J_f, J_d and J_h are the components of the cost function associated respectively to the fusion (DHF), decametric (Landsat-8) and hectometric (GEOV3/PROBA-V) $FAPAR$ data. The first component of the cost functions (J_f in Eq. (3)) measures the discrepancy between the fusion products estimated previously, $FAPAR_i^f(t)$, and the new estimated value, $\widehat{FAPAR_i^f(t)}$ computed with Eq. (1) for all the kN decametric pixels in the spatial window and all the first $D-1$ dekads of the temporal window:

$$J_f = \frac{1}{kND} \sum_{i=1}^{kN} \sum_{t=1}^{D} (FAPAR_i^f(t) - \widehat{FAPAR_i^f(t)})2 \quad (4)$$

The second component (J_d in Eq. (3)) measures the discrepancy between the decametric $FAPAR$ product derived from a possible observation at date t_d during the last dekad, $FAPAR_i^d(t_d)$, and the estimated DHF product for the same date, $\widehat{FAPAR_i^f(t_d)}$. It is computed over all the $\alpha 2N$ decametric pixels of the spatial window considered, where α is the resolution ratio, i.e. the hectometric spatial resolution divided by the decametric spatial resolution. In our case, the resolution ratio is close to 11.

$$J_d = \frac{1}{\alpha 2N} \sum_{i=1}^{\alpha 2N} (FAPAR_i^d(t_d) - \widehat{FAPAR_i^f(t_d)})2 \quad (5)$$

The third component of the cost function (J_h in Eq. (3)) measures the discrepancy between the hectometric products and the FAPAR values computed using the estimated decametric fusion products $\widehat{FAPAR_I^f(T)}$. This is evaluated over all the N hectometric pixels of the spatial window for the last date T of the temporal window. PSF_i corresponds to the PSF value for each pixel i that is computed in an independent step. This third component introduces constraints between the individual decametric pixels. Further, because of the PSF, J_h introduces also explicit dependency between neighboring hectometric pixels since common decametric pixels are shared by adjacent hectometric pixels.

$$J_h = \frac{1}{N} \sum_{I=1}^{N} (FAPAR_I^h(T) - \sum_{i=1}^{k} PSF_i \widehat{FAPAR_i^f(T)})2 \quad (6)$$

Note that the three terms of the cost function are normalized by the number of times the individual contributions are summed up, i.e. $[\frac{1}{kND}, \frac{1}{\alpha 2N}, \frac{1}{N}]$ respectively for $[J_f, J_d, J_h]$. If there is no decametric Landsat-8 images available for some temporal windows, J_d is set to zero. Moreover, J_h is set to zero when the hectometric pixel is invalid. Similarly, when the algorithm is initialized, no DHF products are available and J_f is set to zero.

3.1.2. Spatial and temporal operating windows

The spatial and temporal windows used in the algorithm must be specified. The temporal window should be long enough to provide sufficient DHF, decametric and hectometric data, while being short enough to describe the temporal profile faithfully by a second-degree polynomial function. Previous studies (Verger et al., 2011b) showed that a second degree polynomial describes accurately the temporal profile over a 60-days period in most of the cases. A 60-days temporal window provides 7 dekadal DHF values among which the last one is to be estimated, 0 to 5 potential decametric images in the case of the Landsat-8 sensor, and 7 dekadal hectometric FAPAR products (GEOV3/PROBA-V). A 60-days temporal operating window ($D = 6$) is therefore selected. The temporal window is moved towards the future with a dekadal time step. When initializing the algorithm, the temporal window may also be moved towards the past. In this case, the first DHF value among the 7 available one in the 60-days period will be estimated similarly as we will see later.

The size of the spatial operating window should allow accounting for the overlap of the PSF between hectometric pixels while being small enough to ease the computation. A 3 × 3 hectometric pixels window that corresponds to a square kilometer was selected. However, because the extent of the PSF is generally larger than the ground sampling distance (the length of a side of a pixel), a border with decametric pixels will also need to be accounted for. The center of the spatial moving window is moved sequentially over the center over all hectometric pixels in the image. Therefore, except for the borders, the coefficients of all the decametric pixels in Eq. (1) belonging strictly (PSF not accounted for) to a hectometric pixel is estimated 9 times. A weighted average of the 9 DHF FAPAR estimates is computed to provide a unique value:

$$FAPAR_i^f(T) = \sum_{r=1}^{9} \widehat{\omega(r)\, FAPAR_{i,r}^f(T)} \tag{7}$$

where $\widehat{FAPAR_{i,r}^f(T)}$ is the DHF estimates for pixel i at date T coming from one of the 9 spatial windows r and $\omega(r)$ is the associated weight. The weight, $\omega(r=1)$, of the window centered on the considered hectometric pixel is assigned to be equal to that of the other 8 surrounding pixels $\omega(r>1)$. Weights are thus computed as:

$$\omega(r=1) = 0.5;\ \omega(r>1) = 0.0625 \tag{8}$$

This averaging process stabilizes the solution and prevents from discontinuities between spatial windows.

3.1.3. Initialization of the algorithm

The algorithm requires 6 existing DHF dekadal values at each dekadal time step when running forward in near real time. When the algorithm is applied over the first temporal window of the time series, no DHF decametric products is available yet. An initialization process should therefore be developed to get a first estimate of the DHF. This is completed in two steps: (1) find along the available time series a temporal window that contains enough Landsat decametric images to provide a good estimate of the DHF products; (2) then run backward the algorithm from this initialization window to generate the DHF values down to the start of the first temporal window of the time series (Fig. 3). The algorithm is run in the forward regular mode as described in Fig. 2 to increase the time series by including the most recent dekads.

The initialization step should start by identifying the temporal operating window in the time series that provides the maximum number of Landsat-8 images with a maximum of valid pixels. The inputs of the processing for this first window include all the 7 dekadal hectometric FAPAR images and all the available decametric images. Outputs are the DHF products for the 7 dekadal dates. At least three Landsat-8 decametric images should be used. When it is not possible to find three Landsat-8 decametric images within a 60-day temporal window, the time period should be extended to include three decametric images. If the decametric images have invalid pixels, it is not possible to fill them with the DHF estimates since they do not exist yet. In this case, small clusters of invalid pixels are filled with the neighboring values. If larger clusters of invalid pixels are observed, specific actions are undertaken that will not be detailed here for the sake of brevity. The reader can find the full description in the product ATBD (Baret et al., 2016).

If the initialization temporal window does not correspond to the first temporal window of the time series, the backward mode is triggered. It runs similarly to what is described for the regular forward near real time mode, except that the DHF of the first dekad of the temporal window is estimated instead of the last one (compare Fig. 2 with Fig. 3). This process is repeated down to the start of the temporal series.

3.2. Calibrating the point-spread-function of hectometric FAPAR products

The weights, PSF_i, of the point spread function (Eq. (2)) describing the aggregation process of decametric images to obtain the equivalent hectometric values need thus to be estimated. They account for several factors (Weiss et al., 2007) including the PSF of the instrument for each band, the geolocation uncertainty, the effect of the reprojection (from raw images to plate-carrée then to UMT), the atmospheric scattering, the viewing geometry and the temporal compositing of the daily hectometric images to produce the dekadal FAPAR values (Baret et al., 2013b). The PSF is described by truncated Gaussian functions using the Full Width at Half Maximum independently for the longitudinal ($FWHM_x$) and the latitudinal ($FWHM_y$) directions (Mira et al., 2015). The PSF is truncated when > 95% of the contribution to the signal is reached. The total extent of the PSF defined by ($Xmax, Ymax$) thus depends on the FWHM. Because of possible geolocation differences between the hectometric and decametric images, a shift in East-West (Δx) and North-South (Δy) directions is also considered. The four unknowns $[FWHM_x, FWHM_y, \Delta x, \Delta y]$ are retrieved by maximizing the correlation coefficient between the aggregated decametric (Landsat-8) FAPAR images and the hectometric (GEOV3) FAPAR products according to the scheme shown by Mira et al. (2015). For each image pair of decametric and hectometric images with about the same date, the $[FWHM_x, FWHM_y]$ are allowed to vary from 120 m to 960 m by 30 m steps in both directions, while the Landsat-8 shifts, $[\Delta x, \Delta y]$ varied from − 330 m to 330 m by 15 m steps. In total, 379,456 combinations of PSF values in x and y directions are generated and the one providing the highest correlation between the actual GEOV3 FAPAR and the aggregated Landsat-8 FAPAR is selected. The aggregated pixels that include invalid Landsat-8 pixels are discarded from the computation.

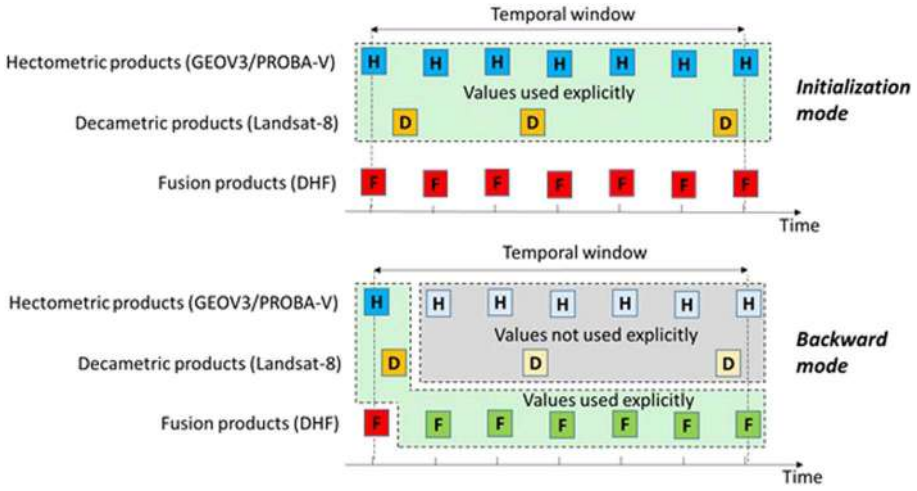

Fig. 3. Scheme showing the initialization and backward modes. The same conventions as used in Fig. 2 to describe the forward mode are used here.

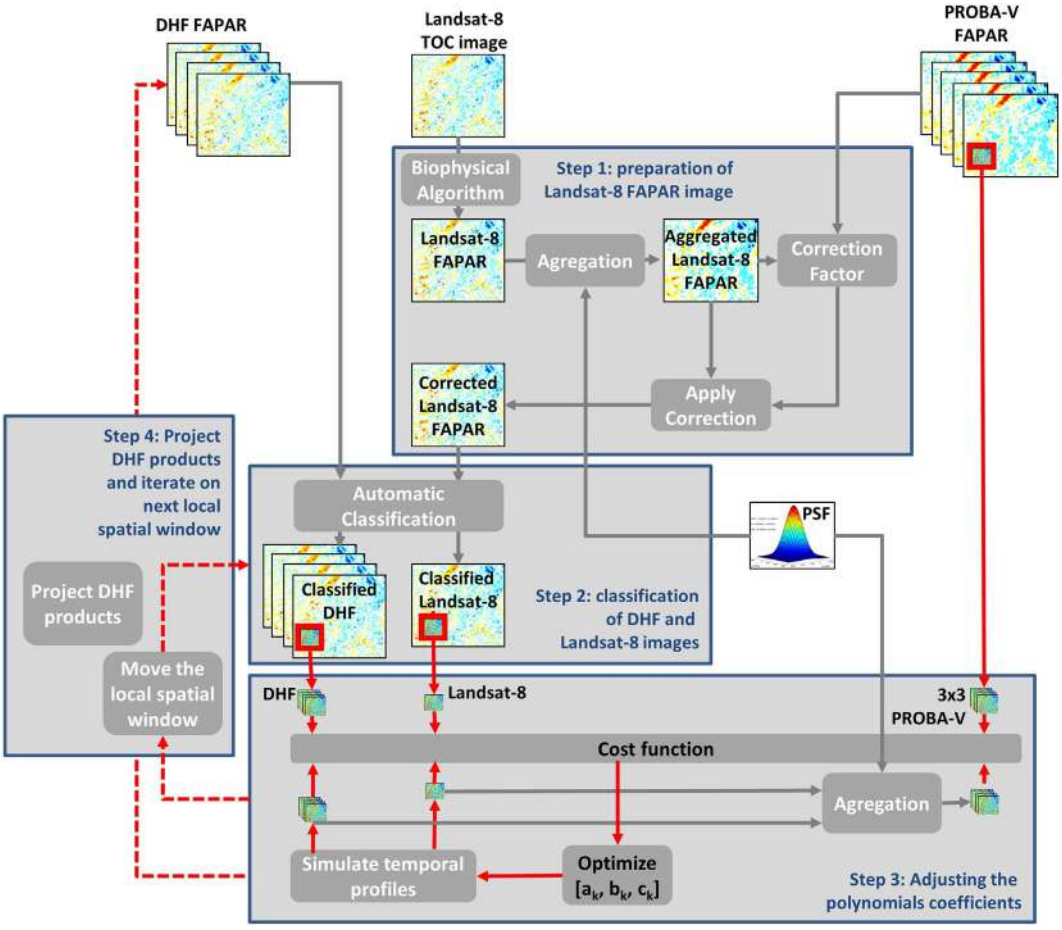

Fig. 4. Flowchart of the four steps of fusion main algorithm.

3.3. Implementation

The algorithm includes four steps: (1) preparation of the decametric images to fill possible invalid pixels and make the FAPAR values consistent with the hectometric products; (2) classification of the pixels to reduce the dimensionality of the problem; (3) adjusting the polynomial coefficients; (4) and production of the DHF FAPAR value and iterate on the next local spatial window. These four steps are sketched in Fig. 4 and detailed in the following.

3.3.1. Preparation of the decametric Landsat-8 FAPAR images (step1)

The algorithm combines hectometric resolution data (GEOV3/PROBA-V) with decametric resolution data (Landsat-8) when available. The aggregation process described by Eq. (2) requires completeness of the Landsat-8 image. When a Landsat-8 pixel is flagged as invalid, cloud or cloud shadow, it is filled using an estimation derived from a second degree polynomial fit over the 6 corresponding DHF values in the considered temporal window. When the estimated value is outside the [0, 0.94] domain of validity for FAPAR, it is set to the closest bound. This filling process is thus fully consistent with the way DHF products are generated.

The combination of Landsat-8 and GEOV3/PROBA-V resolution FAPAR data requires a high degree of consistency between both products. However, some biases may be observed due to differences between sensor characteristics, atmospheric correction or retrieval algorithms. A correction is therefore necessary to remove these differences to keep high degree of consistency between the two products. This correction is applied to the Landsat-8 images that may show less temporal consistency as compared to the GEOV3 FAPAR products that already results from a temporal compositing. It is calibrated on each individual Landsat-8 image by comparing the aggregated Landsat-8 FAPAR values using Eq. (2), with the GEOV3 FAPAR value estimated at the same date. For this purpose, a second-degree polynomial interpolation is applied using the 7 dekadal GEOV3 products available over the temporal operating window. Finally, a linear fit between the aggregated Landsat-8 FAPAR values and the corresponding interpolated GEOV3 FAPAR values is computed. The corresponding slope and intercept are used to correct the Landsat-8 FAPAR values.

3.3.2. Considering classes rather than pixels and classification (step2)

Running the algorithm over all individual decametric pixels is computationally very demanding. It was therefore preferred running it at the class level considering that a limited number of classes may represent the dynamics of each Landsat-8 pixel with a good accuracy in a restricted spatial and temporal window. A classification of each pixel is made using the FAPAR temporal profiles described by the 6 first DHF products and the possible Landsat-8 images available. The classification is applied over the whole image rather than over the local operating spatial windows to prevent from possible discontinuities between operating spatial windows. The 'Kmeans' automatic classification algorithm is used because of its performances and computational efficiency (Hartigan and Wong, 1979). The algorithm requires the number of classes to be specified. It should compromise between a large number required to accurately describe the heterogeneity of the study area and a limited number of classes to ease the computation. In our case, after trial and error tests (results not presented for the sake of brevity) 25 classes were selected as optimal. The reduction of the problem size is thus drastic: 25 sets of coefficients to be estimated in a 3×3 hectometric window as compared to > 900 sets of coefficients when considering the pixels separately.

3.3.3. Estimating $[a_k, b_k, c_k]$ coefficients for each class (step3)

The 3 coefficients of the second degree polynomials are estimated for each individual operating spatial and temporal window according to the general principles presented earlier. The fitting of the three coefficients for the 25 classes is completed by minimizing the cost function [3] under the constraints that the estimated FAPAR values keep within the physical bounds of FAPAR. The interior-point algorithm (Byrd et al., 2000; Byrd et al., 1999) is used to estimate coefficients $[a_k, b_k, c_k]$ simultaneously for the 25 classes. This algorithm is selected due to its ability to handle large and sparse optimization problems. The values from the previous dekad of the same temporal window are used as the initial guess for the three coefficients of each class. Finally, the FAPAR value for the last dekad (respectively every dekads for the initialization, and first dekad for the backward mode) of the temporal window is computed for each class and then distributed on the spatial operating window according to the classification map of the corresponding current temporal window.

3.3.4. Project DHF products and iterate on the next local spatial window (step4)

Once the polynomial coefficients of a spatial window are estimated, the DHF products corresponding to the decametric FAPAR values of the last day of the considered temporal window is computed. The algorithm then moves to the next local spatial window in an iterative way, until DHF FAPAR in all spatial windows are calculated. The new generated DHF FAPAR data will later participate to the computation of DHF for the next temporal window.

A quality flag associated to each dekad and pixel of the DHF product provides information on the number of valid Landsat-8 images available in the temporal window and the nature of the Landsat-8 pixel (out of range, cloud, water or snow). Further, two additional quantitative quality indicators document the difference (1) between the DHF product and the possible (corrected) Landsat-8 FAPAR value at the date of this Landsat-8 image, and (2) between the aggregated DHF value and the corresponding GEOV3 FAPAR product. Finally, when the estimated FAPAR value is out of range (including the tolerance margins), a specific flag is raised.

4. Results

The calibration of the GEOV3 PSF is first presented. Then, the spatial and temporal consistency of the DHF products is discussed at the decametric and then at the hectometric resolutions. Finally, the DHF products are compared with available ground measurements for accuracy assessment.

4.1. PSF of the GEOV3 products

We selected six pairs of GEOV3 and Landsat-8 FAPAR images having less than two days difference on which we adjusted the $[FWHM_x, FWHM_y, \Delta x, \Delta y]$ parameters (Table 1). Results show that the correlation between the aggregated Landsat-8 values and the GEOV3 products is always very high (Table 1), providing confidence in the parameter adjustment. Further, a single prominent maximum of the correlation coefficient was observed for all the dates when the PSF was evaluated, confirming the uniqueness of the solution. The optimal FWHM varies from 270 m to 360 m in the East-West direction, and from 330 m to 360 m in the North-South direction. This led to a PSF full extent of $810\,m \le X_{max} \le 870\,m$ and $690\,m \le Y_{max} \le 870\,m$, i.e. between two to three times the GEOV3 ground sampling distance (330 m). The shift between Landsat-8 and GEOV3 is around 100 m and is relatively constant with time. It is close to 0.3 PROBA-V pixels that correspond to the expected geolocation uncertainty.

Because of the good consistency in the PSF and shift values obtained across several pairs of Landsat-8 and GEOV3 images, it was proposed to calibrate the PSF only once over a set of pairs of Landsat-8 and GEOV3 images before triggering the fusion algorithm. The median value of the PSF and shift observed over the 6 pairs of images (Table 1) were used in this study for all the Landsat-8 and GEOV3 images over the South-West site in 2014: $[FWHM_x, FWHM_y, \Delta x, \Delta y] = [330, 360, 105, 75]$. However, the PSF probably needs to be recalibrated from site to site, particularly when the latitude changes because of the impact of the re-projection of the GEOV3 images into the Landsat-8 grid system.

Finally, the linear relationship between the aggregated Landsat-8 and GEOV3 FAPAR products provides a correction for the Landsat-8 FAPAR ($FAPAR_{Landsat\_8}{}^{original}$), to get values ($FAPAR_{Landsat\_8}{}^{corrected}$) that are more consistent with the GEOV3 FAPAR. Results over the six pairs of images show that the correction equation appears relatively stable for the study area (Table 1):

$$FAPAR^{corrected}_{Landsat,8} = 0.84 FAPAR^{original}_{Landsat,8} + 0.11 \quad (9)$$

4.2. Consistency between DHF and Landsat-8 FAPAR products

4.2.1. Temporal consistency

A sample of four pixels located on the edge and center of the image is used to illustrate the temporal consistency of the products. The original Landsat-8 FAPAR shows artifacts and gaps over the whole year (Fig. 5), confirming the observations by Li et al. (2015). This may be due to residual effects of the atmospheric correction and possible directional effects that are poorly accounted for. The correction of Landsat-8 FAPAR values achieved using the GEOV3 FAPAR as a reference (see §3.3.1) improves the smoothness. However, some fluctuations are still observed probably because the correction is computed over all the GEOV3 pixels, averaging possible particularities on some decametric pixels.

The DHF temporal profile is much smoother than that of the corrected Landsat-8 (Fig. 5). This comes mainly from the polynomials fitting and partly from a possible class averaging effect as well as smoothness induced by the GEOV3 constraint. However, the general agreement between DHF and Landsat-8 corrected FAPAR temporal

Table 1
The optimal PSF and shift observed over the 6 pairs of Landsat-8 and GEOV3 FAPAR products. $FWHM_x$ (respectively $FWHM_y$) represents the Full Width at Half Maximum in the East-west (respectively North-south) directions. X_{max} (respectively Y_{max}) represents the full width of the PSF in the East-west (respectively North-south directions).Δx (respectively Δy) represents the Landsat-8 image shift in East-west (respectively North-south) directions with the starting reference on the top-left corner of GEOV3 pixel.

Date		FWHM (m)		Full width (m)		Shift (m)		R^2	Correction		
GEOV3	Landsat-8	$FWHM_x$	$FWHM_y$	X_{max}	Y_{max}	Δx	Δy		Slope	Offset	RMSE
10/02/2014	12/02/2014	330	360	870	810	105	75	0.83	0.84	0.07	0.07
10/03/2014	09/03/2014	360	360	870	870	105	105	0.87	0.92	0.08	0.08
10/04/2014	10/04/2014	330	360	870	810	105	75	0.88	0.84	0.07	0.07
20/05/2014	19/05/2014	270	330	810	690	75	15	0.85	0.79	0.08	0.08
20/06/2014	20/06/2014	330	360	870	810	105	75	0.87	0.80	0.05	0.05
31/08/2014	01/09/2014	330	360	870	810	105	75	0.92	0.94	0.07	0.07
Median		330	360	870	810	105	75	0.87	0.84	0.11	0.07

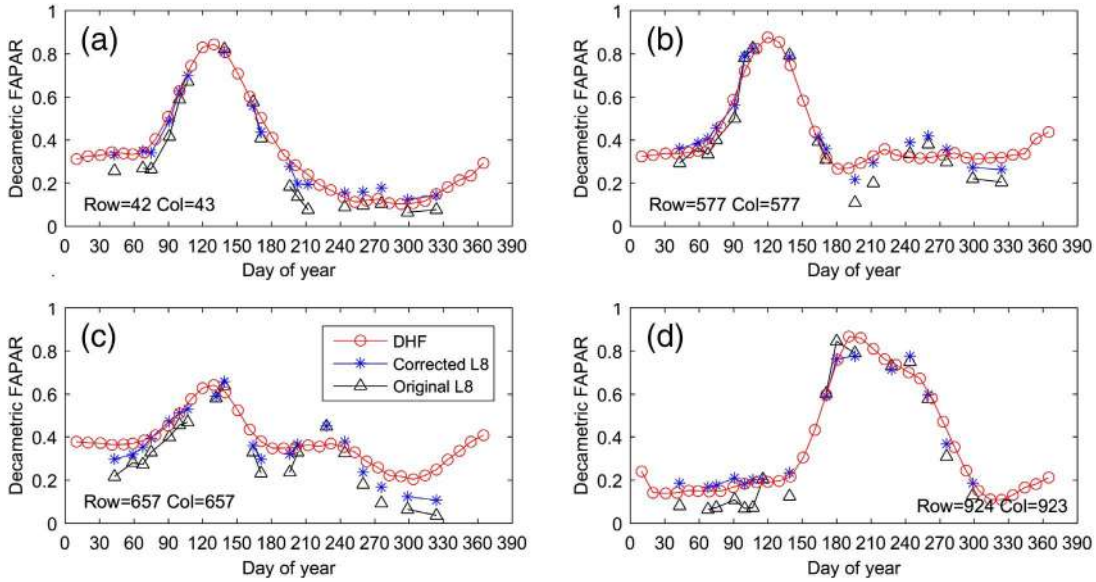

Fig. 5. Temporal distribution of DHF FAPAR, corrected Landsat-8 FAPAR and original Landsat-8 FAPAR over the four sample pixels in 2014. Row and Col correspond to the position of the decametric pixel in the whole 30 km × 30 km study area (Fig. 1).

profiles indicates that very little information was lost when operating the algorithm at the class level rather than at the pixel level. The predicting capacity of the algorithm is demonstrated at the beginning of the year when no Landsat-8 images are available: in this case, DHF provides reasonable estimates of FAPAR using the information coming from the GEOV3 FAPAR.

4.2.2. Spatial consistency

The spatial distribution of DHF FAPAR products is evaluated by mapping the difference with the original Landsat-8 FAPAR and corrected Landsat-8 FAPAR over two particular dates.

On March the 16th corresponding to the first temporal window (DOY 41–DOY 100), the original Landsat-8 FAPAR is almost complete (no clouds), although it shows several small gaps due to the input reflectance or output FAPAR out of the expected range as well as gaps on the border of the image (Fig. 6a). The corrected Landsat-8 FAPAR shows the same gaps as in the original Landsat-8 FAPAR image because no temporal interpolation is performed in the first temporal window. The estimated DHF image (Fig. 6c) presents a spatial distribution very close to the corrected Landsat-8 images (Fig. 6b) with a RMSE value of 0.04 (Fig. 6d). The larger differences between DHF and original Landsat-8 FAPAR are mainly due to the inherent bias between Landsat-8 and GEOV3 FAPAR. Note that the DHF image (Fig. 6c) presents a border of 330 m width with missing values due to the PSF effect of GEOV3 products.

On the 31st of July, the algorithm is run in the forward mode (DOY 161–DOY 222). The Landsat-8 original image shows a significant fraction of pixels contaminated by clouds (Fig. 7a). Cloudy pixels are filled with the values computed from the polynomial fit of the existing DHF values. The correction factor to get Landsat-8 FAPAR values consistent with those of GEOV3 may therefore be slightly biased. Indeed, the cloudy pixels are filled with DHF products generated from already corrected FAPAR values. The bias should therefore be maximum when clouds represent 50% cover fraction. However, the gap filling is mandatory since the computation of the correction requires aggregating the Landsat-8 pixels to be compared with those of GEOV3. But the projection corresponding to the application of the polynomial function on dates out of the period where it was adjusted can lead to values out of the expected range. These pixels will be flagged as invalid and will not be used (Fig. 7b). The DHF derived FAPAR (Fig. 7c) shows a complete spatial coverage and agrees well with the corrected Landsat-8 FAPAR (Fig. 7d), with however degraded performances (RMSE = 0.08) due to the presence of clouds and the associated loss of information. Nevertheless, the spatial patterns appear quite well preserved, even at the location of the clouds on the Landsat-8 image.

4.2.3. Validation of DHF using the leave-one-out method

The performances of the DHF products are evaluated by comparison with each individual Landsat-8 derived FAPAR values. However, to better evaluate the accuracy of the DHF products without comparing

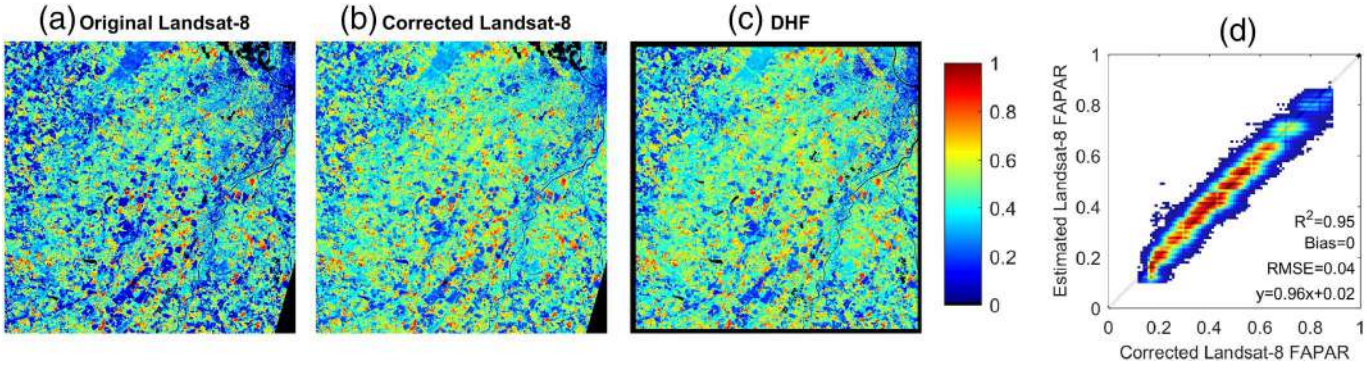

Fig. 6. Spatial distribution observed over Southwest site on 16 March 2014 of (a) the original Landsat-8 FAPAR; (b) the corrected Landsat-8 FAPAR; (c) the DHF FAPAR; (d) the relationship between the corrected Landsat-8 and the DHF FAPAR values. Black pixels represent invalid pixels due to clouds, cloud shadow, water, snow or image borders.

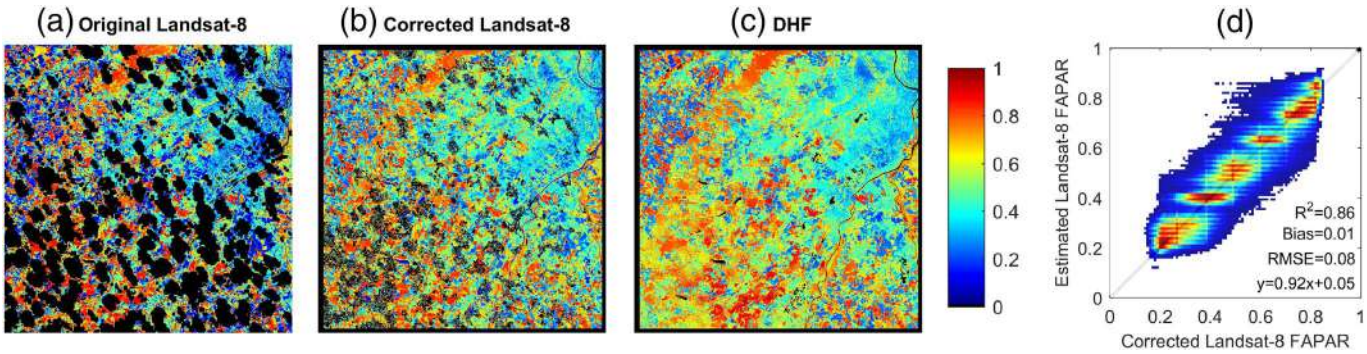

Fig. 7. Spatial distribution observed over Southwest site on 31 July 2014 of (a) the original Landsat-8 FAPAR; (b) the corrected Landsat-8 FAPAR; (c) the DHF FAPAR; (d) the relationship between the corrected Landsat-8 and the DHF FAPAR values. Black pixels represent invalid pixels due to clouds, cloud shadow, water, snow or image borders.

with the Landsat-8 images that were used in the algorithm, a leave-one-out method was introduced: a Landsat-8 image will not be used in the algorithm and the resulting DHF product will be compared to this Landsat-8 image derived FAPAR values. This process is repeated on each Landsat-8 image of the time series. The initial temporal window is not used in the leave-one-out test, therefore the first Landsat-8 measurement date starts from DOY107 of 2014. This analysis is performed on a sub region of 5 km × 5 km area for computation efficiency. The DHF products are interpolated at the date of the Landsat-8 image. The comparison is achieved both with the original Landsat-8 derived FAPAR values as well as with the corrected Landsat-8 FAPAR values ensuring better consistency with the GEOV3 FAPAR products.

As expected, results show that the correction of the Landsat-8 derived FAPAR products improves significantly the agreement with the DHF products (Table 2). The correction improves the RMSE by 0.05, R^2 by 0.04 and the bias is reduced by 0.01 both for the leave-one-out DHF version (remove) and the DHF computed using all the Landsat-8 images (used) (Table 2).

The DHF computed with all the Landsat-8 images available used (used in Table 2) agrees well with the Landsat-8 corrected FAPAR values with $0.05 < RMSE < 0.12$, $0.66 < R^2 < 0.97$ and $-003 < bias < 0.03$ (Table 2). When comparing with the corrected Landsat-8 FAPAR image not used to compute the DHF product (remove in Table 2), the RMSE and R^2 degrades only slightly. This demonstrates the robustness of the proposed algorithm for estimating DHF FAPAR values on most situations. However, the algorithm partly fails on DOY171 (RMSE = 0.12 and R^2 = 0.47 in Table 2), when no Landsat-8 FAPAR is used to document the high rate of change of FAPAR profile as observed here during the senescence period of winter crops.

4.3. Consistency between aggregated DHF FAPAR and original GEOV3 FAPAR products

Four GEOV3 pixels located on the edge and center of the GEOV3 image are selected for visual inspection of the temporal consistency between the DHF FAPAR aggregated at GEOV3 FAPAR spatial resolution using the PSF (Eq. (2)) and the original GEOV3 FAPAR. Results (Fig. 8) confirm the expected very good agreement between the dynamics of both FAPAR values. However, some small differences are observed due to remaining discrepancies between the Landsat-8 FAPAR corrected values and the GEOV3 products.

The consistency between both products is further analyzed by comparing their spatial distribution for three specific dates: doy 10 in the backward mode, doy 100 in the first initial temporal window and doy 283 in the forward mode. Results (Fig. 9) show a very good agreement (R^2 = 0.81–0.9, RMSE = 0.03–0.06) between the aggregated DHF FAPAR images and GEOV3 FAPAR for these three dates. However, some missing values are observed on the aggregated DHF image. This can be due to FAPAR values estimated out of the physical range, which prevents from applying the aggregation process. These situations mostly correspond to low values of FAPAR and when a limited constraint by the Landsat-8 information is imposed because of large cloud contamination of the Landsat-8 images.

A systematic evaluation of the RMSE values computed over each

Table 2
RMSE, R^2 and Bias between DHF products and the original ('Original') or corrected ('Corrected') Landsat-8 products on each Landsat-8 measurement date. The DHF FAPAR products were generated using either all the Landsat-8 images available ('Used') or when the Landsat-8 image used for performance evaluation was removed ('Remove') from the time series for DHF computation using the leave-one-out method.

	Day of year												
	107	132	139	164	171	180	196	203	212	228	244	260	276
RMSE													
Remove/Original	0.115	0.095	0.138	0.100	0.133	0.156	0.171	0.139	0.135	0.159	0.161	0.175	0.164
Remove/Corrected	0.078	0.053	0.113	0.088	0.120	0.099	0.140	0.072	0.101	0.090	0.126	0.125	0.119
Used/Original	0.090	0.090	0.090	0.080	0.080	0.100	0.120	0.140	0.110	0.130	0.160	0.130	0.160
Used/Corrected	0.050	0.050	0.070	0.070	0.070	0.060	0.090	0.070	0.070	0.060	0.120	0.090	0.100
R^2													
Remove/Original	0.915	0.894	0.810	0.717	0.473	0.555	0.656	0.825	0.826	0.657	0.577	0.590	0.641
Remove/Corrected	0.915	0.957	0.810	0.727	0.471	0.705	0.684	0.909	0.828	0.853	0.578	0.590	0.641
Used/Original	0.960	0.918	0.933	0.818	0.800	0.826	0.878	0.815	0.907	0.815	0.660	0.759	0.748
Used/Corrected	0.960	0.965	0.933	0.824	0.799	0.884	0.884	0.909	0.908	0.905	0.661	0.759	0.748
Bias													
Remove/Original	0.058	− 0.019	0.054	− 0.020	0.008	− 0.013	0.004	− 0.022	0.053	− 0.065	0.054	0.095	0.079
Remove/Corrected	0.034	− 0.012	0.039	− 0.038	− 0.025	− 0.004	− 0.031	− 0.039	0.012	− 0.046	− 0.001	0.032	0.012
Used/Original	0.043	− 0.014	0.038	− 0.012	0.017	− 0.006	0.013	− 0.011	0.043	− 0.054	0.074	0.056	0.093
Used/Corrected	0.019	− 0.010	0.023	− 0.031	− 0.015	− 0.016	− 0.021	− 0.031	0.004	− 0.034	0.019	− 0.007	0.026

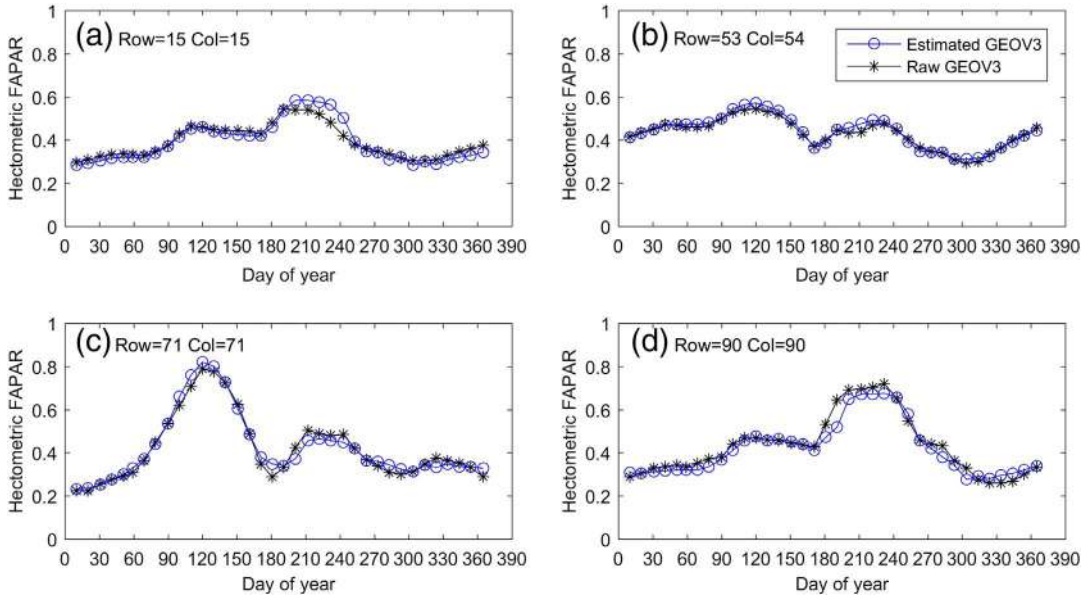

Fig. 8. Temporal distribution of estimated GEOV3 from aggregation of DHF FAPAR and original GEOV3 FAPAR profiles. Four sample pixels are selected on the center or edge of GEOV3 images.

dekad of the time series confirms the very good agreement between the aggregated DHF FAPAR products and the GEOV3 FAPAR values (Fig. 10). The RMSE ranges from 0.03 (DOY 31) to 0.08 (DOY 253).

4.4. Validation with ground measurements

The FAPAR values measured with DHP over the 14 sunflower ESUs available along the growing season are compared with the DHF and original or corrected Landsat-8 FAPAR values. To minimize the effect of the delay between the date of the ground measurements and that of the Landsat-8 FAPAR products, the ground FAPAR measurements are linearly interpolated at the Landsat-8 image acquisition dates if there is < 5 days difference. This resulted in 29 data points. Conversely, for comparing the DHF products with the ground measurements, the DHF products are interpolated at the ground measurements dates since DHF products are dekadal smooth products. Results focusing on the 29 data points used for comparison with the original or corrected Landsat-8 data show that the original Landsat-8 FAPAR correlates well with the ground measurements (Fig. 11a). The performances are only slightly improved after the correction using GEOV3 FAPAR (Fig. 11b). Both Landsat-8 FAPAR estimates have 75% of the points within the Global climate observing system (GCOS) requirements (dotted lines in Fig. 11) (max 10% accuracy, GCOS, 2011). Over the same 29 points, the performance of DHF FAPAR is very close to the original and the corrected Landsat-8 FAPAR data (Table 3). Finally, the DHF FAPAR products were compared with 36 additional available ground measurements over the sunflower fields. They correspond to ground data collected outside the ± 5 days period around the Landsat-8 image dates. Results over the total 65 point data available show a slight degradation of the performances (Fig. 11c, Table 3) with some underestimation for the medium to large FAPAR values. Nevertheless, still 75% of the points are lying within the GCOS requirements for FAPAR products.

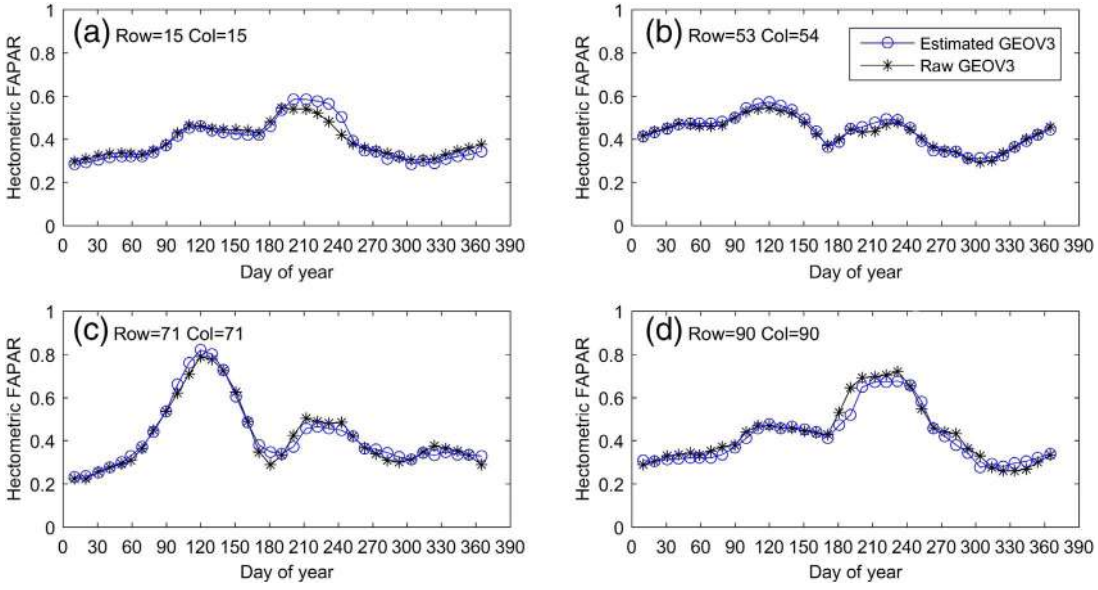

Fig. 9. Spatial distribution of (a, d, g) original GEOV3 FAPAR, (b, e, h) aggregated DHF FAPAR at GEOV3 spatial resolution and (c, f, i) frequency of their differences; (a, b, c) correspond to DOY 10, (d, e, f) to DOY 100 and (g, h, i) to DOY 283.

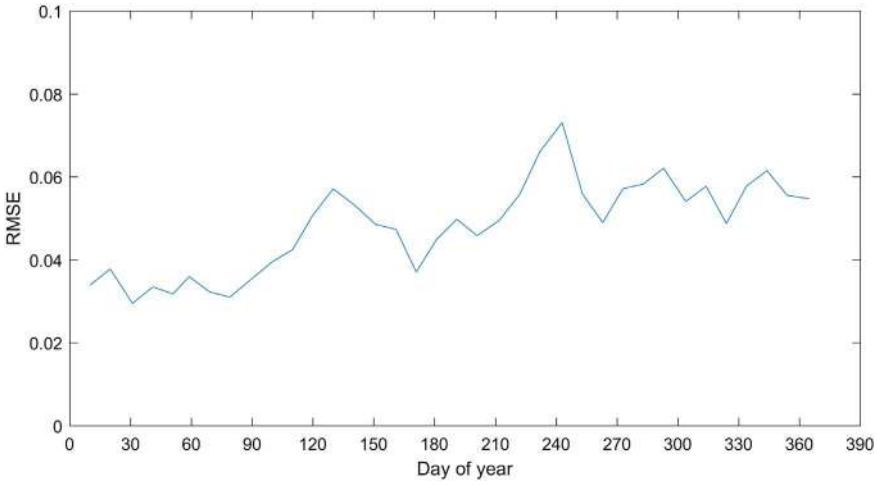

Fig. 10. The seasonal variation of RMSE between aggregated DHF FAPAR at GEOV3 spatial resolution and original GEOV3 FAPAR in 2014 over Southwest site.

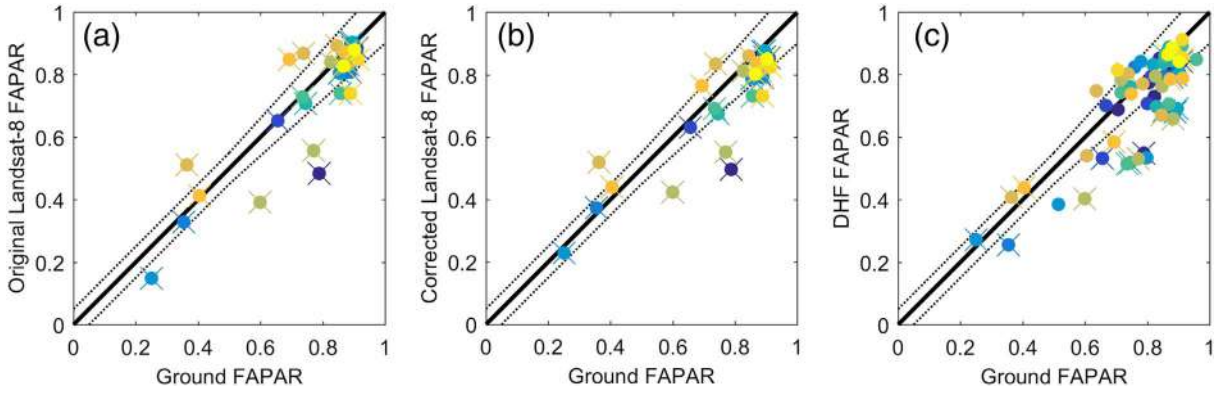

Fig. 11. Comparison of the ground FAPAR measurements with (a) the original Landsat-8 FAPAR, (b) the corrected Landsat-8 FAPAR and (c) the DHF FAPAR products. Results observed on 29 data points over the 14 sunflower fields. Each field corresponds to a particular color. The black solid line is the 1:1 line. Dotted lines represent the GCOS (2011) requirements boundaries.

Table 3
Comparison between the ground FAPAR measurements and the original Landsat-8 FAPAR, the corrected Landsat-8 FAPAR and the DHF FAPAR products. N represents the number of ground data used in the validation.

	N	R^2	Bias	RMSE	Linear regression
Original Landsat-8	29	0.76	− 0.04	0.104	y = 0.94x + 0.01
Corrected Landsat-8	29	0.78	− 0.05	0.102	y = 0.82x + 0.08
DHF FAPAR	29	0.75	− 0.09	0.12	y = 0.84x + 0.02
DHF FAPAR	65	0.66	− 0.07	0.11	y = 0.87x + 0.04

5. Discussion

The proposed DHF algorithm uses a biophysical product, FAPAR, which is assumed to present a smooth dynamics as outlined earlier. An alternative method was proposed by Lewis et al. (2012) using reflectance as inputs and outputs of an assimilation scheme. It preserves the spectral consistency thanks to a radiative transfer model. Such approaches are thus very appealing as already outlined by Geiger et al. (2004). The spectral consistency between the decametric and hectometric data is also well preserved in the DHF algorithm since the fusion between the two resolution data is achieved at the biophysical FAPAR product level.

The proposed DHF algorithm is based on a physically sound approach that bears on two main assumptions: (1) the smoothness of the FAPAR temporal course over a restricted temporal window (60 days in this case) and (2) the scaling independency of FAPAR. The first assumption is mostly verified over the study site considered here. However, it may be violated particularly in case of harvest occurring during the vegetation growth cycle such as for cultivated grasslands, silage maize, forest clear cut or when hazards are suddenly changing the surface characteristics such as fire or flood events. The second assumption on the scaling properties appears to be largely verified according to the good agreement observed between the decametric DHF or Landsat-8 aggregated FAPAR products and the GEOV3 hectometric products. The algorithm provides smooth and consistent FAPAR estimates at the decametric resolution, with an accuracy close to RMSE ≈ 0.1 while 75% of the values are within the GCOS requirements. The good performances of the algorithm are also coming from the fact that the hectometric constraint is relatively strong since only a limited number of classes of land cover are contained in a hectometric pixel as compared to what is contained in a kilometric pixel for which the constraint would be much weaker. Although the ground validation exercise was restricted to sunflower crops, the good agreement between the original Landsat-8 and the DHF values observed with the leave-one-out method indicates the potentials of the proposed method.

The performances of the DHF algorithm were evaluated using GEOV3/PROBA-V dekadal FAPAR products and Landsat-8 images over a place where the Landsat sensor swaths are overlapping between two consecutive tracks, dividing by about two the 16 days nominal Landsat-8 revisit period. Over the considered time series and site, the actual average delay between two consecutive clear pixels was around 20 days due to cloud coverage if the whole year is considered. It is reduced to around 12 days during the growing season because only few images are taken at the beginning or the end of year. The results of the leave-one-out validation test demonstrated that the performances are only little dependent on the presence of the last Landsat-8 image before the

considered dekadal date when the DHF product is computed. However, further investigation should evaluate the actual impact of the number of clear decametric observations on the product performances.

The recent availability of the Sentinel-2 (Drusch et al., 2012) and Sentinel-3 (Donlon et al., 2012) images will probably reinforce the interest of this type of algorithm, particularly in places with frequent cloud occurrence. The PSF of the FAPAR products derived at the hectometric resolution with Sentinel-3 should be properly calibrated. Although the PSF appeared to be relatively stable over time on the studied site, this should be further verified in more diversified situations, particularly regarding the expected effect of the latitude of the site.

6. Conclusion

This study presented an algorithm to generate a dekadal FAPAR product at decametric resolution from the combination of existing decametric (Landsat-8) and hectometric (GEOV3) FAPAR products. It applies to any vegetation type without prior knowledge on the land cover. The method can be run in near real time mode. The proposed method assumes that FAPAR time course can be described by a second-polynomial function during a 60-days temporal window for each decametric pixel. The coefficients of the polynomial function are optimized using temporal courses of the available Landsat-8 FAPAR and GEOV3 FAPAR. The generated DHF FAPAR captures faithfully the temporal and spatial distribution of Landsat-8 FAPAR, and improves the temporal resolution and smoothness of Landsat-8 FAPAR. Using the leave-one-out method, the DHF FAPAR products correspond well with the Landsat-8 FAPAR (RMSE = 0.05–0.14) that are not used in the DHF algorithm. The DHF FAPAR products show also good agreement with ground measurements over 14 sunflower fields (RMSE = 0.11, R^2 = 0.66). Further developments of the algorithm would include its application to the actual Sentinel-2 and Sentinel-3 datasets, as well as its adaptation to other biophysical variables such as LAI.

Supplementary data to this article can be found online at http://dx.doi.org/10.1016/j.rse.2017.08.018.

Acknowledgements

The authors are grateful for the financial support of FP7 IMPLEMENTING MULTI-SCALE AGRICULTURAL INDICATORS EXPLOITING SENTINELS (IMAGINES) project under Grant Agreement No. 311766. Hervé Gibrin, Arnaud Micheneau, Oliva Mas Erauso and Bernard Marciel are acknowledged for their help in ground measurements and Can-Eye processing. We would also gratefully thank the two anonymous reviewers for their thoughtful comments.

References

Anderson, M.C., Kustas, W.P., Norman, J.M., Hain, C.R., Mecikalski, J.R., Schultz, L., González-Dugo, M.P., Cammalleri, C., d'Urso, G., Pimstein, A., Gao, F., 2011. Mapping daily evapotranspiration at field to continental scales using geostationary and polar orbiting satellite imagery. Hydrol. Earth Syst. Sci. 15, 223–239.

Baret, F., Hagolle, O., Geiger, B., Bicheron, P., Miras, B., Huc, M., Berthelot, B., Niño, F., Weiss, M., Samain, O., Roujean, J.L., Leroy, M., 2007. LAI, fAPAR and fCover CYCLOPES global products derived from VEGETATION part 1: principles of the algorithm. Remote Sens. Environ. 110, 275–286.

Baret, F., Weiss, M., Lacaze, R., Camacho, F., Makhmara, H., Pacholcyzk, P., Smets, B., 2013a. GEOV1: LAI and FAPAR essential climate variables and FCOVER global time series capitalizing over existing products. Part1: principles of development and production. Remote Sens. Environ. 137, 299–309.

Baret, F., Weiss, M., Verger, A., Smets, B., 2013b. Algorithm Theoretical Basis Documents of LAI, FAPAR, FCover at 300m from PROBA-V(GEOV3). INRA, Avignon. http://fp7-imagines.eu/pages/documents.php.

Baret, F., Li, W., Weiss, M., Buis, S., 2016. ATBD OF 10-M (30-M) FAPAR FOR S2 (LANDSAT-8) AND S3 (+ PROBA-V). INRA, Avignon. http://fp7-imagines.eu/pages/documents.php.

Byrd, R.H., Hribar, M.E., Nocedal, J., 1999. An interior point algorithm for large-scale nonlinear programming. SIAM J. Optim. 9, 877–900.

Byrd, R.H., Gilbert, J.C., Nocedal, J., 2000. A trust region method based on interior point techniques for nonlinear programming. Math. Program. 89, 149–185.

Camacho, F., Cernicharo, J., Lacaze, R., Baret, F., Weiss, M., 2013. GEOV1: LAI, FAPAR essential climate variables and FCOVER global time series capitalizing over existing products. Part 2: validation and intercomparison with reference products. Remote Sens. Environ. 137, 310–329.

Camacho, F., Sánchez, J., Latorre, C., 2016. Gio Global Land Component – Lot I "Operation of the Global Land Component": Quality Assessment Report LAI, FAPAR, FCover Collection 300 m Version1. EOLAB, Valencia. http://land.copernicus.eu/global/sites/default/files/products/GIOGL1_QAR_FAPAR300m-V1_I1.10.pdf.

Cardot, H., Maisongrande, P., Faivre, R., 2008. Varying-time random effects models for longitudinal data: unmixing and temporal interpolation of remote-sensing data. J. Appl. Stat. 35, 827–846.

Demarez, V., Duthoit, S., Baret, F., Weiss, M., Dedieu, G., 2008. Estimation of leaf area and clumping indexes of crops with hemispherical photographs. Agric. For. Meteorol. 148, 644–655.

Donlon, C., Berruti, B., Buongiorno, A., Ferreira, M.-H., Féménias, P., Frerick, J., Goryl, P., Klein, U., Laur, H., Mavrocordatos, C., Nieke, J., Rebhan, H., Seitz, B., Stroede, J., Sciarra, R., 2012. The global monitoring for environment and security (GMES) sentinel-3 mission. Remote Sens. Environ. 120, 37–57.

Drusch, M., Bello, U.D., Carlier, S., Colin, O., Fernandez, V., Gascon, F., Hoersch, B., Isola, C., Laberinti, P., Martimort, P., Meygret, A., Spoto, F., Sy, O., Marchese, F., Bargellini, P., 2012. Sentinel-2: ESA's optical high-resolution mission for GMES operational services. Remote Sens. Environ. 120, 25–36.

Faivre, R., Delecolle, R., 1997. Synthetic map of crop leaf area index dynamics estimated with satellite data. In: MODSIM'97: International Congress on Modelling and Simulation. Hobart, Australie (p. 6).

Faivre, R., Fischer, A., 1997. Predicting crop reflectances using satellite data observing mixed pixels. J. Agric. Biol. Environ. Stat. 2, 87–107.

Ganguly, S., Nemani, R.R., Zhang, G., Hashimoto, H., Milesi, C., Michaelis, A., Wang, W., Votava, P., Samanta, A., Melton, F., Dungan, J.L., Vermote, E., Gao, F., Knyazikhin, Y., Myneni, R.B., 2012. Generating global leaf area index from Landsat: algorithm formulation and demonstration. Remote Sens. Environ. 122, 185–202.

Gao, F., Masek, J., Schwaller, M., Hall, F., 2006. On the blending of the Landsat and MODIS surface reflectance: predicting daily Landsat surface reflectance. IEEE Trans. Geosci. Remote Sens. 44, 2207–2219.

Garrigues, S., Lacaze, R., Baret, F., Morisette, J.T., Weiss, M., Nickeson, J.E., Fernandes, R., Plumme, S., Shabanov, N.V., Myneni, R.B., Knyazikhin, Y., Yang, W., 2008. Validation and intercomparison of global Leaf Area Index products derived from remote sensing data. J. Geophys. Res. 113.

GCOS, 2011. Systematic Observation Requirements for Satellite-Based Products for Climate, 2011 Update, Supplemental Details to the Satellite-Based Component of the Implementation Plan for the Global Observing System for Climate in Support of the UNFCCC (2010 Update). http://www.wmo.int/pages/prog/gcs/Publications/gcos-154.pdf.

Geiger, B., Samain, O., Baret, F., Hagolle, O., Bicheron, P., Roujean, J.-L., Franchistéguy, L., Leroy, M., 2004. Multi-sensor data fusion for deriving bio-physical variables in the Cyclopes project. In: I. International (Ed.), Geoscience and Remote Sensing Symposium, 2004. IGARSS '04. Proceedings. Anchorage, Alaska, USA.

Gevaert, C.M., García-Haro, F.J., 2015. A comparison of STARFM and an unmixing-based algorithm for Landsat and MODIS data fusion. Remote Sens. Environ. 156, 34–44.

Guyon, D., Guillot, M., Vitasse, Y., Cardot, H., Hagolle, O., Delzon, S., Wigneron, J.-P., 2011. Monitoring elevation variations in leaf phenology of deciduous broadleaf forests from SPOT/VEGETATION time-series. Remote Sens. Environ. 115, 615–627.

Hagolle, O., Dedieu, G., Mougenot, B., Debaecker, V., Duchemin, B., Meygret, A., 2008. Correction of aerosol effects on multi-temporal images acquired with constant viewing angles: application to Formosat-2 images. Remote Sens. Environ. 112, 1689–1701.

Hagolle, O., Huc, M., Pascual, D.V., Dedieu, G., 2010. A multi-temporal method for cloud detection, applied to FORMOSAT-2, VENμS, LANDSAT and SENTINEL-2 images. Remote Sens. Environ. 114, 1747–1755.

Hartigan, J.A., Wong, M.A., 1979. Algorithm AS 136: a k-means clustering algorithm. J. R. Stat. Soc. 28, 100–108.

Hilker, T., Wulder, M.A., Coops, N.C., Linke, J., McDermid, G., Masek, J.G., Gao, F., White, J.C., 2009. A new data fusion model for high spatial- and temporal-resolution mapping of forest disturbance based on Landsat and MODIS. Remote Sens. Environ. 113, 1613–1627.

Jacquemoud, S., Verhoef, W., Baret, F., Bacour, C., Zarco-Tejada, P.J., Asner, G.P., François, C., Ustin, S.L., 2009. PROSPECT + SAIL models: a review of use for vegetation characterization. Remote Sens. Environ. 113, 56–66.

Jiang, J., Xiao, Z., Wang, J., Song, J., 2016. Multiscale estimation of leaf area index from satellite observations based on an ensemble multiscale filter. Remote Sens. 8 (3), 229.

Knyazikhin, Y., Martonchik, J.V., Myneni, R.B., Diner, D.J., Running, S.W., 1998. Synergistic algorithm for estimating vegetation canopy leaf area index and fraction of absorbed photosynthetically active radiation from MODIS and MISR data. J. Geophys. Res. 103, 257–275.

Lewis, P., Gomez-Dans, J., Kaminski, T., Settle, J., Quaife, T., Gobron, N., Styles, J., Berger, M., 2012. Data assimilation of sentinel-2 observations: preliminary results from EO-LDAS and Outlook. In: ESA-SP, L.O. (Ed.), First Sentinel-2 Preparatory Symposium. ESRIN, Frascati, Italy.

Li, W., Fang, H., 2015. Estimation of direct, diffuse, and total FPARs from Landsat surface reflectance data and ground-based estimates over six FLUXNET sites. J. Geophys. Res. Biogeo. 120, 96–112.

Li, W., Weiss, M., Waldner, F., Defourny, P., Demarez, V., Morin, D., Hagolle, Olivier, Baret, Frédéric, 2015. A generic algorithm to estimate LAI, FAPAR and FCOVER variables from SPOT4_HRVIR and Landsat sensors: evaluation of the consistency and comparison with ground measurements. Remote Sens. 7, 15494–15516.

Liang, S., Zhao, X., Liu, S., Yuan, W., Cheng, X., Xiao, Z., Zhang, X., Liu, Q., Cheng, J., Tang, H., Qu, Y., Bo, Y., Qu, Y., Ren, H., Yu, K., Townshend, J., 2013. A long-term

Global LAnd Surface Satellite (GLASS) data-set for environmental studies. Int. J. Digital Earth 6 (Sup. 1), 5–33.
Mira, M., Weiss, M., Baret, F., Courault, D., Hagolle, O., Gallego-Elvira, B., Olioso, A., 2015. The MODIS (collection V006) BRDF/albedo product MCD43D: temporal course evaluated over agricultural landscape. Remote Sens. Environ. 170, 216–228.
Semmens, K.A., Anderson, M.C., Kustas, W.P., Gao, F., Alfieri, J.G., McKee, L., Prueger, J.H., Hain, C.R., Cammalleri, C., Yang, Y., Xia, T., Sanchez, L., Mar Alsina, M., Vélez, M., 2016. Monitoring daily evapotranspiration over two California vineyards using Landsat 8 in a multi-sensor data fusion approach. Remote Sens. Environ. 185, 155–170.
Shabanov, N.V., Wang, Y., Buermann, W., Dong, J., Hoffman, S., Smith, G.R., Tian, Y., Knyazikhin, Y., Myneni, R.B., 2003. Effect of foliage spatial heterogeneity in the MODIS LAI and FPAR algorithm over broadleaf forests. Remote Sens. Environ. 85, 410–423.
Verger, A., Baret, F., Camacho, F., 2011a. Optimal modalities for radiative transfer-neural network estimation of canopy biophysical characteristics: evaluation over an agricultural area with CHRIS/PROBA observations. Remote Sens. Environ. 115, 415–426.
Verger, A., Baret, F., Weiss, M., 2011b. A multisensor fusion approach to improve LAI time series. Remote Sens. Environ. 115, 2460–2470.
Verger, A., Baret, F., Weiss, M., Kandasam, S., Vermote, E., 2011c. In: Quantification of LAI interannual anomalies by adjusting climatological patterns. IEEE Transactions on Geoscience and Remote Sensing (AGU Conference).
Weiss, M., Baret, F., 2010. In: fAPAR (fraction of Absorbed Photosynthetically Active Radiation) estimates at various scale. 34th International Symposium on Remote Sensing and Environment (ISRSE). Sydney, Australia.
Weiss, M., Baret, F., Garrigues, S., Lacaze, R., 2007. LAI and fAPAR CYCLOPES global products derived from VEGETATION. Part 2: validation and comparison with MODIS collection 4 products. Remote Sens. Environ. 110, 317–331.
Weng, Q., Fu, P., Gao, F., 2014. Generating daily land surface temperature at Landsat resolution by fusing Landsat and MODIS data. Remote Sens. Environ. 145, 55–67.
Xiao, Z., Liang, S., Sun, R., JindiWang, & Jiang, B., 2015. Estimating the fraction of absorbed photosynthetically active radiation from the MODIS data based GLASS leaf area index product. Remote Sens. Environ. 171, 105–117.
Zhu, X., Chen, J., Gao, F., Chen, X., Masek, J.G., 2010. An enhanced spatial and temporal adaptive reflectance fusion model for complex heterogeneous regions. Remote Sens. Environ. 114, 2610–2623.
Zhu, Z., Woodcock, C.E., Holden, C., Yang, Z., 2015. Generating synthetic Landsat images based on all available Landsat data: predicting Landsat surface reflectance at any given time. Remote Sens. Environ. 162, 67–83.

Remote Sens. **2015**, *7*, 15494-15516; doi:10.3390/rs71115494

OPEN ACCESS

remote sensing

ISSN 2072-4292

www.mdpi.com/journal/remotesensing

Article

A Generic Algorithm to Estimate LAI, FAPAR and FCOVER Variables from SPOT4_HRVIR and Landsat Sensors: Evaluation of the Consistency and Comparison with Ground Measurements

Wenjuan Li [1,*], Marie Weiss [1], Francois Waldner [2], Pierre Defourny [2], Valerie Demarez [3], David Morin [3], Olivier Hagolle [3] and Frédéric Baret [1]

[1] INRA-EMMAH UMR 1114, 84914 Avignon , France; E-Mails: marie.weiss@avignon.inra.fr (M.W.); baret@avignon.inra.fr (F.B.)

[2] Earth and Life Institute, Université catholique de Louvain, 2 Croix du Sud, 1348 Louvain-la-Neuve, Belgium; E-Mails: francois.waldner@uclouvain.be (F.W.); pierre.defourny@uclouvain.be (P.D.)

[3] CESBIO, UMR CNES-CNRS-IRD-UPS, 18 avenue Edouard Belin, 31401 Toulouse Cedex 4, France; E-Mails: valerie.demarez@orange.fr (V.D.); morind@cesbio.cnes.fr (D.M.); olivier.hagolle@cnes.fr (O.H.)

* Author to whom correspondence should be addressed; E-Mail: wenjuan.li@paca.inra.fr; Tel.: +33-762-038-907.

Academic Editors: Benjamin Koetz, Olivier Arino, Magaly Koch and Prasad S. Thenkabail

Received: 31 August 2015 / Accepted: 9 November 2015 / Published: 18 November 2015

Abstract: The leaf area index (LAI) and the fraction of photosynthetically active radiation absorbed by green vegetation (FAPAR) are essential climatic variables in surface process models. FCOVER is also important to separate vegetation and soil for energy balance processes. Currently, several LAI, FAPAR and FCOVER satellite products are derived moderate to coarse spatial resolution. The launch of Sentinel-2 in 2015 will provide data at decametric resolution with a high revisit frequency to allow quantifying the canopy functioning at the local to regional scales. The aim of this study is thus to evaluate the performances of a neural network based algorithm to derive LAI, FAPAR and FCOVER products at decametric spatial resolution and high temporal sampling. The algorithm is generic, *i.e.*, it is applied without any knowledge of the landcover. A time series of high spatial resolution SPOT4_HRVIR (16 scenes) and Landsat 8 (18 scenes) images acquired in 2013 over the France southwestern site were used to generate the LAI, FAPAR and FCOVER products. For each sensor and each biophysical variable, a neural network was first trained over PROSPECT+SAIL radiative transfer model simulations of top of canopy

reflectance data for green, red, near-infra red and short wave infra-red bands. Our results show a good spatial and temporal consistency between the variables derived from both sensors: almost half the pixels show an absolute difference between SPOT and LANDSAT estimates of lower that 0.5 unit for LAI, and 0.05 unit for FAPAR and FCOVER. Finally, downward-looking digital hemispherical cameras were completed over the main land cover types to validate the accuracy of the products. Results show that the derived products are strongly correlated with the field measurements (R^2 > 0.79), corresponding to a RMSE = 0.49 for LAI, RMSE = 0.10 (RMSE = 0.12) for black-sky (white sky) FAPAR and RMSE = 0.15 for FCOVER. It is concluded that the proposed generic algorithm provides a good basis to monitor the seasonal variation of the vegetation biophysical variables for important crops at decametric resolution.

Keywords: LAI; FAPAR; FCOVER; Landsat 8; SPOT4_HRVIR; time series

1. Introduction

Leaf area index (LAI) is defined as half the total developed area of green elements per unit horizontal ground area [1]. The fraction of photosynthetically absorbed radiation (FAPAR) is defined as the faction of the photosynthetically radiation (PAR) absorbed by the green leaves. It is a weighted sum of the direct FAPAR and diffuse FAPAR, depending on the source of the incoming radiation [2]. LAI and FAPAR have been recognized as Essential Climate Variables (ECV) by GCOS [3], for their key roles in energy, mass and momentum exchanges between the land surface and the atmosphere. FAPAR is also used as one of the main inputs in light use efficiency models [4]. Besides LAI and FAPAR variables, FCOVER, the fraction of the green vegetation in the nadir direction, is used to separate vegetation and soil in energy balance processes, including temperature and evapotranspiration. Over the last decade, several global LAI, FAPAR and FCOVER products have been generated from SPOT-VGT, SEAWIFS, MERIS, MODIS and AVHRR sensors at a spatial resolution close to 1km and a temporal sampling of 8 to 16 days [5–10]. However, this kilometric resolution is generally much larger than the typical length scales of most landscapes, limiting therefore the applications to the regional and local scales [11]. The development of LAI, FAPAR and FCOVER biophysical products from decametric spatial resolution sensors will be better suited for addressing these applications closely related to agriculture, ecosystem and environmental management. However, the monitoring capacity and actual use of such sensors is still limited by the revisit frequency or the cost of the images. The European Sentinel-2 Mission [12] (https://earth.esa.int/web/guest/missions/esa-future-missions/sentinel-2) will fulfill most of the requirements by providing global images with decametric resolution (10–20 m) every five days with two satellites, under constant viewing angles at each location.

A SPOT4 (Take5) experiment was started in 2013 by the French Agency Centre National d'Etudes Spatiales (CNES), aiming at providing time series of images with similar revisit frequency and resolution as Sentinel-2 data (http://www.cesbio.ups-tlse.fr/multitemp/) to prepare for the use of the data of this satellite that has just been launched in June 2015. However, the experiment lasted only few

months, which is not enough to cover a full vegetation cycle. The series was therefore completed with Landsat 8 images at a 30m spatial resolution and 16 days revisit period, taking advantage of the overlap between satellite tracks allowing to double the revisit frequency.

Several studies demonstrated the capacity to derive biophysical products with a reasonable accuracy from decametric surface reflectance data. Among several authors, Ganguly *et al.* [13] generated 30-m LAI from LANDSAT-5 surface reflectance data based on the canopy spectral invariants theory and look-up table method. Panferov [14] generated LAI from LANDSAT ETM+ data over forests and Verger *et al.* [15,16] estimated FAPAR, FCOVER and LAI over crops using LANDSAT-5 data. Li and Fang [17] generated the FAPAR data over six FLUXNET sites from the lookup table method using the LANDSAT-5 images. However, these studies focus on single sensors, limiting the length and continuity of the time series that could be derived.

The objective of this study is to evaluate the performances of a generic algorithm to generate consistent time series of LAI, FAPAR and FCOVER products from the combination of SPOT4_HRVIR and Landsat 8 surface reflectance data acquired during a growth season, without any prior knowledge of the landcover. The study area and data sets will first be presented. Then, the algorithm developed to derive the products will be described. Finally, the performances of the products will be analyzed, with emphasis on the spatial and temporal consistency between products and the comparison with field measurements.

2. Study Area and Data Description

2.1. The Experimental Site: Southwest France

The site is a 13.2 × 14.4 km^2 area located near Toulouse, southwest France (43.54°N, 1.13°E, Figure 1). The region experiences a typical temperate continental climate with hot and dry summer and cold and humid winter [18]. More than 65% of the study area is covered by crops, including barley, rapeseed, wheat, maize and sunflower. Barley, rapeseed and wheat are winter crops sown from October to November and harvested in the beginning of July. Corn and sunflower are summer crops sown from mid-April to beginning of June and harvested until September to October. Most fields were located on flat soil with relatively uniform soil properties and cultural practices and are therefore relatively homogeneous. Grassland is distributed in the center and south west of the region, while broadleaf and needleleaf forests are mainly observed in the northwestern parts (Figure 1).

2.2. SPOT4_HRVIR and Landsat 8 Data

The SPOT4_HRVIR satellite was launched in March, 1998. In 2013, CNES lowered the altitude of SPOT4 by 2 km to increase the repeat cycle. On its nominal orbit, SPOT4 did 14.17 orbits per day, but reducing the altitude by two kilometers enabled it to reach 14.2 orbits per day, which results in exactly 71 orbits every five days. Therefore, on this sun-synchronous orbit inclined at 96.7°, it provided observations every five days over 45 sites distributed on the globe with an equatorial crossing time of 10:30. The images are acquired with varying viewing angles at a spatial resolution of 20m. Four spectral bands are available, including green, red, near-infra red (NIR) and short wave infra-red (SWIR, Figure 2). The raw images were firstly ortho-rectified based on the SIGMA tool developed by

CNES [19,20]. Then the ortho-rectified top of atmosphere reflectance data were processed by the Multi-Sensor Atmospheric Correction Software (MACCS) [21,22] to generate top of canopy reflectance data, along with a cloud/cloud shadows/water/snow masks. The method uses multi-temporal criteria to build various masks and to quantify the aerosol optical thickness [23]. Sixteen SPOT4_HRVIR scenes were used in this study.

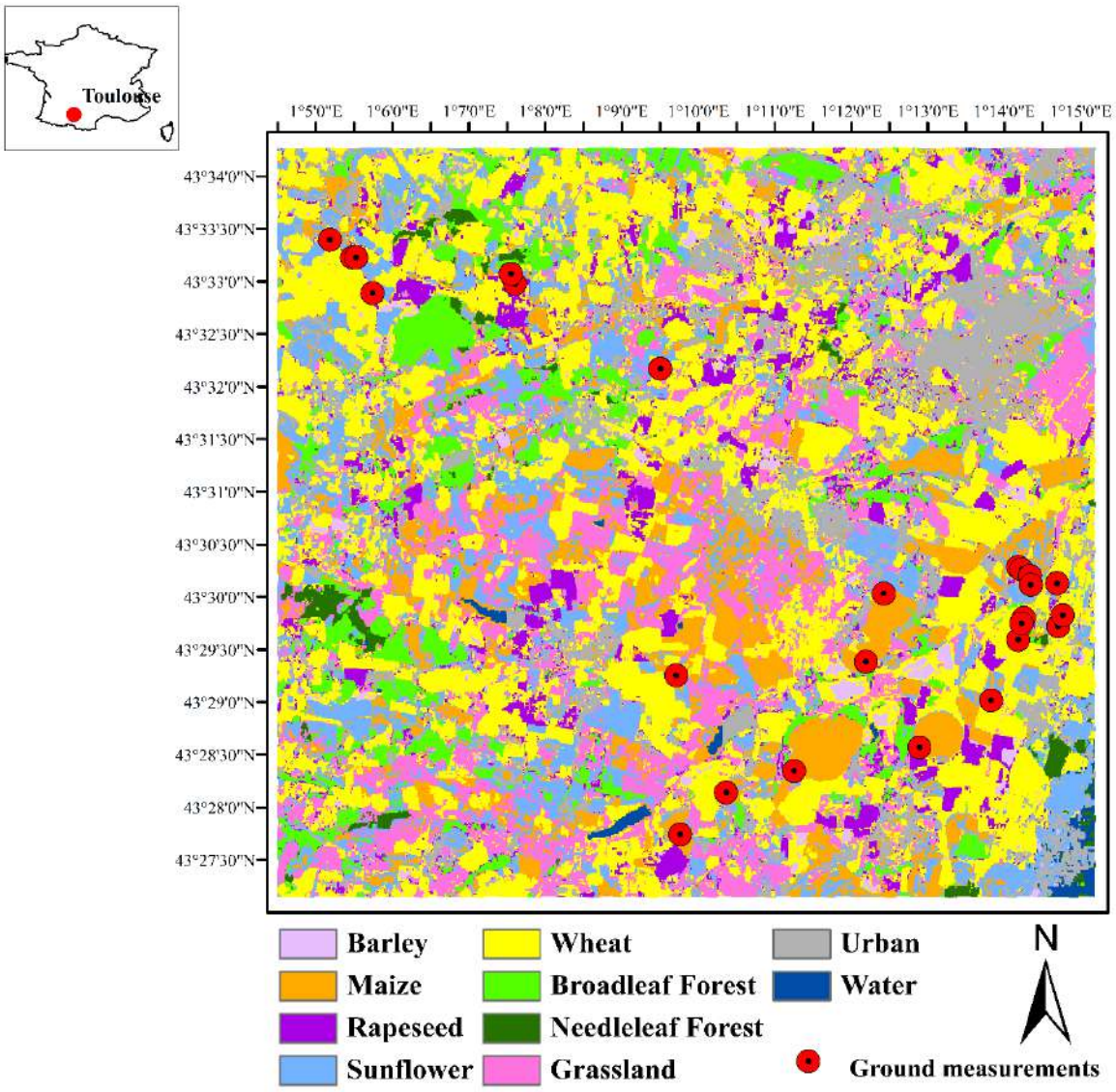

Figure 1. The location and land cover types of the study area (Landsat 8, 17 April 2013). The location of the ground measurements correspond to the red circles.

Landsat 8 launched on 11 February 2013, is the latest in a series of Landsat spacecrafts going back 40 years. Landsat 8 observes the world at a 705 km altitude orbit, with an inclination angle of 98.2°, a revisit frequency of 16 days and an equatorial crossing time of 10:00. The OLI sensor aboard Landsat 8 includes nine spectral bands with a spatial resolution of 30m for Bands 1 to 7 and 9 while band 8 has 15m spatial resolution. Only four bands (green (Band 3), red (band 4), NIR (Band 5) and SWIR-1 (Band 6)) will be used in this study (Figure 2) to keep the band setting consistent with that of SPOT4_HRVIR. The Level 1T Landsat 8 data were first ortho-rectified by USGS, using a global data base of ground control points. Radiometric calibration was performed using the coefficients provided

with the Level 1T products. The data were further processed using the same MACCS algorithm as that used for SPOT4_HRVIR [21,22]. Note that because of the overlap between 2 Landsat 8 tracks over the site considered, the revisit frequency was doubled. 18 Landsat 8 scenes were used in this study.

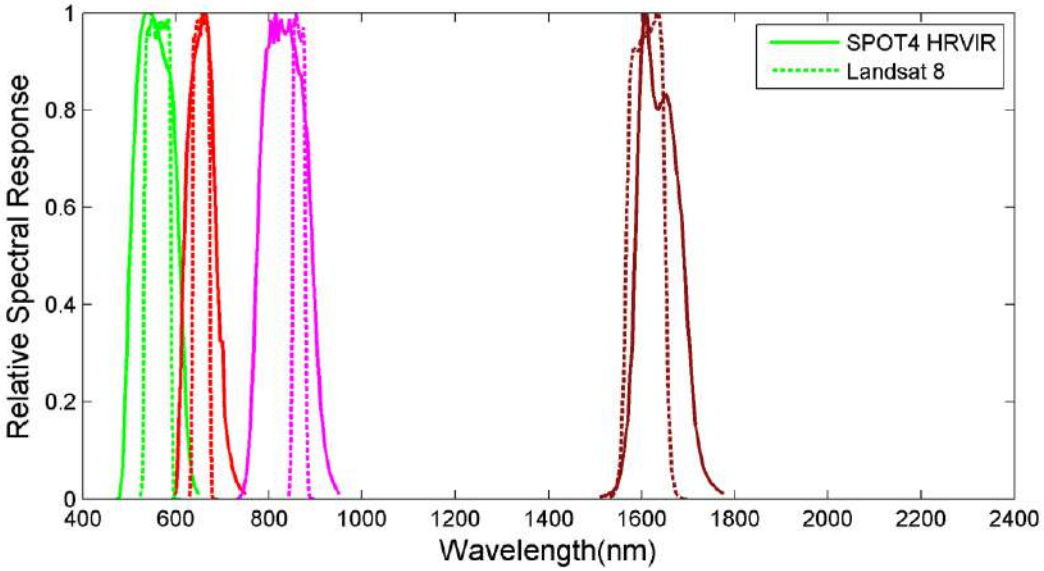

Figure 2. The relative spectral responses of SPOT4_HRVIR (solid lines) and Landsat 8 (dashed lines) bands used in this study.

A total of 16 SPOT4_HRVIR and 18 Landsat 8 top of canopy reflectance images, combined with a cloud/cloud shadow mask were downloaded through the THEIA land data center website (http://spirit.cnes.fr/take5/). The pixels contaminated by the clouds/cloud shadow or flagged as snow were not used in this study. The SPOT4_HRVIR data was resampled to 30m to be consistent with the Landsat 8 data.

2.3. Landcover Data

Although the proposed generic algorithm should apply to any landcover, its performances will be analyzed for the main landcover classes observed over the study site. The land cover types were produced based on the random forest classification method [24]. The random forest was trained using all the spectral information of 34 SPOT4_HRVIR Take 5 images and Landsat 8 images acquired from February 2013 to December 2013 [25]. Based on the knowledge of land cover and crop type distribution in the study area, 5 crop types (barley, wheat, rapeseed, sunflower and corn), needleleaf and broadleaf forests, grassland, urban areas and water bodies were identified as the final classes. The resulting map yielded an overall accuracy of 87% (Figure 1). Winter crops (Wheat, barley, rapeseed) are dominant (39.8%) followed (25.7%) by summer crops (Maize, sunflower) (Table 1). Forests and water bodies are marginally represented.

Table 1. The proportion of the each land cover type in the study area.

Type	Barley	Rapeseed	Wheat	Maize	Sunflower	Grassland	Broadleaf Forests	Needleleaf Forests	Urban	Water
Proportion (%)	1.7	5.86	32.26	11.29	14.41	13.84	6.65	1.19	12.28	0.52

2.4. Ground Data

Ground measurements data over wheat, maize, and sunflower were collected from 17 April to 23 October 2013 using digital hemispherical photographs (DHPs). For each landcover class, the measurements were conducted within a 20 × 20 m^2 Elementary sampling unit (ESU) around every 10 days. The location of each ESU was recorded by a GPS instrument within an accuracy of few meters (Figure 1). Each ESU was sampled with 12–20 DHPs according to the VALERI spatial sampling protocol (http://w3.avignon.inra.fr/valeri). The DHPs were taken using a Nikon CoolPix 8400 camera equipped with a FC-E8 fisheye lens. The downward-looking camera was fixed at the top of a pole. The height of the pole changes throughout the measurements to keep a constant distance (~1.5 m) between the lens and top of the canopy [26]. All valid photos within an ESU were processed simultaneously using the CAN-EYE software (http://www4.paca.inra.fr/can-eye) to extract the LAI, FAPAR and FCOVER variables [27]. Effective LAI was derived by inverting the turbid medium transmittance model [28,29].

For green canopy, FAPAR is approximated as the fraction of intercepted PAR (FIPAR) calculated from the gap fraction [27]. This assumption is valid in the growing season due to the strong absorption capacity of the photosynthetic pigments [30] and the fact that the green leaves are mainly located at the top of the canopy. In this study, FIPAR is used for the validation since all field data were collected during the growing season. Both instantaneous black-sky ($FIPAR_b$) at 10:00 local solar time and white-sky FIPAR ($FIPAR_w$) were computed as follows:

$$FIPAR_b = GF(\theta_{10:00}) \tag{1}$$

$$FIPAR_w = 2\int_0^{\pi/2}(GF(\theta))\cos\theta\sin\theta d\theta \tag{2}$$

where GF is the measured green fraction on each viewing zenith angle θ and $\theta_{10:00}$ is the sun zenith angle at 10:00 local solar time. Note that the instantaneous black sky FIPAR at 10:00 local solar time is a close approximation of the daily integrated black sky FIPAR [5].

As it is impossible to get a green fraction in the exact nadir direction from the hemispherical photos, FCOVER in CAN-EYE is approximated from the green fraction ranging from nadir direction to ±10°.

$$FCOVER = GF(\theta_{0-10}) \tag{3}$$

where $GF(\theta_{0-10})$ represents the integrated green fraction from nadir to ±10°.

3. Methods

The principle of this generic algorithm is to derive LAI, FAPAR and FCOVER using a neural network trained over a database generated by a radiative transfer model simulation. Many inversion algorithms have been proposed to estimate LAI, FAPAR and FCOVER. Among the several possible retrieval methods available [31], we selected a machine learning approach based on neural network technique because (i) they can describe any linear and nonlinear relationship between input and output variables if enough neurons and layers are used [32]; (ii) they are computationally efficient after the training process; (iii) they are able to provide good estimation results as the optimization operates

directly over the target variables and they have efficient interpolation capacity [31]. Such machine learning inversion algorithm has been applied with success in many studies [5,16,33–35]. The outline of the algorithm is summarized in Figure 3. A training data set is first populated by simulating top of canopy reflectance corresponding to a large number of possible cases using a radiative transfer model. This training data set will be also used to build the definition domain, *i.e.*, the convex hull of input reflectances in the space of the 4 bands used. Then, the architecture and the coefficients of the neurons are adjusted to provide the best match between the variables in the training database and those estimated by the neural network. More details are given in the following.

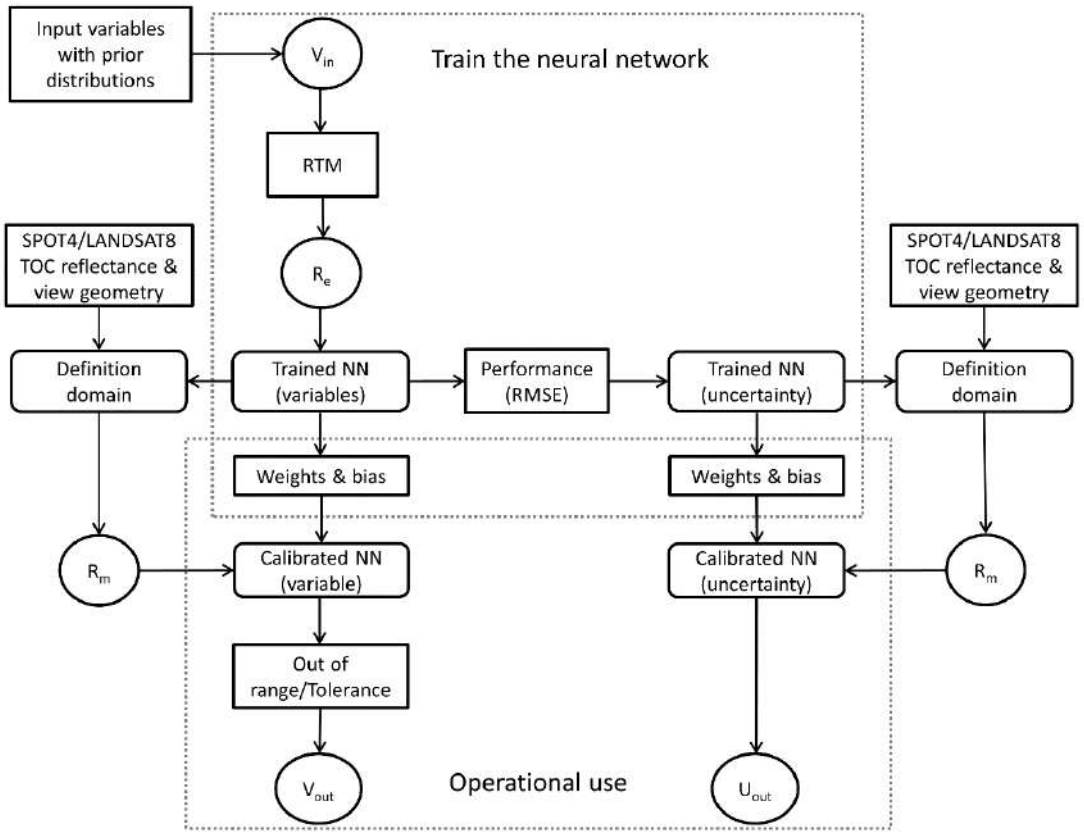

Figure 3. The outline of the algorithm. V_{in} represents the input variables for the radiative transfer model (RTM). R_e and R_m represent the estimated and measured top of canopy reflectance, respectively. NN is the neural network. V_{out} donates the output variables and U_{out} is the output uncertainties.

3.1. Reflectance Models

The widely used PROSAIL radiative transfer model [36] was selected in this study. The model couples the SAIL canopy reflectance model [37] and the PROSPECT leaf optical model [38]. The SAIL model assumes the canopy as a turbid medium within which the leaves are randomly located. This model has been already used with success in a number of studies to estimate the considered biophysical variables. Canopy structure is characterized by LAI, the average leaf angle (ALA) assuming an ellipsoidal distribution [39], and a hot spot parameter (HOT) [40]. The PROSPECT model is widely used to simulate leaf optical properties through several structural and chemistry

characteristics. In this study, the PROSPECT model with the updated absorption coefficients proposed by [41] was used. The soil reflectance data was simulated using five typical soil reflectance spectra multiplied by a brightness coefficient allowing to accurately represent a large soil dataset where soil types, roughness, moisture and observational geometry vary [42].

3.2. Generate the Learning Database

To generate a learning database that could best represent the possible types and states of actual canopies, the distribution law of the variable should be well considered [5]. Table 2 lists the range and distribution law for all variables of PROSAIL model. Some constraints on the co-distributions between variables were also introduced to restrict the space of canopy realization while keeping high degree of realism. More detailed justifications of the range and distribution of values used to build the training database can be found in the Sentinel-2 algorithm report [43]. The variables distribution laws in this study are very similar as the ones used to generate the Sentinel-2 algorithm prototype, except for ALA and N with narrower distribution for this study due to the limited number of land cover types. Because of the generic nature of the proposed algorithm, the same training dataset, therefore the same neural network, will be applied to all land cover types.

Table 2. List of variables required to run PROSAIL model. The distribution law was described by using mode and standard deviation. Nb_Class represents the number of classes for each variable.

	Variable	Minimum	Maximum	Mode	Std	Nb_Class	Law
Canopy	LAI	0.0	15.0	2.0	2.0	6	Gauss
	ALA (°)	15	80	40	20	4	Gauss
	HOT	0.1	0.5	0.2	0.5	1	Gauss
Leaf	N	1.20	1.80	1.50	0.30	3	Gauss
	Cab ($\mu g.m^{-2}$)	20	90	45	30	4	Gauss
	Cdm ($g.m^{-2}$)	0.003	0.011	0.005	0.005	4	Gauss
	Cw_Rel	0.60	0.85	0.75	0.08	4	Uniform
	Cbp	0.00	2.00	0.00	0.30	3	Gauss
Soil	Bs	0.50	3.50	1.20	2.00	4	Gauss

A full orthogonal experimental plan was adopted to randomly sample the variables according to the number of classes, variation range and distribution law defined above [44]. This sampling scheme could account for all the interactions between variables and generate a learning data base evenly but quasi-randomly populated. For each combination of variables in the learning data base, the top of canopy reflectance on each wavelength was simulated by running the PROSAIL model in a forward mode. Then the reflectance was spectrally integrated to represent actual SPOT4_HRVIR and Landsat 8 bands according to the spectral response function of the sensor (Figure 2). Instantaneous black-sky FAPAR, at the satellite pass-by time (10:00 am for Landsat 8, 10:30 am for SPOT4_HRVIR), white-sky FAPAR and FCOVER were simulated by running the PROSAIL model in the forward mode using the same input variables.

The radiative transfer model introduces uncertainties associated with the simulated reflectance due to its adequacy to represent the actual canopy architecture. This mainly results in structured errors. The

accuracy of actual measured top of canopy reflectance is also influenced by several possible factors, including the instrumental noise, radiometric calibration, atmospheric correction and cloud or cloud shadow contamination. These factors will lead to multiplicative or additive uncertainties to the measured reflectance [16]. To get a more realistic canopy reflectance simulated value, an uncertainty model was used to describe the additive and multiplicative uncertainties based on a white Gaussian noise:

$$R^*(\lambda) = R(\lambda)\ (1+(MD(\lambda)+MI)/100)+AD(\lambda)+AI \quad (4)$$

where $R(\lambda)$ is the raw simulated reflectance, $R^*(\lambda)$ is the reflectance contaminated with noise, MD is the multiplicative wavelength dependent noise, MI is the multiplicative wavelength independent noise, AD is the additive wavelength independent noise, and AI is the additive wavelength independent noise. In this study, the MD, MI, AD and AI were fixed to 0.02, 0.02, 0.01, and 0.01 for all bands of each sensor.

A total of 55,296 cases were simulated for each sensor with input canopy variables and output reflectance, FAPAR and FCOVER.

A definition domain was generated by the co-distribution of the simulated reflectance on each band. Figure 4 shows the definition domain for the four Landsat 8 bands used in this study (a similar definition domain was generated for SPOT4_HRVIR bands but was not shown for the sake of brevity). Pixels with reflectance values outside of the definition domain will be reported as "input out of range". The solar zenith angle for each image was also calculated. Only the images with solar zenith angle smaller than 65° will be used in further analysis: atmospheric and directional effects are considered as too important for zenith angles larger than 65°.

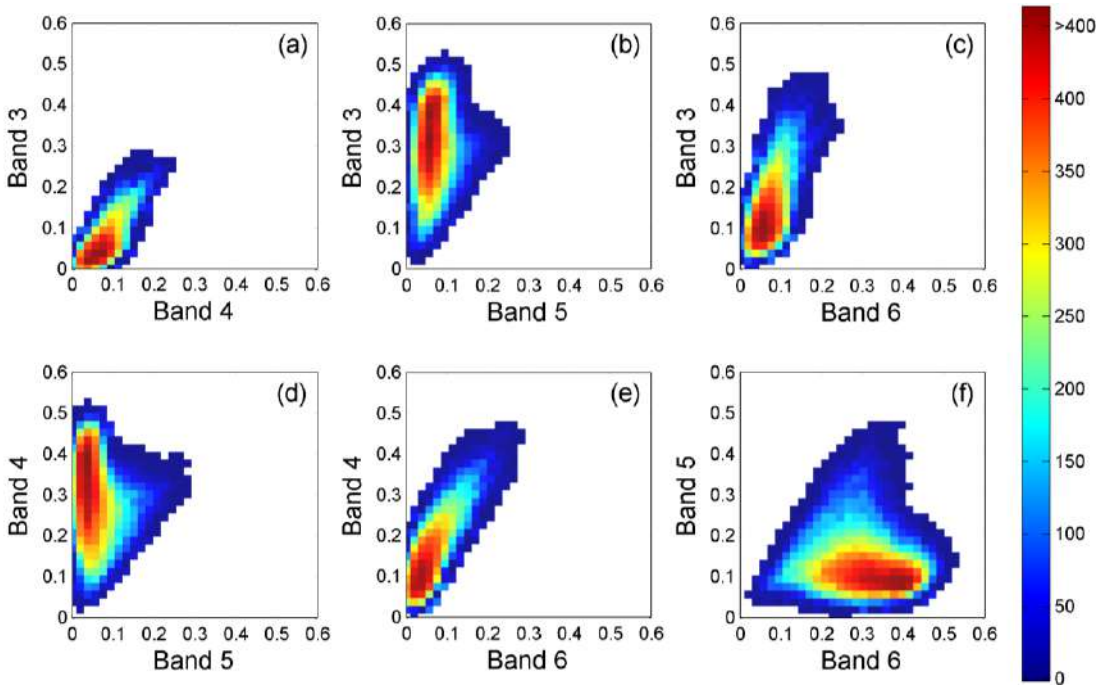

Figure 4. The definition domain (colorful region) of the simulated TOC reflectance on four Landsat 8 bands (3, 4, 5, 6). (**a**) Band 4 and Band 3; (**b**) Band 5 and Band 3; (**c**) Band 6 and Band 3; (**d**) Band 5 and Band 4 (**e**) Band 6 and Band 4; (**f**) Band 6 and Band 5.

3.3. Train the Neural Network

Two distinct databases were generated for LANDSAT8 and for SPOT4_HRVIR. Each database was divided into two parts: two thirds of the simulations were randomly selected to train the neural network, and the remaining simulations were used for the hyper-specialization control and the evaluation of the theoretical performances. For both sensors, a back-propagation artificial neural network [45] made of one input layer composed of the normalized input data, one hidden layer composed of 5 neurons with tangent sigmoid transfer functions and one output layer with a linear transfer function was selected. The input layer of the network corresponds to the surface reflectance for each band and the geometrical configurations: the cosine of the view zenith angle, the cosine of the sun zenith angle and the cosine of the relative azimuth angle between sun and view directions; the outputs are LAI, instantaneous black-sky FAPAR, white-sky FAPAR and FCOVER. The normalization applied to the input and output variables is expected to increase the performances of the Levenberg-Marquardt minimization algorithm [46] used in the training process. For each output variable and each sensor, five networks were trained with different initial solutions. The best one is then selected based on the smallest RMSE between the outputs (estimated variable) and the corresponding "reference" biophysical variables in the test data set. Results show that the theoretical performances of the 5 neural networks were very close. The best neural network achieved very good theoretical performances as observed in Figure 5 for Landsat 8. Table 3 shows that the theoretical performances are very close for SPOT4_HRVIR and Landsat 8.

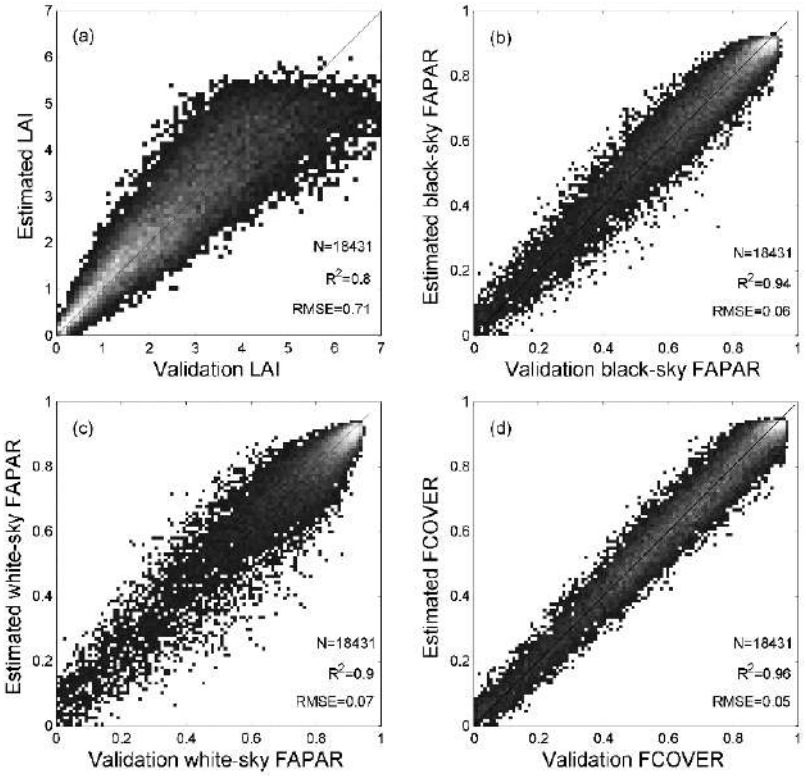

Figure 5. The theoretical performances of the neural network for (**a**) LAI, (**b**) black-sky FAPAR, (**c**) white-sky FAPAR, and (**d**) FCOVER. This neural network was trained for Landsat 8.

Table 3. Comparison of the theoretical performances (R^2 and RMSE in bracket) between SPOT4_HRVIR and Landsat 8.

	LAI	Black-Sky FAPAR	White-Sky FAPAR	FCOVER
SPOT4_HRVIR	0.77 (0.84)	0.94 (0.06)	0.88 (0.08)	0.96 (0.05)
Landsat 8	0.8 (0.71)	0.94 (0.06)	0.9 (0.07)	0.96 (0.05)

Finally, the uncertainty of each variable is estimated. Based on the training dataset and validation dataset, the theoretical performances of algorithm can be calculated from the RMSE between the estimated and validation biophysical values (Figure 5 and Table 3). A specific neural network was then trained for each product to relate the theoretical performances of the neural network to the input reflectance and observation geometry values. More details can be found in [43].

3.4. Inversion

Once trained, the neural network can be applied over each pixel for a given sensor. However, the input reflectance in the four bands is first checked to verify if it belongs to the definition domain to ensure consistency with the training database. If the observation is outside the definition domain, a flag "inputs out of range" is raised. In addition, the output estimated variables should be also within a predefined range determined by the training dataset and extended by a small tolerance interval (Table 4, Equations (5) and (6)). Otherwise, an "output out of range" flag will be raised for the pixel. Only the data without the input or output "out of range" flag were used in the following analysis

$$\text{if } X_{min} - Tol \leq X \leq X_{min}, \text{ then } X = X_{min} \quad (5)$$

$$\text{if } X_{max} \leq X \leq X_{max} + Tol, \text{ then } X = X_{max} \quad (6)$$

where X is the output variable value, Xmin, Xmax and Tol are the minimum, maximum and tolerance values of the variable, respectively.

For each pixel, variable and the considered sensor, the corresponding uncertainties were finally computed.

Table 4. The minimum, maximum range and tolerance for each output product.

	Minimum	Maximum	Tolerance
LAI	0	7	0.2
Black-sky FAPAR	0	0.94	0.05
White-sky FAPAR	0	0.94	0.05
FCOVER	0	1	0.05

4. Results

4.1. Spatial Consistency

The spatial consistency of the satellite products was assessed over cloud-free images acquired within few days for SPOT4_HRVIR (17 April 2013) and Landsat 8 (14 April 2013). Results show that for LAI products, 62.8% of the total pixels are within the absolute difference 0.5 unit, and less than 2.5% of the pixels showing differences larger than 2 (Table 5). For the black-sky FAPAR products, 42.8% of the total pixels have an absolute difference lower than 0.05 units (Figure 6) while results

degrade slightly for white sky FAPAR and FCOVER with respectively 32.5% and 28.5% pixels with absolute difference lower than 0.05 (Table 5).

The statistical relationship between the products derived from the two sensors shows that SPOT4_HRVIR and Landsat 8 LAI products are very consistent with, however, systematically higher values for SPOT4_HRVIR (Figure 7a) in agreement with the previous observations (Figure 6). The SPOT4_HRVIR black-sky FAPAR is very consistent with the Landsat 8 (Figure 7b). The white-sky FAPAR and FCOVER products are also very consistent with however a small bias of 0.07 (Figure 7c,d). The higher values of the SPOT4_HRVIR products may be partly resulted from the rapid development of the vegetation in April (Figure 7e). For all land cover types, similar consistency trends can be observed between SPOT4_HRVIR and Landsat 8 products (Table 6).

Table 5. The percentage of pixels from the difference map of the SPOT4_HRVIR (17 April 2013) and Landsat 8 (14 April 2013) estimated products. The difference units for LAI are ±0.5, ±1 and ±2. Values in the bracket represent the difference units for black-sky FAPAR, white-sky FAPAR and FCOVER products.

	±0.5 (±0.05)	**±1 (±0.1)**	**±2 (±0.2)**
LAI	62.8%	86.2%	97.5%
Black-sky FAPAR	42.8%	68.5%	89.7%
White-sky FAPAR	32.5%	61.0%	88.6%
FCOVER	28.5%	53.0%	82.2%

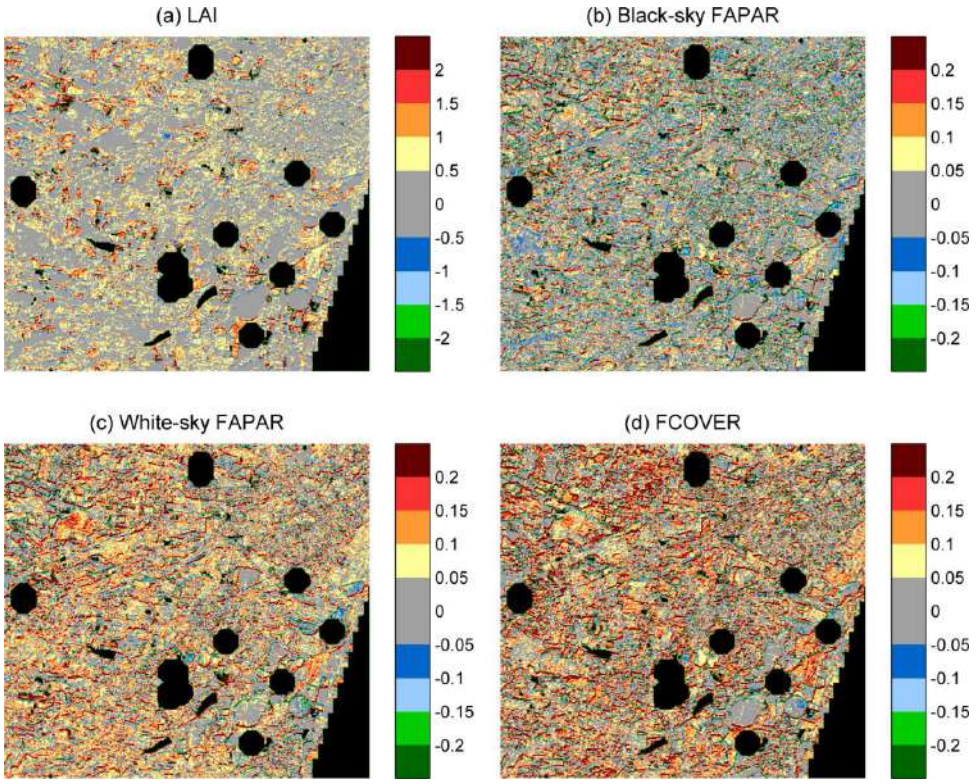

Figure 6. Spatial distribution of the differences between SPOT4_HRVIR (17 April 2013) and Landsat 8 (14 April 2013) estimated products, (**a**) LAI, (**b**) black-sky FAPAR, (**c**) white-sky FAPAR and (**d**) FCOVER. The black areas denote pixels where differences are not evaluated due to cloud or cloud shadow contamination, input or output out of range from both sensors.

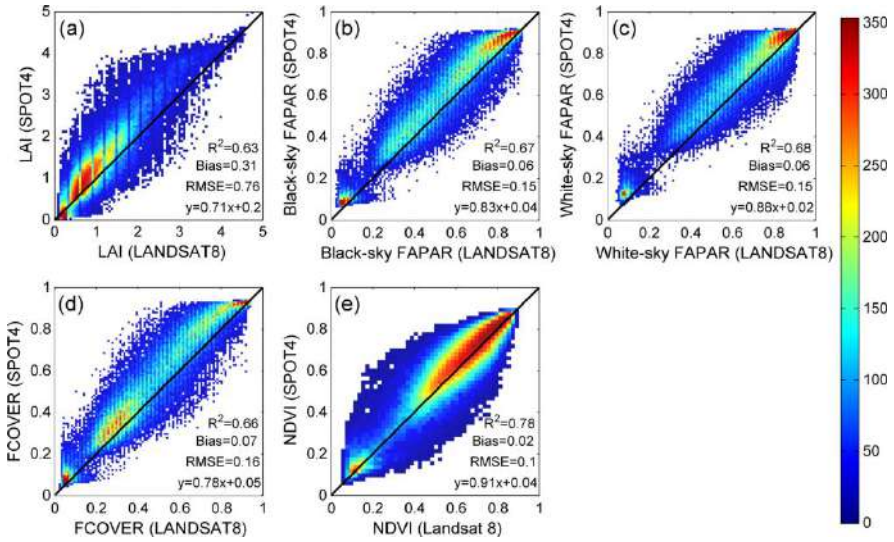

Figure 7. Regression between SPOT4_HRVIR (17 April 2013) and Landsat 8 (14 April 2013) estimated products, (**a**) LAI, (**b**) black-sky FAPAR, (**c**) white-sky FAPAR and (**d**) FCOVER. Subplot (**e**) shows the regression between the NDVI values of two images as reference.

Table 6. R square and bias (in bracket) values between SPOT4_HRVIR (Take5) (17 April 2013) and Landsat 8 (14 April 2013) estimated products over each land cover type.

	Barley	**Rapeseed**	**Wheat**	**Corn**	**Sunflower**	**Grassland**	**Broadleaf**	**Needleleaf**
LAI	0.763 (0.270)	0.770 (0.312)	0.772 (0.325)	0.773 (0.325)	0.765 (0.321)	0.762 (0.327)	0.776 (0.326)	0.769 (0.318)
Black-sky FAPAR	0.783 (0.050)	0.798 (0.060)	0.799 (0.060)	0.798 (0.060)	0.791 (0.060)	0.787 (0.060)	0.804 (0.060)	0.798 (0.060)
White-sky FAPAR	0.782 (0.047)	0.799 (0.059)	0.799 (0.059)	0.798 (0.059)	0.791 (0.059)	0.786 (0.060)	0.805 (0.060)	0.799 (0.057)
FCOVER	0.773 (0.057)	0.788 (0.067)	0.790 (0.069)	0.790 (0.069)	0.782 (0.068)	0.778 (0.069)	0.795 (0.069)	0.785 (0.066)

4.2. Temporal Consistency

The temporal consistency of SPOT4_HRVIR and Landsat 8 products was evaluated by averaging the products for each landcover class for each date of image acquisition. The fraction of valid pixels on each image was calculated for each landcover class. Dates with the fractions smaller than 50% of valid pixels were not considered for a given landcover class.

Results show that the profile captures well the expected seasonal variation of each landcover class (Figure 8). The barley LAI increases around the beginning of March, reaches a maximum in April and May, and then decreases around the end of May (Figure 8a). The next growth cycle starts around September with the early sowing. For the other two winter crops that are rapeseed and wheat (Figure 8b,c), similar seasonal variation of the LAI can be observed. For the summer crops (Figure 8d), the LAI of corn increases from the beginning of June to a peak value of 2.5 in July, and then decreases slowly in September. The sunflower LAI shows a slight seasonal variation throughout the year (Figure 8e), ranging around 1. For the grassland (Figure 8f), the seasonal profile starts in the beginning of March, reaches the highest value of nearly 3 in May, and then decreases from June to remain nearly

constant from August to the end of the year because of the lack of available water. The broadleaf and needleleaf forests follow a similar seasonal profile, although the needleleaf LAI is slightly higher than the broadleaf LAI in the beginning of the season as expected (Figure 8g,h). LAI values higher than 3 can be obtained for both forests in July.

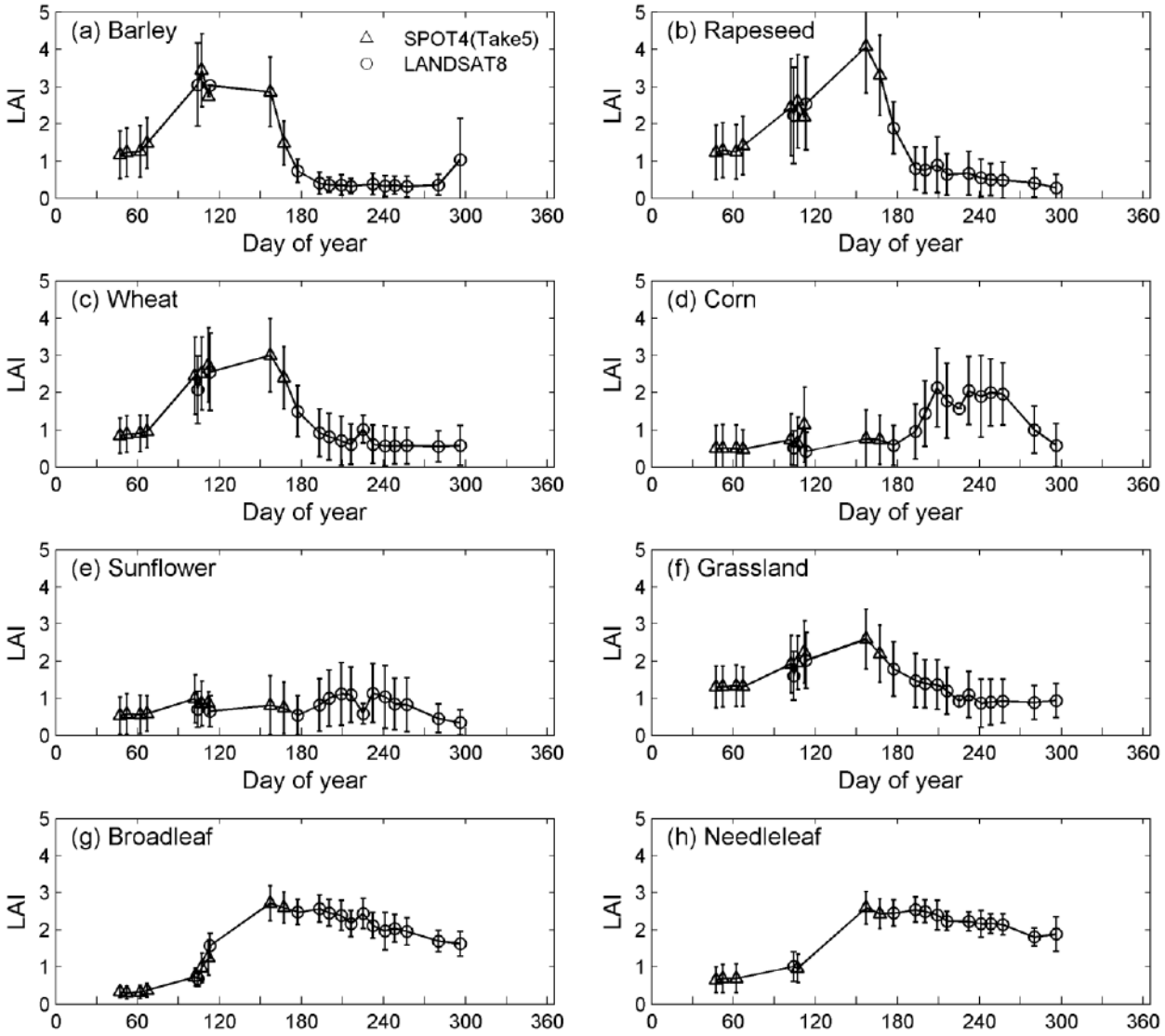

Figure 8. Seasonal variation of LAI products estimated from SPOT4_HRVIR (Take5) and Landsat 8 sensors for eight biomes ((**a**) Barley, (**b**) Rapeseed, (**c**) Wheat, (**d**) Corn, (**e**) Sunflower, (**f**) Grassland, (**g**) Broadleaf and (**h**) Needleleaf) over the study area. Vertical bars represent the standard deviation of values from all pixels belonging to same landcover type.

Black-sky FAPAR and white-sky FAPAR (Figure 9) follow seasonal profiles similar to those of LAI. The white-sky FAPAR is higher than the black-sky FAPAR in the growing season. However, it is close or even lower than the black-sky FAPAR in the beginning and the end of growing season: when the sun zenith angle increases, the direct illumination has long penetration path in the canopy, leading to a higher absorption than that of the diffuse illumination. This has been demonstrated in the model simulation from Li and Fang [17]. The seasonal profiles for FCOVER are also similar to those of LAI and black-sky FAPAR (Figure 10).

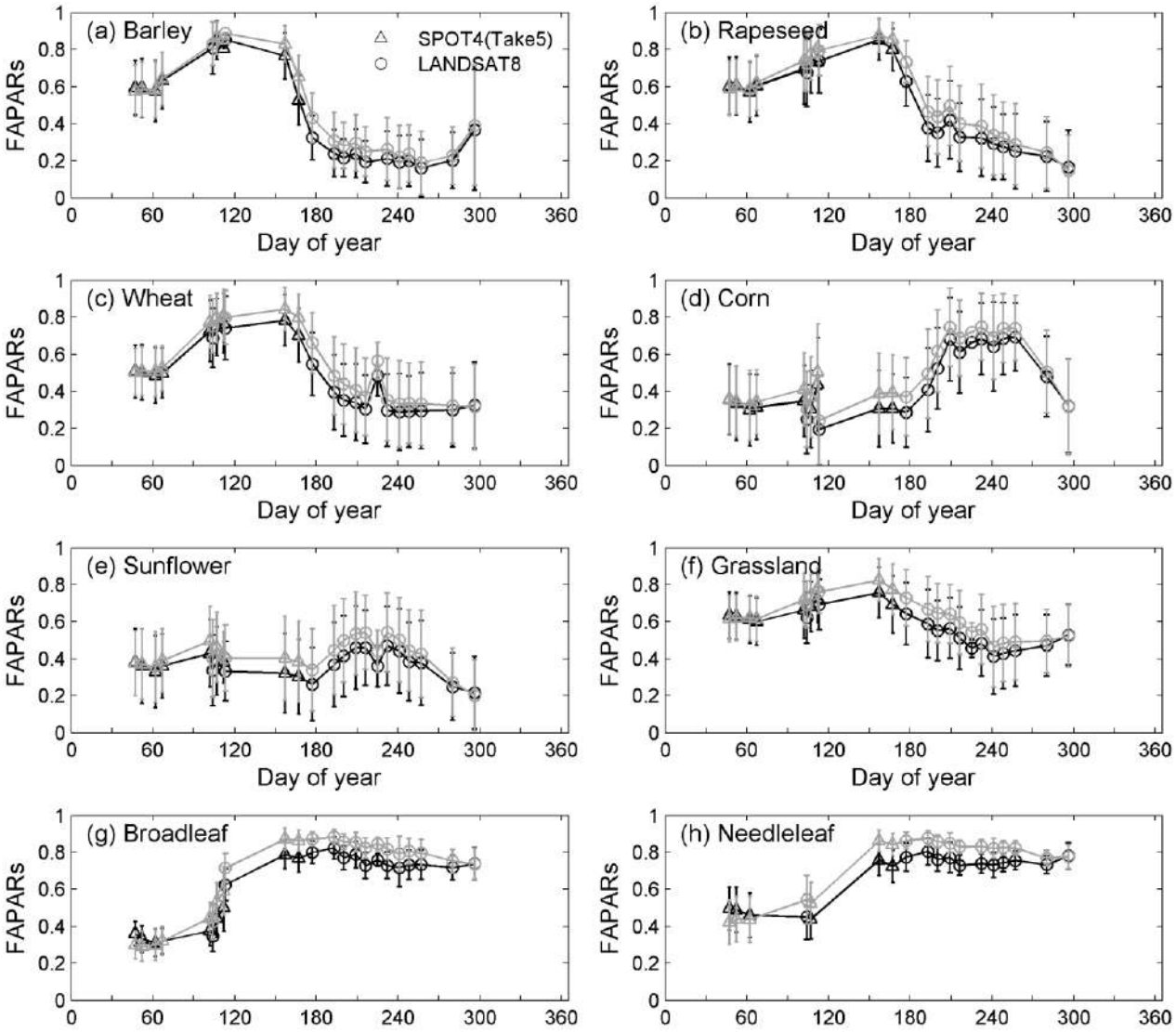

Figure 9. Seasonal variation of black-sky FAPAR (black symbols) and white-sky FAPAR (gray symbols) products estimated from SPOT4_HRVIR (Take5) and Landsat 8 sensors for eight biomes ((**a**) Barley, (**b**) Rapeseed, (**c**) Wheat, (**d**) Corn, (**e**) Sunflower, (**f**) Grassland, (**g**) Broadleaf and (**h**) Needleleaf) over the study area. Vertical bars represent the standard deviation of values from all pixels belonging to same landcover type.

The average profiles per landcover class shows a smooth behavior, demonstrating that high temporal consistency of the algorithm. Further, only marginal differences could be observed between SPOT4_HRVIR and Landsat 8 profiles, proving that a single algorithm adapted to two different sensors provides consistent estimates, confirming the previous observations on the spatial consistency. However, the averaging process per landcover class masks possible variability within a class due to environmental or cultural practices differences. Nevertheless, inspection of profiles of individual fields (data not shown for the sake of brevity) confirms the high temporal consistency (temporal smoothness) as well as the good match between SPOT4_HRVIR and Landsat 8 derived products.

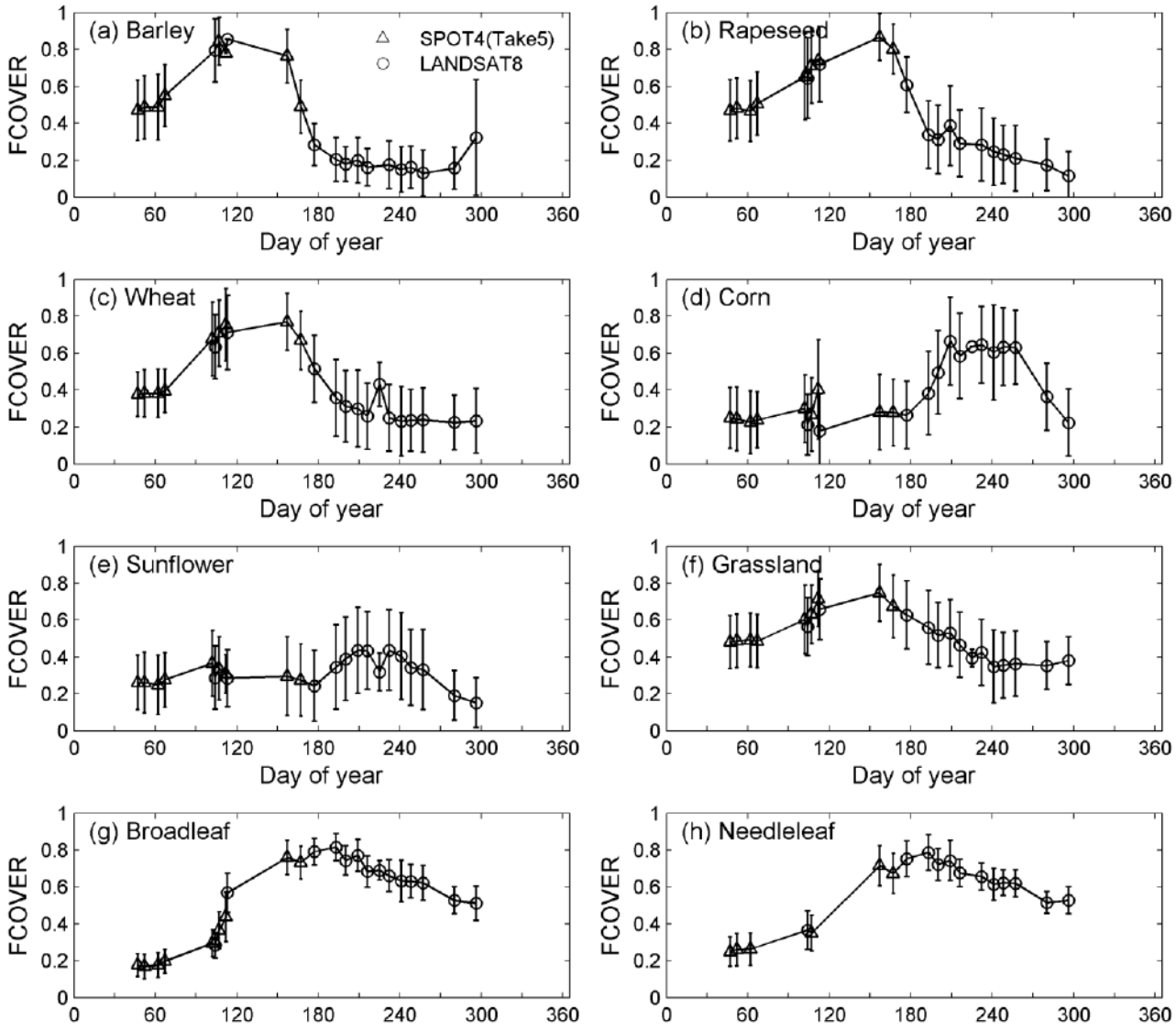

Figure 10. Seasonal variation of FCOVER products estimated from SPOT4_HRVIR (Take5) and Landsat 8 sensors for eight biomes ((**a**) Barley, (**b**) Rapeseed, (**c**) Wheat, (**d**) Corn, (**e**) Sunflower, (**f**) Grassland, (**g**) Broadleef and (**h**) Needleleaf) over the study area. Vertical bars represent the standard deviation of values from all pixels belonging to same landcover type.

4.3. Direct Validation

The retrieved biophysical products were compared to the corresponding field measurements over three landcover classes. Single date field measurements were linearly interpolated to match the date of the satellite observation on the same location. The satellite estimated LAI corresponds well to the field measurements over all landcover classes (R^2 = 0.83, bias = 0.07) (Figure 11a). However, the satellite estimated LAI slightly overestimates the field LAI over the wheat and sunflower, while a small negative bias is observed for maize (Bias = −0.09) (Table 7). The underestimations over maize is mainly observed for the larger LAI values (LAI > 2.5). The satellite black-sky FAPAR estimates are strongly related to the field measured values, although showing a positive offset corresponding to an overestimation of the satellite black-sky and white sky FAPAR mainly for the lowest FAPAR values.

(Figure 11b,c). The best relationship and lowest bias were observed on maize (R^2 = 0.91, bias = 0.01), while the largest bias of 0.11 was found on wheat. The FCOVER product is closely related to the field measured data, however some overestimations are observed over all the crops (0.05–0.13) (Figure 11d, Table 7). Table 8 shows the proportion of validation pixels that could meet the GCOS requirements for LAI, FAPAR and FCOVER products. LAI products have the best performance, with 77% of validation pixels within the GCOS boundaries (max(0.5, 20%)). However, more sunflower and maize validation pixels meet the GCOS requirement as compared to wheat. For FAPAR, 50% of the black-sky FAPAR and 52% of white-sky FAPAR meet the GCOS requirements (max(0.05, 10%)). For FCOVER, using the same requirements as for FAPAR, only 32% of validation pixels are within the GCOS range. Note that these percentage values are only calculated from the validation pixels, not the whole image.

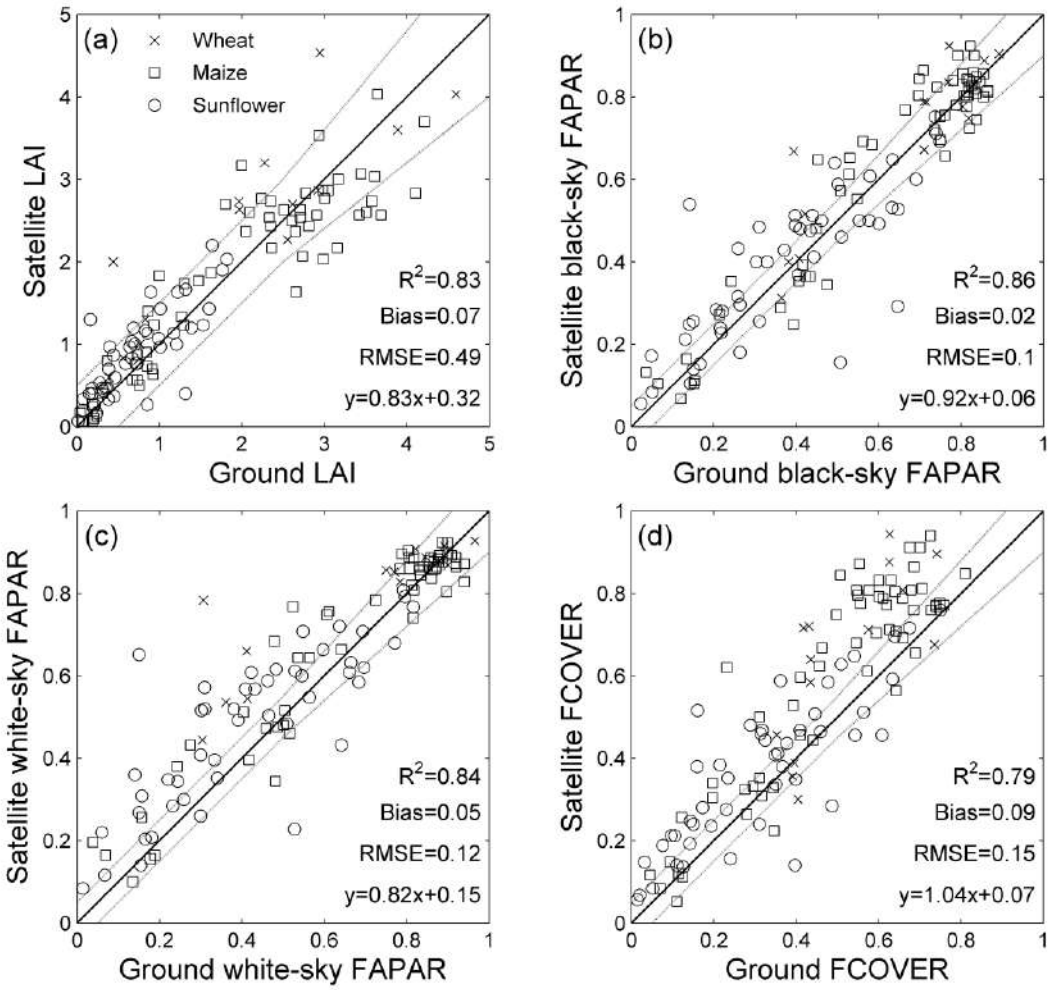

Figure 11. Direct validation of (**a**) LAI, (**b**) black-sky FAPAR, (**c**) white-sky FAPAR and (**d**) FCOVER products derived from the SPOT4_HRVIR (Take5) and Landsat 8 sensors with the ground measurements over three biomes. The dark line is the 1:1 line. Dashed lines represent the GCOS (2011) requirements boundaries.

Table 7. Statistics of the direct validation results for satellite derived LAI, black-sky FAPAR, white-sky FAPAR and FCOVER with the ground measurements over wheat, maize and sunflowers.

	Wheat			Maize			Sunflower		
	R^2	Bias	RMSE	R^2	Bias	RMSE	R^2	Bias	RMSE
LAI	0.76	0.4	0.74	0.82	−0.09	0.5	0.65	0.16	0.36
Black-sky FAPAR	0.81	0.04	0.1	0.91	0.01	0.08	0.65	0.02	0.12
White-sky FAPAR	0.76	0.11	0.17	0.91	0.03	0.08	0.67	0.06	0.14
FCOVER	0.56	0.13	0.19	0.83	0.11	0.15	0.69	0.05	0.12

Table 8. Percentage of the validation pixels that meet the GCOS requirements.

	Wheat (%)	Maize (%)	Sunflower (%)	All (%)
LAI	64.29	72.88	85.11	76.67
Black-sky FAPAR	57.14	55.93	40.43	50
White-sky FAPAR	38.46	67.24	36.17	51.69
FCOVER	21.43	33.90	31.95	31.67

5. Discussions

A neural network based algorithm was developed in this study to retrieve LAI, FAPAR and FCOVER products from either SPOT4_HRVIR or Landsat 8 surface reflectance data. The neural networks were trained over a simulated learning data base by taking into account the distribution and co-distribution laws of the input variables. As the algorithm is not land cover dependent, we used a truncated Gaussian distribution law to be most representative of a wide range of landcover types and thus, mimic the actual distribution of the radiative transfer model input variables [16]. Furthermore, by considering the co-distribution law of variables with LAI, the realism of the learning data base is expected to be improved. However, the information related to the distribution and co-distribution laws of variables is actually limited. More studies should be conducted on this topic to improve the learning database generation.

The products derived from SPOT4_HRVIR and Landsat 8 data show very good spatial and temporal consistency (Figures 6–10). For very close acquisition dates, SPOT4_HRVIR and Landsat 8 products are very similar and most of the differences are within a limited range. The results demonstrate the robustness of the proposed algorithm and its suitability to be applied to several satellites. The temporal profiles show that two sensors complement themselves to describe the seasonal variation of vegetation: the combination of sensors may overcome the typical low revisit frequency of decametric sensors, allowing to build virtual constellations.

The comparisons with the field measurements demonstrate the good quality of the derived products (Figure 11, Tables 7 and 8). Seventy-seven percent of the satellite LAI meets the GCOS requirement although it shows a slight underestimation over the maize crops when LAI is larger than 2. The assumptions made on canopy structure in the SAIL model may partly explain these artifacts. Further, the satellite derived LAI product corresponds to the green LAI, while the field measured LAI from the upward looking DHPs includes all components of the canopy (green and non-green elements). Both black-sky and white-sky FAPAR products show good relationships with the field measurements. More

than half of FAPAR validation pixels meet the GCOS requirements. The RMSE value for FAPAR is in the same range as those reported by several studies [16,47,48]. For FCOVER, only 32% of FCOVER validation pixels are within the max (0.05, 10%) accuracy range, showing a small overestimation compared with the ground FCOVER value. The overestimation may result from the higher sensitivity of FCOVER to the contribution of soil reflectance, the clumping effect which is maximum in the vertical direction, as well as uncertainties related to the field measurements of FCOVER. Nevertheless, the RMSE value for FCOVER (RMSE = 0.15) is close to the values reported in other studies [16,49] .

6. Conclusions

This study shows the interest of this generic algorithm to derive LAI, FAPAR and FCOVER consistent products from SPOT4_HRVIR and Landsat 8 over the study area. These principles will be applied to the recently launched Sentinel-2 mission with a high revisit frequency and a decametric spatial resolution that will contribute to a large range of applications. To further improve the accuracy of the algorithm to apply for Sentinel-2, efforts should devoted towards three complementary directions: (i) first, more sites with field measurements need to be considered to better describe the limits of the algorithm; (ii) second, this algorithm is by construction "generic": it applies potentially to all landcover types. Major improvements are expected from the development of more specific algorithms, *i.e.*, when the training is achieved over a limited set of cases defined for each landcover type. This will imply that one could achieve a near real time estimation of the landcover class associated to each pixel. The temporal profiles generated from the output of the generic algorithm would help identifying the landcover class associated to each pixel. Then the "specific" biophysical algorithm will be run to fine tune the solution by exploiting the knowledge of the landcover class. (iii) Finally, the expected smoothness of the temporal profiles of these biophysical variables and their typical shape for each landcover type should be exploited to smooth out possible residual artifacts and help filling gaps due to cloud or snow cover.

Acknowledgments

This research was carried out within the ImagineS project in the 326 FP7-SPACE-2012-1 Grant Agreement Number 311766. The SPOT4 (Take5) and Landsat 8 surface reflectance data were downloaded from the THEIA site (http://spirit.cnes.fr/take5/).

Author Contributions

Wenjuan Li contributed to the biophysical products generation, data analysis and paper writing. Frédéric Baret and Marie Weiss designed the research and the prototype of the algorithm. Francois Waldner and Pierre Defourny conducted the land cover classification. Valerie Demarez provided the field measurements data. David Morin and Olivier Hagolle generated the surface reflectance data. All the authors shared equally the editing of the manuscript.

Conflicts of Interest

The authors declare no conflict of interest.

References

1. Chen, J.M.; Black, T.A. Defining leaf area index for non-flat leaves. *Plant Cell Environ.* **1992**, *45*, 421–429.
2. Weiss, M.; Baret, F. FAPAR (fraction of Absorbed Photosynthetically Active Radiation) estimates at various scale. In Proceedings of the 34th International Symposium on Remote Sensing and Environment (ISRSE), Sydney, Australia, 10–15 April 2010; pp. 1–4.
3. GCOS. *Systematic Observation Requirements for Satellite-Based Productsfor Climate, 2011 Update, Supplemental Details to the Satellite-Based Com-ponent of the Implementation Plan for the Global Observing System for Climate in Support of the UNFCCC (2010 Update)*; World Meteorological Organization (WMO): Geneva, Switzerland, 2011.
4. McCallum, I.; Wagner, W.; Schmullius, C.; Shvidenko, A.; Obersteiner, M.; Fritz, S.; Nilsson, S. Satellite-based terrestrial production efficiency modeling. *Carbon Balance Manag.* **2009**, doi:10.1186/1750-0680-4-8.
5. Baret, F.; Hagolle, O.; Geiger, B.; Bicheron, P.; Miras, B.; Huc, M.; Berthelot, B.; Niño, F.; Weiss, M.; Samain, O.; *et al.* LAI, fAPAR and fCOVER CYCLOPES global products derived from VEGETATION: Part 1: Principles of the algorithm. *Remote Sens. Environ.* **2007**, *110*, 275–286.
6. Baret, F.; Weiss, M.; Lacaze, R.; Camacho, F.; Makhmara, H.; Pacholcyzk, P.; Smets, B. GEOV1: LAI and FAPAR essential climate variables and FCOVER global time series capitalizing over existing products. Part1: Principles of development and production. *Remote Sens. Environ.* **2013**, *137*, 299–309.
7. Gobron, N.; Pinty, B.; Verstraete, M.; Govaerts, Y. The MERIS Global Vegetation Index (MGVI): Description and preliminary application. *Int. J. Remote Sens.* **1999**, *20*, 1917–1927.
8. Knyazikhin, Y.; Martonchik, J.V.; Myneni, R.B.; Diner, D.J.; Running, S.W. Synergistic algorithm for estimating vegetation canopy leaf area index and fraction of absorbed photosynthetically active radiation from MODIS and MISR data. *J. Geophys. Res.* **1998**, *103*, 257–275.
9. Pinty, B.; Andredakis, I.; Clerici, M.; Kaminski, T.; Taberner, M.; Verstraete, M.M.; Gobron, N.; Plummer, S.; Widlowski, J.L. Exploiting the MODIS albedos with the Two-stream Inversion Package (JRC-TIP): 1. Effective leaf area index, vegetation, and soil properties. *J. Geophys. Res.* **2011**, doi:10.1029/2010JD015372.
10. Liang, S.; Zhao, X.; Liu, S.; Yuan, W.; Cheng, X.; Xiao, Z.; Zhang, X.; Liu, Q.; Cheng, J.; Tang, H.; *et al.* A long-term Global LAnd Surface Satellite (GLASS) data-set for environmental studies. *Int. J. Digit. Earth* **2013**.
11. Garrigues, S.; Allard, D.; Baret, F.; Morisette, J. Multivariate quantification of landscape spatial heterogeneity using variogram models. *Remote Sens. Environ.* **2008**, *112*, 216–230.
12. Berger, M.; Moreno, J.; Johannessen, J.A.; Levelt, P.F.; Hanssen, R.F. ESA's Sentinel missions in support of Earth system science. *Remote Sens. Environ.* **2012**, *120*, 84–90.
13. Ganguly, S.; Nemani, R.R.; Zhang, G.; Hashimoto, H.; Milesi, C.; Michaelis, A.; Wang, W.; Votava, P.; Samanta, A.; Melton, F.; *et al.* Generating global leaf area index from Landsat: Algorithm formulation and demonstration. *Remote Sens. Environ.* **2012**, *122*, 185–202.

14. Propastin, P.; Panferov, O. Retrieval of remotely sensed LAI using Landsat ETM+ data and ground measurements of solar radiation and vegetation structure: Implication of leaf inclination angle. *Int. J. Appl. Earth Obs. Geoinf.* **2013**, *25*, 38–46.
15. Verger, A.; Martínez, B.; Camacho-de Coca, F.; García-Haroa, F.J. Accuracy assessment of fraction of vegetation cover and leaf area index estimates from pragmatic methods in a cropland area. *Int. J. Remote Sens.* **2009**, *30*, 2685–2704.
16. Verger, A.; Baret, F.; Camacho de Coca, F. Optimal modalities for radiative transfer-neural network estimation of canopy biophysical characteristics: Evaluation over an agricultural area with CHRIS/PROBA observations. *Remote Sens. Environ.* **2011**, *115*, 415–426.
17. Li, W.; Fang, H. Estimation of direct, diffuse, and total FPARs from Landsat surface reflectance data and ground-based estimates over six FLUXNET sites. *J. Geophys. Res.: Biogeosci.* **2015**, *120*, 96–112.
18. Claverie, M.; Demarez, V.; Duchemin, B.; Hagolle, O.; Ducrot, D.; Marais-Sicre, C.; Dejoux, J.-F.; Huc, M.; Keravec, P.; Béziat, P.; *et al.* Maize and sunflower biomass estimation in southwest france using high spatial and temporal resolution remote sensing data. *Remote Sens. Environ.* **2012**, *124*, 844–857.
19. Bignalet-Cazalet, F.; Baillarin, S.; Greslou, D.; Panem, C. Automatic and generic mosaicing of satellite images. In Proceedings of the IEEE International Geoscience and Remote Sensing Symposium, Honolulu, HI, USA, 25–30 July 2010; pp. 3158–3161.
20. Baillarin, S.; Gigord, P.; Hagolle, O. Automatic registration of optical images, a stake for future missions: Application to ortho-rectification, time series and mosaic products. In Proceedings of the IEEE International Geoscience and Remote Sensing Symposium, Boston, MA, USA, 7–11 July 2008; pp. 1112–1115.
21. Hagolle, O.; Dedieu, G.; Mougenot, B.; Debaecker, V.; Duchemin, B.; Meygret, A. Correction of aerosol effects on multi-temporal images acquired with constant viewing angles: Application to Formosat-2 images. *Remote Sens. Environ.* **2008**, *112*, 1689–1701.
22. Hagolle, O.; Huc, M.; Pascual, D.V.; Dedieu, G. A multi-temporal method for cloud detection, applied to FORMOSAT-2, VENμS, LANDSAT and SENTINEL-2 images. *Remote Sens. Environ.* **2010**, *114*, 1747–1755.
23. Hagolle, O.; Huc, M.; Dedieu, G.; Sylvander, S.; Houpert, L.; Leroy, M.; Clesse, D.; Daniaud, F.; Arino, O.; Koetz, B.; *et al.* SPOT4 (Take 5) time series over 45 sites to prepare Sentinel-2 applications and methods. In Proceedings of the ESA Living Planet Symposium, Edinburgh, UK, 9–13 September 2013; pp. 1–7.
24. Breiman, L.; Friedman, J.; Stone, C.J.; Olshen, R.A. *Classification and Regression Trees*; CRC press: Boca Raton, FL, USA, 1984.
25. Waldner, F.; Lambert, M.-J.; Li, W.; Weiss, M.; Demarez, V.; Hagolle, O.; Baret, F.; Defourny, P. Land cover and crop type classification along the season based on biophysical variables retrieved from multi-sensor high-resolution time series. *Remote Sens.* **2015**, *7*, 10400–10424.
26. Demarez, V.; Duthoit, S.; Baret, F.; Weiss, M.; Dedieu, G. Estimation of leaf area and clumping indexes of crops with hemispherical photographs. *Agric. For. Meteorol.* **2008**, *148*, 644–655.
27. Weiss, M.; Baret, F. *Can-Eye v6.1 User Manual*; Available online: http://www6.paca.inra.fr/can-eye/Documentation-Publications/Documentation (accessed on 16 June 2010).

28. Nilson, T. A theoretical analysis of the frequency of gaps in plant stands. *Agric. Meteorol.* **1971**, *8*, 25–38.
29. Weiss, M.; Baret, F.; Smith , G.J.; Jonckheered, I.; Coppin, P. Review of methods for *in situ* leaf area index determination, part II: Estimation of LAI, errors and sampling. *Agric. For. Meteorol.* **2004**, *121*, 37–53.
30. Andrieu, B.; Baret, F. Indirect methods of estimating crop structure from optical measurements. In *Crop Structure and Light Microclimate—Characterization and Applications*; Varlet-Grancher, R.B.C., Sinoquet, H., Eds.; INRA: Paris, France, 1993; pp. 285–322.
31. Baret, F.; Buis, S. Estimating canopy characteristics from remote sensing observations. Review of methods and associated problems. In *Advances in Land Remote Sensing: System, Modeling, Inversion and Application*; Liang, S., Ed.; Springer: Dordrecht, The Netherlands, 2007.
32. Krasnopolsky, V.M.; Chevallier, F. Some neural network applications in environmental sciences. Part II: Advancing computational efficiency of environmental numerical models. *Neural Netw.* **2003**, *16*, 335–348.
33. Weiss, M.; Baret, F.; Leroy, M.; Hautecœur, O.; Bacour, C.; Prévot, L.; Bruguier, N. Validation of neural net techniques to estimate canopy biophysical variables from remote sensing data. *Agronomie* **2002**, *22*, 547–553.
34. Fang, H.; Liang, S.; McClaran, M.P.; van Leeuwen, W.J.D.; Drake, S.; Marsh, S.E.; Thomson, A.M.; Izaurralde, R.C.; Rosenberg, N.J. Biophysical characterization and management effects on semiarid rangeland observed from landsat ETM+ data. *IEEE Trans. Geosci. Remote Sens.* **2005**, *43*, 125–134.
35. Bacour, C.; Baret, F.; Béal, D.; Weiss, M.; Pavageau, K. Neural network estimation of *LAI*, *fAPAR*, *fCOVER* and $LAI \times C_{ab}$, from top of canopy MERIS reflectance data: Principles and validation. *Remote Sens. Environ.* **2011**, *105*, 313–325.
36. Jacquemoud, S.; Verhoef, W.; Baret, F.; Bacour, C.; Zarco-Tejada, P.J.; Asner, G.P.; François, C.; Ustin, S.L. PROSPECT+SAIL models: A review of use for vegetation characterization. *Remote Sens. Environ.* **2009**, *113*, 56–66.
37. Verhoef, W. Light scattering by leaf layers with application to canopy reflectance modeling: The sail model. *Remote Sens. Environ.* **1984**, *16*, 125–141.
38. Jacquemoud, S.; Baret, F. PROSPECT: A model of leaf optical properties spectra. *Remote Sens. Environ.* **1990**, *34*, 75–91.
39. Campbell, G.S. Extinction coefficients for radiation in plant canopies calculated using an ellipsoidal inclination angle distribution. *Agric. For. Meteorol.* **1986**, *36*, 317–321.
40. Kuusk, A. Determination of vegetation canopy parameters from optical measurements. *Remote Sens. Environ.* **1991**, *37*, 207–218.
41. Fourty, T.; Baret, F. *Amelioration de la Precision des Coefficients D'absorption Specifique de la Matiere Seche et des Pigments Photosynthetiques*; INRA: Avignon, France 1997.
42. Liu, W.; Baret, F.; Gu, X.; Zhang, B.; Tong, Q.; Zheng, L. Evaluation of methods for soil surface moisture estimation from reflectance data. *Int. J. Remote Sens.* **2003**, *24*, 2069–2083.
43. Baret, F.; Weiss, M.; Berthelot, B. *Sentinel-2 MSI Products - WP1152 Algorithm Theoretical Basis Document for Product Group B*; INRA-EMMAH: Avignon, France, 2009.

44. Bacour, C.; Jacquemoud, S.; Tourbier, Y.; Dechambre, M.; Frangi, J.-P. Design and analysis of numerical experiments to compare four canopy reflectance models. *Remote Sens. Environ.* **2002**, *79*, 72–83.
45. Rummelhart, D.E.; Hinton, G.E.; Williams, R.J. Learning internal representations by error propagation. In *Parallel Data Processing*; Rummelhart, D., Mc Clelland, J., Eds.; MIT Press: Cambridge, MA, USA, 1986; Volume 1, pp. 318–362.
46. Ngia, L.S.H.; Sjoberg, J. Efficient training of neural nets for nonlinear adaptive filtering using a recursive Levenberg–Marquardt algorithm. *IEEE Trans. Signal Process.* **2000**, *48*, 1915–1927.
47. Gobron, N.; Pinty, B.; Aussedat, O.; Chen, J.M.; Cohen, W.B.; Fensholt, R.; Gond, V.; Huemmrich, K.F.; Lavergne, T.; Mélin, F.; Privette, J.L.; *et al.* Evaluation of fraction of absorbed photosynthetically active radiation products for different canopy radiation transfer regimes: Methodology and results using Joint Research Center products derived from SeaWiFS against ground-based estimations. *J. Geophyis. Res.* **2006**, doi:10.1029/2005JD006511.
48. Weiss, M.; Baret, F.; Block, T.; Koetz, B.; Burini, A.; Scholze, B.; Lecharpentier, P.; Brockmann, C.; Fernandes, R.; Plummer, S.; *et al.* On line validation exercise (OLIVE): A web based service for the validation of medium resolution land products. Application to FAPAR products. *Remote Sens.* **2014** *6*, 4190–4216.
49. Camacho, F.; Cernicharo, J.; Lacaze, R.; Baret, F.; Weiss, M. GEOV1: LAI, FAPAR essential climate variables and FCOVER global time series capitalizing over existing products. Part 2: Validation and intercomparison with reference products. *Remote Sens. Environ.* **2013**, *137*, 310–329.

AGU PUBLICATIONS

JGR

Journal of Geophysical Research: Biogeosciences

RESEARCH ARTICLE
10.1002/2014JG002754

Key Points:
- Landsat direct, diffuse, and total FPARs estimation
- Field direct and diffuse FPAR estimation
- Differences between FPAR definitions and influences on APAR

Correspondence to:
W. Li,
wenjuan.li122@gmail.com

Citation:
Li, W., and H. Fang (2015), Estimation of direct, diffuse, and total FPARs from Landsat surface reflectance data and ground-based estimates over six FLUXNET sites, *J. Geophys. Res. Biogeosci.*, *120*, 96–112, doi:10.1002/2014JG002754.

Received 28 JUL 2014
Accepted 13 DEC 2014
Accepted article online 18 DEC 2014
Published online 22 JAN 2015

Estimation of direct, diffuse, and total FPARs from Landsat surface reflectance data and ground-based estimates over six FLUXNET sites

Wenjuan Li[1,2] and Hongliang Fang[1]

[1]LREIS, Institute of Geographic Sciences and Natural Resources Research, Chinese Academy of Sciences, Beijing, China, [2]University of Chinese Academy of Sciences, Beijing, China

Abstract The fraction of photosynthetically active radiation (PAR) absorbed by green elements (FPAR) is an essential climate variable in quantifying canopy absorbed PAR (APAR) and gross and net primary production. Current satellite FPAR products typically correspond to black-sky FPAR under direct illumination only, but the radiation transfer and vegetation absorption processes differ for direct and diffuse PARs. To address this, the present study developed a new approach to estimate direct, diffuse, and total FPARs, separately, from Landsat surface reflectance data. Field-measured direct and diffuse FPARs were first derived for crops, deciduous broadleaf forests, and evergreen needleleaf forests at six FLUXNET sites. Then, a coupled soil-leaf-canopy radiative transfer model (SLC) was used to simulate surface reflectance under direct and diffuse illumination conditions. Direct, diffuse, and total FPARs were estimated by comparing Landsat-5 Thematic Mapper (TM) data and simulated surface reflectances using a lookup table approach. The differences between the Landsat-estimated and the field-measured FPARs are less than 0.05 (10%). The diffuse FPAR is higher than the direct FPAR by up to 19.38%, whereas the total FPAR is larger than the direct FPAR by up to 16.07%. The direct APAR is higher than the diffuse APAR under clear-sky conditions, but underestimates the total APAR by $-277.72\ \mu mol\ s^{-1}\ m^{-2}$ on average. The approach described here can be extended to estimate direct, diffuse, and total FPARs from other satellite data and the obtained FPAR variables could be helpful to improve modeling of vegetation processes.

1. Introduction

The fraction of photosynthetically active radiation (PAR) absorbed by green elements (FPAR) can be defined as the ratio of total absorbed PAR (APAR) to incoming PAR at the top of the canopy and represents the energy absorption efficiency of the canopy for downwelling PAR. Specified as an essential climate variable by the Global Climate Observing System [*Global Climate Observing System*, 2011], FPAR is a critical parameter in characterizing energy, mass, and momentum exchanges between the canopy and the atmosphere and is required for photosynthesis and primary production simulations [*Gobron and Verstraete*, 2009].

FPAR represents the summed canopy absorption efficiency for both direct and diffuse PAR. It has been demonstrated that FPAR is larger under totally diffuse than clear-sky conditions because all canopy parts can absorb lights effectively under diffuse conditions, whereas some portions of the canopy will be shaded under direct light conditions [*Goward and Huemmrich*, 1992; *Nouvellon et al.,* 2000; *Thomas et al.,* 2006]. Therefore, the direct and diffuse FPARs are commonly defined, separately, as the FPAR values obtained under clear (most sunny) and overcast (most cloudy) conditions, respectively [*Thomas et al.,* 2006].

In the field, direct and diffuse FPARs can be calculated from the transmitted and reflected PARs measured separately under direct and diffuse illumination conditions [*Gobron et al.,* 2006]. However, field measurements are usually difficult to obtain under variable sky conditions [*Gu et al.,* 2002]. Direct and diffuse FPARs have also been estimated as a function of leaf area index (LAI), leaf transmission, or scattering coefficients in land surface models, such as the Common Land Model [*Dai et al.,* 2003], Basin Irrigation System [*Foley et al.,* 1996], and Simple Biosphere 2 [*Sellers*, 1985]. However, several studies have reported that both direct and diffuse FPARs are underestimated in current land surface models because of the simplification of radiative transfer processes [*Senna et al.,* 2005; *Tian et al.,* 2004].

Satellite FPAR products have been generated at different temporal and spatial resolutions, such as Moderate Resolution Imaging Spectroradiometer (MODIS) [*Knyazikhin et al.,* 1998], VGT bioGEOphysical product Version 1(GEOV1) [*Baret et al.,* 2013], Medium-Resolution Imaging Spectrometer (MERIS) [*Gobron et al.,* 1999], and Joint Research Centre Two-stream Inversion Procedure (JRC-TIP) [*Pinty et al.,* 2011]. MODIS FPAR product is derived from the inversion of biome-based 3-D radiative transfer model using the lookup table approach. The GEOV1 product is generated from neural networks trained by using the "best estimates" of FPAR obtained by fusion of MODIS and CYCLOPES FPAR products. The MERIS FPAR product is computed as a function of rectified red and near-infrared (NIR) bands reflectance and several polynomial coefficients which are optimized using a training dataset generated from a 1-D semidiscrete land-surface-atmosphere coupled RT model. The JRC-TIP FPAR product is derived based on MODIS broadband visible and NIR albedo (black-sky and white-sky) products from combined Terra-Aqua data sets. The MODIS, GEOV1, and MERIS FPAR products are retrieved as the instantaneous black-sky FPAR under direct illumination, without considering the relative proportion of diffuse radiation in the total radiation. However, even under fully clear-sky conditions, the proportion of diffuse PAR over the surface cannot be ignored [*Gu et al.,* 2002]. Otherwise, FPAR will be underestimated, especially for small leaf area index (LAI) region [*Goward and Huemmrich*, 1992; *Tian et al.,* 2004]. The JRC-TIP algorithm generates direct FPAR and diffuse FPARs, separately, but the product has not been fully validated due to the lack of companion field measurements.

The present study aims to estimate direct, diffuse, and total FPARs from Landsat reflectance data. The advantages of the high-resolution (30 m) Landsat data make them appealing for local photosynthesis and primary production studies and for the validation of current moderate-resolution FPAR products. In this study, a coupled soil-leaf-canopy (SLC) radiative transfer model [*Verhoef and Bach*, 2007] was used to estimate direct and diffuse FPARs from 30 m Landsat surface reflectance data. Six FLUXNET sites including crops, deciduous broadleaf forests, and evergreen needleleaf forests were selected to derive field direct and diffuse FPARs and to validate the Landsat estimates. Here the total and direct FPARs are compared and the influences of different FPAR components on APAR estimation are explored. The results of this study will be invaluable for the generation of FPAR products and future studies utilizing regional and global direct, diffuse, and total FPAR products.

2. Methods and Measurements

2.1. Theory

The instantaneous total APAR at the top of the canopy (TOC) is a sum of the direct and diffuse APARs.

$$\mathrm{APAR}_t(\theta_s) = \mathrm{APAR}_{\mathrm{dir}}(\theta_s) + \mathrm{APAR}_{\mathrm{dif}}(\theta_s) \tag{1}$$

where APAR_t, $\mathrm{APAR}_{\mathrm{dir}}$, and $\mathrm{APAR}_{\mathrm{dif}}$ represent total APAR, direct APAR, and diffuse APAR at solar zenith angle θ_s, respectively.

$$\mathrm{APAR}_{\mathrm{dir}}(\theta_s) = \mathrm{PAR}_{\mathrm{dir}}(\theta_s) \times \mathrm{FPAR}_{\mathrm{dir}}(\theta_s) \tag{2}$$

$$\mathrm{APAR}_{\mathrm{dif}}(\theta_s) = \mathrm{PAR}_{\mathrm{dif}}(\theta_s) \times \mathrm{FPAR}_{\mathrm{dif}} \tag{3}$$

where $\mathrm{PAR}_{\mathrm{dir}}$, $\mathrm{FPAR}_{\mathrm{dir}}$, $\mathrm{PAR}_{\mathrm{dif}}$, and $\mathrm{FPAR}_{\mathrm{dif}}$ represent instantaneous direct PAR, direct FPAR, diffuse PAR, and diffuse FPAR, respectively. Direct and diffuse FPAR corresponds to the canopy absorption capacity for direct and diffuse incoming PAR, respectively. Note that diffuse FPAR is invariant with the solar zenith angle (SZA) (section 3.1).

By substituting equations (2) and (3) into equation (1), and dividing by total PAR on both sides, the total FPAR at the top of the canopy (TOC) can be expressed as a weighted sum of direct and diffuse FPARs, as follows:

$$\mathrm{FPAR}_{\mathrm{tol}}(\theta_s) = (1 - \mathrm{skyl}(\theta_s)) \cdot \mathrm{FPAR}_{\mathrm{dir}}(\theta_s) + \mathrm{skyl} \cdot \mathrm{FPAR}_{\mathrm{dif}} \tag{4}$$

where $\mathrm{FPAR}_{\mathrm{tol}}$ and skyl represent total FPAR and the instantaneous proportion of diffuse PAR in the total incoming PAR, respectively.

According to equation (4), the instantaneous direct FPAR can be calculated if the total FPAR, diffuse ratio and diffuse FPAR are known

$$\mathrm{FPAR}_{\mathrm{dir}}(\theta_s) = (\mathrm{FPAR}_{\mathrm{tol}}(\theta_s) - \mathrm{skyl} \cdot \mathrm{FPAR}_{\mathrm{dif}}) / (1 - \mathrm{skyl}(\theta_s)) \tag{5}$$

Journal of Geophysical Research: Biogeosciences 10.1002/2014JG002754

Table 1. Six FLUXNET Sites and the Available Landsat Scenes[a]

Station Name	Country	Location	Surface Type	Canopy Height	Sensors Height	Period	Landsat Path/Row	Scene Time	References
Mead Irrigated (Mead NE1)	USA	41.17° N, 96.48° W	Continuous maize	3.5 m	TOC: 5.5 m (↓), 5.5 m (↑) BOC: ground (↓↑)	2003.1 to 2010.10	28/31	May–September	*Verma et al.* [2005]
Mead Irrigated Rotation (Mead NE2)	USA	41.17° N, 96.47° W	Maize-soybean	3.4 m (maize) 1 m (soybean)	TOC: 5.5 m (↓), 5.5 m (↑) BOC: ground (↓↑)	2003.1 to 2010.10	28/31	May–September	*Verma et al.* [2005]
Mead Rainfed (Mead NE3)	USA	41.18° N, 96.44° W	Maize-soybean	2.7 m (maize) 0.8 m (soybean)	TOC: 5.5 m (↓), 5.5 m (↑) BOC: ground (↓↑)	2003.1 to 2010.12	28/31	May–September	*Verma et al.* [2005]
Bartlett Experimental Forest (Bartlett)	USA	44.07° N, 71.29° W	Deciduous broadleaf forest	19 m	TOC: 25 m (↓), 23.8 m (↑), BOC: 1 m (↓)	2004.7 to 2007.9	13/29	April–September	*Jenkins et al.* [2007] *Ollinger and Smith* [2005]
Soroe	Denmark	55.49° N, 11.65° E	Deciduous broadleaf forest	30 m	TOC: 57 m (↓), 53.5 m (↑), BOC:*	2006.9 to 2010.10	195/21	April–September	*Pilegaard et al.* [2001]
Tharandt	Germany	50.96° N, 13.57° E	Evergreen needleleaf forest	30 m	TOC: 37 m (↓), 37 m (↑), BOC: 17 m (↓)	2004.8 to 2010.10	192/25	January–December	*Grumwald and Bernhofer* [2007]

[a]Canopy height represents the height at peak stage, and sensor height is the distance between sensor and ground. Downward (↓) and upward (↑) arrows indicate downwelling radiation and upwelling radiation measurements. TOC: the top of canopy; BOC: bottom of canopy. The information about the below-canopy PAR sensors used to measure the soil reflected PAR is from personal contact with the PI. The time of Landsat scenes was determined from the field measurements.

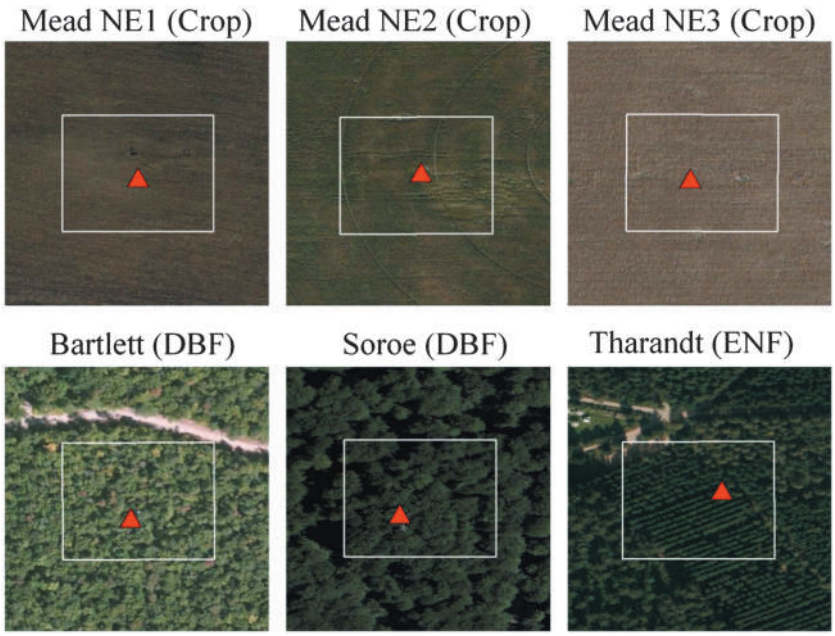

Figure 1. High-resolution images of six flux sites acquired from map.bing.com/maps in spatial scale of 1:1500. White squares represent the 3 × 3 Landsat pixels (90 × 90 m), with central pixel covering each tower (red rectangles). DBF: deciduous broadleaf forest; ENF: evergreen needleleaf forest.

2.2. Estimation of FPARs From Field Measurements

2.2.1. Site Descriptions

Six sites from the FLUXNET project (http://public.ornl.gov/FLUXNET/), covering crops, deciduous broadleaf forests (DBF), and evergreen needleleaf forests (ENF) were assembled for this study (Table 1). The selection of sites was based on spatial homogeneity, the representativeness of each vegetation type, and the available PAR measurements (total downwelling PAR, diffuse PAR, above-canopy reflected PAR, below-canopy transmitted PAR, and the soil reflected PAR). Since the field measurements were to be compared with the satellite-derived variables, each site had to be spatially homogeneous around the tower. Figure 1 shows the area and dominant vegetation type for a 90 m × 90 m area (3 by 3 Landsat pixels) centered on each tower.

All selected sites are equipped with two PAR sensors above the canopy, with one pointing toward the sky to measure the incoming total PAR, and the other facing downward to measure the surface reflected PAR. At each site, a sunshine sensor is mounted above the canopy to measure the total downwelling and diffuse component of the downwelling PAR. Direct PAR can be calculated from the differences between total and diffuse PAR. Three crop sites, Mead NE1, NE2, and NE3, are equipped with downward looking PAR sensors below the canopy to measure the reflected background PAR. For forest sites, the background albedo was ignored because most of the Landsat scenes were acquired during the growing season when the background albedo was negligibly small [*D'Odorico et al.,* 2014; *Jenkins et al.,* 2007; *Nouvellon et al.,* 2000]. Five upward looking PAR sensors at the three Mead sites and six at the Bartlett site [*Jenkins et al.,* 2007] are installed below the canopy to measure the transmitted PAR. At the other sites, one upward PAR sensor is used to measure the transmitted PAR.

As FPAR varies with the solar zenith angle, the instantaneous FPAR close to the satellite overpass time (10:00 A.M. for Landsat thematic mapper (TM) was extracted. At the Mead sites, field FPAR measurements are obtained every hour. For the present study, the instantaneous FPAR value was calculated by averaging FPAR from 9:30 A.M. to 10:30 A.M. At all forest sites, field measurements are typically made every half hour; here, the FPAR data at 10:00 am were selected for comparison with Landsat estimates. The instantaneous diffuse ratio was calculated as the ratio of the diffuse PAR to the total PAR.

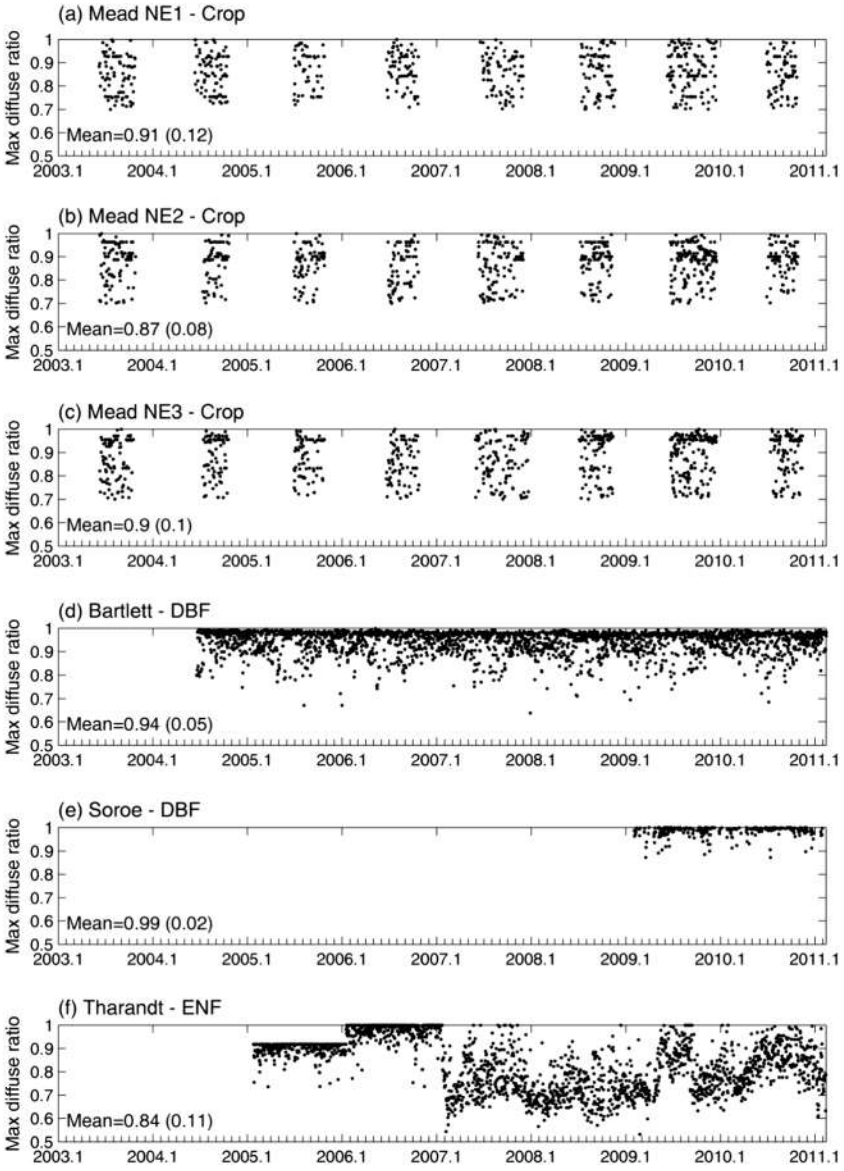

Figure 2. Seasonal variation of daily maximum diffuse ratio from field measurements at six sites, (a) Mead NE1, (b) Mead NE2, (c) Mead NE3, (d) Bartlett, (e) Soroe, and (f) Tharandt. The mean maximum diffuse ratio (and the standard deviation) is also shown in the lower left corner.

2.2.2. Estimation of Field FPARs

The instantaneous total FPAR can be estimated from the PAR measurements described above, as follows [*Goward and Huemmrich*, 1992]:

$$\mathrm{FPAR_{tol}} = \frac{\mathrm{PAR}_i - \mathrm{PAR}_r - (\mathrm{PAR}_t - \mathrm{PAR}_s)}{\mathrm{PAR}_i} \tag{6}$$

where PAR_i is the total incoming PAR at TOC, PAR_r is the canopy reflected PAR, PAR_t is the canopy transmitted PAR, and PAR_s is the PAR reflected from the soil surface. The term in parenthesis represent the PAR absorbed by the soil. At the three forest sites, PAR_s is ignored.

When the canopy remains stable (no sudden changes), the diffuse FPAR can be considered as an intrinsic attribute of the canopy and is independent of atmospheric conditions and solar zenith angles. In this case,

Table 2. List of Variables Required to Run SLC Model and Their Ranges

	Variables	Description	Unit	Ranges or Values
Geometric configuration	θ_v	View zenith angle	°	0
	θ_s	Solar zenith angle	°	0 5 10 15 20 25 30 35 45 50 55 60
	θ_z	Relative azimuth angle	°	90
Canopy structure	LAI	Leaf area index		0–15.0
	$LIDF_a$	LIDF parameter a, controls the average leaf slope		−0.35
	$LIDF_b$	LIDF parameter b, controls the distribution's bimodality		−0.15
	S_l	Hot spot parameter		0.1–0.5
	fb	Fraction of brown components		0 (crops)0–0.5 (forests)
	D	Layer dissociation factor		0–0.5
	C_v	Crown cover		0.6–1.0
	zeta	Crown diameter/crown height		0.5–1.0
Leaf optical properties of green layer	C_{ab}	Leaf chlorophyll a + b content	$\mu g\ cm^{-2}$	20–90
	C_w	Relative water		0.6–0.85
	C_{dm}	Leaf dry matter content	$g\ cm^{-2}$	0.003–0.01
	C_s	Leaf brown pigment		0
	N	Leaf mesophyll structure		1.2–2.2
Leaf optical properties of brown layer	C_{ab}	Leaf chlorophyll a + b content	$\mu g\ cm^{-2}$	0
	C_w	Relative water		0.6–0.85
	C_{dm}	Leaf dry matter content	$g\ cm^{-2}$	0.003–0.01
	C_s	Leaf brown pigment		0.1–3.5
	N	Leaf mesophyll structure		1.2–2.2
Soil	soil_b	Soil brightness		0.5–1.0

the total FPAR measured with the largest diffuse ratio (close to 1.0) can be approximated as the diffuse FPAR. Based on the instantaneous diffuse ratio at 10:00 A.M., the sky conditions are divided into clear (diffuse ratio < 0.2), partly clear (diffuse ratio $0.2 \sim 0.8$), and overcast (diffuse ratio > 0.8) conditions. The overcast sky was excluded from the direct FPAR calculation. For clear and partly clear-sky conditions, the instantaneous diffuse ratio during a day was calculated and the diffuse FPAR was determined based on three criteria: (1) the instantaneous diffuse ratio was the largest; (2) the next diffuse ratio measurement should also be large in case of sudden clouds; (3) the incoming PAR measurement is larger than 10.0 $\mu mol\ s^{-1}\ m^{-2}$ and the calculated total FPAR is within 0 to 1.0. The daily maximum diffuse ratio satisfying these criteria along the year was shown in Figure 2. The instantaneous total FPAR measured with the maximum diffuse ratio was treated as a proxy of the diffuse FPAR, and the direct FPAR in the morning was estimated from the diffuse FPAR, the total FPAR, and diffuse ratio at the same time (equation (5)). Besides, the daily instantaneous direct and diffuse APARs at 10:00 A.M. were also calculated from the corresponding PAR and FPAR (equations (2) and (3)). Note that the FPARs measured in these sites include the contributions from all components of the canopy (green leaves, yellow leaves, branches, trunks, and seeds). The rainy days (precipitation > 0) were excluded from the analysis because of the large deviations in the field measurements.

2.3. Estimation of FPARs From Landsat

2.3.1. SLC Model and Simulation

A hybrid soil-leaf-canopy (SLC) model [*Verhoef and Bach*, 2007] was used in this study. The model couples the 4SAIL2 canopy reflectance model, the PROSPECT leaf optical model [*Jacquemoud and Baret*, 1990] and 4SOIL soil reflectance model. 4SAIL2 model is a revised version of the SAIL model [*Verhoef*, 1984]. It separates the canopy into green and brown components by using the fraction brown elements (fb) and the dissociation factor (D), which determines the distribution of the two layers. If the brown leaves are homogeneously distributed, the D value equals to 0; and if all the brown elements are at the bottom of the canopy, the D value equals to 1.0 [*Laurent et al.,* 2011a]. The 4SAIL2 model also includes the crown clumping effect through the crown cover (C_v) and the shape factor (zeta), calculated as the ratio of the crown diameter to the height of

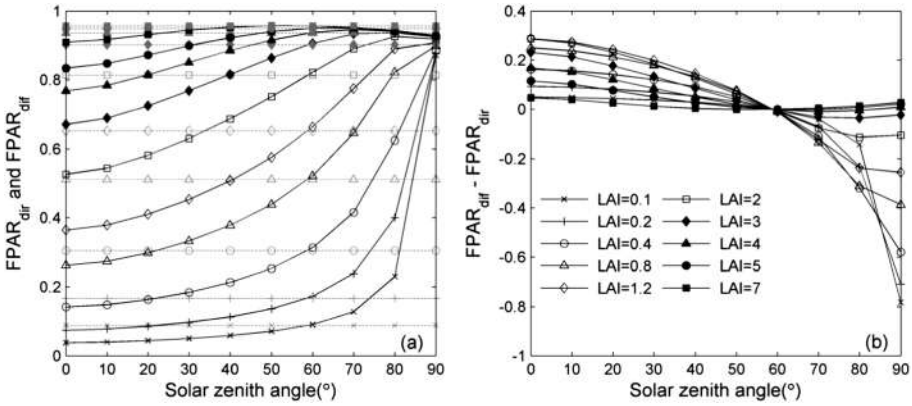

Figure 3. Characteristics of diffuse and direct FPARs under different SAZ and LAI values simulated with SLC model. (a) Diffuse ($FPAR_{dif}$) (gray dashed line) and direct FPAR ($FPAR_{dir}$) (black solid line) variations and (b) the difference between diffuse and direct FPAR, as a function of solar zenith angle and LAI. SLC model parameters: $\theta_v = 0°$, $\theta_z = 90°$, $LIDF_a = -0.35$, $LIDF_b = -0.15$, $S_l = 0.05$, $fb = 0$, $D = 0$, $C_v = 1$, $zeta = 0.2$, $C_{ab} = 60$, $C_w = 0.005$, $C_{dm} = 0.002$, $C_s = 0.03$, $N = 2$, and soil_$b = 0.5$.

the crown center above ground. To simulate the optical properties of green and brown elements, the PROPECT model [*Jacquemoud and Baret*, 1990] includes the concentration in brown material (C_s) [*Verhoef and Bach*, 2003] was used. The leaf optical model was run twice for the green layer and brown layer separately if the fb value is larger than 0. The soil bidirectional reflectance distribution function (BRDF) model 4SOIL was used in SLC, which is an extended version of the Hapke model [*Laurent et al.,* 2011a] that includes hotspot and soil moisture effect.

Table 2 lists the input SLC parameters and their values. The view zenith angle was set as nadir due to the small BRDF effect within a single Landsat scene [*Meroni et al.,* 2013]. To avoid too wide input parameters, the spherical leaf inclination distribution function ($LIDF_a = -0.35$, $LIDF_b = -0.15$) was considered. The fraction brown component (fb) was fixed to 0 for crops, as only the greenup to senescence stages maturation stages were simulated. The fb varies between 0 and 0.5 for forests to take into account the impact of nongreen vegetation (barks, tree trunk, etc.) [*Laurent et al.,* 2011b]. The *D* value was varying from 0 to 0.5 to simulate the distribution of green and brown elements in a canopy. The values of other input parameters were selected in agreement with the literatures [*Baret et al.,* 2007; *Laurent et al.,* 2011b; *Laurent et al.,* 2013; *Verhoef and Bach*, 2007; *Zhang et al.,* 2005].

2.3.2. Landsat Surface Reflectance Data

The Landsat-5 TM surface reflectance products are available through the U.S. Geological Survey Landsat Surface Reflectance Climate Data Record web portal (http://landsat.usgs.gov/CDR_LSR.php). The reflectance product is derived from standard L1t files using the Landsat Ecosystem Disturbance Adaptive Processing System at the NASA Goddard Space Flight Center [*Masek et al.,* 2006]. This product has been validated over several sites and proven to perform successfully over vegetated areas with no adjacent water [*Maiersperger et al.,* 2013]. The reflectance product has been used as an input for deriving global LAI [*Ganguly et al.,* 2012], albedo [*Shuai et al.,* 2011], and crop gross primary production [*Gitelson et al.,* 2012].

A total of 119 Landsat TM scenes without visual cloud and cloud shadow contamination over the study area were selected to derive direct, diffuse, and total FPARs (Table 1). For the crop and DBF sites, images from greenup to senescence stages were used, while all yearlong images were used for the ENF site. For each scene, a 3×3 grid area (90×90 m) centered on the pixel covering the observation tower was extracted to represent the average status of each site. The green, red, and NIR bands were used because they are highly responsive to leaf pigment content, canopy architecture, and leaf structure [*Houborg et al.,* 2009].

2.3.3. The Lookup Table Approach

A widely used lookup table (LUT) approach was selected to invert direct and diffuse FPARs as it could find the global minimum of the cost function. The LUT was generated by running the SLC model in the forward mode with the input variables listed in Table 2. Two separate LUT databases were generated for forests and non-forests sites with different brown pigment fraction values (Table 2). For each SZA, 500,000 randomly

distributed cases were simulated for different variable combinations. The top of canopy reflectance was simulated for each wavelength, and then integrated into the Landsat 5 bands. The final LUT databases used for inversion contain SZA, LAI, the simulated direct and diffuse FPARs, and the simulated surface reflectance in the nadir direction on each Landsat 5 band.

In the actual inversion, the measured Landsat surface reflectance on green, red, and NIR bands, and geometric configuration of each observation (SZA) are required. The nearest simulated geometric configuration was first determined by comparing the simulated and real SZA values. Under this geometric condition, a cost function was established to minimize the differences between simulated and measured surface reflectance for all bands by calculating the relative root-mean-square error (RRMSE) [*Weiss et al.,* 2000]:

$$\mathrm{RRMSE} = \sqrt{\frac{1}{N}\cdot\sum_{i=1}^{N}\left(\frac{\rho_i^{\mathrm{mea}}-\rho_i^{\mathrm{sim}}}{\rho_i^{\mathrm{mea}}}\right)^2} \tag{7}$$

where N is the total number of bands used in the inversion, and ρ_i^{mea} and ρ_i^{sim} are the simulated and satellite-estimated surface reflectances, respectively, for band i.

The RRMSE values were sorted, the first 100 records with the smallest RRMSE were selected and averaged for each pixel [*Darvishzadeh et al.,* 2008]. Site level results were calculated by averaging all pixels within the site. The $\mathrm{FPAR}_{\mathrm{tol}}$ value was calculated from equation (4), using the field-measured diffuse ratio.

3. Results

3.1. The Simulated Direct and Diffuse FPARs

Figure 3 illustrates the relationship between the simulated direct and diffuse FPARs and SZA and LAI. At a given solar zenith angle, both direct and diffuse FPARs increase with LAI. When the solar zenith angle is zero, the direct and diffuse FPARs increase from 0.04 to 0.84 when LAI is less than 2.0. Moreover, these FPARs are nearly saturated ($>$0.9) and increase slightly ($-$0.01) when LAI is larger than 4.0.

The relationship between direct FPAR and SZA is influenced by the LAI value (Figure 3a). At low and intermediate LAIs (LAI $<$ 4), the direct FPAR increases substantially with SZA. And the change rate of direct FPAR with SZA increases with LAI. This can be explained by the longer path of direct radiation penetrating the canopy at higher SZA. When LAI is greater than 4.0, the change rate of direct FPAR with SZA remains invariant for SZA from 0° to 70° and decreases slightly ($-$0.04) for large SZA near the horizon, which can be attributed to FPAR saturation at large LAI. In contrast, for a given LAI, the diffuse FPAR remains invariant for varying SZA values.

The differences between the direct and diffuse FPARs also vary with SZA and LAI (Figure 3b). For canopies with small and intermediate LAIs (LAI $<$ 4), the diffuse FPAR is systematically larger than the direct FPAR (0.02–0.3) when the SZA is smaller than 60°. In contrast, for larger SZA (SZA $>$ 60°), the direct FPAR increases greatly, and the diffuse FPAR is smaller than the direct FPAR ($-0.8 \sim -0.15$). The long penetrating path resulting from large SZA increases the efficiency of a small canopy in absorbing direct PAR. But for canopy with LAI greater than 4, the diffuse FPAR is slightly larger than the direct FPAR for all solar zenith angles.

3.2. The Field FPARs

3.2.1. Seasonal Variation of Field-Measured FPARs

The field FPARs from three crop sites and two DBF sites exhibit a clear seasonal variation (Figure 4). The crop FPAR values increase around the end of May or early June, reach maximum in August and September, and begin to decrease around October. The small phonological variation (e.g., Figure 4c) in different years is mainly due to the plant rotation between maize and soybean [*Verma et al.,* 2005]. At the Bartlett site, the FPARs start to increase in April, reach the peak during June to September, and begin to decrease in early October. The lowest total FPAR of nearly 0.3 can be obtained in the winter season. The FPARs in the Soroe site follow a similar seasonal cycle, with the highest total FPAR (0.98) in July to September and the lowest value (around 0.4) in winter season. The FPARs at the ENF site show little variation throughout the year.

At all sites, the diffuse FPAR is consistently higher than the direct FPAR by 0.02–0.06 (2.53–8.56%) before the senescent (Figure 4 and Table 3), indicating that the green canopy generally absorbs the diffuse PAR more

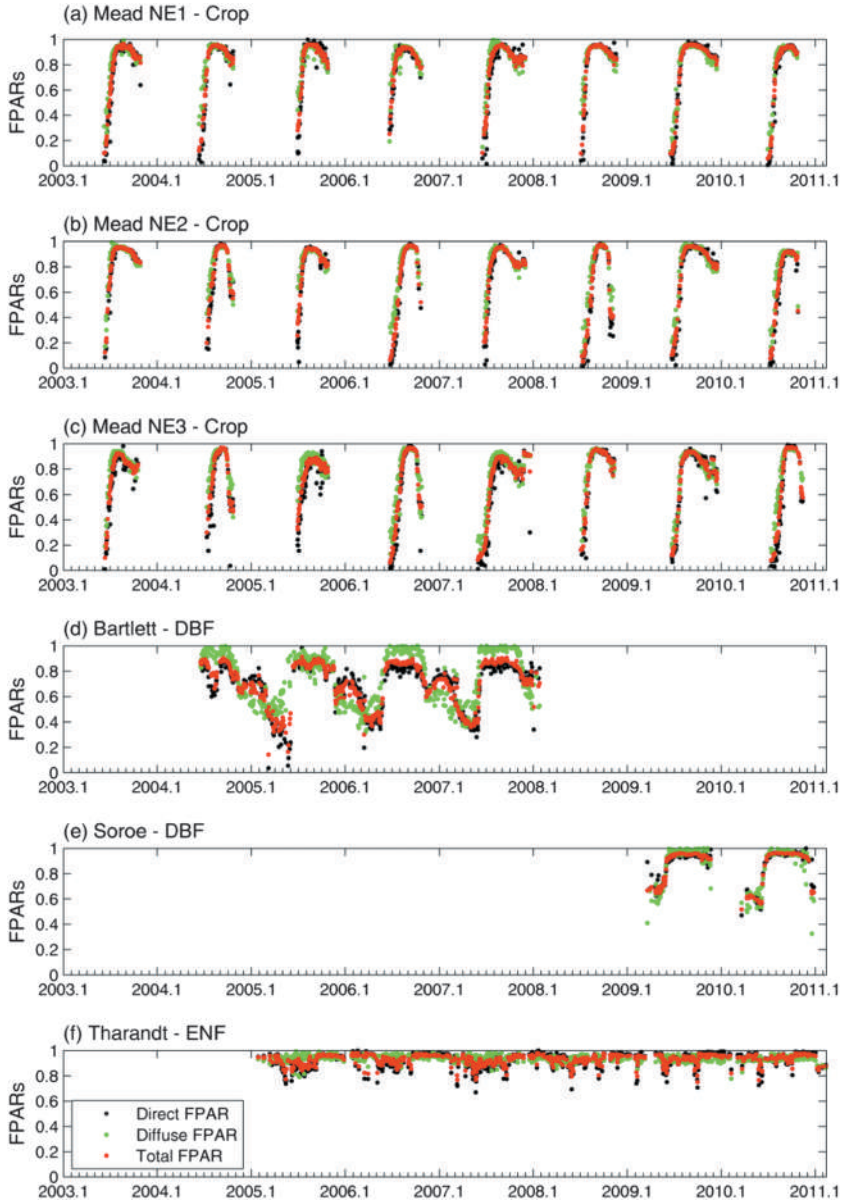

Figure 4. Seasonal variation of field-measured direct FPAR, diffuse FPAR, and total FPAR at six sites, (a) Mead NE1, (b) Mead NE2, (c) Mead NE3, (d) Bartlett, (e) Soroe, and (f) Tharandt.

efficiently than the direct PAR. Moreover, the field measured total FPAR is systematically higher than the direct FPAR (1.38–3.14%). In contrast, the total FPAR is slightly lower than the diffuse FPAR (−4.99 to −1.13%). The field-measured direct FPAR corresponds well to the total FPAR over crops and DBF sites ($R^2 >= 0.85$). It should be noted that the FPARs at the crop and DBF sites include contributions from all parts of the canopy (green leaves, yellow leaves, stems, branches, and seeds), whereas the ENF FPARs correspond only to the top canopy layer (green leaves and branches) as the PAR sensor is 17 m above the ground (Table 1).

The relative differences between field-measured diffuse and direct FPARs vary across the season (Figure 5). For the crops sites, the diffuse FPAR is larger than the direct FPAR during the beginning and ending of the season, and reach a minimum in summer (Figure 5a). The average differences for crop sites before and after the senescence are 9.95% and −3.45%, respectively (Table 4a). For the Bartlett and Soroe sites, the diffuse FPAR is larger than the direct FPAR by 19.38% and 2.68%, respectively, from April to September, but smaller than the latter by −7.56% and −14.74%, respectively, in winter (Figure 5b and Table 4a). Conversely, for the

Table 3. The Linear Regression Relationship Between Field Measured FPAR Components[a]

	Crops				DBF				ENF			
	N	R^2	RMSE	Bias (Relative)	*N*	R^2	RMSE	Bias (Relative)	*N*	R^2	RMSE	Bias (Relative)
$FPAR_{dif}$ versus $FPAR_{dir}$	2169	0.82	0.14	0.06 (8.56%)	935	0.45	0.17	0.04 (5.75%)	1673	0.18	0.07	0.02 (2.53%)
$FPAR_{tol}$ versus $FPAR_{dir}$	2169	0.96	0.06	0.02 (3.14%)	935	0.85	0.08	0.01 (1.81%)	1673	0.67	0.04	0.01 (1.38%)
$FPAR_{tol}$ versus $FPAR_{dif}$	2169	0.91	0.09	−0.04 (−4.99%)	935	0.75	0.11	−0.03 (−3.73%)	1673	0.4	0.04	−0.01 (−1.13%)

[a]$FPAR_{dir}$, $FPAR_{dif}$, and $FPAR_{tol}$ correspond to direct FPAR, diffuse FPAR, and total FPAR, respectively. DBF and ENF represent deciduous broadleaf forest and evergreen needleleaf forest, respectively. *N* represents the number of data points.

ENF site, the seasonality of the differences between direct and diffuse FPARs is less clear than those of the crop and DBF sites (Figure 5c). The diffuse FPAR is slightly lower than the direct FPAR by −1.51% in winter, but higher in other months (2.27%).

The relative differences between field-measured total and direct FPARs also vary across the season (Figure 6). For the crops sites, the relative differences are larger during the early growing season but are close to zero in the peak growing season. The total FPAR is higher than the direct FPAR by 8.0% –14.39% before senescence, but slightly lower than the latter by around 1% after senescent stage. On the DBF sites, the relative differences are generally within ±10%, although there is some scatters in the data points (particularly in winter). The average difference is 4.65% from April to September, and −6.20% during the other months (Table 4b). For the ENF site, the relative differences between the total FPAR and direct FPARs remain constantly small (<1.0%) throughout the year (Table 4b).

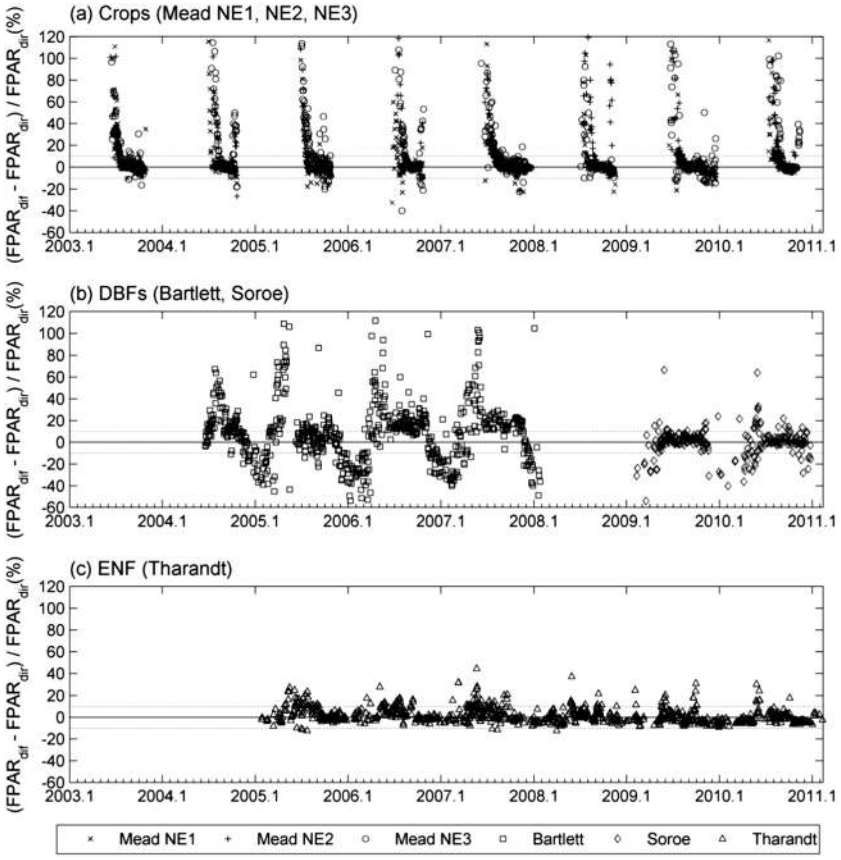

Figure 5. Seasonal variation of the relative difference between diffuse FPAR ($FPAR_{dif}$) and direct FPAR ($FPAR_{dir}$) from field measurements over (a) three crops sites including Mead NE1, NE2, and NE3 sites, (b) two DBF sites including Bartlett and Soroe sites, and (c) Tharandt site. DBF and ENF correspond to deciduous broadleaf forest and evergreen needleleaf forest, respectively. The dashed lines represent the ±10% relative differences.

Table 4a. $FPAR_{dif} - FPAR_{dir}$[a]

	Mead NE1	Mead NE2	Mead NE3	Bartlett	Soroe	Tharandt
Greenup to senescence	5.53%	11.14%	13.17%	19.38%	2.68%	2.27%
Other months	−4.87%	−5.05%	0.42%	−7.56%	−14.74%	−1.51%

[a]The relative difference between field measured diffuse FPAR ($FPAR_{dif}$) and direct FPAR ($FPAR_{dir}$) on five sites during the greenup to senescent stage and the other months. The greenup to senescent stages for crops and DBFs are May to September and April to September, respectively. For ENF site, only the nonwinter and winter (November to February) stages are separated.

3.3. The Landsat-Estimated FPARs

Figure 7 shows examples of direct, diffuse, and total FPARs estimated from Landsat during the summer season over three sites. On crops and DBF sites, the diffuse FPAR exhibits higher values and smaller spatial variation compared to the total FPAR (0.51–3.83%), whereas the direct FPAR is lower than the diffuse FPAR and total FPAR but exhibits a greater spatial variation (0.71–5.65%). On the Tharandt site, direct FPAR show slightly higher FPAR value than the diffuse and total FPAR, but with a smaller spatial variation (2.9%).

The Landsat-estimated diffuse FPAR corresponds very well to the direct FPAR over all sites ($R^2 > 0.98$) (Figure 8a). The diffuse FPAR is higher than the direct FPAR over the crops and DBFs sites by 0.87–2.95%, but slightly lower over the ENF site (−6.8%) (Table 5). The total FPAR has a very good relationship with the direct and diffuse FPAR ($R^2 > 0.99$). On crops and DBF sites, the total FPAR is slightly larger than the direct FPAR by 0.52–0.78%, but lower than the diffuse FPAR by −2.24–0.34%. Conversely, the total FPAR is smaller than the direct FPAR (−3.23%), whereas larger than the diffuse FPAR on the ENF site (3.84%).

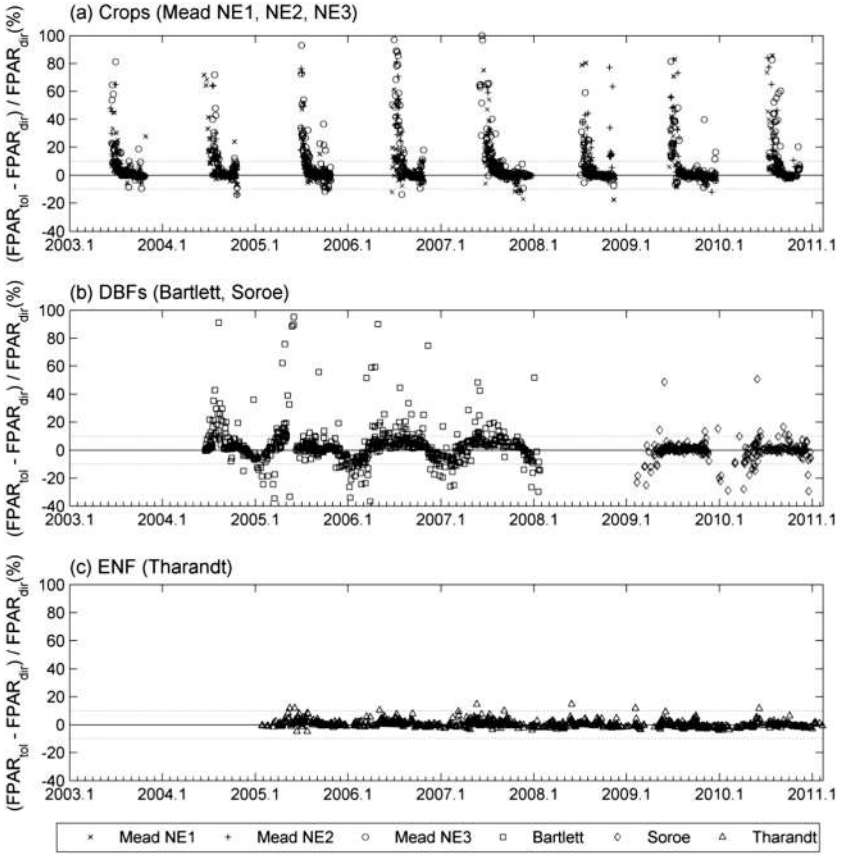

Figure 6. Seasonal variation of the relative difference between total FPAR ($FPAR_{tol}$) and direct FPAR ($FPAR_{dir}$) from field measurements over (a) three crops sites including Mead NE1, NE2, and NE3 sites, (b) two DBF sites including Bartlett and Soroe sites, and (c) Tharandt site. DBF and ENF correspond to deciduous broadleaf forest and evergreen needleleaf forest, respectively. The dashed lines represent the ±10% relative differences.

Table 4b. $FPAR_{tol} - FPAR_{dir}$ [a]

	Mead NE1	Mead NE2	Mead NE3	Bartlett	Soroe	Tharandt
Greenup to senescence	14.39%	16.07%	8.00%	7.87%	1.42%	0.64%
Other months	−1.37%	−1.55%	0.79%	−3.43%	−8.96%	−0.58%

[a]The relative difference between field measured total FPAR ($FPAR_{tol}$) and direct FPAR ($FPAR_{dir}$) on five sites from greenup to senescence and the other months. The greenup to senescent stages for crops and DBFs are May to September and April to September, respectively. For ENF site, only the nonwinter and winter (November to February) stages are separated.

Figure 9 compares the Landsat-estimated FPAR with corresponding field measurements. In general, all Landsat-estimated FPARs correspond well with the field measurements. The Landsat-estimated direct FPAR is slightly higher than the field measurements by 1.17%, whereas the Landsat diffuse FPAR is lower than the field measurements by −6.77%. Compared with the field-measured total FPAR, the Landsat total FPAR is larger by 1.64%, whereas the Landsat direct FPAR is slightly lower by 0.2%.

3.4. The Landsat-Estimated APARs

The differences between FPARs will influence the estimation of APARs. The direct and diffuse APARs were calculated using the field-measured direct and diffuse PAR, multiplied by the corresponding Landsat-estimated direct and diffuse FPARs (equations (2) and (3)) (Figure 10a). Generally, the relative difference between the direct and diffuse APAR decreases with increasing diffuse ratio ($R^2 = 0.76$), and the diffuse APAR tends to be lower than the direct APAR when diffuse ratio smaller than 50%. Conversely, the diffuse APAR is higher than the direct APAR when the diffuse ratio is larger than 50%. On average, the diffuse APAR is lower than the direct APAR by $-421.36\ \mu mol\ s^{-1}\ m^{-2}$ (−37.03%). The Landsat-estimated direct and total APARs were also calculated by multiplying the corresponding Landsat direct and total FPARs, respectively, by the field-measured downwelling

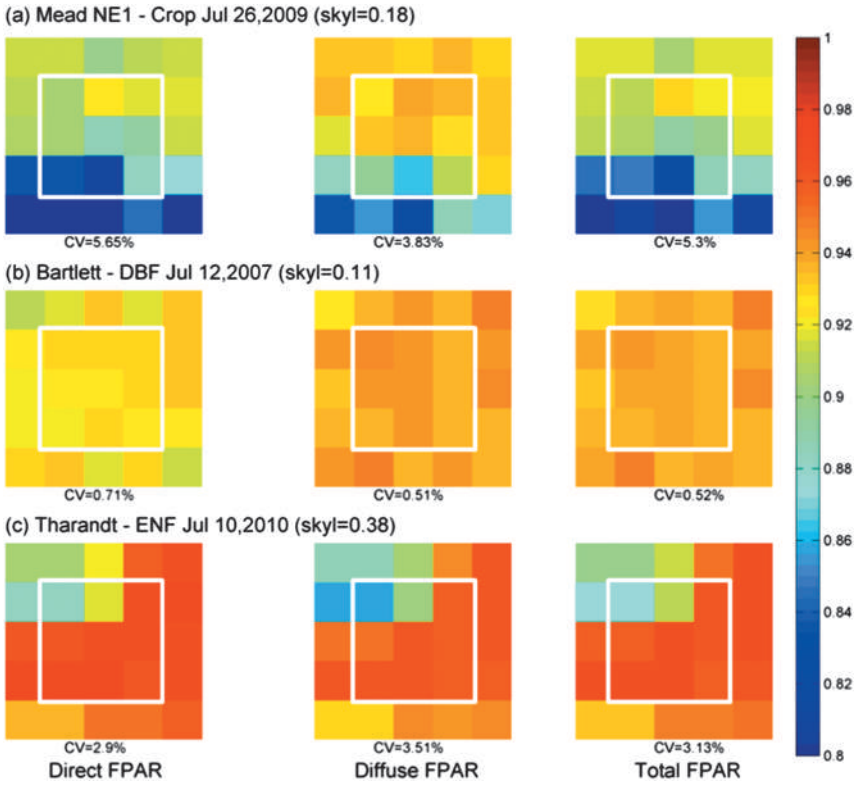

Figure 7. Landsat-estimated direct, diffuse, and total FPAR over three sites, (a) Mead NE1, (b) Bartlett, and (c) Tharandt. skyl represents the diffuse ratio measured in the field. DBF and ENF represent the deciduous broadleaf forest and the evergreen needleleaf forest, respectively. CV represents the coefficient of variation, which is calculated as the ratio of the standard deviation to the mean values. The white square represents the 3 × 3 pixel boarder.

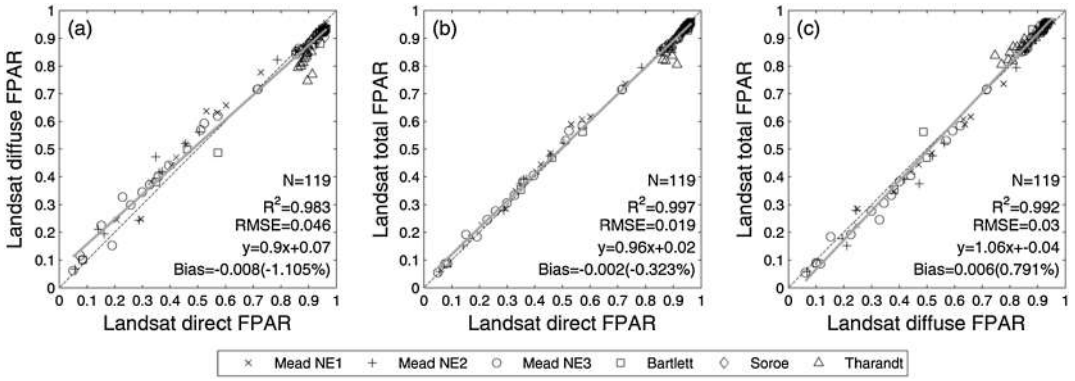

Figure 8. Comparison between Landsat-estimated FPAR components on six FLUXNET sites.

PAR. In general, the total APAR is higher than the direct APAR (277.72 μmol s^{-1} m^{-2}, 62.97%), and the difference increases with the diffuse ratio ($R^2 = 0.76$) (Figure 10b).

4. Discussion

4.1. Comparison of Direct and Diffuse FPARs

Both field and Landsat-estimated direct and diffuse FPARs demonstrate that green canopies have stronger absorption efficiency for diffuse PAR compared to direct PAR for crops, DBFs, and ENF. Our results are similar to those of other studies [*Nouvellon et al.,* 2000; *Thomas et al.,* 2006]. The separated direct and diffuse FPAR information is required in the gross primary production (GPP) calculation in a two-leaf light use efficiency model [*He et al.,* 2013]. Previous studies have also suggested that regional and global primary production models should consider the partition of direct and diffuse PAR [*Gu et al.,* 2002]. The direct and diffuse FPAR estimated in this study would help simulate canopy APAR, photosynthesis, and primary production for direct and diffuse PAR separately.

The relative difference between the direct and diffuse FPAR is mainly related to the canopy structure and the solar zenith angle. When LAI and solar zenith angle are small for crops and DBFs in the spring (Figures 3, 4a, and 4b), the diffuse FPAR is considerably higher than the direct FPAR (5.53–19.38%) because the evenly distributed diffuse radiation can be efficiently absorbed without obvious blocking from the upper layer. When LAI reaches the maximum, the diffuse FPAR is slightly smaller than or equal to the direct FPAR because the top green layer of the canopy absorb most of the direct and diffuse radiation and block the lower parts from the radiation FPAR. During the senescent stage, the decreasing LAI and increasing solar zenith angle lead to a stronger canopy absorption capacity for direct PAR. For the evergreen forests, the canopy structure remains stable during the whole year. The slight seasonal variation of the difference on the ENF site is mainly due to the changes of solar zenith angle. The large solar zenith angle in the winter (>70°) may have diminished the difference of canopy absorption for diffuse and direct FPARs. The nongreen elements of crops and DBFs in senescent stage and of ENF may also influence canopy absorption efficiency for direct and diffuse PARs.

Table 5. The Linear Regression Relationship Between Landsat-Estimated FPAR Components[a]

	Crops				DBF				ENF			
	N	R^2	RMSE	Bias (Relative)	*N*	R^2	RMSE	Bias (Relative)	*N*	R^2	RMSE	Bias (Relative)
$FPAR_{dif}$ versus $FPAR_{dir}$	82	0.988	0.04	0.01 (0.87%)	22	0.99	0.04	0.02 (2.95%)	15	0.17	0.07	−0.06 (−6.80%)
$FPAR_{tol}$ versus $FPAR_{dir}$	82	0.999	0.02	0.004 (0.52%)	22	0.99	0.01	0.01 (0.78%)	15	0.27	0.04	−0.03 (−3.23%)
$FPAR_{tol}$ versus $FPAR_{dif}$	82	0.994	0.03	−0.002 (−0.34%)	22	0.99	0.03	−0.02 (−2.24%)	15	0.75	0.04	0.03 (3.84%)

[a]$FPAR_{dir}$, $FPAR_{dif}$, and $FPAR_{tol}$ correspond to direct FPAR, diffuse FPAR, and total FPAR, respectively. DBF and ENF represent deciduous broadleaf forest and evergreen needleleaf forest, respectively. *N* represents the number of data points.

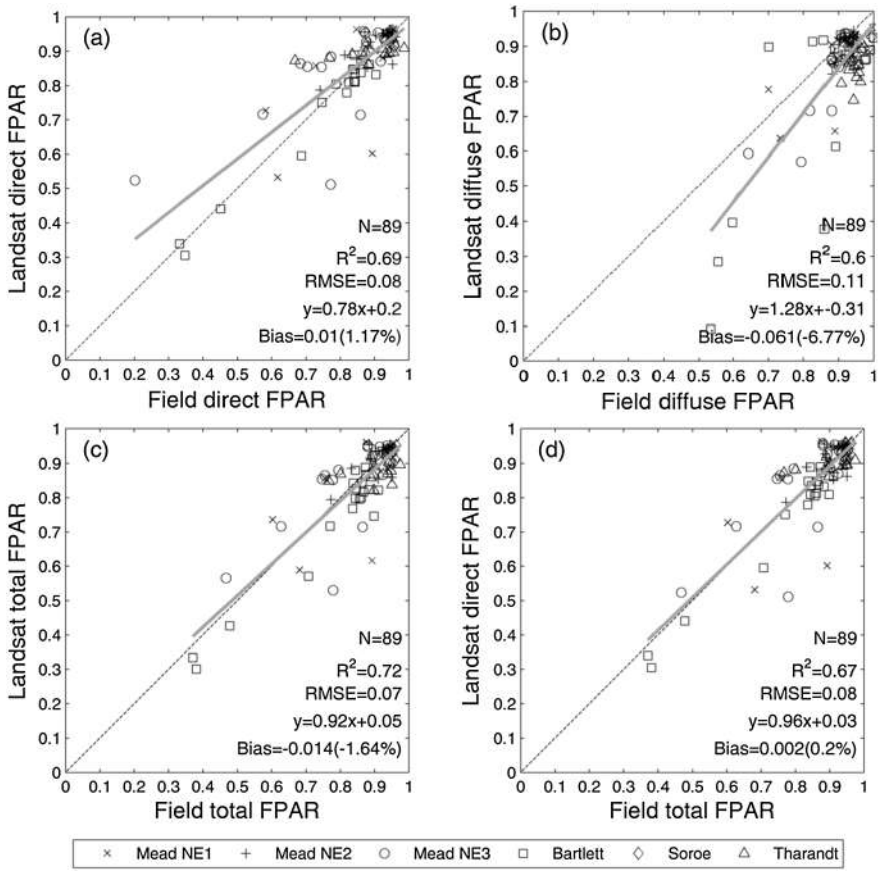

Figure 9. Validation of Landsat-5 estimated FPARs with field measured values. All field measurements are instantaneous values at 10:00 A.M.

The difference between the direct and diffuse APARs is closely related to the diffuse ratio (Figure 10a). This difference is also affected by the amount of the direct and diffuse PARs. In the present study, field-measured direct and diffuse PARs were used in the calculation of APAR. However, extension of the method to a large scale will be limited by the number of sites equipped with diffuse sensors. To date, several remote sensing PARs products have been generated [*Liang et al.,* 2013, 2006; *Zheng et al.,* 2008], but few of them provide direct and diffuse PARs separately. To better estimate canopy photosynthesis and primary production for direct and diffuse PAR separately, both PAR and FPAR may need to be partitioned.

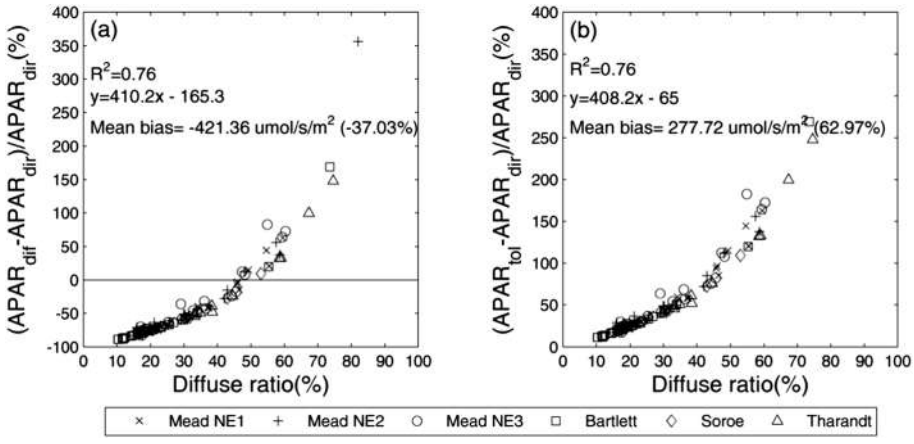

Figure 10. (a) The relative differences between diffuse APAR ($APAR_{dif}$) and direct APAR ($APAR_{dir}$) as a function of diffuse ratio. (b) The relative differences between total APAR ($APAR_{tol}$) and direct APAR ($APAR_{dir}$) as a function of diffuse ratio.

4.2. Comparison of Direct and Total FPARs

The direct FPAR is a function of canopy structure and Sun position but is not impacted by atmospheric conditions. Conversely, the diffuse FPAR is only influenced by the canopy structure. As the weighted sum of direct and diffuse FPAR, the total FPAR is influenced by the canopy structure, solar zenith angle, and the diffuse ratio. Our results from both satellite and field estimates indicate that the direct FPAR is lower than the total FPAR, especially for small LAI (Figure 5 and Table 4b). *Goward and Huemmrich* [1992] have demonstrated that the direct FPAR could underestimate the total FPAR by 10% for LAI < 2. Similar underestimation of the direct FPAR has also been reported by *Tian et al.* [2004]. Our results also show that the differences between direct and total FPARs are very small during the LAI peak stage (Figure 6 and Table 5), indicating that the direct FPAR may be used as a proxy of the total FPAR during this stage.

The direct usage of direct FPARs estimated by satellite in biogeochemical models may underestimate light absorption, gross primary production, and net primary production, especially for canopies with small LAI. The results show that the APAR calculated from direct FPAR is systematically smaller than that calculated from the total FPAR (on average 277.72 μmol s^{-1} m^{-2}). Even under the clear-sky conditions (skyl $< 20\%$), the direct APAR can underestimate the total APAR by up to 20.51% (Figure 10b). It has been reported that the standard MODIS GPP products, estimated from the MODIS black-sky FPAR, underestimate the ground values in tropical forests [*Propastin et al.,* 2012]. The MODIS GPP algorithm may also underestimate the field measurements under cloudy conditions because of the usage of the lower black-sky FPAR caused by the higher diffuse ratio [*Running and Zhao*, 2011]. However, this underestimation can be rectified by using the field-measured total FPAR [*He et al.,* 2010] or satellite-based total FPAR.

Many previous studies have validated the black-sky FPAR products using the field-measured total FPAR [*D'Odorico et al.,* 2014; *Fensholt et al.,* 2004; *Huemmrich et al.,* 2005; *Olofsson and Eklundh*, 2007], and underestimation of the black-sky FPARs has been reported for MODIS [*D'Odorico et al.,* 2014; *Olofsson and Eklundh*, 2007; *Senna et al.,* 2005], Spinning Enhanced Visible and Infrared Imager [*Martínez et al.,* 2013], and MERIS Global Vegetation Index [*D'Odorico et al.,* 2014; *Martínez et al.,* 2013]. These underestimations may be explained, to some degree, by the differences between the black-sky and total FPARs. To meet the requirements of the vegetation modeling community, the total FPAR can be generated in future from satellite data and validated with the corresponding field values.

4.3. Uncertainties and Prospects

The nongreen parts of the canopy will inevitably influence the comparison between field measurements and Landsat estimations. The field-measured FPAR through above and below-canopy PAR sensors includes contributions from the whole canopy, whereas the Landsat estimation only corresponds to the green FPAR. One green layer canopy was simulated and green FPARs were generated for crops. For forests, the brown bark influences the absorption throughout the year. A two-layer canopy consisting of one green and one brown layer was thus simulated using the SLC model. The generated FPARs are not strictly green FPAR but close to the field measurements in definition. Moreover, only images from greenup to senescent stages were selected. The good correspondence between the Landsat-estimated and field-measured FPAR values has shown the feasibility of our method. Indeed, more robust validation of the Landsat FPAR would require the separation of green parts from nongreen parts in field measurements.

The present study provides a means of estimating the direct and diffuse FPARs from the field measurements, by taking the total FPAR obtained with the largest diffuse ratio during a day as an approximation of the diffuse FPAR. The uncertainty of this approximation depends on the diffuse ratio error (compared with 1.0) and the difference between the direct and diffuse FPAR. In this study, the average maximum diffuse fractions (and the standard deviation) during the study period are 0.92 (0.12), 0.87 (0.08), 0.90 (0.1), 0.94 (0.05), 0.99 (0.02), and 0.84 (0.11) on the six sites, respectively (Figure 2). The errors for the diffuse ratio in the ENF site could be up to 16%. The uncertainties of estimated diffuse and direct FPARs could range from 0 (LAI > 3) to 15% (LAI $<= 3$). For other sites, the errors for the diffuse ratio are less than 10%, indicating the uncertainties in the estimated direct and diffuse FPARs may have an inherent error smaller than 10%. The estimated direct and diffuse FPARs can certainly be improved using a diffuse ratio of close to 1.0 when more frequent field PAR measurements (e.g., every minute) are available instead of the 30 min data used.

The Landsat-estimated direct and diffuse FPAR data set in this study can be used to validate the moderate-resolution FPAR products (e.g., black-sky FPAR from MODIS, GEOV1, and JRC-TIP; white-sky FPAR from JRC-TIP). The field-measured diffuse ratio, obtained concurrently with the satellite overpass, is crucial in estimating the total FPARs from the satellite. However, field data are usually limited by the sparse number of observations and clouds. For regional and global FPAR estimation, the diffuse ratio data may be obtained through satellite observations. The digital hemispheric photography provides a promising way to measure the direct and diffuse FPAR in the field [*Weiss and Baret,* 2010a, 2010b]. Separated estimations of PAR and FPAR for direct and diffuse components provide an opportunity to improve the estimation of canopy photosynthesis and primary production.

5. Conclusions

This paper developed a method to estimate the direct, diffuse, and total FPARs from Landsat 30 m surface reflectance data by using a canopy radiative transfer model and a lookup table inversion algorithm. Instantaneous direct and diffuse FPARs were estimated from field-measured FPAR over crops, deciduous broadleaf forests, and evergreen needleleaf forests. The differences between the direct and diffuse FPARs are mainly related to canopy structure and the solar zenith angle. The direct FPAR is generally lower than the total FPAR, and this difference increases for canopies with small LAI. The total FPAR should be generated from current satellite sensors, and the differences in FPAR definitions should be considered in the estimation of APAR in vegetation models. More frequent field measurements are necessary to improve the accuracy of ground FPAR measurements and to validate instantaneous satellite products. The present approach can be extended to estimate regional and global direct and diffuse FPAR products utilizing existing and future satellite data.

Acknowledgments

This study was supported by the Hundred Talent Program of the Chinese Academy of Sciences and the National Natural Science Foundation of China (41171333) (H. F.). We thank the FLUXNET network (http://public.ornl.gov/FLUXNET/), the site principal investigators, data collection and processing staff, and the agencies and institutions that funded long-term measurements at these sites. We thank the Landsat Surface Reflectance CDR project (http://landsat.usgs.gov/CDR_LSR.php) for providing long-term Landsat surface reflectance. The authors are thankful for the fruitful discussions with Frederic Baret and the comments from Shanshan Wei on an early version of the manuscript. We thank Wout Verhoef for the SLC software. We thank two anonymous reviewers and the Editors whose constructive comments help improved the manuscript.

References

Baret, F., et al. (2007), LAI, fAPAR and fCover CYCLOPES global products derived from VEGETATION Part 1: Principles of the algorithm, *Remote Sens. Environ.*, *110*, 275–286.

Baret, F., M. Weiss, R. Lacaze, F. Camacho, H. Makhmara, P. Pacholcyzk, and B. Smets (2013), GEOV1: LAI and FAPAR essential climate variables and FCOVER global time series capitalizing over existing products. Part1: Principles of development and production, *Remote Sens. Environ.*, *137*, 299–309.

Dai, Y., X. Zeng, R. E. Dickinson, I. Baker, and G. B. Bonan (2003), The Common Land Model (CLM) version 1.0, *Bull. Am. Meteorol. Soc.*, *84*, 1013–1023.

Darvishzadeh, R., A. Skidmore, M. Schlerf, and C. Atzberger (2008), Inversion of a radiative transfer model for estimating vegetation LAI and chlorophyll in a heterogeneous grassland, *Remote Sens. Environ.*, *112*, 2592–2604.

D'Odorico, P., A. Gonsamo, B. Pinty, N. Gobron, N. Coops, E. Mendez, and M. E. Schaepman (2014), Intercomparison of fractional absorbed photosynthetically active radiation products derived from satellite data over Europe, *Remote Sens. Environ.*, *142*, 141–154.

Fensholt, R., I. Sandholt, and M. S. Rasmussen (2004), Evaluation of MODIS LAI, fAPAR and the relation between fAPAR and NDVI in a semi-arid environment using in situ measurements, *Remote Sens. Environ.*, *91*, 490–507.

Foley, J. A., C. Prentice, N. Ramankutty, S. Levis, D. Pollard, S. Sitch, and A. Haxeltine (1996), An integrated biosphere model of land surface processes, terrestrial carbon balance, and vegetation dynamics, *Global Biogeochem. Cycles*, *10*, 603–628, doi:10.1029/96GB02692.

Ganguly, S., et al. (2012), Generating global Leaf Area Index from Landsat: Algorithm formulation and demonstration, *Remote Sens. Environ.*, *122*, 185–202.

GCOS (2011), Systematic observation requirements for satellite-based products for climate, 2011 update, supplemental details to the satellite-based component of the implementation plan for the Global Observing System for Climate in Support of the UNFCCC (2010 update), Reference Number GCOS-154, 138 pp. [Available at http://www.wmo.int/pages/prog/gcos/Publications/gcos-154.pdf.]

Gitelson, A. A., Y. Peng, J. G. Masek, D. C. Rundquist, S. Verma, A. Suyker, J. M. Baker, J. L. Hatfield, and T. Meyers (2012), Remote estimation of crop gross primary production with Landsat data, *Remote Sens. Environ.*, *121*, 404–414.

Gobron, N., and M. M. Verstraete (2009), Assessment of the status of the development of the standards for the terrestrial essential climate variables: Fraction of Absorbed Photosynthetically Active Radiation (FAPAR), Version 10, Version 10, 23 pp., Global Terrestrial Observing System, Rome. [Available at http://www.fao.org/gtos/doc/ECVs/T10/T10.pdf.]

Gobron, N., B. Pinty, M. Verstraete, and Y. Govaerts (1999), The MERIS Global Vegetation Index (MGVI): Description and preliminary application, *Int. J. Remote Sens.*, *20*(9), 1917–1927.

Gobron, N., et al. (2006), Evaluation of fraction of absorbed photosynthetically active radiation products for different canopy radiation transfer regimes: Methodology and results using Joint Research Center products derived from SeaWiFS against ground-based estimations, *J. Geophys. Res.*, *111*, D13110, doi:10.1029/2005JD006511.

Goward, S. N., and K. F. Huemmrich (1992), Vegetation canopy PAR absorptance and the normalized difference vegetation index: An assessment using the SAIL model, *Remote Sens. Environ.*, *39*, 119–140.

Grumwald, T., and C. Bernhofer (2007), A decade of carbon, water and energy flux measurements of an old spruce forest at the Anchor Station Tharandt, *Tellus*, *59B*, 387–396.

Gu, L., D. Baldocchi, S. B. Verma, T. A. Black, T. Vesala, E. M. Falge, and P. R. Dowty (2002), Advantages of diffuse radiation for terrestrial ecosystem productivity, *J. Geophys. Res.*, *107*(D6), 4050, doi:10.1029/2001JD001242.

He, M., Y. Zhou, G. Liu, W. Ju, X. Li, and G. Zhu (2010), Validation of MODIS gross primary productivity for a subtropical coniferous plantation in Southern China, in *Geoinformatics*, *2010 18th International Conference on June 18–20*.

He, M., et al. (2013), Development of a two-leaf light use efficiency model for improving the calculation of terrestrial gross primary productivity, *Agric. For. Meteorol.*, *173*, 28–39.

Houborg, R., M. Anderson, and C. Daughtry (2009), Utility of an image-based canopy reflectance modeling tool for remote estimation of LAI and leaf chlorophyll content at the field scale, *Remote Sens. Environ.*, *113*, 259–274.
Huemmrich, K. F., J. L. Privette, M. Mukelabai, R. B. Myneni, and Y. Knyazikhin (2005), Time-series validation of MODIS land biophysical products in a Kalahari woodland, Africa, *Int. J. Remote Sens.*, *26*, 4381–4398.
Jacquemoud, S., and F. Baret (1990), PROSPECT: A model of leaf optical properties spectra, *Remote Sens. Environ.*, *34*, 75–91.
Jenkins, J. P., A. D. Richardson, B. H. Braswell, S. V. Ollinger, D. Y. Hollinger, and M.-L. Smith (2007), Refining light-use efficiency calculations for a deciduous forest canopy using simultaneous tower-based carbon flux and radiometric measurements, *Agric. For. Meteorol.*, *143*, 64–79.
Knyazikhin, Y., J. V. Martonchik, R. B. Myneni, D. J. Diner, and S. W. Running (1998), Synergistic algorithm for estimating vegetation canopy leaf area index and fraction of absorbed photosynthetically active radiation from MODIS and MISR data, *J. Geophys. Res.*, *103*, 257–275, doi:10.1029/97JA02771.
Laurent, V. C. E., W. Verhoef, J. G. P. W. Clevers, and M. E. Schaepman (2011a), Estimating forest variables from top-of-atmosphere radiance satellite measurements using coupled radiative transfer models, *Remote Sens. Environ.*, *115*, 1043–1052.
Laurent, V. C. E., W. Verhoef, J. G. P. W. Clevers, and M. E. Schaepman (2011b), Inversion of a coupled canopy–atmosphere model using multi-angular top-of-atmosphere radiance data: A forest case study, *Remote Sens. Environ.*, *115*, 2603–2612.
Laurent, V. C. E., W. Verhoef, A. Damm, M. E. Schaepman, and J. G. P. W. Clevers (2013), A Bayesian object-based approach for estimating vegetation biophysical and biochemical variables from APEX at-sensor radiance data, *Remote Sens. Environ.*, *139*, 6–17.
Liang, S., T. Zheng, R. Liu, H. Fang, S.-C. Tsay, and S. Running (2006), Estimation of incident photosynthetically active radiation from Moderate Resolution Imaging Spectrometer data, *J. Geophys. Res.*, *111*, D15208, doi:10.1029/2005JD006730.
Liang, S., et al. (2013), A long-term Global LAnd Surface Satellite (GLASS) data-set for environmental studies, *Int. J. Digital Earth*, doi:10.1080/17538947.2013.805262.
Maiersperger, T. K., P. L. Scaramuzza, L. Leigh, S. Shrestha, K. P. Gallo, C. B. Jenkerson, and J. L. Dwyer (2013), Characterizing LEDAPS surface reflectance products by comparisons with AERONET, field spectrometer, and MODIS data, *Remote Sens. Environ.*, *136*, 1–13.
Martínez, B., F. Camacho, A. Verger, F. J. García-Haro, and M. A. Gilabert (2013), Intercomparison and quality assessment of MERIS, MODIS and SEVIRI FAPAR products over the Iberian Peninsula, *Int. J. Appl. Earth Obs. Geoinformation*, *21*, 463–476.
Masek, J. G., E. F. Vermote, N. E. Saleous, R. Wolfe, F. G. Hall, K. F. Huemmrich, F. Gao, J. Kutler, and T.-K. Lim (2006), A Landsat surface reflectance dataset for North America, 1990–2000, *IEEE Geosci. Remote Sens. Lett.*, *3*, 68–72.
Meroni, M., C. Atzberger, C. Vancutsem, N. Gobron, F. Baret, R. Lacaze, H. Eerens, and O. Leo (2013), Evaluation of agreement between space remote sensing SPOT-VEGETATION fAPAR time series, *IEEE Trans. Geosci. Remote Sens.*, *51*, 1951–1962.
Nouvellon, Y., A. Bégué, M. S. Moran, D. L. Seen, S. Rambal, D. Luquet, G. Chehbouni, and Y. Inoue (2000), PAR extinction in shortgrass ecosystems: Effects of clumping, sky conditions and soil albedo, *Agric. For. Meteorol.*, *105*, 21–41.
Ollinger, S. V., and M.-L. Smith (2005), Net primary production and canopy nitrogen in a temperate forest landscape: An analysis using imaging spectroscopy modeling and field data, *Ecosystem*, *8*, 760–778.
Olofsson, P., and L. Eklundh (2007), Estimation of absorbed PAR across Scandinavia from satellite measurements. Part II: Modeling and evaluating the fractional absorption, *Remote Sens. Environ.*, *110*, 240–251.
Pilegaard, K., P. Hummelshøj, N. O. Jensen, and Z. Chen (2001), Two years of continuous CO2 eddy-flux measurements over a Danish beech forest, *Agric. For. Meteorol.*, *107*, 29–41.
Pinty, B., I. Andredakis, M. Clerici, T. Kaminski, M. Taberner, M. M. Verstraete, N. Gobron, S. Plummer, and J. L. Widlowski (2011), Exploiting the MODIS albedos with the Two-stream Inversion Package (JRC-TIP): 1. Effective leaf area index, vegetation, and soil properties, *J. Geophys. Res.*, *116*, D09105, doi:10.1029/2010JD015372.
Propastin, P., A. Ibrom, A. Knohl, and S. Erasmi (2012), Effects of canopy photosynthesis saturation on the estimation of gross primary productivity from MODIS data in a tropical forest, *Remote Sens. Environ.*, *121*, 252–260.
Running, S., and M. Zhao (2011), Note to users on use of MODIS GPP/NPP (MOD17) datasets. [Available at https://lpdaac.usgs.gov/sites/default/files/public/about/docs/MOD17_NTSG_Note.pdf.]
Sellers, P. J. (1985), Canopy reflectance, photosynthesis and transpiration, *Int. J. Remote Sens.*, *6*, 1335–1372.
Senna, M. C. A., M. H. Costa, and Y. E. Shimabukuro (2005), Fraction of photosynthetically active radiation absorbed by Amazon tropical forest: A comparison of field measurements, modeling, and remote sensing, *J. Geophys. Res.*, *110*, G01008, doi:10.1029/2004JG000005.
Shuai, Y., J. G. Masek, F. Gao, and C. B. Schaaf (2011), An algorithm for the retrieval of 30-m snow-free albedo from Landsat surface reflectance and MODIS BRDF, *Remote Sens. Environ.*, *115*, 2204–2216.
Thomas, V., D. A. Finch, J. H. McCaughey, T. Noland, L. Rich, and P. Treitz (2006), Spatial modelling of the fraction of photosynthetically active radiation absorbed by a boreal mixedwood forest using a lidar-hyperspectral approach, *Agric. For. Meteorol.*, *140*, 287–307.
Tian, Y., et al. (2004), Comparison of seasonal and spatial variations of leaf area index and fraction of absorbed photosynthetically active radiation from Moderate Resolution Imaging Spectroradiometer (MODIS) and Common Land Model, *J. Geophys. Res.*, *109*, D01103, doi:10.1029/2003JD003777.
Verhoef, W. (1984), Light scattering by leaf layers with application to canopy reflectance modeling: The SAIL Model, *Remote Sens. Environ.*, *16*, 125–141.
Verhoef, W., and H. Bach (2003), Simulation of hyperspectral and directional radiance images using coupled biophysical and atmospheric radiative transfer models, *Remote Sens. Environ.*, *87*, 23–41.
Verhoef, W., and H. Bach (2007), Coupled soil–leaf-canopy and atmosphere radiative transfer modeling to simulate hyperspectral multi-angular surface reflectance and TOA radiance data, *Remote Sens. Environ.*, *109*, 166–182.
Verma, S. B., et al. (2005), Annual carbon dioxide exchange in irrigated and rainfed maize-based agroecosystems, *Agric. For. Meteorol.*, *131*, 77–96.
Weiss, M., and F. Baret (2010a), CAN-EYE V6.1 User Manual. [Available at http://www6.paca.inra.fr/can-eye/Documentation-Publications/Documentation.]
Weiss, M., and F. Baret (2010b), fAPAR (fraction of Absorbed Photosynthetically Active Radiation) estimates at various scale, *34th International Symposium on Remote Sensing of Environment*. [Available at http://www.isprs.org/proceedings/2011/ISRSE-34/211104015Final00926.pdf.]
Weiss, M., F. Baret, R. B. Myneni, A. Pragnère, and Y. Knyazikhin (2000), Investigation of a model inversion technique to estimate canopy biophysical variables from spectral and directional reflectance data, *Agronomie*, *20*, 3–22.
Zhang, Q., X. Xiao, B. Braswell, E. Linder, F. Baret, and B. Moore III (2005), Estimating light absorption by chlorophyll, leaf and canopy in a deciduous broadleaf forest using MODIS data and a radiative transfer model, *Remote Sens. Environ.*, *99*, 357–371.
Zheng, T., S. Liang, and K. Wang (2008), Estimation of incident photosynthetically active radiation from GOES visible imagery, *J. Appl. Meteorol. Climatol.*, *47*, 853–868.